Interneuronal mechanisms of hippocampal theta oscillations in a full-scale model of the rodent CA1 circuit

Marianne J. Bezaire[2#], Ivan Raikov[1,2], Kelly Burk[2], Dhrumil Vyas[2], and Ivan Soltesz[1]

[1]Department of Neurosurgery, Stanford University, Stanford, CA 94305

[2]Department of Anatomy and Neurobiology, University of California, Irvine, CA 92697

[#]Present address: Department of Psychological and Brain Sciences, Boston University, Boston, MA 02215

Key words: Network, model, oscillation, diversity, theta, inhibition, hippocampus

Correspondence

Marianne Bezaire, PhD

Email: marianne.bezaire@gmail.com

Abstract

The hippocampal theta rhythm plays important roles in information processing; however, the mechanisms of its generation are not well understood. We developed a data-driven, supercomputer-based, full-scale (1:1) model of the rodent CA1 area and studied its interneurons during theta oscillations. Theta rhythm with phase-locked gamma oscillations and phase-preferential discharges of distinct interneuronal types spontaneously emerged from the isolated CA1 circuit without rhythmic inputs. Perturbation experiments identified parvalbumin-expressing interneurons and neurogliaform cells, as well as interneuronal diversity itself, as important factors in theta generation. These simulations reveal new insights into the spatiotemporal organization of the CA1 circuit during theta oscillations.

Introduction

The hippocampal CA1 area supports diverse cognitive tasks including learning, memory, and spatial processing (Squire, 1992; Remondes and Schuman, 2004; Manns et al., 2007; Moser et al., 2008). These cognitive tasks are thought to require coordination of neuronal activity provided by physiological network oscillations, including the theta rhythm (Buzsáki, 2002; Buzsáki and Moser, 2013). In rodents, hippocampal theta is a 5-10 Hz oscillation in the local field potential (LFP) and neuronal firing probabilities (Soltesz and Deschenes, 1993; Lee et al., 1994; Ylinen et al., 1995; Klausberger and Somogyi, 2008; Varga et al., 2012, 2014), occurring during locomotion and in REM sleep (Buzsáki, 2002). Though several major afferents provide theta-frequency rhythmic input to the CA1 *in vivo* (Soltesz and Deschenes, 1993; Buzsáki, 2002; Fuhrmann et al., 2015), recent reports indicate the presence of spontaneous theta-frequency LFP oscillations even in the isolated whole CA1 preparation *in vitro* (Goutagny et al., 2009; Amilhon et al., 2015). Therefore, the latter studies suggest an intrinsic ability of the CA1 circuit to generate some form of theta waves even without rhythmic external inputs. However, the intra-CA1 mechanisms that may contribute to the generation of the theta rhythm are not well understood (Colgin, 2013, 2016).

Here we investigated the ability of the CA1 to generate intrinsic theta oscillations using a uniquely biological data-driven, full-scale computer model of the isolated CA1 network. Recent advances in supercomputing power and high-quality synaptic connectivity data present the intriguing opportunity to develop full-scale models where every biological synapse and neuron is explicitly represented. In principle, such full-scale models of mammalian circuits comprising hundreds of thousands of neurons of distinct types advantageously avoid the connectivity scaling tradeoff that besets reduced-scale models: smaller models of large networks with realistic single cell electrophysiological properties (e.g., input resistance and resting membrane potential) remain silent unless synaptic strengths or numbers are arbitrarily increased beyond the biologically relevant levels to compensate for fewer inputs to their model cells (e.g., Dyhrfjeld-Johnsen et al. (2007b); Sterratt et al. (2011)). Biological relevance may also increase as other network components are modeled in greater detail. However, full-scale models

require considerable computational resources. Further, such detailed models have a large parameter space which risks being sub-optimally constrained by neurobiological properties that are only partially quantified (Sejnowski et al., 1988). Because the CA1 area is one of the most extensively studied brain regions, there are abundant anatomical and electrophysiological data about its organization, making it a logical choice for the development of a full-scale model. The CA1 area is also worth modeling at full-scale because of the diverse cognitive tasks it supports. These tasks likely require the simultaneous processing of thousands of incoming and outgoing signals, and full-scale network models, at least in principle, have the potential to match this *in vivo* processing capacity.

In this paper, we describe the development of a full-scale CA1 computational network model of unprecedented biological detail and its application to gain insights into the roles and temporal organization of CA1 interneurons during theta rhythm. The simulated full-scale CA1 circuit was able to spontaneously generate theta waves as well as phase-locked gamma oscillations. Furthermore, distinct interneuron types discharged at particular phases of theta, demonstrating that phase-preferential firing (Klausberger et al., 2003, 2004, 2005; Ferraguti et al., 2005; Jinno et al., 2007; Fuentealba et al., 2008; Klausberger and Somogyi, 2008; Varga et al., 2012; Lapray et al., 2012; Katona et al., 2014; Varga et al., 2014) originates in part within the CA1 network. Perturbation experiments revealed that parvalbumin-expressing (PV+) interneurons, neurogliaform cells, connections beween CA1 pyramidal cells, and interneuronal diversity were important for theta generation. These results provide new mechanistic insights into the emergence of the theta rhythm from within the CA1 circuitry and the role of interneurons in theta oscillations.

Results

Development of data-driven, full-scale model of the isolated CA1

Details of the full-scale model are described in the Methods, and the most important features are illustrated in Figures 1 and 2 and summarized here. Briefly, CA1 model cells were evenly distributed

within their respective layers in a 3-dimensional prism with realistic dimensions for the rodent hippocampal CA1 region (Figure 1A and 1B). The model network contained 338,740 cells (similar to the biological CA1 in rats, including 311,500 pyramidal cells and 27,240 interneurons) (Figure 1D-1E and Figure 1 - figure supplement 1). In addition, the network also incorporated 454,700 artificial stimulating cells (spiking units with random, Poisson-distributed inter-spike intervals) to simulate afferents to CA1; the cell type-specific distribution, dendritic position, amplitude and kinetics of the excitatory input synapses were all experimentally constrained by afferent CA3 and entorhinal cortical data. Cell type-specific connectivity data, including cell numbers (Figure 1D) and convergence and divergence values (Figure 1E; Figure 1 - figure supplement 1 and Table 1) were taken without alteration from our previously published, in-depth, quantitative assessment of the CA1 circuit (Bezaire and Soltesz, 2013). Anatomical constraints of the connectivity were implemented in the model by accounting for the distribution of the axonal boutons as a function of longitudinal and transverse distance from the presynaptic cell soma (Figure 1 - figure supplement 2). The afferent divergence and convergence onto the cells were also anatomically patterned, maintaining the topographical arrangement seen experimentally (Hongo et al., 2015), for a total of 5.19 billion synaptic connections in the model network. In addition, the remaining parameters that could not be constrained by experimental data were documented, with the assumptions used to arrive at them explicitly listed in Table 2 of Bezaire and Soltesz (2013) and additional parameter calculations described in the Appendix Section 3 of the present paper. To highlight the many constraints applied in the current work and address the unconstrained model parameters, we characterized all model components (constrained and unconstrained) in experimental terms, comparing with experimental data where possible (Figure 2; Appendix). For a four second simulation, the full-scale model required 3-4 terabytes (TB) of RAM and four hours of execution time on a supercomputer using ~3000 processors (or up to 12 hours for simulations calculating a high-accuracy local field potential (LFP) analog). Additional details and data about model performance are available in Table 2 and Bezaire et al. (2016).

An important set of constraints was the electrophysiology and other properties of individual cells and synapses (Figure 2; Figure 2 - Source Data 3 - 27; Tables 3 and 4) that were based on ex-

perimental data Lee et al. (2016); Quattrocolo and Maccaferri (2016). Briefly, our pyramidal cell model (Poolos et al., 2002) contained 200 compartments in a realistic morphology and six fully characterized ion channel types with kinetics and densities based on anatomical location within the cell (Figure 2A-2C; Figure 2 - Source Data 1 - 2). We included eight model interneuron types (Klausberger and Somogyi, 2008; Soltesz, 2006; Armstrong and Soltesz, 2012): PV+ basket cells (these fast-spiking cells synapse on the somata and proximal dendrites of CA1 pyramidal cells), cholecystokinin+ (CCK+) basket cells (these regular-spiking cells also innervate the somata and proximal dendrites, but have properties and functions distinct from the PV+ basket cells), bistratified cells (these PV+ and somatostatin+ (SOM+) fast-spiking cells innervate the basal and apical dendritic trees), axo-axonic cells (these PV+ fast-spiking cells exclusively synapse on the axon initial segments of pyramidal cells and are also known as chandelier cells), Schaffer Collateral-Associated (SC-A) cells (these CCK+, regular-spiking cells innervate dendrites in the stratum radiatum), oriens-lacunosum-moleculare (O-LM) cells (these SOM+ cells project to the distal dendrites in the stratum lacunosum-moleculare though their somata are located in the stratum oriens), neurogliaform cells (these cells have relatively small dendrites and a dense axonal cloud, and they innervate distal dendrites in the stratum lacunosum-moleculare), and ivy cells (these cells are similar to neurogliaform cells, but innervate proximal dendrites) (Figure 2D-2J). Some interneurons in the model, as in the biological network, also innervated other interneurons (Table 1). For greater detail of model connectivity, including convergence per single cell, synaptic amplitude, and other factors, see the Appendix. These cell types collectively comprise the majority (~70%) of known CA1 interneurons (Bezaire and Soltesz, 2013). The remaining 30% of the interneurons were not included in the model due to paucity of quantitative data (Bezaire and Soltesz, 2013). We differentiated the interneurons by their electrophysiological profiles, connectivity patterns, synaptic properties, and anatomical abundance (Gulyas et al., 1991; Hajos and Mody, 1997; Maccaferri et al., 2000; Megías et al., 2001; Lee et al., 2010; Krook-Magnuson et al., 2011; Bezaire and Soltesz, 2013; Lee et al., 2014). The synaptic connections were implemented using double exponential mechanisms to better fit experimental data on rise and decay time constants. We used experimental data to constrain the synaptic kinetics, am-

plitudes, and locations on the postsynaptic cell (Figures 1E, 2K, and 2L). We implemented the model in parallel NEURON (Carnevale and Hines, 2005) and executed the simulations on several supercomputers. All model results, characterizations, and experimental comparisons are publically available.

Emergence of spontaneous theta and gamma oscillations in the full-scale model in the absence of rhythmic external inputs

First, we examined whether the well-constrained, biologically detailed, full-scale CA1 model could oscillate spontaneously within the physiological range. Based on reports of spontaneous theta-frequency LFP oscillations in the isolated CA1 preparation (Goutagny et al., 2009), we expected a sufficiently constrained CA1 model to generate spontaneous theta rhythm when given tonic, arrhythmic excitation. We varied the magnitude of arrhythmic, tonic excitation to the network (by systematically changing the mean spiking frequency of the artificial stimulating cells, see above) and identified excitation levels where the network developed a stable, spontaneous theta rhythm (5-10 Hz; Figures 3 and 4; Figure 3 - Source Data 1 - 3 and Figure 4 - Source Data 1 - 2). The pyramidal cell spikes (Figures 3C and 3D) exhibited peak power around the theta frequency of 7.8 Hz (Figure 4 and Table 7). Importantly, every measure of network activity showed theta oscillations, including the somatic intracellular membrane potential from individual cells (Figure 3D), the spike times of individual cells and all cells collectively (Figure 3C), and aggregate measures such as the spike density function (Szűcs, 1998) per cell type and the LFP analog (Figures 3A and 4; see also Figure 4 - figure supplement 1). In all of these measures of network activity, theta was apparent within one theta period of the simulation start. The theta oscillation was stable, maintaining a steady power level throughout the duration of the oscillation (Figure 4A). To our knowledge, this is the first strictly data-driven, full-scale computational network model of the CA1 that exhibits spontaneous theta rhythm without rhythmic synaptic inputs.

In addition to theta rhythm, the model network displayed gamma oscillations (25-80 Hz; Figures 3B and 4D), as expected based on *in vivo* data (Soltesz and Deschenes, 1993; Tort et al., 2009;

Colgin and Moser, 2010) and *in vitro* slice data showing 65-75 Hz gamma oscillations arising in response to theta rhythmic network stimulation (Butler et al., 2016). The amplitude envelope of the gamma oscillation was phase-locked to the theta rhythm (Figure 3A, 3B and 4C), as it is in the biological CA1, representing cross-frequency coupling (Soltesz and Deschenes, 1993; Bragin et al., 1995; Buzsáki et al., 2003; Jensen and Colgin, 2007; Belluscio et al., 2012). The highest amplitude of the gamma oscillations in the model was observed at the theta trough ($0^o/360^o$) in the pyramidal layer LFP analog (Figure 4C). Because the current study focused primarily on theta oscillations and experimental data from the isolated CA1 are available only for the theta rhythm (Goutagny et al., 2009; Amilhon et al., 2015), the gamma oscillations were not examined further in the present study.

These results demonstrate that, in spite of gaps in our knowledge, our model was sufficiently well-constrained by experimental data that it generated theta and gamma oscillations on its own, without extrinsic rhythmic inputs or deliberate tuning of intrinsic parameters.

Although in this paper we generally refrained from deliberately compensating for missing parameters, it is of course possible to do so. For example, as mentioned above, no sufficiently detailed information was available for certain interneuron types. Therefore, these lesser-known interneurons were not included in the model, which meant that inhibition received by the pyramidal cells was probably weaker than in the biological situation. Indeed, the pyramidal cells in our model described above (Figures 3 and 4) tended to fire more than they typically do so during theta oscillations *in vivo* (e.g., Soltesz and Deschenes (1993); Robbe et al. (2006)). Is the higher firing frequency of the pyramidal cells related to the weaker inhibition? To answer to latter question, in a subset of the simulations we artificially scaled up inhibition in the model to match the inhibitory synapse numbers on CA1 pyramidal cells that were expected from electron microscopic reconstructions of pyramidal cell dendrites and somata (Megías et al., 2001; Bezaire and Soltesz, 2013). The rationale for scaling up inhibition in this way was that, as described in detail in Bezaire and Soltesz (2013), the estimates of local inhibitory inputs to pyramidal cells were different when based on experimental observations of presynaptic anatomy (local boutons available for synapsing from distinct types of intracellularly filled and reconstructed interneurons) as opposed to postsynaptic anatomy (inhibitory post-synaptic

densities on pyramidal cell dendrites). In simulations with the model containing this rationally scaled up inhibition, only 1% of the pyramidal cells were active, and they fired at a low rate of 1.8 Hz (data not shown), closely resembling the *in vivo* condition (Soltesz and Deschenes, 1993; Robbe et al., 2006). Therefore, the model was capable of reproducing the experimentally observed relatively low firing frequencies for the principal cells during theta oscillations in vivo. However, because the source of the additional inhibition onto CA1 principal cells has not yet been experimentally identified, we used the connectivity estimates as constrained by experimental observations of axonal boutons and lengths in the full scale model (without the scaled-up inhibition) described above (Figures 3 and 4) in the subsequent computational experiments.

Mechanism of theta generation and phase-preferential firing of interneurons in the full-scale model of the isolated CA1

Next, we examined the onset of the theta rhythm and the firing patterns of the various cell types in the model circuit during theta oscillations (Figure 5, Table 5, and Figure 5 - Source Data 1 - 11). As mentioned above, distinct interneuronal types, defined based on their selective axonal innervation patterns of the postsynaptic domains of pyramidal cells, exhibit characteristic, cell-type-specific preferred phases of firing during theta oscillations *in vivo* (Klausberger et al., 2003, 2004, 2005; Ferraguti et al., 2005; Jinno et al., 2007; Fuentealba et al., 2008; Varga et al., 2012; Lapray et al., 2012; Katona et al., 2014; Varga et al., 2014). Importantly, this fundamental property emerged spontaneously from the full-scale model, without purposeful tuning of parameters except the mean spiking frequency and synaptic strength of the artificial stimulating cells to set the incoming excitation levels from afferents (see Methods for details). As expected, the numerically dominant pyramidal cells, whose intracellular membrane potential oscillations to a large extent generate and underlie the extracellular LFP signal during theta oscillations (Buzsáki et al., 2012), preferentially discharged around the trough $0^o/360^o$ of the LFP analog theta rhythm (Figure 5A).

Interneurons in the model preferentially fired at specific phases of theta oscillations, depending

on the cell type. Their phase preferences fell into two broad categories (Figure 5A). The cells belonging to the first group, including the PV+ basket cells, bistratified cells and O-LM cells, were most likely to fire at the theta trough compared to other theta phases. Since these cells received substantial excitatory inputs from local CA1 pyramidal cells both in the biological state and in the model (Bezaire and Soltesz, 2013), their firing in the isolated CA1 model was probably driven by the pyramidal cell discharges around the theta trough. In contrast, the second group of cells, including the ivy and neurogliaform cells, the CCK+ basket cells and the axo-axonic cells, fired least around the theta trough, leading to an inverted firing probability distribution relative to the first group of interneurons (Figure 5A). Their differing phase preferences were most likely due to a combination of weak or non-existent excitatory inputs from local CA1 pyramidal cells and inhibition from the interneurons that prominently discharged around the theta trough. In general agreement with the first group of cells being strongly and rhythmically driven by the local pyramidal cells, there was a correlation between the phase preference and the strength of modulation (Figure 5C; see Methods), with the cells discharging around the trough all showing strong modulation of firing.

These results were in line with recent data from the isolated CA1 preparation *in vitro* (Ferguson et al., 2015) which showed that cells belonging to the broadly defined SOM+ and PV+ classes (identified using genetic drivers) displayed phase preferences similar to the O-LM, PV+ basket and bistratified cells in our model (note that Ferguson and colleagues used LFP theta recorded in the stratum radiatum as reference, which is approximately 180 degrees out of phase with the pyramidal cell layer theta used in this paper). In addition, the interneuronal phase preferences in the model were also remarkably similar to *in vivo* data from anesthetized animals (Figure 5B; because no data are available on the phase preferential firing of morphologically identified interneurons from the isolated CA1 preparation, comparison is made here with results from anesthetized animals, from which the most complete data sets are available; see also Discussion). Specifically, the majority (71%; 5/7) of the interneuron types for which there were experimental data, including the CCK+ basket, axo-axonic, bistratified, O-LM and neurogliaform cells, showed similar preferential maxima in their firing probabilities in the model (Figure 5A) and *in vivo* (Figure 5B). The largest differences between the model and the *in vivo*

phase-preferential firing occurred for the PV+ basket cells and the ivy cells, suggesting that during theta oscillations *in vivo* these cells may be strongly driven by CA3 afferents active during the late falling phase of the theta cycle (Colgin and Moser, 2010); note that PV+ cells receive a high number of excitatory inputs on their dendrites compared to other interneuron classes (Gulyas et al., 1999). A comparison of the model and the anesthetized *in vivo* data is illustrated in Figure 5D, where the arrows indicate the shift required for the model phase preferences (Figure 5A) to equal the *in vivo* (Figure 5B) phase preferences; note that the required shifts (arrows) are small for all interneuron types except PV+ basket and ivy cells. A clear majority of the interneuronal types in the model showed phase preferences similar to the *in vivo* condition where rhythmically discharging afferent inputs are present, indicating that theta-preferential discharges are to a large extent determined by the wiring properties of the CA1 circuit itself.

Perturbation experiments indicate a key role for interneuronal diversity in the emergence of spontaneous theta

Importantly, the ability to generate theta oscillations, phase-locked gamma oscillations, and theta-related phase-preferential firing of distinct interneuronal subtypes was not a universal property of the model. As shown in Figure 6A, our strongly constrained model only exhibited spontaneous theta oscillations at certain levels of afferent excitation. The results described above (Figures 3-5) were obtained with an afferent excitation level of 0.65 Hz (labeled as "Control" in Figure 6A), meaning that each excitatory afferent cell excited the model network with a Poisson-distributed spike train having a Poisson mean interspike interval (ISI) corresponding to a firing rate of 0.65 Hz. When the excitation level decreased below 0.65 Hz, the theta rhythm fell apart, and when the excitation level increased beyond 0.80 Hz, theta power also started to drop significantly as the oscillation frequency rose out of theta range (Figure 6 and Figure 6 - figure supplement 1; Figure 6 - Source Data 1 -2), evolving into a beta oscillation (Engel and Fries, 2010). These data indicate that while synaptic-cellular organization of the CA1 circuit enables the intrinsic, within-CA1 generation of theta waves,

the circuit is predisposed to exhibit theta oscillations only under particular excitatory input conditions. The observation that, under certain conditions the model network can oscillate at frequencies between 12 and 20 Hz, is in agreement with recent experimental findings that rhythmic driving of septal PV+ cells can reliably entrain the hippocampus in a 1:1 ratio up to frequencies of 20 Hz (Dannenberg et al., 2015).

Does the parameter sensitivity of the theta rhythm also apply to recurrent excitation from pyramidal cells and inhibition from CA1 interneurons? In order to answer the latter question, we tested whether the theta rhythm was differentially sensitive to the contribution of each inhibitory cell type (Figure 6B). We characterized the contribution of each local CA1 cell type to the theta rhythm by muting the output of the cell type so that its activity had no effect on the network. First, we studied the role of the recurrent collaterals of pyramidal cells, which contact mostly interneurons and, less frequently, other pyramidal cells (Bezaire and Soltesz, 2013). When we muted all the outputs from pyramidal cells, theta rhythm disappeared (bar labeled "Pyr" in Figure 6B), indicating that the recurrent collaterals of pyramidal cells play a key role in theta oscillations.

Interestingly, muting the relatively rare CA1 pyramidal cell to pyramidal cell excitatory connections alone (each pyramidal cell contacts 197 other pyramidal cells in the CA1; Bezaire and Soltesz (2013)) was sufficient to collapse the theta rhythm (bar labeled "None" in Figure 6C); key roles for inter-pyramidal cell excitatory synapses within CA1 have been suggested for sharp wave ripple oscillations as well (Maier et al., 2011). Furthermore, the parameter-sensitivity of the theta rhythm was also apparent when examining the role of pyramidal cell to pyramidal cell connections, because theta power dramatically decreased when these connections were either increased (doubled) or decreased (halved) from the biologically observed 197 (Figure 6C). Next, we investigated the effects of muting the output from each interneuron type. Silencing the output from any of the fast-spiking, PV family interneurons (PV+ basket, axo-axonic, or bistratified cells), CCK+ basket cells, or neurogliaform cells also strongly reduced theta power in the network (Figure 6B). In contrast, muting other interneuronal types (S.C.-A cells, O-LM cells, or ivy cells) had no effect on this form of theta oscillations generated by the intra-CA1 network (Figure 6B). In additional disinhibition studies simulating optogenetic experimental

configurations, partial muting of all PV+ outputs (PV+ basket, bistratified, and axo-axonic cells together) had a larger effect than partial muting of all SOM+ outputs (O-LM and bistratified cells); see Figure 6D. Reassuringly, these results were in overall agreement with experimental data from the isolated CA1 preparation indicating that optogenetic silencing of PV+ cells, but not SOM+ cells such as the O-LM cells, caused a marked reduction in theta oscillations (Amilhon et al., 2015). The differential effects of silencing PV+ versus SOM+ cells could also be obtained in a rationally simplified model called the Network Clamp, where a single pyramidal cell was virtually extracted from the full-scale CA1 network with all of its afferent synapses intact (for further details, see Bezaire et al. (2016)).

Since the diverse sources of inhibition from the various interneuronal types are believed to enable networks to achieve more complex behaviors, including oscillations (Soltesz, 2006; Rotstein et al., 2005; Kepecs and Fishell, 2014), we next tested if reducing the diversity of interneurons in the model would affect its ability to produce spontaneous theta oscillations. Surprisingly, giving all interneurons a single electrophysiological profile appeared to create conditions that were not conducive for the appearance of spontaneous theta oscillations regardless of which interneuronal profile was used (Figure 6E; note that the cells still differed in the strengths, distribution, and identities of their incoming and outgoing connections after this manipulation). To probe this finding further, we focused on PV+ basket cells, which have been implicated in theta generation *in vivo* (Soltesz and Deschenes, 1993; Buzsáki, 2002; Stark et al., 2013; Hu et al., 2014) and exhibited strong theta power in their spiking in the control network model (Figure 4B). We gradually altered ("morphed") the properties of all other model interneuron types until they became PV+ basket cells, by first converging their electrophysiological profiles, then additionally their synaptic kinetics and incoming synapse weights, then also their incoming synapse numbers, and finally their outgoing synaptic weights and numbers (Figure 6F; Table 7). Theta was not apparent in any intermediate steps nor in the final network where all interneurons had become PV+ basket cells ("All PV+B" in Figure 6F). Furthermore, introduction of cell to cell variability in the resting membrane potential of interneurons in the "All PV+B" configuration at the biologically observed values for PV+ basket cells also failed to restore theta ("Var PV+B" in Figure 6F shows results with standard deviation of (SD) = 8 mV in the resting membrane potential; SD = 5

mV and SD = 2 mV also yielded no theta; biological SD value: approximately 5 mV in Tricoire et al. (2011) and 2 mV in Mercer et al. (2012)). Therefore, although PV basket cells appear to be important for theta-generation both in the biological and the model CA1 network, endowing all interneurons with PV basket cell-like properties does not lead to a network configuration conducive to theta oscillations (Hendrickson et al., 2015).

To rule out the possibility that the lack of theta could be due to an inappropriate excitation level in these reduced diversity configurations, we subjected the "All PV+ B" network to a wide range of incoming excitation levels (Figure 6G). Theta rhythm did not appear at any of these excitation levels. While we could not rule out a hypothetical theta regime somewhere in the parameter space of such low-diversity configurations, any theta solution space would likely be smaller and more elusive than we were able to determine in the control configuration (Figure 6A).

Taken together, these results indicated, for the first time, that interneuronal diversity itself is an important factor in the emergence of spontaneous theta oscillations from the CA1 network.

Neurogliaform cell signaling and theta generation in the isolated CA1 model

In agreement with previous predictions (Capogna, 2011), the perturbation experiments described above suggested that neurogliaform cells were a necessary component for spontaneous theta to arise in the isolated CA1. We wondered why muting the output from neurogliaform cells, but not the closely related ivy cells, affected theta oscillations (Figure 6B), especially since there were fewer neurogliaform cells than ivy cells, and they were less theta modulated (Figure 5A). These two model interneuron groups mainly differed in that the neurogliaform cells evoked mixed $GABA_{A,B}$ postsynaptic events (Price et al., 2005), whereas the model ivy cells only triggered $GABA_A$ IPSPs (in agreement with a lack of evidence for ivy cell-evoked $GABA_B$ IPSPs). Could the slow kinetics of $GABA_B$ IPSPs contribute to the pacing of the theta oscillations? Indeed, when we selectively removed the $GABA_B$ component of all neurogliaform cell outgoing synaptic connections, theta power was strongly reduced

(Figure 6H). To test whether the contribution of the $GABA_B$ receptors was due to their slow kinetics, we artificially sped up the $GABA_B$ IPSPs so that they had $GABA_A$ kinetics but conserved their characteristic large charge transfer. This alteration was implemented by scaling up the $GABA_A$ synaptic conductance at neurogliaform cell output synapses to achieve a similar total charge transfer as the control $GABA_{A,B}$ mixed synapse (Figure 6 - figure supplement 2). As shown in Figure 6H (green bar), theta activity was restored when the neurogliaform cell output synapses had no slow $GABA_B$ component, only a scaled up fast $GABA_A$ IPSP with a charge transfer equivalent to the mixed $GABA_{A,B}$ synapses. Therefore, muting the neurogliaform cells strongly disrupted the theta oscillations not because the theta oscillations required the slow kinetics of $GABA_B$ IPSPs specifically, but because the slow kinetics enabled a large total charge transfer.

Discussion

Emergence of theta oscillations from a biological data-driven, full-scale model of the CA1 network

We produced a biologically detailed, full-scale CA1 network model constrained by extensive experimental data (Bezaire and Soltesz, 2013). When excited with arrhythmic inputs at physiologically relevant levels (see below), the model displayed spontaneous theta (and gamma) oscillations with phase preferential firing across the nine model cell types (pyramidal cells and eight interneuron classes). Consistent with experimental results (Goutagny et al., 2009; Amilhon et al., 2015), these oscillations emerged from the network model without explicit encoding, rhythmic inputs or purposeful tuning of intra-CA1 parameters (all anatomical connectivity parameters were exactly as previously published in Bezaire and Soltesz (2013)). Cell type-specific perturbations of the network showed that each interneuronal type contributed uniquely to the spontaneous theta oscillation, and that the presence of diverse inhibitory dynamics was a necessary condition for sustained theta oscillations. In addition to characterizing roles for specific network components, these model results generally suggest

that the presence of diverse interneuronal types and the intrinsic circuitry of the CA1 network are sufficient and necessary to enable the isolated CA1 to oscillate at spontaneous theta rhythms while supporting distinct phase preferences of each class of hippocampal neuron. These abilities may serve to maintain the stability and robustness of the theta oscillation mechanism as it operates *in vivo* in diverse behavioral states. The theta rhythm is thought to be important for organizing disparate memory tasks (Lisman and Idiart, 1995; Hasselmo et al., 2002; Hasselmo, 2005; Lisman and Jensen, 2013; Siegle and Wilson, 2014), and a CA1 network which has evolved a predisposition to oscillate at theta and gamma frequencies may enable more efficient processing of the phasic input it receives *in vivo* (Akam and Kullmann, 2012; Fries, 2015). In turn, phase preferential firing may aid information processing tasks by providing order and allowing multiple channels of information to be processed in parallel (Jensen and Lisman, 2000; Hasselmo et al., 2002; Womelsdorf et al., 2007; Schomburg et al., 2014; Jeewajee et al., 2014; Maris et al., 2016).

Importantly, theta oscillations appeared only within certain levels of excitatory afferent activity, around 0.65 Hz for the average firing rate of the Poisson-distributed spike trains. When the 454,700 stimulating afferents in the model (representing the CA3 and entorhinal synapses; calculated in Bezaire and Soltesz (2013)) are active at a Poisson mean of 0.65 Hz, they generate approximately 37,900 incoming spikes / theta cycle, given a theta frequency of 7.8 Hz (Equation 1).

$$454{,}700 \text{ afferents} * \frac{0.65 \text{ spikes/s}}{7.8 \text{ theta cycles/s}} = 37{,}892 \text{ spikes/cycle} \quad (1)$$

Is the latter number of spikes in the afferents to the CA1 network within a physiologically plausible range? The biological CA1 network receives most of its input from CA3 and entorhinal cortical layer III (ECIII), and it has been estimated that about 4% of CA3 pyramidal cells fire up to four spikes per theta wave (Gasparini and Magee, 2006). We previously estimated 204,700 pyramidal cells in ipsilateral CA3 (Bezaire and Soltesz, 2013), giving an estimated 32,750 spikes from ipsilateral CA3

per theta cycle (Equation 2).

$$204,700 \text{ cells} * .04 \text{ cell fraction} * 4 \text{ spikes/cell} = 32,752 \text{ spikes} \quad (2)$$

About 250,000 principal cells from ipsilateral ECIII synapse onto the CA1 region (Andersen et al., 2006), and approximately 2% of these cells are active per theta cycle at a low firing rate (Csicsvari et al., 1999; Mizuseki et al., 2009). Therefore, ECIII cells could provide 5,000 input spikes to ipsilateral CA1 (Equation 3).

$$250,000 \text{ cells} * .02 \text{ cell fraction} * 1 \text{ spike/cell} = 5,000 \text{ spikes} \quad (3)$$

Therefore, about 37,750 spikes per theta cycle arrive from ipsilateral CA3 and entorhinal cortex to the CA1 network *in vivo*, which is reassuringly close to the our modeling results indicating that robust theta emerged when the CA1 network model received approximately 37,900 afferent spikes per theta cycle. Thus, the model has the capacity to process a biologically realistic number of spike inputs per cycle while maintaining the theta rhythm.

Our results obtained using the 0.65 Hz excitation indicated that the CA1 model network exhibited phenomena that corresponded well with experimental results, for example, on the differential roles of PV+ basket cells and OLM cells. In addition, the simulations unexpectedly revealed that interneuronal diversity itself may also be important in theta generation, since conversion of all interneurons into fast spiking PV+ basket cells did not result in a network that was conducive for the emergence of theta, in spite of the key role of the PV+ basket cells in hippocampal oscillations. The modeling results also provided the interesting insight that $GABA_B$ receptors may play important roles in slow oscillations such as the theta rhythm not because their slow kinetics pace the oscillations, but because their slow kinetics enable a massive charge transfer. This insight was illuminated by the fact that slow $GABA_B$ synapses were not necessary for theta as long as their large charge was carried by the fast $GABA_A$ synapses. However, we had to increase the conductance of the $GABA_A$ synapse almost 300 times to achieve a similar charge transfer as that conveyed by the $GABA_B$ synapse. Such a large

conductance is not biologically realistic, indicating that the key role for $GABA_B$ synapses may be to allow the temporal distribution of the large synaptic charge transfer. Indeed, the importance of $GABA_B$ receptors has also been indicated by a number of recent experimental studies, for example, in the modulation of theta and gamma oscillations (Kohl and Paulsen, 2010), setting of spike timing of neuron types during theta (Kohl and Paulsen, 2010), and playing a role in cortical oscillations and memory processes (Craig and McBain, 2014).

In addition to identifying key roles for certain inhibitory components (PV+ interneurons, neurogliaform cells, $GABA_B$, and interneuron diversity), our results also highlighted the importance of the recurrent excitatory collaterals from CA1 pyramidal cells in theta generation in the model of the isolated CA1 network. While it may be expected that isolated theta generation would require local pyramidal cells to provide rhythmic, recurrent excitation to interneurons, our simulations additionally showed that the relatively rare pyramidal cell to pyramidal cell local excitatory connections were also required.

Based on our results, we hypothesize that the inhibitory and excitatory connections within CA1 that were identified to be critical in our perturbation ("muting") simulations (Figure 6B) interact to generate the theta waves in the model as follows. Pyramidal cells preferentially discharge at the trough of the LFP analog, strongly recruiting especially the PV+ basket and bistratified cells (green and brown raster plots in Figure 3C), which, in turn, cause a silencing of the pyramidal cells (blue raster plot in Figure 3C) for about the first third of the rising half (i.e., from 0^o to about 60^o) of the LFP analog theta cycle. As the pyramidal cells begin to emerge from this period of strong inhibition, initially only a few, then progressively more and more pyramidal cells reach firing threshold, culminating in the highest firing probability at the theta trough, completing the cycle. The progressive recruitment of pyramidal cells during the theta cycle appears to be paced according to gamma (see blue raster plot in Figure 3C), and it is likely that the intra-CA1 collaterals of the discharging pyramidal cells play key roles in the step-wise (gamma-paced) recruitment of more and more pyramidal cells as the cycle approaches the following trough. The predicted key roles for physiological pyramidal cell to pyramidal cell connections in theta-gamma generation during running may be tested in future

experiments.

Rationale for bases of comparison between modeling results with experimental data

Because our model represented the isolated CA1 network, the modeling results were compared with experimental data from the isolated CA1 preparation when possible. Modeling results for which no corresponding experimental data were available from the isolated CA1 preparation, such as the phase preferential firing of individual interneuron types during theta oscillations, were compared with *in vivo* data from anesthetized animals (Figure 5B). Experimental results from anesthetized animals offered the most complete data set (e.g., no experimental data were available on CCK basket cells and neurogliaform cells from awake animals, see Figure 5 - figure supplement 2). Out of the four interneuronal types for which *in vivo* data were available from both the awake and anesthetized conditions (Figure 5 - figure supplement 2), the phase preference of the axo-axonic cell in the model (163°) was closer to the anesthetized phase (185°) than to the awake phase (251°), whereas the PV+ basket cells in the model displayed phase preferential firing (357°) closer to data reported from awake (289°-310°) than anesthetized animals (234°-271°); the precise reasons underlying these differences are not yet clear. In contrast, bistratified and O-LM cells fired close to the trough in the model, under anesthesia and in awake animals, potentially indicating the primary importance of pyramidal cell inputs in driving these interneurons to fire during theta oscillations under all conditions.

While our model is fundamentally a model of the rat CA1 (e.g., in terms of cell numbers and connectivity; see Table 3 in Bezaire and Soltesz (2013)), some of the electrophysiology data used for constructing the single cell models (Appendix) came from the mouse. In addition, the experimental data on the isolated CA1 preparation were obtained from both rat (Goutagny et al., 2009) and mouse (Amilhon et al., 2015), similar to the experimental results on the phase specific firing *in vivo* (e.g., awake rat: Lapray et al. (2012); awake mouse: Varga et al. (2014)). Because there is no reported

evidence for major, systematic differences in key parameters such as the phase specific firing of rat and mouse interneurons in vivo, we did not compare our modeling results with rat and mouse data separately.

A final point concerns the nature of the theta rhythm that emerged in our model. In general, the *in vivo* theta rhythm has been reported to be either atropine resistant or atropine sensitive, where the former is typically associated with walking and may not be dependent on neuromodulatory inputs, while the latter requires intact, rhythmic cholinergic inputs (Kramis et al., 1975). Given that our model did not explicitly represent neuromodulatory inputs, it is likely that the theta that emerged from our model most closely resembled the atropine resistant form. However, it also plausible that both forms of theta benefit from occurring in a network that is predisposed to oscillate at the theta frequency, as the model network results suggested.

An accessible approach to modeling that balances detail, scale, flexibility and performance

Our results from the strictly data-driven, full-scale CA1 model are consistent with those of earlier models that elegantly demonstrated the basic ingredients capable of producing emergent network oscillations at a range of frequencies in microcircuits and small networks (Rotstein et al., 2005; Siekmeier, 2009; Neymotin et al., 2011b,a; Ferguson et al., 2013). In addition, our modeling approach also provides a full-scale option to advance the recent studies of network activity propagation and information processing during theta (Cutsuridis et al., 2010; Cutsuridis and Hasselmo, 2012; Taxidis et al., 2013; Saudargiene et al., 2015). Here, we demonstrated that emergent theta and gamma oscillations and theta phase preferential firing are possible even as additional interneuron types are incorporated and the network is scaled up to full size with realistic connectivity including 5 billion synapses between the 300,000-plus cells of our network model.

This work is one step in our broader effort to build a 1:1 model of the entire temporal lobe using a hypothesis-driven model development process, where at each stage of model development the models are used to address specific questions. For example, here we employed our newly developed full-scale

CA1 model to gain mechanistic insights into the ability of the intra-CA1 circuitry to generate theta oscillations (Goutagny et al., 2009). The current CA1 network model can be developed into a whole hippocampal or temporal lobe model by replacing the designed CA3 and entorhinal cortical afferents with biophysically detailed CA3, ECIII, and septal networks. While we design our model networks with the motivation to answer a particular question, we keep in mind their potential usage for a broad range of questions. Previously, we built a dentate gyrus model to study epileptic network dynamics (Santhakumar et al., 2005b; Morgan and Soltesz, 2008b) that was then used by several groups to study disparate topics including epilepsy, network mechanisms of inhibition and excitability, simulation optimization, and modeling software (Migliore et al., 2006; Gleeson et al., 2007; Hines et al., 2008a,b; Hines and Carnevale, 2008; Thomas et al., 2009; Winkels et al., 2009; Cutsuridis et al., 2010; Jedlicka et al., 2010a,b; Thomas et al., 2010; Tejada and Roque, 2014). Our previous model has demonstrated how the resource intensive process of designing a detailed, large-scale model is offset by its potential usage in numerous ways by a multitude of groups. On the other hand, future efforts will be needed to continue to incorporate experimental data obtained by the scientific community on additional, not yet represented parameters into the platform offered by our full-scale CA1 network model, e.g., on cell type-specific gap junctions and short-term plasticity, neuromodulators, diversity of pyramidal cells, glial dynamics, cell to cell variability (e.g., Schneider et al. (2014)) and others.

We developed a flexible and biologically relevant model that uses computational resources efficiently, positioning the model to be used by the broader community for many future questions. Importantly, the model can be run on the Neuroscience Gateway, an online portal for accessing supercomputers that does not require technical knowledge of supercomputing (`https://www.nsgportal.org/`). The model is public, well documented, and also well characterized in experimentally relevant terms (See Appendix and online links given in Methods). In addition, all the model configurations and simulation result data sets used in this work are available online (Bezaire et al., 2015) at (`http://doi.org/10.6080/K05H7D60`) so the same simulations can easily be repeated with a future, updated model using SimTracker (Bezaire et al., 2016). Mindful that this model could be used by people with a broad range of modeling experience, we have made freely available our custom software

SimTracker (http://dx.doi.org/10.1101/081927) that works with the model code to support each step of the modeling process (Bezaire et al., 2016).

Conclusion and Outlook

As highlighted by the BRAIN Initiative, there is an increasing recognition in neurobiology that we must compile our collective experimental observations of the brain into something more cohesive and synergistic than what is being conveyed in individual research articles if we are to fully benefit from the knowledge that we collectively produce (Ramaswamy et al., 2015; Markram et al., 2015). By assimilating our collective knowledge into something as functional as a model, we can further probe the gaps in our experimental studies, setting goals for future experimental work. On the other hand, as powerful new tools are gathering vast quantities of neuroscience data, the extraction and organization of the data itself are becoming a challenge. At least three large programs are undertaking this challenge: the Hippocampome project (for neuroanatomical and electrophysiological data in the hippocampus of mice; Wheeler et al. (2015)), the Human Brain Project (currently for neuroanatomical and electrophysiological data and models of the rat neocortex, Ramaswamy et al. (2015)), and NeuroElectro (for electrophysiological data from all species and brain areas; Tripathy et al. (2014)). These comprehensive databases create the opportunity to build strongly biology-inspired models of entire networks, with all the cells and synapses explicitly represented. Such models are not subject to the connectivity scaling tradeoff wherein smaller networks have unrealistically low levels of input or unrealistically high connectivity between cells. In addition, such models are usable for investigations into an almost infinite number of questions at any level from ion channels, to synapses, to cell types, to microcircuit contributions. This approach represents a new strategy in computational neuroscience, distinct from and complementary to the use of more focused models whose role is to highlight the potential mechanism of a small number of network components.

The scale, flexibility, and accessibility of our strictly data-driven, full-scale CA1 model should aid the modeling of other large scale, detailed, biologically constrained neural networks. The current CA1

network model produces results in agreement with experimental data, but also extends the results to probe the mechanisms of spontaneous theta generation. It provides specific testable predictions that enable focused design of future experiments, as well as providing an accessible resource for the broader community to explore mechanisms of spontaneous theta and gamma generation. Because the model is available at full scale, it is a relevant resource for exploring the transformation of incoming spatial and contextual information to outgoing mnemonic engrams as part of spatial and memory processing, and other pertinent network dynamics.

Methods

All results presented in this work were obtained from simulations of computational models. We implemented our CA1 model in parallel NEURON 7.4, a neural network simulator (Carnevale and Hines, 2005). The model simulations were run with a fixed time step between 0.01 and 0.025 ms, for a simulation duration of 2,000 or 4,000 ms (except for Figure 6D where one simulation ran for 1,600 ms). We executed the simulations on several supercomputers, including Blue Waters at the National Center for Supercomputing Applications at University of Illinois, Stampede and Ranger (retired) at the Texas Advanced Computing Center (TACC), Comet and Trestles at the San Diego Supercomputing Center (SDSC), and the High Performance Computing Cluster at the University of California, Irvine. We used our MATLAB-based SimTracker software tool to design, execute, organize, and analyze the simulations (Bezaire et al., 2016).

Model Development

The CA1 network model included one type of multicompartmental pyramidal cell with realistic morphology and eight types of interneurons with simplified morphology, including PV+ basket cells, CCK+ basket cells, bistratified cells, axo-axonic cells, O-LM cells, Schaffer Collateral-associated cells, neurogliaform cells, and ivy cells.

Model neurons sometimes behave much differently than expected when subjected to current sweep

protocols or synaptic inputs that are outside the range of the original protocols used to construct the model. To ensure the model cells exhibited robust biophysical behavior in a wide range of network conditions, we implemented a standard, thorough characterization strategy for each cell type (Appendix).

The behavior of each cell type was characterized using a current injection sweep that matched experimental conditions reported in the literature. Published experimental data was compared side-by-side with model cell simulation results (Appendix). Model cells were connected via NEURON's double exponential synapse mechanism (Exp2Syn), with each connection comprising an experimentally observed number of synapses (see Table 1).

The connections between cells were determined with the following algorithm, for each postsynaptic and presynaptic cell type combination:

1. Calculate the distances between every presynaptic cell and postsynaptic cell of the respective types;
2. Compute the desired number and distance of connections, as defined by the presynaptic axonal distance distribution and total number of desired connections of this type; the total number of incoming connections expected by each postsynaptic cell type is divided into radial distance bins and distributed among the bins according to the Gaussian axonal bouton distribution of the presynaptic cell;
3. Assign each of the possible connections determined in step 2 (connections within the axonal extent of the presynaptic cell) to their respective distance bins, and randomly select a specific number of connections from each bin (the specific number calculated to follow the axonal bouton distribution).

When determining which cells of the model to connect, we distributed all cells evenly within their respective layers in 3D space and enabled random connectivity for cell connections where the postsynaptic cell body fell within the axonal extent of the presynaptic cell (looking in the XY plane only). Each time a connection was established between two cells, the presynaptic cell innervated the experi-

mentally observed number of synapses on the postsynaptic cell. The synapse locations were randomly chosen from all possible places on the cell where the presynaptic cell type had been experimentally observed to innervate. The random number generator used was NEURON's nrnRan4int.

Biological Constraints

The cell number and connectivity parameters were exactly as we reported previously in our in-depth quantitative assessment of anatomical data about the CA1 (Bezaire and Soltesz, 2013). In the latter paper that formed the data-base for the current full-scale model, we combined immunohistochemical data about laminar distribution and coexpression of markers to estimate the number of each interneuron type in CA1. We then extracted from the experimental literature bouton and input synapse counts for each cell type and multiplied these counts by our estimated number of each cell and determined the available input synapses and boutons in each layer of CA1. The number of connections each cell type was likely to make with every other cell type was based on the results of our quantitative assessment. As the quantitative assessment did not make detailed, interneuron type-specific estimates of connections between interneurons, we performed additional calculations to arrive at the numbers of connections between each type of interneuron in our model. Briefly, we determined the number of inhibitory boutons available for synapsing on interneurons within each layer of CA1. Then, we distributed these connections uniformly across the available incoming inhibitory synapses onto interneurons that we had calculated for that layer. We calculated available incoming synapses by using published experimental observations of inhibitory synapse density on interneuron dendrites by cell class and layer in CA1, which we combined with known anatomical data regarding the dendritic lengths of each interneuron type per layer. We therefore made the following assumption: All available incoming inhibitory synapses onto interneurons in a layer have an equal chance of being innervated by the available inhibitory boutons targeting interneurons in that layer. For further details of the exact calculations, please see the Appendix.

The electrophysiology of each cell was tuned using a combination of manual and optimization techniques. We first fit each cell's resting membrane potential, capacitance, time constant, and in-

put resistance, followed by hyperpolarized properties such as the sag amplitude and time constant, followed by subthreshold depolarized properties such as a transient peak response, and finally active properties such as spike threshold, rheobase, firing rate, action potential width, height, and after-hyperpolarization. For some cells, we employed the Multiple Run Fitter tool within NEURON to simultaneously fit multiple ion channel conductances. The characterization of each cell type, as well as its comparison to experimental data from the same cell type, is included in the the Appendix.

After fitting the cell model properties, we simulated paired recordings to characterize the connections between our model cells. Where experimental data existed for paired recordings, we matched the experimental holding potential and synapse reversal potential, then performed 10 different paired recordings. We characterized the average synapse properties from those 10 runs, including the synaptic amplitude, 10% - 90% rise time, and decay time constant. Finally, we tuned the synaptic weights and time constants to fit our averages to the experimental data.

To determine the synaptic weights and kinetics for those connections that have not yet been experimentally characterized, we used a novel modeling strategy we call Network Clamp, described in Bezaire et al. (2016). As experimental paired recording data were not available to directly constrain the synapse properties, we instead constrained the firing rate of the cell in the context of the *in vivo* network, for which experimental data have been published. We innervated the cell with the connections it was expected to receive *in vivo*, and then sent artificial spike trains through those connections, ensuring that the properties of the spike trains matched the behavior expected from each cell *in vivo* during theta (firing rate, level of theta modulation, preferred theta firing phase). Next, we adjusted the weight of the afferent excitatory synapses onto the cell (starting from experimentally observed values for other connections involving that cell type) until the cell achieved a realistic firing rate similar to had been experimentally observed *in vivo*.

Stimulation

As none of the model neurons in the CA1 network are spontaneously active, it was necessary to provide excitatory input to them by stimulating their CA3 and entorhinal cortex synapses. Although the

model code is structured to allow the addition of detailed CA3 and cortical inputs, the stimulation patterns used in the present study were not representative of the information content thought to be carried via inputs from those areas, because the focus was on the function of the CA1 network in isolation from rhythmic extra-CA1 influences. In accordance with experimental evidence of spontaneous neurotransmitter release (Kavalali, 2015), we modeled the activation of CA3 and entorhinal synapses as independent Poisson stochastic processes. The model neurons were connected to a subset of these afferents, such that they received a constant level of excitatory synaptic input.

We constrained the synapse numbers and positions of the stimulating afferents using anatomical data. To constrain the afferent synapse weights, we used an iterative process to determine the combinations of synaptic weights that enabled most of the interneurons to fire similar to their observed *in vivo* firing rates (Figure 5 - figure supplement 1 and Table 6). First, we used the output of an initial full-scale simulation to run network clamp simulations on a single interneuron type, altering the incoming afferent synapse weights (but not the incoming spike trains) until the interneuron type fired at a reasonable rate. Then, we applied the synaptic weight to the afferent connections onto that interneuron type in the full-scale model. The resulting simulation then led to a new network dynamic as the constrained activity of that interneuron type caused changes in other interneuron activity. We then performed this exercise for each interneuron type as necessary until we achieved a network where all cell types participated without firing at too high of a level. CCK+ cells had a steep response to the weight of the incoming afferent synapses, remaining silent until the weight was increased significantly and then spiking at a high rate, see Figure 5 - figure supplement 1; the particular difficulty in obtaining the in vivo observed firing rate for CCK+ cells in the model may indicate that *in vivo* they may be strongly regulated by extra-CA1 inhibitory inputs (e.g., from the lateral entorhinal cortex; see Basu et al. (2016) that are not included in the isolated CA1 model).

Analysis of Simulation Results

We analyzed the results of each simulation with standard neural data analysis methods provided by our SimTracker software, RRID:SCR_014735, discussed in Bezaire et al. (2016), including the spike

density function (SDF) of all pyramidal neuron spikes (Szűcs, 1998), the periodogram of the SDF, and the spectrogram of the LFP analog. We determined the dominant theta and gamma frequencies for the network as the peak in the power spectral density estimate obtained by the spectrogram, and confirmed that those peaks are identical for the SDF and the LFP analog. After finding a dominant theta or gamma frequency, we then analyzed the level of modulation and preferred firing phase for each cell type. Finally, we calculated the firing rate of each cell type.

LFP analog

We calculated an approximation of the LFP generated by the model neurons based on the method described by Schomburg et al. (2012). For each pyramidal cell within 100 μm of a reference electrode location in stratum pyramidale (coordinates = longitudinal: 200 μm; transverse: 500 μm; height from base of stratum oriens: 120 μm), the contribution to extracellular potential at each point along the dendritic and axonal morphology was recorded using NEURON's extracellular mechanism and scaled in inverse proportion to the distance from the electrode. In order to reduce the computational load of the simulation, 10% of the pyramidal cells outside the 100 μm radius were randomly selected; their distance-scaled extracellular potentials were scaled up by a factor of 10 and then added to the contributions of the inner cells. We performed reference simulations and LFP analog calculations with the inner radius set to 200 μm and 500 μm and obtained results identical with those in Figures 3 and 4 (where an inner radius of 100 μm was used), except for negligible increases in the theta oscillation power found in the LFP analog spectrogram.

Spike Density Function

We calculated the spike density function (SDF) of all pyramidal cell spikes using a Gaussian kernel with a window of 3 ms and a bin size of 1 ms (Szűcs, 1998). To see how a cell's spiking activity is related to its SDF, see Figure 4 - figure supplement 1.

Oscillations

To quantify the frequency and power of the oscillations of the network, we computed a one-sided Welch's Periodogram of the SDF (Colgin et al., 2009) using a Hamming window with 50% overlap. To characterize the stability of the theta oscillation, we ran the control network for 4 seconds and then computed the spectrogram of the SDF and of the LFP analog using an analysis script from Goutagny et al. (2009) based on the `mtspecgramc` function from the Chronux toolbox (`http://chronux.org/`).

Spike Phases and Theta Modulation

We calculated the preferred firing theta phases of each cell, using all the spikes of that cell type that occurred after the first 50 ms of the simulation, relative to the filtered LFP analog. The spike times were converted to theta phases, relative to the troughs of the LFP analog theta cycle in which they fired. We then subjected the spike phases to a Rayleigh test to determine the level of theta modulation of the firing of each cell type (Varga et al., 2014).

Firing Rates

The firing rates of the cells were calculated by cropping the first 50 ms of the simulation to remove the initial effects, and then dividing the resulting number of spikes of each cell type by the total number of cells of that type and the duration of the simulation. An alternate average firing rate was calculated by dividing by the number of active cells of that type rather than all of the cells of that type, which gave the average firing rate over all firing cells instead, to better compare with experimentally observed firing rate averages.

Statistical Comparison of Theta Power

For the $GABA_B$-related simulations, we ran three of each condition and then performed an ANOVA to test for significance in the difference of theta power among the conditions.

Cross correlation of theta and gamma

To investigate whether a relationship existed between the simultaneous theta and gamma oscillations found in the LFP analog of our control simulation, we filtered the LFP analog signal within the theta range (5-10 Hz) and the gamma range (25-80 Hz). We applied a Hilbert transform to each filtered signal and then compared the phase of the theta-filtered signal with the envelope of the gamma-filtered signal to determine the extent to which theta could modulate the gamma oscillation.

Accessibility

Our model code is available online at ModelDB, entry #187604 (code version used to produce results in this work) and Open Source Brain, project nc_ca1 (most recent code version). Open Source Brain provides tools for users to characterize and inspect model components. The model is also characterized online at `http://mariannebezaire.com/models/ca1`, along with a graphical explanation of our quantitative assessment used to constrain the model connectivity Bezaire and Soltesz (2013), as well as links to our model code and model results, and detailed instruction manuals for our NEURON code and SimTracker tool, RRID:SCR_014735 (Bezaire et al., 2016).

For those who wish to view and analyze our simulation results without rerunning the simulation, our simulation results are available on CRCNS.org (RRID:SCR_005608) as dataset sim-1 and can be freely accessed after obtaining a free account (Bezaire et al., 2015). Our analyses of these data can be recreated using our publicly available SimTracker tool.

Our custom software tool, SimTracker, is further discussed in our companion paper, Bezaire et al. (2016). SimTracker is freely available online at `http://mariannebezaire.com/simtracker/` and is also listed in SimToolDB, entry #153281. The tool is offered both as a stand-alone, compiled version for those without access to MATLAB (for Windows, Mac OS X, and Linux operating systems), and as a collection of MATLAB scripts for those with MATLAB access.

Acknowledgements

In addition to the direct funding provided to the authors from NIH and NFS (listed separately), the authors wish to thank several researchers and programs operating under their own grants to make this work possible. Immeasurable support was provided by NEURON developers Michael Hines and Ted Carnevale under NIH NINDS grant R01-NS11613 (to M.H.) and NSF grant 1458495 (to T.C.). This work used the Extreme Science and Engineering Discovery Environment (XSEDE), which is supported by National Science Foundation grant number ACI-1053575; the project was supported by XSEDE Research and Startup Allocations to the authors (see funding information listed separately) and via the Neuroscience Gateway with the support of NSF grants 1458840 and 1146949 (to Majumdar et al.). The authors acknowledge the Texas Advanced Computing Center (TACC) at The University of Texas at Austin for providing high performance computing resources that have contributed to the research results reported within this paper (http://www.tacc.utexas.edu). Additionally, this research is part of the Blue Waters sustained-petascale computing project, which is supported by the National Science Foundation (awards OCI-0725070 and ACI-1238993) and the state of Illinois. Blue Waters is a joint effort of the University of Illinois at Urbana-Champaign and its National Center for Supercomputing Applications (NCSA). Parallel supercomputers used in this work include: Blue Waters, owned by the University of Illinois and NCSA; Stampede and the retired Ranger, owned by the University of Texas' Texas Advanced Computing Center (TACC); Trestles and Comet, owned by the San Diego Supercomputing Center; University of California at Irvine's High Performance Computer and the retired Broadcom Distributed Unified Cluster.

We would like to thank the University of Texas' Texas Advanced Computing Center team, the San Diego Supercomputing Center and Neuroscience Gateway teams (especially Glenn Lockwood, Amitava Majumdar, Subhashini Sivagnanam, Mahidhar Tatineni, and Kenneth Yoshimoto), and UC Irvine's HPC team (especially Joseph Farran and Harry Mangalam) for their excellent technical support throughout this work. We would also like to thank Padraig Gleeson, Andras Ecker, Tom Morse, and Jeff Teeters for assistance making our code and model results public, and Jesse Jackson and Sylvain

Williams for the use of their spectrogram analysis script.

Figures

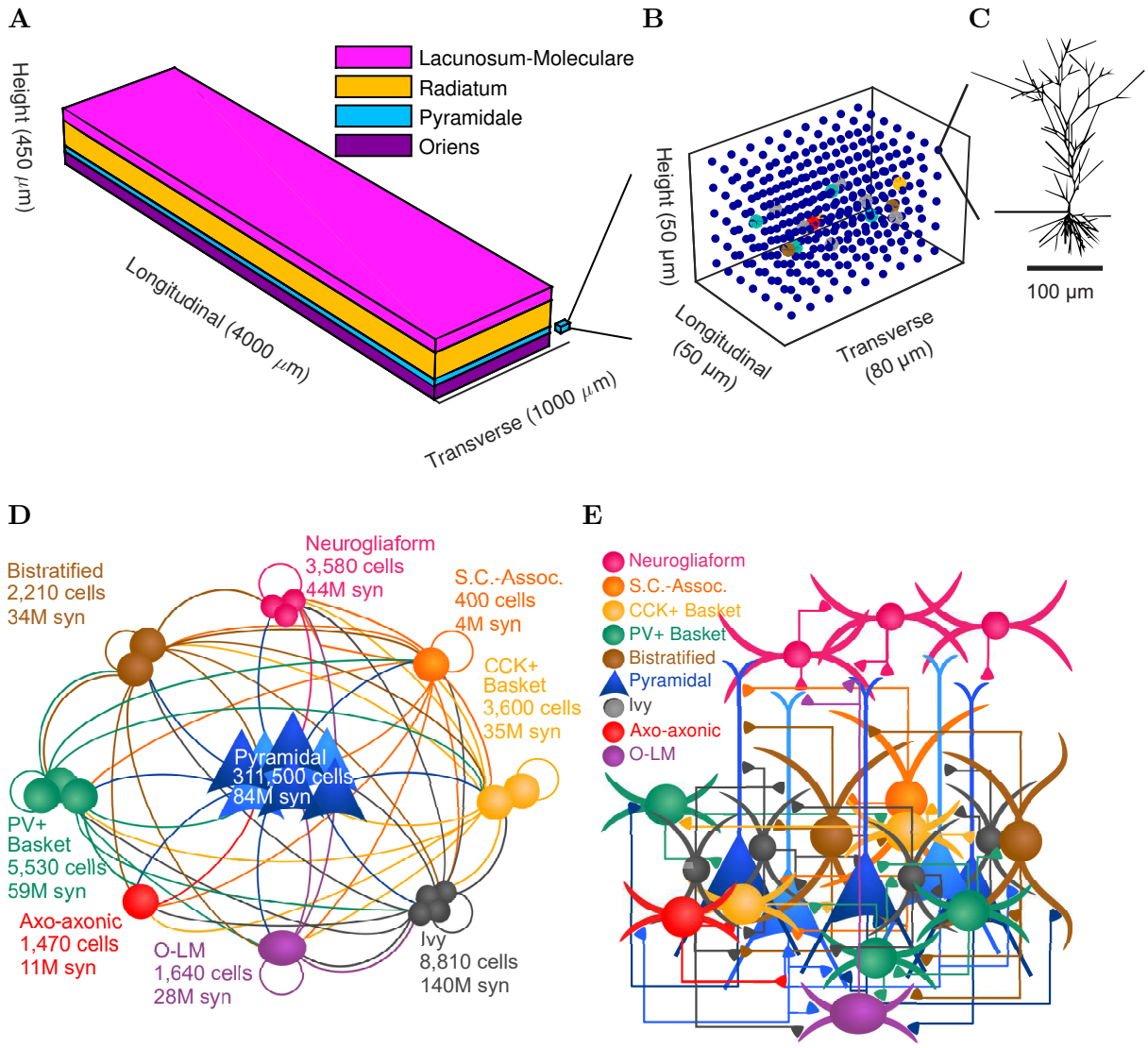

Figure 1: **CA1 network connectivity.** (A) The model network is arranged in a layered prism with the lengths of each dimension similar to the actual dimensions of the CA1 region and its layers. (B) The model cell somata within a small chunk of stratum pyramidale (as depicted in A) are plotted to show the regular distribution of model cells throughout the layer in which they are found. (C) Each pyramidal cell in the network has detailed morphology with realistic incoming synapse placement along the dendrites and soma. (D-E) Diagrams illustrate connectivity between types of cells. (D) The network includes one principal cell type (pyramidal cells) and eight interneuron types. Cell types that may connect are linked by a line colored according to the presynaptic cell type. Most cell types can connect to most other cell types. Total number of cells of each type are displayed, as are the number of local output synapses (boutons) from all cells of each type. (E) The number, position, and cell types of each connection are biologically constrained, as are the numbers and positions of the cells. See Figure 1 - figure supplement 1 for details about the convergence onto each cell type. Also see Table 1 and Figure 1 - figure supplement 2 for information about the cell-type combinations of the 5 billion connections and the axonal distributions followed by each cell type, as well as detailed connectivity results at http://doi.org/10.6080/K05H7D60.

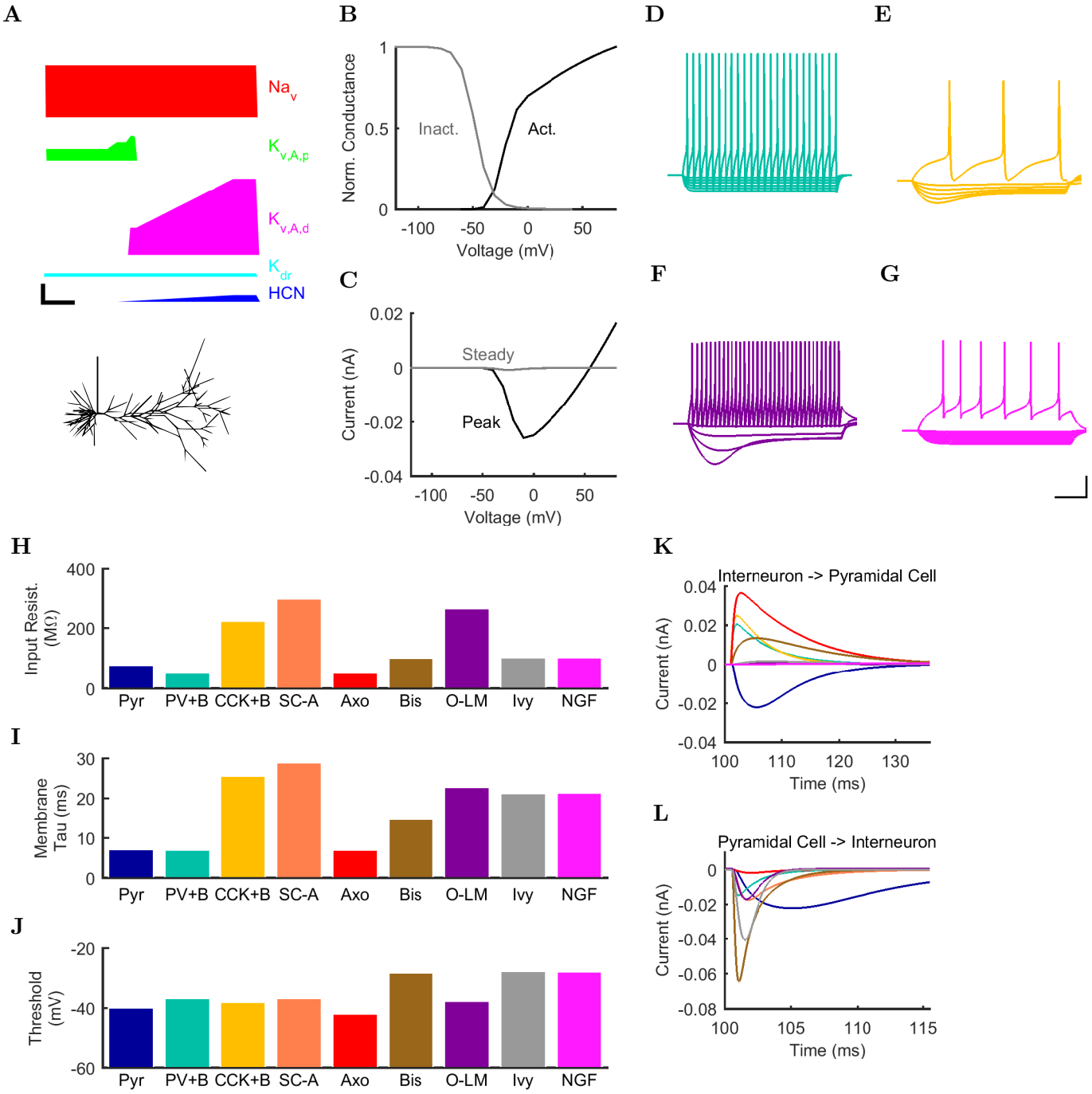

Figure 2: **Electrophysiology of the model network components.** (A) Ion channel densities vary as a function of location (top) in the morphologically detailed pyramidal cell model (bottom; adapted from Poolos et al. (2002)). Scale bar: 100 μm and 0.01 μF/cm^2. (B - C) The sodium channel found in the pyramidal cell soma is characterized in terms of (B) the activation/inactivation curves and (C) the current-voltage relation at peak (transient) current and steady state. (D - (G)) Current sweeps are shown for 4 model cell types: (D) PV+ basket cell, (E) CCK+ basket cell, (F) O-LM cell, and (G) neurogliaform cell. Scale bar: 100 ms and 20 mV. (H-J) Electrophysiological properties for each cell type, including (H) input resistance, (I) membrane time constant, and (J) action potential threshold. (K - L) Pyramidal cell synaptic connections are characterized as post-synaptic currents with the postsynaptic cell voltage clamped at -50 mV; (K) synapses made onto the pyramidal cell from all other cell types and (L) synapses made by the pyramidal cell onto all network cell types. Cells represented by same colors as in Figure 1. Source Data available for electrophysiological characterizations shown here. Additional details available in the Methods, Table 3, and the Appendix.

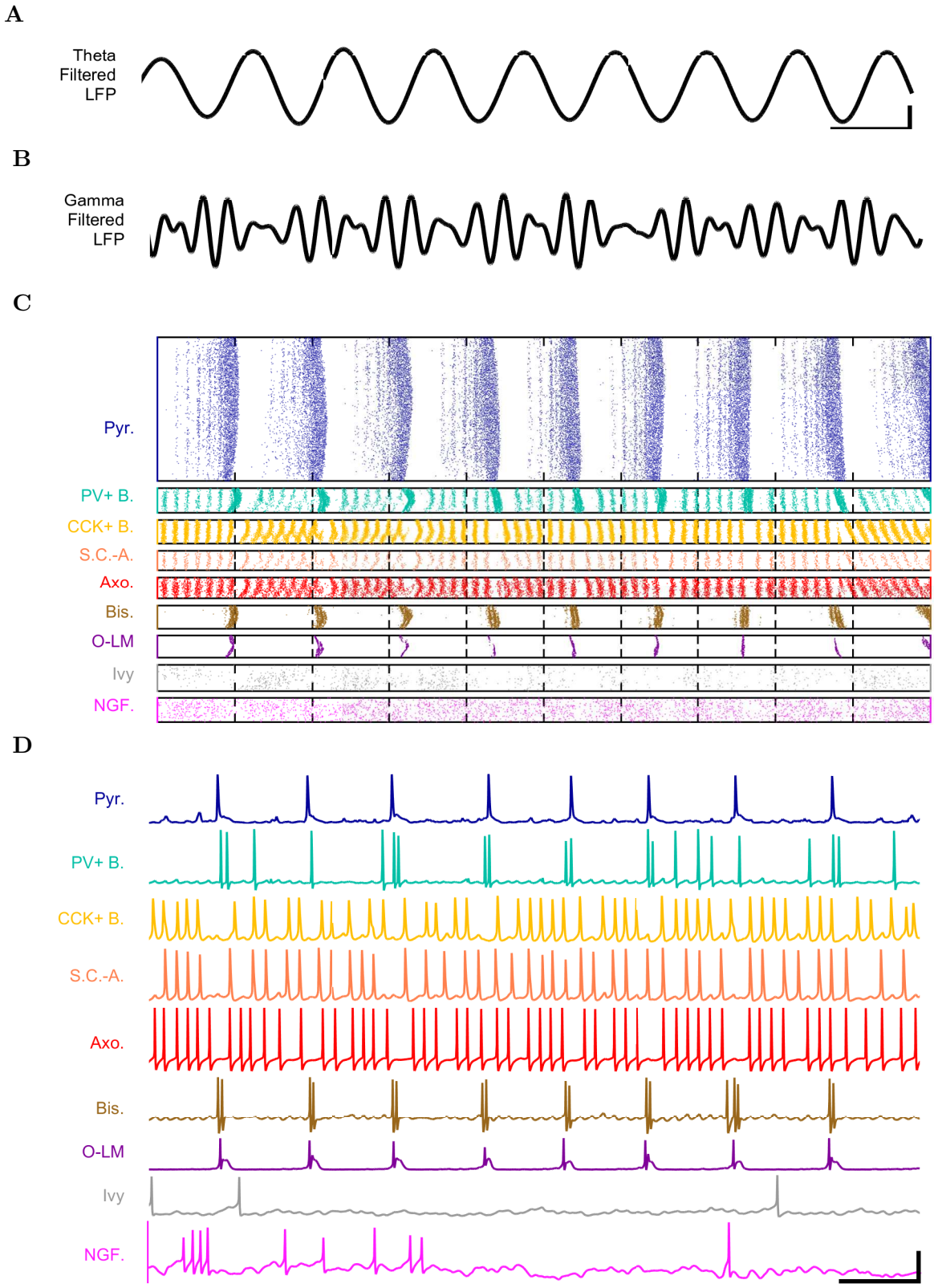

Figure 3: **Detailed network activity.** (A-D) One second of network activity is shown. (A - B) The LFP analog, filtered at (A) the theta range of 5-10 Hz and (B) the low gamma range of 25-40 Hz, shows consistent theta and gamma signals. Scale bar represents 100 ms and 0.2 mV (theta) or 0.27 mV (gamma) for filtered LFP traces. (C) Raster of all spikes from cells within 100 μm of the reference electrode point. (D) Representative intracellular somatic membrane potential traces from cells near the reference electrode point. Scale bar represents 100 ms and 50 mV for the intracellular traces. Source Data available.

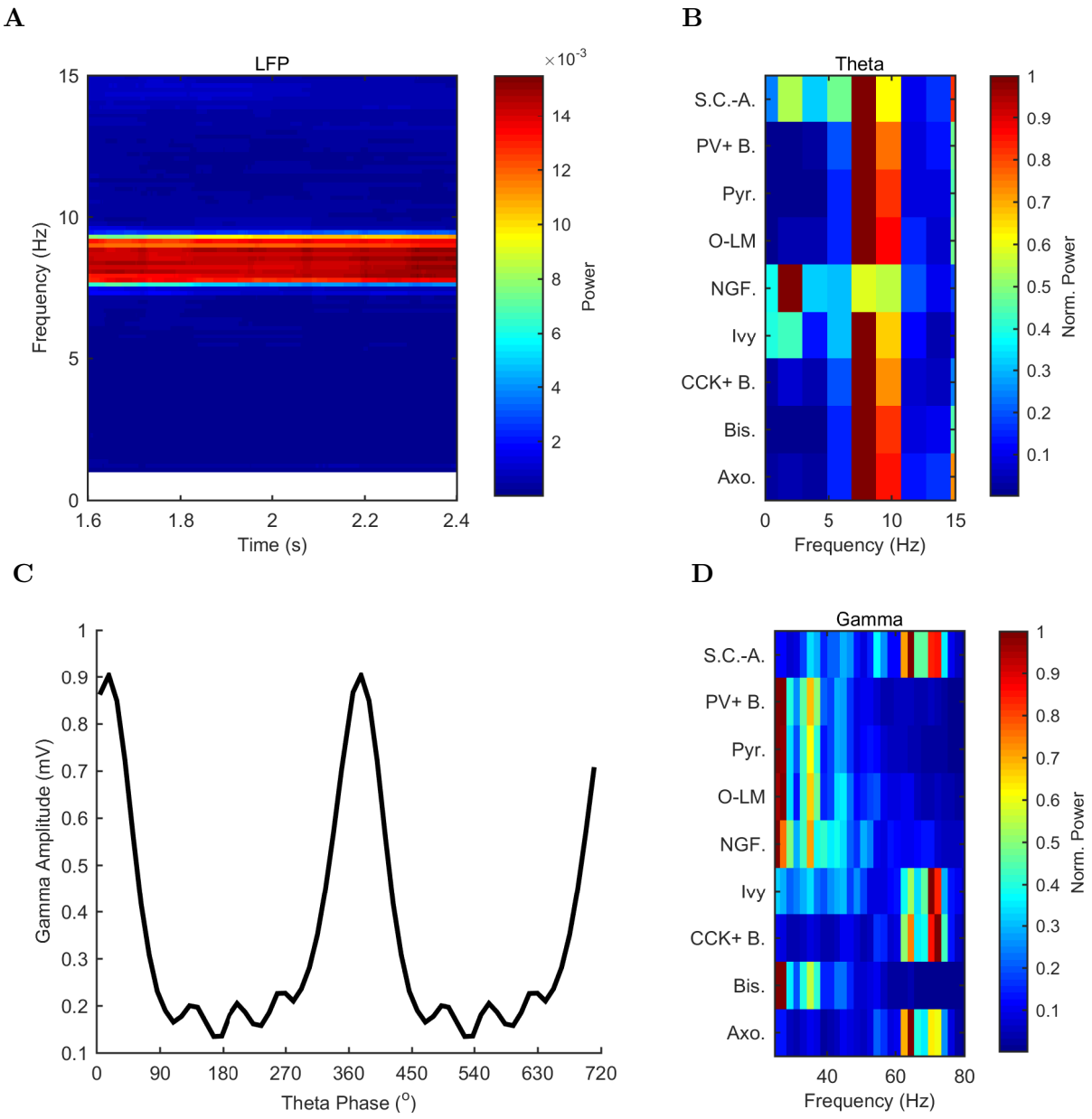

Figure 4: **Spectral analysis of model activity.** (A) A spectrogram of the local pyramidal-layer LFP analog (including contributions from all pyramidal cells within 100 μm of the reference electrode and 10% of pyramidal cells outside that radius) shows the stability and strength of the theta oscillation over time. The oscillation also featured strong harmonics at multiples of the theta frequency of 7.8 Hz. (B,D) Welch's periodogram of the spike density function for each cell type, normalized by cell type and by displayed frequency range, shows the dominant network frequencies of (B) theta (7.8 Hz) and (D) gamma (71 Hz). Power is normalized to the peak power displayed in the power spectrum for each cell type. (C) Cross-frequency coupling between theta and gamma components of the LFP analog shows that the gamma oscillation is theta modulated. The gamma envelope is a function of the theta phase with the largest amplitude gamma oscillations occurring at the trough of the theta oscillation. Following convention, the theta trough was designated 0°/360°; see e.g., Varga et al. (2012). A graphical explanation of the relation between a spike train and its spike density function is shown in Figure 4 - figure supplement 1. Source Data available.

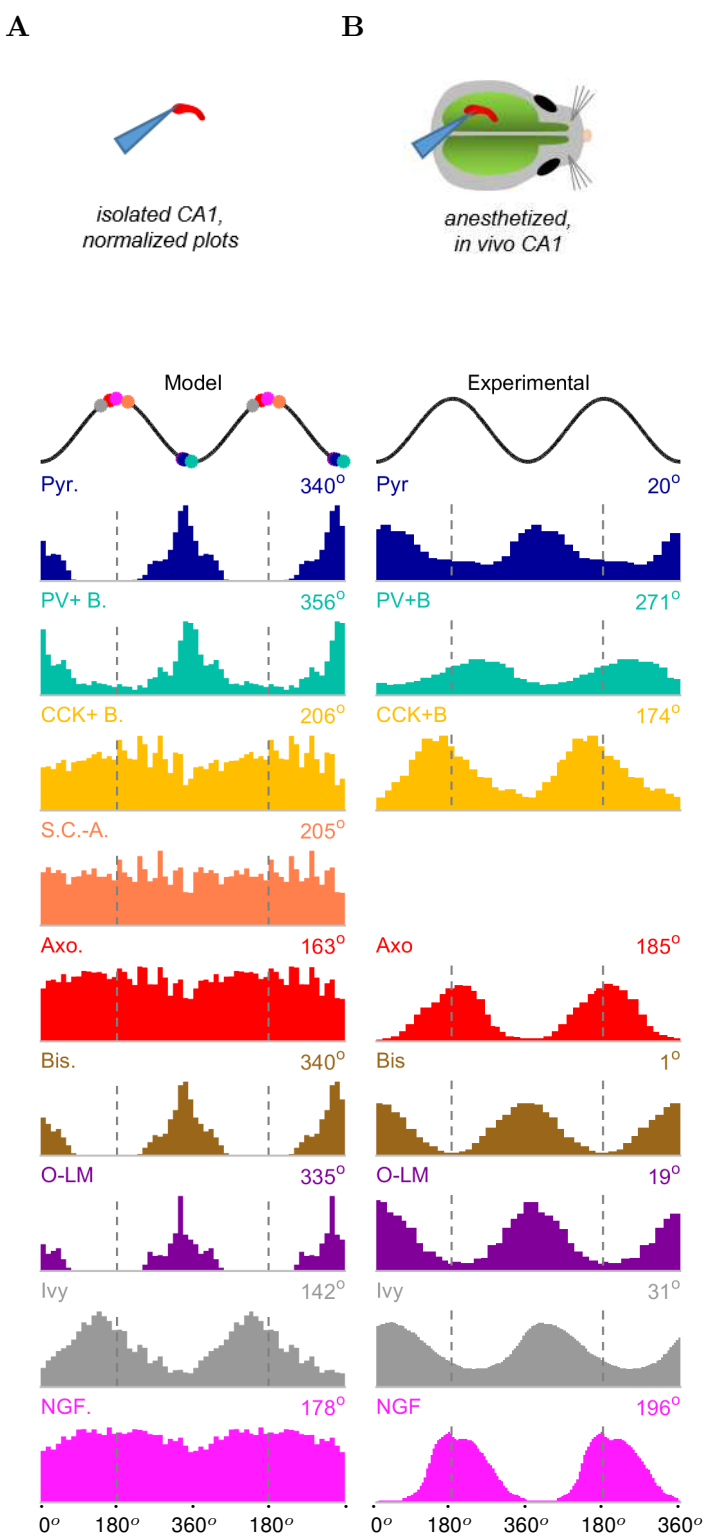

Figure 5: **Model and experimental cell theta phases.** All model results are based on the spiking of the cells within 100 μm of the reference electrode. (A-B) Firing probability by cell type as a function of theta phase for (A) model and (B) experimental cells under anesthesia (histograms adapted with permission from Figure 2, Figure 5B left, and Figure 6F respectively from Klausberger and Somogyi (2008); Fuentealba et al. (2008, 2010)). The model histograms are normalized; see Figure 5 - figure supplement 1 for firing rates. (C) Theta phase preference and theta modulation level were correlated; better modulated cell types spiked closer to the LFP analog trough near the phase preference of pyramidal cells. (D) Theta phase preference plotted on an idealized LFP wave for model data (base of arrow signifies model phase preference and head of arrow shows distance to anesthetized, experimental phase preference). Source Data available.

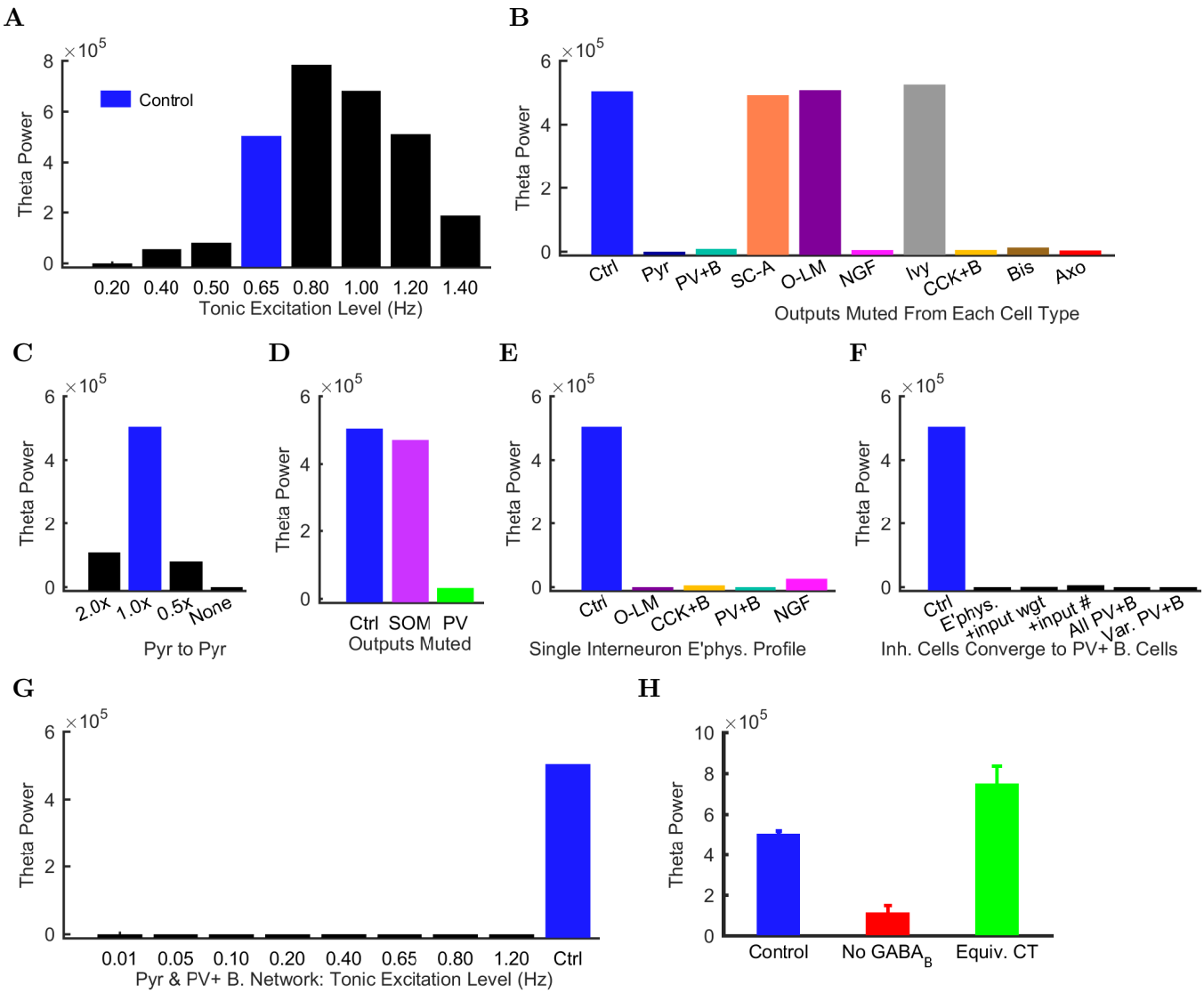

Figure 6: **Altered network configurations.** Oscillation power (in mV^2/Hz) of the spike density function (SDF) for pyramidal cells within 100 μm of the reference electrode, at the peak frequency within theta range (5-10 Hz) in altered network configurations. For corresponding peak frequencies, see Figure 6 - figure supplement 1. (A) Theta is present at some excitation levels. (B) Muting each cell type's output caused a range of effects. (C) The stability and frequency of spontaneous theta in the network was sensitive to the presence and number of recurrent connections between CA1 pyramidal cells. (D) Partially muting the broad classes of PV+ or SOM+ cells by 50% showed that PV+ muting disrupted the network more than SOM+ muting. (E) Theta falls apart when all interneurons are given the same electrophysiological profile, whether it be of a PV+ basket, CCK+ basket, neurogliaform, or O-LM cell. (F) Gradually setting all interneuron properties to those of PV+ basket cells did not restore theta. From left to right: control network; PV+ basket cell electrophysiology; also weights of incoming synapses; also numbers of incoming synapses; then all interneurons being PV+ basket cells (with the addition of the output synapse numbers, weights, and kinetics); then variable RMP (normal disribution with standard deviation of 8 mV). (G) A wide range in excitation was unable to produce theta in the PV+ B. network. (H) Removing the $GABA_B$ component from the neurogliaform synapses onto other neurogliaform cells and pyramidal cells showed a significant drop in theta power. Massively increasing the weight of the $GABA_A$ component to produce a similar amount of charge transfer restored theta power (compare the IPSCs corresponding to each condition in Figure 6 - figure supplement 2). Standard deviations (n=3) shown; significance (p=1.8e-05). Source Data available.

Tables

Pre/Post	**Axo**	**Bis**	**CCK+B**	**Ivy**	**NGF**	**O-LM**	**Pyr**	**PV+B**	**SC-A**
Axo	0.00e+00	0.00e+00	0.00e+00	0.00e+00	0.00e+00	0.00e+00	1.12e+07	0.00e+00	0.00e+00
Bis	2.35e+05	3.54e+05	5.76e+05	2.64e+05	0.00e+00	6.40e+05	3.12e+07	8.85e+05	6.80e+04
CCK+B	1.41e+05	2.12e+05	9.79e+05	5.64e+05	0.00e+00	2.62e+05	3.24e+07	5.31e+05	8.32e+04
Ivy	3.53e+05	5.30e+05	3.42e+06	2.11e+06	1.00e+06	2.23e+06	1.28e+08	1.33e+06	4.08e+05
NGF	0.00e+00	0.00e+00	0.00e+00	0.00e+00	6.09e+05	0.00e+00	4.36e+07	0.00e+00	0.00e+00
O-LM	1.18e+05	1.77e+05	1.44e+06	0.00e+00	4.65e+05	9.84e+04	2.49e+07	4.42e+05	1.60e+05
Pyr	7.19e+05	2.43e+06	0.00e+00	2.38e+05	0.00e+00	1.17e+07	6.14e+07	7.03e+06	1.26e+05
PV+B	5.73e+04	8.62e+04	1.37e+05	7.05e+04	0.00e+00	0.00e+00	5.83e+07	2.16e+05	9.60e+03
SC-A	8.82e+03	1.33e+04	1.30e+05	1.06e+05	0.00e+00	1.97e+04	3.74e+06	3.32e+04	1.44e+04
CA3	1.23e+07	2.56e+07	1.44e+07	3.39e+07	0.00e+00	0.00e+00	3.73e+09	6.69e+07	1.55e+06
ECIII	1.43e+06	1.91e+06	4.02e+06	0.00e+00	3.75e+06	0.00e+00	8.09e+08	0.00e+00	4.58e+05

Table 1: Number of synapses between each cell type. Connections between cells generally comprise 1 - 10 synapses each. Presynaptic cells are listed down the first column (corresponding to each row) and postsynaptic cells are listed along the first row (corresponding to each column).

Supercomputer	**# Processors**	**Sim Time (s)**	**Exchange Time (s)**	**Load Balance**
Comet	1680	2610.28	1.05	0.999
Comet	1704	2566.76	0.65	0.999
Comet	1728	2601.22	0.86	0.999
Comet via NSG	1728	2060.88	0.83	0.999
Stampede via NSG	2048	2471.64	1.71	1.000
Stampede	2048	2578.32	0.29	1.000
Stampede	2528	2189.56	1.78	0.999
Stampede	3008	1844.22	0.91	0.999
Stampede	3488	1641.91	0.86	0.999

Table 2: Simulation time, exchange time, and load balance for simulations executed on various supercomputers and numbers of processors.

Condition	**Pyr**	**PV+B**	**CCK+B**	**SC-A**	**Axo**	**Bis**	**O-LM**	**Ivy**	**NGF**
Resting Membrane Potential (mV)	-63.0	-65.0	-70.6	-70.5	-65.0	-67.0	-71.5	-60.0	-60.0
Input Resistance (MΩ)	62.2	52.0	211.0	272.4	52.0	98.7	343.8	100.0	100.0
Membrane Tau (ms)	4.8	6.9	22.6	24.4	7.0	14.7	22.4	21.1	21.1
Rheobase (pA)	250.0	300.0	60.0	40.0	200.0	350.0	50.0	160.0	170.0
Threshold (mV)	52.0	-36.6	-40.6	-43.1	-41.6	-28.1	100.2	-27.6	-27.7
Delay to 1st Spike (ms)	12.4	74.6	166.6	127.7	43.5	28.4	8.9	173.3	119.0
Half-Width (ms)	80.7	0.9	1.9	1.6	0.6	0.5	112.9	0.6	0.6

Table 3: Electrophysiological characteristics of each model cell type. For more information about model electrophysiology, see the Appendix.

Cell Type	Hyper. (pA)	Step Size (pA)	Depol. (pA)
PV+ B.	-300	50	+500
CCK+ B.	-100	20	+80
O-LM	-130	30	+80
NGF	-130	20	+190

Table 4: Current injection levels used to characterize interneuron current sweeps in Figure 2D-2G.

Cell Type	Firing Rate (Hz)	Modulation Level	p	Phase (0^o=trough)
Axo.	8.9	0.07	4.58e-130	163.4
Bis.	18.0	0.76	0.00e+00	340.0
CCK+ B.	54.4	0.10	0.00e+00	202.8
Ivy	43.3	0.33	0.00e+00	142.1
NGF.	55.1	0.07	1.46e-32	176.3
O-LM	17.4	0.76	0.00e+00	334.7
Pyr.	6.0	0.74	0.00e+00	339.7
PV+ B.	0.9	0.46	0.00e+00	356.8
S.C.-A.	5.2	0.03	1.13e-07	197.9

Table 5: Preferred theta firing phases for each model cell type.

Cell Type	Firing Rate (Hz) Theta	Non	SWR	Theta Phase (^{o})	State of Animal	Animal	Ref.
ADI	8.60	0.06	0.25	156	anesth: u+k & x	rat	Klausberger et al. (2005)
Axo-axonic	17.10	3.50	2.95	185	anesth: u+k & x	rat	Klausberger et al. (2003)
Axo-axonic	27		27	251	awake, head restraint	mouse	Varga et al. (2014)
Bistratified	5.90	0.90	42.80	1	anesth: u+k & x	rat	Klausberger et al. (2004)
Bistratified	34		36	0	awake, head restraint	mouse	Varga et al. (2014)
Bistratified	30.42	27.65	35.82	2	awake	rat	Katona et al. (2014)
CCK+ Basket	9.40	1.60	2.70	174	anesth: u+k & x	rat	Klausberger et al. (2005)
Ivy	0.70	1.70	0.80	31	anesth: u+k & x	rat	Fuentealba et al. (2008)
Ivy	2.80	2.10	5.20	46	awake, free	rat	Lapray et al. (2012)
Ivy	2.40	3.00	6.70		awake, free	rat	Fuentealba et al. (2008)
NGF	6.00	2.65	2.30	196	anesth: u+k & x	rat	Fuentealba et al. (2010)
O-LM	4.90	2.30	0.23	19	anesth: u+k & x	rat	Klausberger et al. (2003)
O-LM	29.80	10.40	25.40	346	awake, head restraint	mouse	Varga et al. (2012)
O-LM	17.30	11.88	18.95	342	awake	rat	Katona et al. (2014)
PPA	5.75	1.95	1.50	100	anesth: u+k & x	rat	Klausberger et al. (2005)
PV+ Basket	7.30	2.74	32.68	271	anesth: u+k & x	rat	Klausberger et al. (2003)
PV+ Basket				234	anesth: u+k & x	rat	Klausberger et al. (2005)
PV+ Basket	21.00	6.50	122.00	289	awake, free	rat	Lapray et al. (2012)
PV+ Basket	25.00	8.20	75.00	307	awake, head restraint	mouse	Varga et al. (2012)
PV+ Basket	28		77	310	awake, head restraint	mouse	Varga et al. (2014)
Pyramidal				20	anesth: u+k & x	rat	Klausberger et al. (2003)
Trilaminar	0.20	0.10	69.00	trough	anesth: u+k & x	rat	Ferraguti et al. (2005)
Double Proj.	0.90	0.55	26.93	77	anesth: u+k & x	rat	Jinno et al. (2007)
Oriens Retro.	0.53	0.37	53.37	28	anesth: u+k & x	rat	Jinno et al. (2007)
Radiatum Retro.	5.15	1.90	0.70	298	anesth: u+k & x	rat	Jinno et al. (2007)

Table 6: Firing rates and theta phase preferences for various cell types in various conditions. Theta phase is relative to the LFP recorded in the pyramidal layer, where 0^o and 360^o are at the trough of the oscillation. non: non-theta/non-SWR state. SWR: sharp wave/ripple. u+k & x: urethane + supplemental doses of ketamine and xylazine.

	Theta		Gamma		Overall	
Condition	**Frequency**	**Power**	**Frequency**	**Power**	**Frequency**	**Power**
Tonic Excitation Level (Hz)						
0.20	n/a	0.0e+00	n/a	0.0e+00	n/a	0.0e+00
0.40	5.9	5.6e+04	25.4	4.1e+04	13.7	6.5e+04
0.50	9.8	8.1e+04	25.4	1.0e+05	19.5	5.6e+05
0.65 (Ctrl.)	7.8	5.0e+05	25.4	2.0e+05	7.8	5.0e+05
0.80	9.8	7.8e+05	29.3	2.6e+05	9.8	7.8e+05
1.00	9.8	6.8e+05	29.3	1.4e+05	9.8	6.8e+05
1.20	9.8	5.1e+05	33.2	1.8e+05	11.7	8.2e+05
1.40	9.8	1.9e+05	25.4	3.4e+05	11.7	8.6e+05
Single Interneuron E'phys. Profile						
Ctrl	7.8	5.0e+05	25.4	2.0e+05	7.8	5.0e+05
O-LM	n/a	0.0e+00	n/a	0.0e+00	n/a	0.0e+00
CCK+B	9.8	5.7e+03	62.5	6.9e+05	62.5	6.9e+05
PV+B	n/a	0.0e+00	n/a	0.0e+00	n/a	0.0e+00
NGF	5.9	2.6e+04	39.1	2.4e+06	39.1	2.4e+06
Inh. Cells Converge to PV+ B. Cells						
Ctrl	7.8	5.0e+05	25.4	2.0e+05	7.8	5.0e+05
E'phys.	n/a	0.0e+00	n/a	0.0e+00	n/a	0.0e+00
+input wgt	7.8	6.8e+02	44.9	1.6e+06	21.5	3.4e+06
+input #	9.8	6.1e+03	31.3	1.1e+06	15.6	2.0e+06
All PV+B	n/a	0.0e+00	n/a	0.0e+00	n/a	0.0e+00
Var. PV+B	n/a	0.0e+00	n/a	0.0e+00	n/a	0.0e+00
Outputs Muted						
Ctrl	7.8	5.0e+05	25.4	2.0e+05	7.8	5.0e+05
SOM	7.8	4.7e+05	27.3	1.4e+05	7.8	4.7e+05
PV	9.8	3.2e+04	27.3	8.1e+05	13.7	1.5e+06
Pyr to Pyr						
2.0x	9.8	1.1e+05	25.4	7.3e+05	13.7	1.0e+06
1.0x (Ctrl.)	7.8	5.0e+05	25.4	2.0e+05	7.8	5.0e+05
0.5x	7.8	8.0e+04	29.3	2.2e+05	29.3	2.2e+05
None	9.8	1.1e+00	70.3	3.7e+01	70.3	3.7e+01
Outputs Muted From Each Cell Type						
Ctrl	7.8	5.0e+05	25.4	2.0e+05	7.8	5.0e+05
Pyr	7.8	1.1e+00	70.3	3.8e+01	70.3	3.8e+01
PV+B	9.8	8.8e+03	29.3	1.9e+06	29.3	1.9e+06
SC-A	9.8	4.9e+05	27.3	1.8e+05	9.8	4.9e+05
O-LM	7.8	5.1e+05	25.4	8.3e+04	7.8	5.1e+05
NGF	9.8	5.2e+03	27.3	9.1e+05	13.7	1.6e+06
Ivy	7.8	5.3e+05	25.4	2.0e+05	7.8	5.3e+05
CCK+B	5.9	5.5e+03	25.4	3.3e+03	3.9	5.7e+03
Bis	5.9	1.3e+04	29.3	1.7e+06	29.3	1.7e+06
Axo	7.8	4.0e+03	33.2	1.2e+06	15.6	1.9e+06
Pyr & PV+ B. Network: Tonic Excitation Level (Hz)						
0.01	n/a	0.0e+00	n/a	0.0e+00	n/a	0.0e+00
0.05	n/a	0.0e+00	n/a	0.0e+00	n/a	0.0e+00
0.10	n/a	0.0e+00	n/a	0.0e+00	n/a	0.0e+00
0.20	n/a	0.0e+00	n/a	0.0e+00	n/a	0.0e+00
0.40	5.9	2.3e+02	25.4	1.2e+02	3.9	2.4e+02
0.65	n/a	0.0e+00	n/a	0.0e+00	n/a	0.0e+00
0.80	n/a	0.0e+00	n/a	0.0e+00	n/a	0.0e+00
1.20	n/a	0.0e+00	n/a	0.0e+00	n/a	0.0e+00
Ctrl	7.8	5.0e+05	25.4	2.0e+05	7.8	5.0e+05

Table 7: Peak, theta and gamma frequencies and powers of the pyramidal cell spike density function using Welch's Periodogram. As in Figure 6 - figure supplement 1, networks where no pyramidal cells spiked - resulting in zero power within the spectral analysis of the pyramidal cell spike density function - have their peak frequencies listed as "n/a" for "not available".

Figure Supplements

A

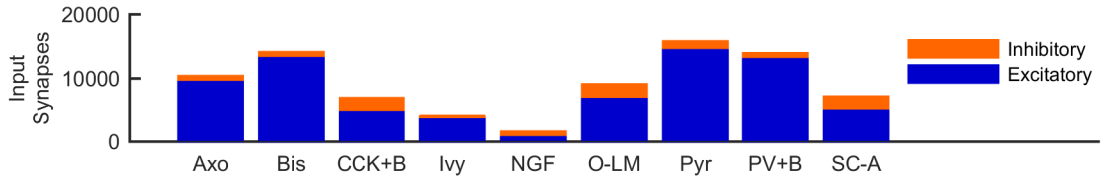

B

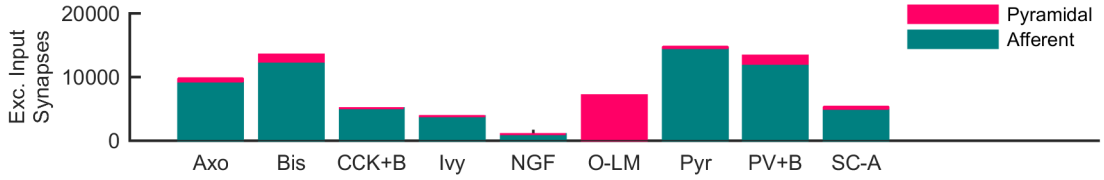

C

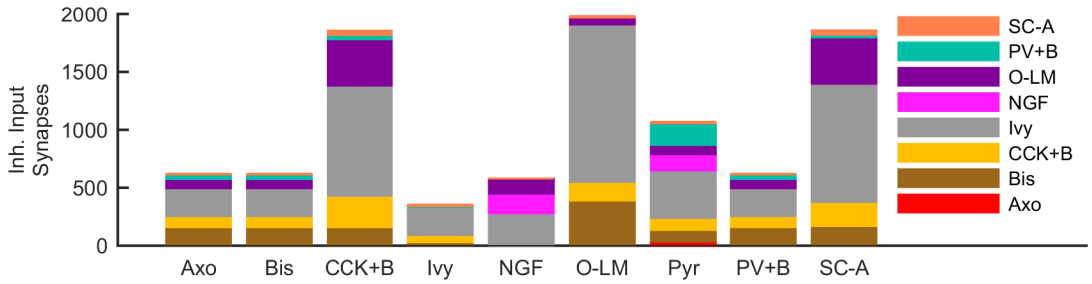

Figure 1 - figure supplement 1: **Quantitative Network Connectivity.** The average number of incoming synapses per postsynaptic cell of the given type are shown for (A) all inputs to the cells, (B) all excitatory inputs to the cells and (C) all inhibitory inputs to the cells.

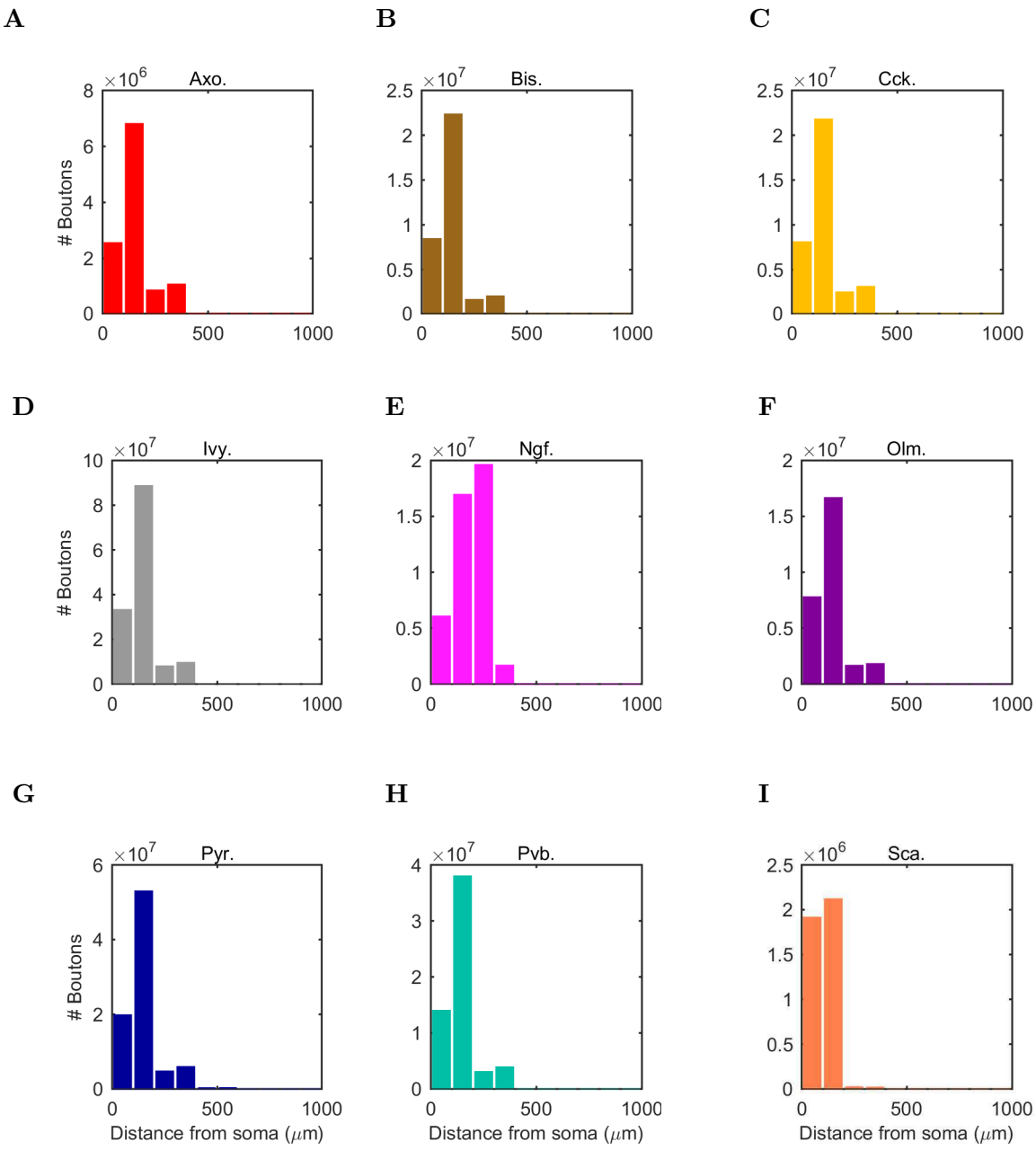

Figure 1 - figure supplement 2: **Anatomically constrained connectivity.** The axonal distributions are shown per presynaptic cell type. The distribution of boutons is plotted as a function of distance from the presynaptic cell's soma. Boutons connecting to all possible types of postsynaptic cells are included in the plot. The colors correspond to each presynaptic cell type using the same color code as previous figures.

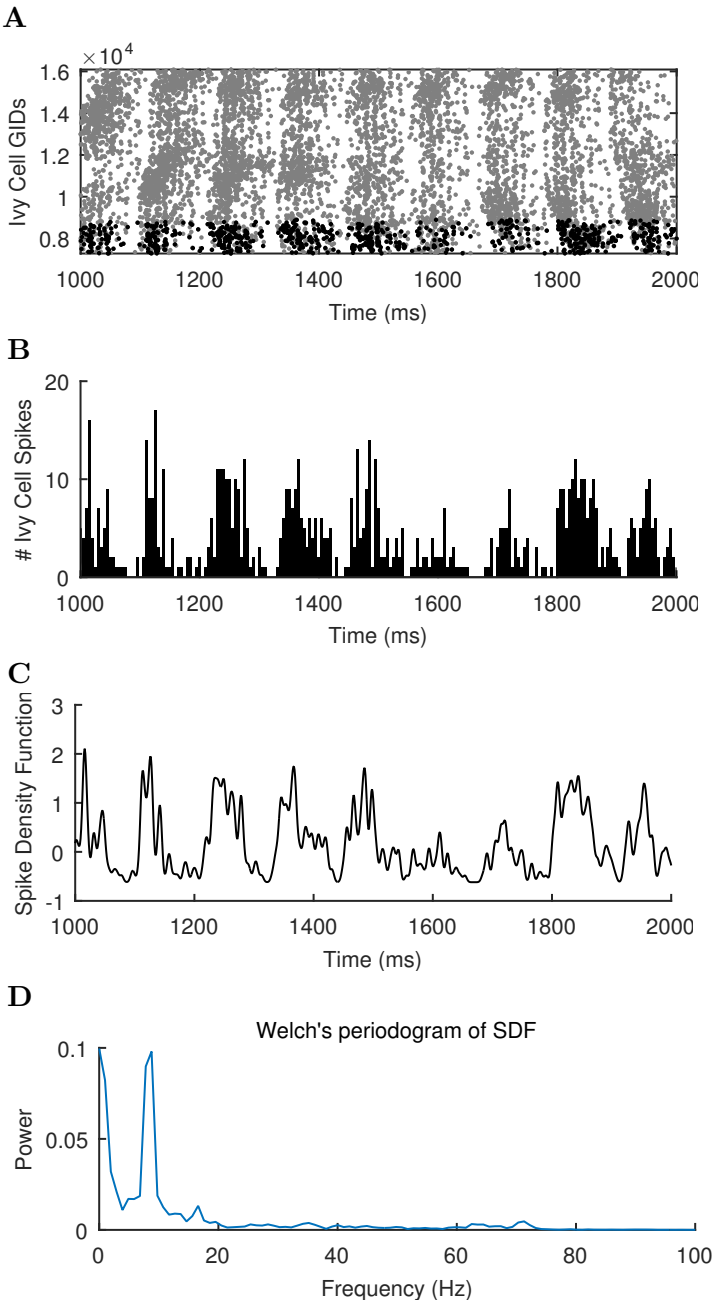

Figure 4 - figure supplement 1: **Different views of cell activity.** Several ways of characterizing model cell activity per cell type are shown using the spikes from the ivy cells as an example. (A) The spike times of each ivy cell are plotted as a function of time and ivy cell number. A subset of ivy cells positioned within 100 μm of the reference electrode location (whose spikes are shown in black) are then carried forward in the remaining calculations. (B) The spikes of the local ivy cells are binned into 1 ms windows to give spike counts per window. (C) A continuous representation of the ivy cell spikes as a function of time is given in the spike density function (SDF) computed from the ivy cell spike times. (D) A Welch's Periodogram is computed, which summarizes the power of each oscillation frequency in the ivy cell SDF Although only a part of the simulation is shown, the full simulation length (except the first 50 ms) was used in the spectral analysis.

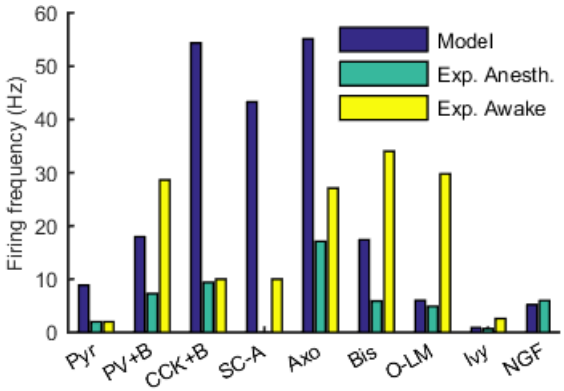

Figure 5 - figure supplement 1: **Firing rates of model and experimental cells of each type.** For experimental cells, firing rates in both the anesthetized and awake states were included where available. See Table 6 for sources of experimental data.

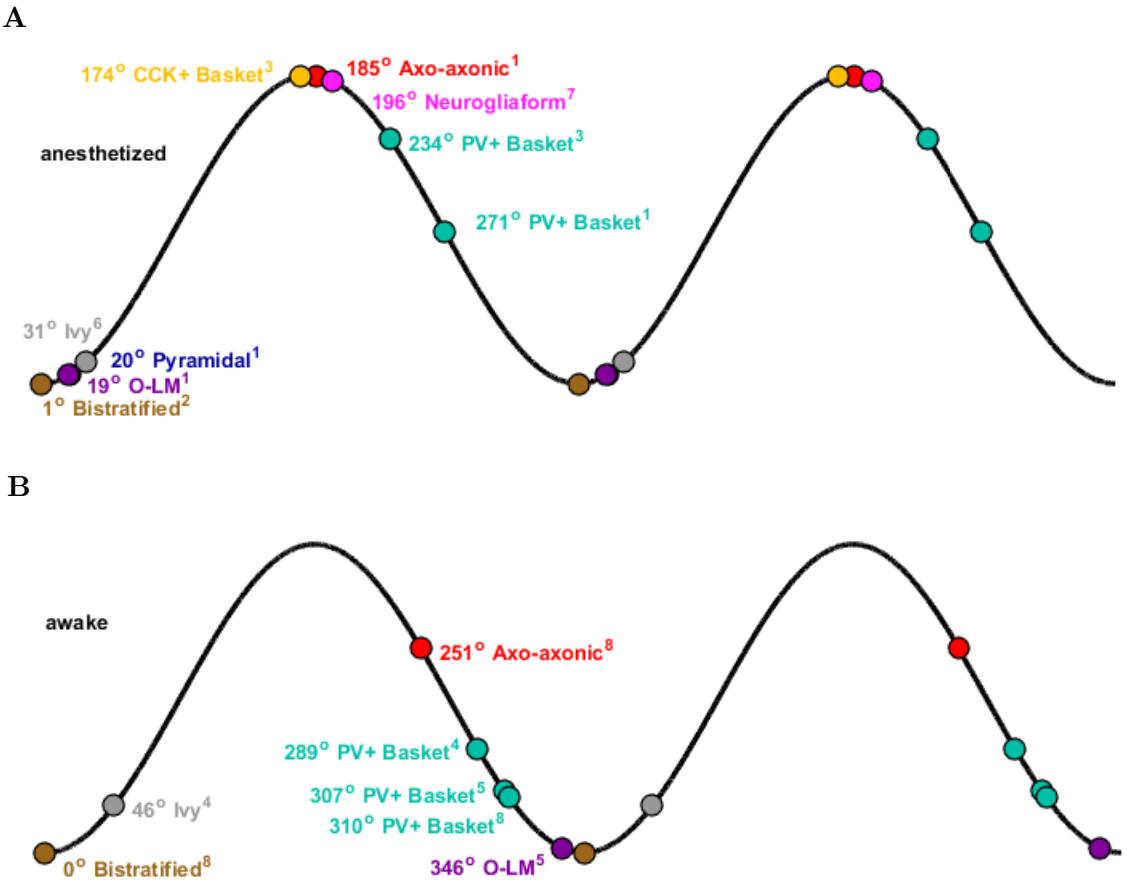

Figure 5 - figure supplement 2: **Theta phase-specific firing preferences of various biological hippocampal cell types as reported in the literature.** The trough of the pyramidal-layer LFP is designated as $0^o/360^o$ and the peak as 180^o. There is variation in phase preference for given cell types as a function of experimental preparation. Shown are (A) anesthetized and (B) awake experimental conditions. Reference subscripts correspond to: 1: Klausberger et al. (2003), 2: Klausberger et al. (2004), 3: Klausberger et al. (2005), 4: Lapray et al. (2012), 5: Varga et al. (2012), 6: Fuentealba et al. (2008), 7: Fuentealba et al. (2010), 8: Varga et al. (2014). See Table 6 for further details.

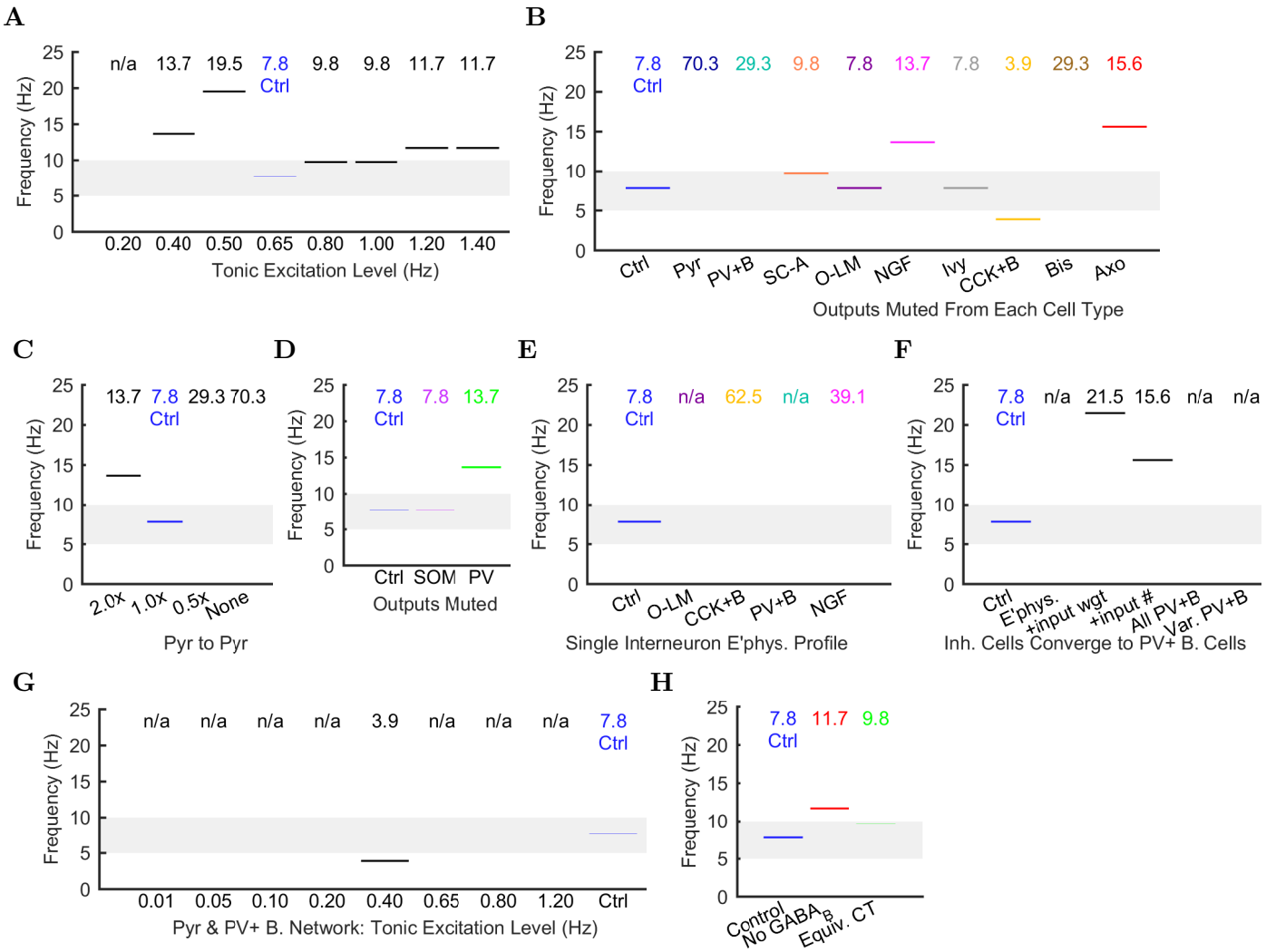

Figure 6 - figure supplement 1: **Peak Frequencies of Oscillations in Altered Networks.** Peak theta frequency (within 5-10 Hz) of the spike density function (SDF) for all pyramidal cells within 100 μm of the reference electrode in each altered network configuration. For networks where no pyramidal cells spiked, resulting in zero power within the spectral analysis of the pyramidal cell spike density function, their peak frequencies are listed as "not available" or "n/a". (A) Spontaneous theta oscillation accelerated out of theta range with more excitation. (B) Muting each cell type shifted the oscillation out of range (neurogliaform, CCK+ basket, and axo-axonic cells), disrupted theta but not gamma (not shown; pyramidal, PV+ basket, and bistratified cells), or had little effect (S.C.-A., O-LM, and ivy cells). (C) Doubling the connections between CA1 pyramidal cells increased the theta frequency, while networks with half the number or no recurrent collaterals lost the slow oscillation but kept gamma. (D) Removing 50% of PV+ cell inhibition (PV+ basket, bistratified, and axo-axonic cells) or 50% of SOM+ cell inhibition (bistratified or O-LM cells) shifted the oscillation out of theta range or lost the slow oscillation entirely but kept gamma. (E) Peak oscillation shifted out of theta range when all interneurons had the same electrophysiological profile, regardless of the profile used. (F) Converging all properties to PV+ basket cells, gamma was restored (not shown) but not theta (left to right: control; network with 1: diverse interneurons with same electrophysiology; 2: also with same weights of incoming synapses; 3: also with same numbers of incoming synapses; 4: complete conversion to PV+ basket cells; 5: added variability in resting membrane potential (normal distribution with st. dev. = 8 mV)). (G) In the all-PV+ basket cell network, a wide range of excitation levels could not produce a spontaneous theta rhythm. (H) Removing $GABA_B$ increased the oscillation frequency.

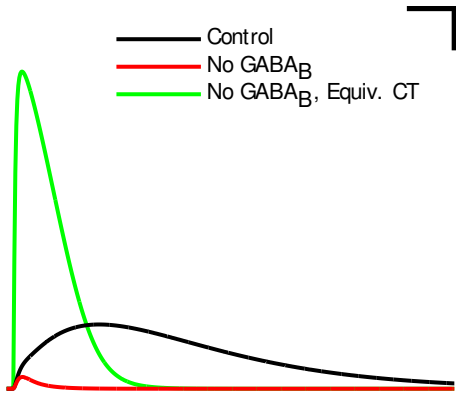

Figure 6 - figure supplement 2: **IPSCs from the neurogliaform to pyramidal cell synapse corresponding to the different conditions in Figure 6H.** These traces are from pyramidal cells clamped at -50 mV during a paired recording from a presynaptic neurogliaform cell with a $GABA_A$ reversal potential of -60 mV and a $GABA_B$ reversal potential of -90 mV. The currents shown are averages from 10 recordings. Scale bar = 100 ms and 5 pA.

Source Data Files

Figure 2 - Source Data 1: Model Sodium Channel Activation The ion channel characterized in this figure was an Na_v channel, inserted into a single compartment cell of diameter and length 16.8 microns (a soma) with a density such that the maximum, macroscopic conductance was .001 $\mu S/cm^2$. The reversal potential of the channel was +55 mV and the settings during the characterization protocol were: temperature=34 degrees Celsius, axial resistance = 210 ohm*cm, $[Ca2+]_{internal}$ = 5.0000e-06 mM, specific membrane capacitance = 1 $\mu F/cm^2$. For activation steps, the cell was held at -120 mV and then stepped to potential levels ranging from -90 mV to +90 mV. For inactivation steps, the cell was held at various potential levels ranging from -90 mV to +40 mV for 500 ms and then stepped to +20 mV. Each current injection step is recorded in three columns, where t: time (ms), i: injection (nA), g: conductance (S/cm^2). The column labels are followed by the voltage (hold or step, according to the file), with activation steps being recorded in the Na_Channel_Step.dat and inactivation steps being recorded in the Na_Channel_Hold.dat file.

File: Figure2BC-Na_Channel_Step.dat

Figure 2 - Source Data 2: Model Sodium Channel Inactivation The ion channel characterized in this figure was an Na_v channel, inserted into a single compartment cell of diameter and length 16.8 microns (a soma) with a density such that the maximum, macroscopic conductance was .001 $\mu S/cm^2$. The reversal potential of the channel was +55 mV and the settings during the characterization protocol were: temperature=34 degrees Celsius, axial resistance = 210 ohm*cm, $[Ca2+]_{internal}$ = 5.0000e-06 mM, specific membrane capacitance = 1 $\mu F/cm^2$. For activation steps, the cell was held at -120 mV and then stepped to potential levels ranging from -90 mV to +90 mV. For inactivation steps, the cell was held at various potential levels ranging from -90 mV to +40 mV for 500 ms and then stepped to +20 mV. Each current injection step is recorded in three columns, where t: time (ms), i: injection (nA), g: conductance (S/cm^2). The column labels are followed by the voltage (hold or step, according to the file), with activation steps being recorded in the Na_Channel_Step.dat and inactivation steps being recorded in the Na_Channel_Hold.dat file.

File: Figure2B-Na_Channel_Hold.dat

Figure 2 - Source Data 3: Model axo-axonic cell current injection sweep Simulated current injection sweep in AxoClamp ATF (tab-delimited) file format.

File: Figure2HIJ-axoaxoniccell.atf

Figure 2 - Source Data 4: Model bistratified cell current injection sweep Simulated current injection sweep in AxoClamp ATF (tab-delimited) file format.

File: Figure2HIJ-bistratifiedcell.atf

Figure 2 - Source Data 5: Model CCK+ basket cell current injection sweep Simulated current injection sweep in AxoClamp ATF (tab-delimited) file format.

File: Figure2HIJ-cckcell.atf

Figure 2 - Source Data 6: Model ivy cell current injection sweep Simulated current injection sweep in AxoClamp ATF (tab-delimited) file format.

File: Figure2HIJ-ivycell.atf

Figure 2 - Source Data 7: Model neurogliaform cell current injection sweep Simulated current injection sweep in AxoClamp ATF (tab-delimited) file format.

File: Figure2HIJ-ngfcell.atf

Figure 2 - Source Data 8: Model O-LM cell current injection sweep Simulated current injection sweep in AxoClamp ATF (tab-delimited) file format.

File: Figure2HIJ-olmcell.atf

Figure 2 - Source Data 9: Model PV+ basket cell current injection sweep Simulated current injection sweep in AxoClamp ATF (tab-delimited) file format.

File: Figure2HIJ-pvbasketcell.atf

Figure 2 - Source Data 10: Model pyramidal cell current injection sweep Simulated current injection sweep in AxoClamp ATF (tab-delimited) file format.

File: Figure2HIJ-pyramidalcell.atf

Figure 2 - Source Data 11: Model Schaffer Collateral-Associated cell current injection sweep Simulated current injection sweep in AxoClamp ATF (tab-delimited) file format.

File: Figure2HIJ-scacell.atf

Figure 2 - Source Data 12: Model paired recording of an Axo-axonic cell to Pyramidal cell connection Simulated paired recordings where the postsynaptic cell was voltage-clamped at -50 mV and the reversal potential of the synapse was kept at its physiological potential, as defined in the network model code. Sodium channels in the postsynaptic cell were blocked to prevent a suprathreshold response. A spike was triggered in the presynaptic cell and the current response was measured in the postsynaptic cell at the soma. This recording was repeated 10 times, with a randomly chosen connection location (from anatomically likely locations) each time. Each of the 10 trials are included in this file.

File: Figure2K-axoaxoniccell.pyramidalcell.all.dat

Figure 2 - Source Data 13: Model paired recording of a Bistratified cell to Pyramidal cell connection Simulated paired recordings where the postsynaptic cell was voltage-clamped at -50 mV and the reversal potential of the synapse was kept at its physiological potential, as defined in the network model code. Sodium channels in the postsynaptic cell were blocked to prevent a suprathreshold response. A spike was triggered in the presynaptic cell and the current response was measured in the postsynaptic cell at the soma. This recording was repeated 10 times, with a randomly chosen connection location (from anatomically likely locations) each time. Each of the 10 trials are included in this file.

File: Figure2K-bistratifiedcell.pyramidalcell.all.dat

Figure 2 - Source Data 14: Model paired recording of a CA3 cell to Pyramidal cell connection Simulated paired recordings where the postsynaptic cell was voltage-clamped at -50 mV and the reversal potential of the synapse was kept at its physiological potential, as defined in the network model code. Sodium channels in the postsynaptic cell were blocked to prevent a suprathreshold response. A spike was triggered in the presynaptic cell and the current response was measured in the postsynaptic cell at the soma. This recording was repeated 10 times, with a randomly chosen connection location (from anatomically likely locations) each time. Each of the 10 trials are included in this file.

File: Figure2K-ca3cell.pyramidalcell.all.dat

Figure 2 - Source Data 15: Model paired recording of a CCK+ basket cell to Pyramidal cell connection Simulated paired recordings where the postsynaptic cell was voltage-clamped at -50 mV and the reversal potential of the synapse was kept at its physiological potential, as defined in the network model code. Sodium channels in the postsynaptic cell were blocked to prevent a suprathreshold response. A spike was triggered in the presynaptic cell and the current response was measured in the postsynaptic cell at the soma. This recording was repeated 10 times, with a randomly chosen connection location (from anatomically likely locations) each time. Each of the 10 trials are included in this file.

File: Figure2K-cckcell.pyramidalcell.all.dat

Figure 2 - Source Data 16: Model paired recording of an ECIII cell to Pyramidal cell connection Simulated paired recordings where the postsynaptic cell was voltage-clamped at -50 mV and the reversal potential of the synapse was kept at its physiological potential, as defined in the network model code. Sodium channels in the postsynaptic cell were blocked to prevent a suprathreshold response. A spike was triggered in the presynaptic cell and the current response was measured in the postsynaptic cell at the soma. This recording was repeated 10 times, with a randomly chosen connection location (from anatomically likely locations) each time. Each of the 10 trials are included in this file.

File: Figure2K-eccell.pyramidalcell.all.dat

Figure 2 - Source Data 17: Model paired recording of an Ivy cell to Pyramidal cell connection Simulated paired recordings where the postsynaptic cell was voltage-clamped at -50 mV and the reversal potential of the synapse was kept at its physiological potential, as defined in the network model code. Sodium channels in the postsynaptic cell were blocked to prevent a suprathreshold response. A spike was triggered in the presynaptic cell and the current response was measured in the postsynaptic cell at the soma. This recording was repeated 10 times, with a randomly chosen connection location (from anatomically likely locations) each time. Each of the 10 trials are included in this file.

File: Figure2K-ivycell.pyramidalcell.all.dat

Figure 2 - Source Data 18: Model paired recording of a Pyramidal cell to Pyramidal cell connection Simulated paired recordings where the postsynaptic cell was voltage-clamped at -50 mV and the reversal potential of the synapse was kept at its physiological potential, as defined in the network model code. Sodium channels in the postsynaptic cell were blocked to prevent a suprathreshold response. A spike was triggered in the presynaptic cell and the current response was measured in the postsynaptic cell at the soma. This recording was repeated 10 times, with a randomly chosen connection location (from anatomically likely locations) each time. Each of the 10 trials are included in this file.

File: Figure2KL-pyramidalcell.pyramidalcell.all.dat

Figure 2 - Source Data 19: Model paired recording of a Neurogliaform cell to Pyramidal cell connection Simulated paired recordings where the postsynaptic cell was voltage-clamped at -50 mV and the reversal potential of the synapse was kept at its physiological potential, as defined in the network model code. Sodium channels in the postsynaptic cell were blocked to prevent a suprathreshold response. A spike was triggered in the presynaptic cell and the current response was measured in the postsynaptic cell at the soma. This recording was repeated 10 times, with a randomly chosen connection location (from anatomically likely locations) each time. Each of the 10 trials are included in this file.

File: Figure2K-ngfcell.pyramidalcell.all.dat

Figure 2 - Source Data 20: Model paired recording of an O-LM cell to Pyramidal cell connection Simulated paired recordings where the postsynaptic cell was voltage-clamped at -50 mV and the reversal potential of the synapse was kept at its physiological potential, as defined in the network model code. Sodium channels in the postsynaptic cell were blocked to prevent a suprathreshold response. A spike was triggered in the presynaptic cell and the current response was measured in the postsynaptic cell at the soma. This recording was repeated 10 times, with a randomly chosen connection location (from anatomically likely locations) each time. Each of the 10 trials are included in this file.

File: Figure2K-olmcell.pyramidalcell.all.dat

Figure 2 - Source Data 21: Model paired recording of a PV+ basket cell to Pyramidal cell connection Simulated paired recordings where the postsynaptic cell was voltage-clamped at -50 mV and the reversal potential of the synapse was kept at its physiological potential, as defined in the network model code. Sodium channels in the postsynaptic cell were blocked to prevent a suprathreshold response. A spike was triggered in the presynaptic cell and the current response was measured in the postsynaptic cell at the soma. This recording was repeated 10 times, with a randomly chosen connection location (from anatomically likely locations) each time. Each of the 10 trials are included in this file.

File: Figure2K-pvbasketcell.pyramidalcell.all.dat

Figure 2 - Source Data 22: Model paired recording of a Pyramidal cell to Axo-axonic cell connection Simulated paired recordings where the postsynaptic cell was voltage-clamped at -50 mV and the reversal potential of the synapse was kept at its physiological potential, as defined in the network model code. Sodium channels in the postsynaptic cell were blocked to prevent a suprathreshold response. A spike was triggered in the presynaptic cell and the current response was measured in the postsynaptic cell at the soma. This recording was repeated 10 times, with a randomly chosen connection location (from anatomically likely locations) each time. Each of the 10 trials are included in this file.

File: Figure2L-pyramidalcell.axoaxoniccell.all.dat

Figure 2 - Source Data 23: Model paired recording of a Pyramidal cell to Bistratified cell connection Simulated paired recordings where the postsynaptic cell was voltage-clamped at -50 mV and the reversal potential of the synapse was kept at its physiological potential, as defined in the network model code. Sodium channels in the postsynaptic cell were blocked to prevent a suprathreshold response. A spike was triggered in the presynaptic cell and the current response was measured in the postsynaptic cell at the soma. This recording was repeated 10 times, with a randomly chosen connection location (from anatomically likely locations) each time. Each of the 10 trials are included in this file.

File: Figure2L-pyramidalcell.bistratifiedcell.all.dat

Figure 2 - Source Data 24: Model paired recording of a Pyramidal cell to Ivy cell connection Simulated paired recordings where the postsynaptic cell was voltage-clamped at -50 mV and the reversal potential of the synapse was kept at its physiological potential, as defined in the network model code. Sodium channels in the postsynaptic cell were blocked to prevent a suprathreshold response. A spike was triggered in the presynaptic cell and the current response was measured in the postsynaptic cell at the soma. This recording was repeated 10 times, with a randomly chosen connection location (from anatomically likely locations) each time. Each of the 10 trials are included in this file.

File: Figure2L-pyramidalcell.ivycell.all.dat

Figure 2 - Source Data 25: Model paired recording of a Pyramidal cell to O-LM cell connection Simulated paired recordings where the postsynaptic cell was voltage-clamped at -50 mV and the reversal potential of the synapse was kept at its physiological potential, as defined in the network model code. Sodium channels in the postsynaptic cell were blocked to prevent a suprathreshold response. A spike was triggered in the presynaptic cell and the current response was measured in the postsynaptic cell at the soma. This recording was repeated 10 times, with a randomly chosen connection location (from anatomically likely locations) each time. Each of the 10 trials are included in this file.

File: Figure2L-pyramidalcell.olmcell.all.dat

Figure 2 - Source Data 26: Model paired recording of a Pyramidal cell to PV+ basket cell connection Simulated paired recordings where the postsynaptic cell was voltage-clamped at -50 mV and the reversal potential of the synapse was kept at its physiological potential, as defined in the network model code. Sodium channels in the postsynaptic cell were blocked to prevent a suprathreshold response. A spike was triggered in the presynaptic cell and the current response was measured in the postsynaptic cell at the soma. This recording was repeated 10 times, with a randomly chosen connection location (from anatomically likely locations) each time. Each of the 10 trials are included in this file.

File: Figure2L-pyramidalcell.pvbasketcell.all.dat

Figure 2 - Source Data 27: Model paired recording of a Pyramidal cell to Schaffer Collateral-Associated cell connection Simulated paired recordings where the postsynaptic cell was voltage-clamped at -50 mV and the reversal potential of the synapse was kept at its physiological potential, as defined in the network model code. Sodium channels in the postsynaptic cell were blocked to prevent a suprathreshold response. A spike was triggered in the presynaptic cell and the current response was measured in the postsynaptic cell at the soma. This recording was repeated 10 times, with a randomly chosen connection location (from anatomically likely locations) each time. Each of the 10 trials are included in this file.

File: Figure2L-pyramidalcell.scacell.all.dat

Figure 3 - Source Data 1: Filtered analog local field potential of model network The theta-filtered and gamma-filtered local field potential (LFP) analog traces

File: Figure3AB-FilteredLFP.txt

Figure 3 - Source Data 2: Spike Raster Spike times for the length of the entire simulation, from the specific cells displayed in raster shown in Figure 3 (spike times of every single cell in the network are available in the CRCNS repository entry for Bezaire et al. (2015)).

File: Figure3C-SpikeRasterLocal.dat

Figure 3 - Source Data 3: Somatic membrane potential recordings Full duration, intracellular somatic membrane potential recordings from the specific cells shown in Figure 3.

File: Figure3D-MembranePotentials.txt

Figure 4 - Source Data 1: Raw analog local field potential of model network The raw local field potential (LFP) analog calculated from the network activity, as detailed in the Methods section.

File: Figure4A-LFP.txt

Figure 4 - Source Data 2: Spike Density Functions of each cell type in control network The power of the Spike Density Functions was calculated from a one-sided periodogram using Welch's method where segments have a 50% overlap with a Hamming Window.

File: Figure4BD-All_SDF.txt

Figure 5 - Source Data 1: Spike times of axo-axonic cells All spike times from all axo-axonic cells, as well as the calculated theta phases (relative to the theta-filtered LFP analog) of each spike.

File: Figure5-axoaxoniccell.txt

Figure 5 - Source Data 2: Spike times of bistratified cells All spike times from all bistratified cells, as well as the calculated theta phases (relative to the theta-filtered LFP analog) of each spike.

File: Figure5-bistratifiedcell.txt

Figure 5 - Source Data 3: Spike times of proximal afferent cells All spike times from all proximal afferent cells, as well as the calculated theta phases (relative to the theta-filtered LFP analog) of each spike.

File: Figure5-ca3cell.txt

Figure 5 - Source Data 4: Spike times of CCK+ basket cells All spike times from all CCK+ basket cells, as well as the calculated theta phases (relative to the theta-filtered LFP analog) of each spike.

File: Figure5-cckcell.txt

Figure 5 - Source Data 5: Spike times of distal afferent cells All spike times from all distal afferent cells, as well as the calculated theta phases (relative to the theta-filtered LFP analog) of each spike.

File: Figure5-eccell.txt

Figure 5 - Source Data 6: Spike times of ivy cells All spike times from all ivy cells, as well as the calculated theta phases (relative to the theta-filtered LFP analog) of each spike.

File: Figure5-ivycell.txt

Figure 5 - Source Data 7: Spike times of neurogliaform cells All spike times from all neurogliaform cells, as well as the calculated theta phases (relative to the theta-filtered LFP analog) of each spike.

File: Figure5-ngfcell.txt

Figure 5 - Source Data 8: Spike times of O-LM cells All spike times from all O-LM cells, as well as the calculated theta phases (relative to the theta-filtered LFP analog) of each spike.

File: Figure5-olmcell.txt

Figure 5 - Source Data 9: Spike times of PV+ basket cells All spike times from all PV+ basket cells, as well as the calculated theta phases (relative to the theta-filtered LFP analog) of each spike.

File: Figure5-pvbasketcell.txt

Figure 5 - Source Data 10: Spike times of pyramidal cells All spike times from all pyramidal cells, as well as the calculated theta phases (relative to the theta-filtered LFP analog) of each spike.

File: Figure5-pyramidalcell.txt

Figure 5 - Source Data 11: Spike times of Schaffer Collateral-associated cells All spike times from all Schaffer Collateral-associated cells, as well as the calculated theta phases (relative to the theta-filtered LFP analog) of each spike.

File: Figure5-scacell.txt

Figure 6 - Source Data 1: Simulation name mapping Map the names of the simulations (used in the header of SDF_All_Conditions.txt) to the bar labels in the graphs of Figure 6.

File: Figure6-Map_Sim_Name_Figure_Panel.txt

Figure 6 - Source Data 2: SDF of each network condition The full length pyramidal cell Spike Density Function computed at a resolution of 1000 Hz from the spikes of all pyramidal cells within the local range of the electrode point in the model network, for each network condition studied in Figure 6.

File: Figure6-SDF_All_Conditions.txt

References

Thomas E Akam and Dimitri M Kullmann. Efficient "communication through coherence" requires oscillations structured to minimize interference between signals. *PLoS Comput Biol*, 8(11):e1002760, 2012. doi: 10.1371/journal.pcbi.1002760.

Bénédicte Amilhon, Carey YL Huh, Frédéric Manseau, Guillaume Ducharme, Heather Nichol, Antoine Adamantidis, and Sylvain Williams. Parvalbumin interneurons of hippocampus tune population activity at theta frequency. *Neuron*, 86(5):1277–1289, 2015. doi: 10.1016/j.neuron.2015.05.027.

Per Andersen, Richard Morris, David Amaral, Tim Bliss, and John O'Keefe. *The hippocampus book*. Oxford University Press, USA, 2006. doi: 10.1093/acprof:oso/9780195100273.001.0001.

Ildikó Aradi and William R Holmes. Role of multiple calcium and calcium-dependent conductances in regulation of hippocampal dentate granule cell excitability. *Journal of computational neuroscience*, 6(3):215–235, 1999. doi: 10.1023/A:1008801821784.

Caren Armstrong and Ivan Soltesz. Basket cell dichotomy in microcircuit function. *The Journal of physiology*, 590(4):683–694, 2012. doi: 10.1113/jphysiol.2011.223669.

Jeremy F Atherton and Mark D Bevan. Ionic mechanisms underlying autonomous action potential generation in the somata and dendrites of gabaergic substantia nigra pars reticulata neurons in vitro. *The Journal of neuroscience*, 25(36):8272–8281, 2005. doi: 10.1523/JNEUROSCI.1475-05.2005.

Jayeeta Basu, Jeffrey D Zaremba, Stephanie K Cheung, Frederick L Hitti, Boris V Zemelman, Attila Losonczy, and Steven A Siegelbaum. Gating of hippocampal activity, plasticity, and memory by entorhinal cortex long-range inhibition. *Science*, 351(6269):aaa5694, 2016.

H Beck, H Clusmann, T Kral, J Schramm, U Heinemann, and CE Elger. Potassium currents in acutely isolated human hippocampal dentate granule cells. *The Journal of physiology*, 498(Pt 1): 73–85, 1997. doi: 10.1113/jphysiol.1997.sp021842.

Mariano A Belluscio, Kenji Mizuseki, Robert Schmidt, Richard Kempter, and György Buzsáki. Cross-frequency phase–phase coupling between theta and gamma oscillations in the hippocampus. *The Journal of Neuroscience*, 32(2):423–435, 2012. doi: 10.1523/JNEUROSCI.4122-11.2012.

Marianne Bezaire. *Modeling physiological oscillations in a biologically constrained CA1 network from two perspectives: full-scale parallel network and rationally reduced Network Clamp*. UNIVERSITY OF CALIFORNIA, IRVINE, 2015. URL http://gradworks.umi.com/37/17/3717051.html.

Marianne J Bezaire and Ivan Soltesz. Quantitative assessment of CA1 local circuits: knowledge base for interneuron-pyramidal cell connectivity. *Hippocampus*, 23(9):751–785, 2013. doi: 10.1002/hipo.22141. URL http://www.ncbi.nlm.nih.gov/pubmed/23674373.

Marianne J. Bezaire, Ivan Raikov, Kelly Burk, Dhrumil Vyas, and Ivan Soltesz. Simulation results from full scale and rationally reduced network models of the isolated hippocampal CA1 subfield in rat. *CRCNS.org*, 2015. doi: 10.6080/K05H7D60. URL http://dx.doi.org/10.6080/K05H7D60.

Marianne J Bezaire, Ivan Raikov, Kelly Burk, Caren Armstrong, and Ivan Soltesz. SimTracker: a tool and code template to design, manage and analyze neural network model simulations in parallel NEURON. *bioRxiv*, 2016. doi: 10.1101/081927. URL http://dx.doi.org/10.1101/081927.

JM Blasco-Ibáñez and TF Freund. Synaptic input of horizontal interneurons in stratum oriens of the hippocampal ca1 subfield: Structural basis of feed-back activation. *European Journal of Neuroscience*, 7(10):2170–2180, 1995. doi: 10.1111/j.1460-9568.1995.tb00638.x.

LYLE J Borg-Graham. Modeling the non-linear conductances of excitable membranes. *Cellular Neurobiology: A Practical Approach*, 13:247–275, 1991.

Anatol Bragin, Gábor Jandó, Zoltán Nádasdy, Jamille Hetke, K Wise, and Gy Buzsáki. Gamma (40-100 hz) oscillation in the hippocampus of the behaving rat. *The Journal of Neuroscience*, 15 (1):47–60, 1995.

James L Butler, Philipe RF Mendonça, Hugh PC Robinson, and Ole Paulsen. Intrinsic Cornu Ammonis Area 1 theta-nested gamma oscillations induced by optogenetic theta frequency stimulation. *The Journal of Neuroscience*, 36(15):4155–4169, 2016. doi: 10.1523/JNEUROSCI.3150-15.2016.

G Buzsáki, DL Buhl, KD Harris, J Csicsvari, B Czeh, and A Morozov. Hippocampal network patterns of activity in the mouse. *Neuroscience*, 116(1):201–211, 2003. doi: 10.1016/S0306-4522(02)00669-3.

György Buzsáki. Theta oscillations in the hippocampus. *Neuron*, 33(3):325–340, 2002. doi: 10.1016/S0896-6273(02)00586-X.

György Buzsáki and Edvard I Moser. Memory, navigation and theta rhythm in the hippocampal-entorhinal system. *Nature neuroscience*, 16(2):130–138, 2013. doi: 10.1038/nn.3304.

György Buzsáki, Costas A Anastassiou, and Christof Koch. The origin of extracellular fields and currents—EEG, ECoG, LFP and spikes. *Nature reviews neuroscience*, 13(6):407–420, 2012. doi: 10.1038/nrn3241.

Emilie Campanac, Célia Gasselin, Agnès Baude, Sylvain Rama, Norbert Ankri, and Dominique Debanne. Enhanced intrinsic excitability in basket cells maintains excitatory-inhibitory balance in hippocampal circuits. *Neuron*, 77(4):712–722, 2013. doi: 10.1016/j.neuron.2012.12.020.

Marco Capogna. Neurogliaform cells and other interneurons of stratum lacunosum-moleculare gate entorhinal–hippocampal dialogue. *The Journal of physiology*, 589(8):1875–1883, 2011. doi: 10.1113/jphysiol.2010.201004.

Nicholas T. Carnevale and Michael L. Hines. *The NEURON Book*. Cambridge University Press, New York, 2005.

Kang Chen, Ildiko Aradi, Niklas Thon, Mariam Eghbal-Ahmadi, Tallie Z Baram, and Ivan Soltesz. Persistently modified h-channels after complex febrile seizures convert the seizure-induced enhancement of inhibition to hyperexcitability. *Nature medicine*, 7(3):331–337, 2001. doi: 10.1038/85480.

Laura Lee Colgin. Mechanisms and functions of theta rhythms. *Annual review of neuroscience*, 36: 295–312, 2013. doi: 10.1146/annurev-neuro-062012-170330.

Laura Lee Colgin. Rhythms of the hippocampal network. *Nature Reviews Neuroscience*, 2016. doi: 10.1038/nrn.2016.21.

Laura Lee Colgin and Edvard I Moser. Gamma oscillations in the hippocampus. *Physiology*, 25(5): 319–329, 2010. doi: 10.1152/physiol.00021.2010.

Laura Lee Colgin, Tobias Denninger, Marianne Fyhn, Torkel Hafting, Tora Bonnevie, Ole Jensen, May-Britt Moser, and Edvard I Moser. Frequency of gamma oscillations routes flow of information in the hippocampus. *Nature*, 462(7271):353–357, 2009. doi: 10.1038/nature08573.

Donald C. Cooper, Shannon J. Moore, Nathan P. Staff, and Nelson Spruston. Psychostimulant-Induced Plasticity of Intrinsic Neuronal Excitability in Ventral Subiculum. *J. Neurosci.*, 23(30): 9937–9946, October 2003.

Michael T Craig and Chris J McBain. The emerging role of GABA B receptors as regulators of network dynamics: fast actions from a 'slow'receptor? *Current opinion in neurobiology*, 26:15–21, 2014. doi: 10.1016/j.conb.2013.10.002.

Jozsef Csicsvari, Hajime Hirase, András Czurkó, Akira Mamiya, and György Buzsáki. Oscillatory coupling of hippocampal pyramidal cells and interneurons in the behaving rat. *The Journal of neuroscience*, 19(1):274–287, 1999.

Vassilis Cutsuridis and Michael Hasselmo. GABAergic contributions to gating, timing, and phase precession of hippocampal neuronal activity during theta oscillations. *Hippocampus*, 2012. doi: 10.1002/hipo.21002.

Vassilis Cutsuridis, Stuart Cobb, and Bruce P Graham. Encoding and retrieval in a model of the hippocampal CA1 microcircuit. *Hippocampus*, 20(3):423–446, 2010. doi: 10.1002/hipo.20661.

Holger Dannenberg, Milan Pabst, Oliver Braganza, Susanne Schoch, Johannes Niediek, Melike Bayraktar, Florian Mormann, and Heinz Beck. Synergy of direct and indirect cholinergic septo-hippocampal pathways coordinates firing in hippocampal networks. *The Journal of Neuroscience*, 35(22):8394–8410, 2015. doi: 10.1523/JNEUROSCI.4460-14.2015.

Jonas Dyhrfjeld-Johnsen, Vijayalakshmi Santhakumar, Robert J Morgan, Ramon Huerta, Lev Tsimring, and Ivan Soltesz. Topological determinants of epileptogenesis in large-scale structural and functional models of the dentate gyrus derived from experimental data. *Journal of neurophysiology*, 97(2):1566–1587, 2007a. doi: 10.1152/jn.00950.2006.

Jonas Dyhrfjeld-Johnsen, Vijayalakshmi Santhakumar, Robert J Morgan, Ramon Huerta, Lev Tsimring, and Ivan Soltesz. Topological determinants of epileptogenesis in large-scale structural and functional models of the dentate gyrus derived from experimental data. *Journal of neurophysiology*, 97(2):1566–1587, 2007b. doi: 10.1152/jn.00950.2006.

Andreas K Engel and Pascal Fries. Beta-band oscillations—signalling the status quo? *Current opinion in neurobiology*, 20(2):156–165, 2010. doi: 10.1016/j.conb.2010.02.015.

Katie A Ferguson, Carey YL Huh, Bénédicte Amilhon, Sylvain Williams, and Frances K Skinner. Experimentally constrained CA1 fast-firing parvalbumin-positive interneuron network models exhibit sharp transitions into coherent high frequency rhythms. *Frontiers in computational neuroscience*, 7, 2013. doi: 10.3389/fncom.2013.00144.

Katie A Ferguson, Carey YL Huh, Bénédicte Amilhon, Frédéric Manseau, Sylvain Williams, and Frances K Skinner. Network models provide insights into how oriens–lacunosum-moleculare and bistratified cell interactions influence the power of local hippocampal CA1 theta oscillations. *Frontiers in systems neuroscience*, 9, 2015. doi: 10.3389/fnsys.2015.00110.

F. Ferraguti, T. Klausberger, P. Cobden, A. Baude, J.D.B. Roberts, P. Szucs, A. Kinoshita, R. Shigemoto, P. Somogyi, and Y. Dalezios. Metabotropic glutamate receptor 8-expressing nerve terminals

target subsets of GABAergic neurons in the hippocampus. *J. Neurosci.*, 25(45):10520–10536, 2005. doi: 10.1523/JNEUROSCI.2547-05.2005.

E Ficker and U Heinemann. Slow and fast transient potassium currents in cultured rat hippocampal cells. *The Journal of physiology*, 445(1):431–455, 1992. doi: 10.1113/jphysiol.1992.sp018932.

Pascal Fries. Rhythms for cognition: communication through coherence. *Neuron*, 88(1):220–235, 2015. doi: 10.1016/j.neuron.2015.09.034.

P. Fuentealba, R. Begum, M. Capogna, S. Jinno, L.F. Márton, J. Csicsvari, A. Thomson, P. Somogyi, and T. Klausberger. Ivy cells: a population of nitric-oxide-producing, slow-spiking GABAergic neurons and their involvement in hippocampal network activity. *Neuron*, 57:917–929, 2008. doi: 10.1016/j.neuron.2008.01.034.

Pablo Fuentealba, Thomas Klausberger, Theofanis Karayannis, Wai Yee Suen, Jojanneke Huck, Ryohei Tomioka, Kathleen Rockland, Marco Capogna, Michèle Studer, Marisela Morales, and Peter Somogyi. Expression of COUP-TFII nuclear receptor in restricted GABAergic neuronal populations in the adult rat hippocampus. *Journal of Neuroscience*, 30:1595–609, 2010. doi: 10.1523/JNEUROSCI.4199-09.2010.

Falko Fuhrmann, Daniel Justus, Liudmila Sosulina, Hiroshi Kaneko, Tatjana Beutel, Detlef Friedrichs, Susanne Schoch, Martin Karl Schwarz, Martin Fuhrmann, and Stefan Remy. Locomotion, theta oscillations, and the speed-correlated firing of hippocampal neurons are controlled by a medial septal glutamatergic circuit. *Neuron*, 86(5):1253–1264, 2015. doi: 10.1016/j.neuron.2015.05.001.

Sonia Gasparini and Jeffrey C. Magee. State-dependent dendritic computation in hippocampal CA1 pyramidal neurons. *J. Neurosci.*, 26:2088–2100, 2006. doi: 10.1523/JNEUROSCI.4428-05.2006.

Padraig Gleeson, Volker Steuber, and R Angus Silver. neuroConstruct: a tool for modeling networks of neurons in 3D space. *Neuron*, 54(2):219–235, 2007. doi: 10.1016/j.neuron.2007.03.025.

Romain Goutagny, Jesse Jackson, and Sylvain Williams. Self-generated theta oscillations in the hippocampus. *Nature neuroscience*, 12(12):1491—1493, December 2009. ISSN 1097-6256. doi: 10.1038/nn.2440. URL http://dx.doi.org/10.1038/nn.2440.

A. I. Gulyas, K. Toth, P. Danos, and T.F. Freund. Subpopulations of GABAergic neurons containing parvalbumin, calbindin D28k, and cholecystokinin in the rat hippocampus. *J Comp Neurol*, 312: 371–378, 1991. doi: 10.1002/cne.903120305.

Attila I Gulyas, Manuel Megias, Zsuzsa Emri, and Tamas F Freund. Total number and ratio of excitatory and inhibitory synapses converging onto single interneurons of different types in the CA1 area of the rat hippocampus. *The Journal of neuroscience*, 19(22):10082–10097, 1999.

N Hajos and I Mody. Synaptic communication among hippocampal interneurons: properties of spontaneous IPSCs in morphologically identified cells. *J. Neurosci.*, 17:8427–8442, 1997.

Michael E Hasselmo. What is the function of hippocampal theta rhythm?—linking behavioral data to phasic properties of field potential and unit recording data. *Hippocampus*, 15(7):936–949, 2005. doi: 10.1002/hipo.20116.

Michael E Hasselmo, Clara Bodelón, and Bradley P Wyble. A proposed function for hippocampal theta rhythm: separate phases of encoding and retrieval enhance reversal of prior learning. *Neural computation*, 14(4):793–817, 2002. doi: 10.1162/089976602317318965.

Phillip J Hendrickson, J Yu Gene, Dong Song, and Theodore W Berger. Interactions between inhibitory interneurons and excitatory associational circuitry in determining spatio-temporal dynamics of hippocampal dentate granule cells: A large-scale computational study. *Frontiers in systems neuroscience*, 9, 2015. doi: 10.3389/fnsys.2015.00155.

Michael L Hines and N Ted Carnevale. Translating network models to parallel hardware in NEURON. *Journal of neuroscience methods*, 169(2):425–455, 2008. doi: 10.1016/j.jneumeth.2007.09.010.

Michael L Hines, Hubert Eichner, and Felix Schürmann. Neuron splitting in compute-bound parallel network simulations enables runtime scaling with twice as many processors. *Journal of computational neuroscience*, 25(1):203–210, 2008a. doi: 10.1007/s10827-007-0073-3.

Michael L Hines, Henry Markram, and Felix Schürmann. Fully implicit parallel simulation of single neurons. *Journal of computational neuroscience*, 25(3):439–448, 2008b. doi: 10.1007/s10827-008-0087-5.

Yoshie Hongo, Koichi Ogawa, Yuji Takahara, Keiko Takasu, Sebastien Royer, Minoru Hasegawa, Gaku Sakaguchi, and Yuji Ikegaya. Topological organization of CA3-to-CA1 excitation. *European Journal of Neuroscience*, 2015. doi: 10.1111/ejn.12969.

Hua Hu, Jian Gan, and Peter Jonas. Fast-spiking, parvalbumin+ GABAergic interneurons: From cellular design to microcircuit function. *Science*, 345(6196):1255263, 2014. doi: 10.1126/science.1255263.

DAVID B Jaffe, WILLIAM N Ross, JOHN E Lisman, NECHAMA Lasser-Ross, HIROYOSHI Miyakawa, and DANIEL Johnston. A model for dendritic ca2+ accumulation in hippocampal pyramidal neurons based on fluorescence imaging measurements. *Journal of neurophysiology*, 71:1065–1065, 1994.

Peter Jedlicka, Thomas Deller, and Stephan W Schwarzacher. Computational modeling of GABAA receptor-mediated paired-pulse inhibition in the dentate gyrus. *Journal of computational neuroscience*, 29(3):509–519, 2010a. doi: 10.1007/s10827-010-0214-y.

Peter Jedlicka, Mrinalini Hoon, Theofilos Papadopoulos, Andreas Vlachos, Raphael Winkels, Alexandros Poulopoulos, Heinrich Betz, Thomas Deller, Nils Brose, Frédérique Varoqueaux, et al. Increased dentate gyrus excitability in neuroligin-2-deficient mice in vivo. *Cerebral cortex*, page bhq100, 2010b. doi: 10.1093/cercor/bhq100.

A Jeewajee, C Barry, V Douchamps, D Manson, C Lever, and N Burgess. Theta phase precession of

grid and place cell firing in open environments. *Philosophical Transactions of the Royal Society of London B: Biological Sciences*, 369(1635):20120532, 2014. doi: 10.1098/rstb.2012.0532.

Ole Jensen and Laura L Colgin. Cross-frequency coupling between neuronal oscillations. *Trends in cognitive sciences*, 11(7):267–269, 2007. doi: 10.1016/j.tics.2007.05.003.

Ole Jensen and John E Lisman. Position reconstruction from an ensemble of hippocampal place cells: contribution of theta phase coding. *Journal of neurophysiology*, 83(5):2602–2609, 2000.

Shozo Jinno, Thomas Klausberger, Laszlo F. Marton, Yannis Dalezios, J. David B. Roberts, Pablo Fuentealba, Eric A. Bushong, Darrell Henze, György Buzsáki, and Peter Somogyi. Neuronal diversity in GABAergic long-range projections from the hippocampus. *J. Neurosci.*, 27:8790–8804, 2007. doi: 10.1523/JNEUROSCI.1847-07.2007.

Linda Katona, Damien Lapray, Tim J Viney, Abderrahim Oulhaj, Zsolt Borhegyi, Benjamin R Micklem, Thomas Klausberger, and Peter Somogyi. Sleep and movement differentiates actions of two types of somatostatin-expressing GABAergic interneuron in rat hippocampus. *Neuron*, 82(4):872–886, 2014. doi: 10.1016/j.neuron.2014.04.007.

Ege T Kavalali. The mechanisms and functions of spontaneous neurotransmitter release. *Nature Reviews Neuroscience*, 16(1):5–16, 2015. doi: 10.1038/nrn3875.

Adam Kepecs and Gordon Fishell. Interneuron cell types are fit to function. *Nature*, 505(7483): 318–326, 2014. doi: 10.1038/nature12983.

Tilman J Kispersky, Fernando R Fernandez, Michael N Economo, and John A White. Spike resonance properties in hippocampal o-lm cells are dependent on refractory dynamics. *The Journal of Neuroscience*, 32(11):3637–3651, 2012. doi: 10.1523/JNEUROSCI.1361-11.2012.

Thomas Klausberger and Peter Somogyi. Neuronal diversity and temporal dynamics: The unity of hippocampal circuit operations. *Science*, 321:53–57, 2008. doi: 10.1126/science.1149381.

Thomas Klausberger, Peter J. Magill, László F. Márton, J. David B. Roberts, Philip M. Cobden, György Buzsáki, and Peter Somogyi. Brain-state- and cell-type-specific firing of hippocampal interneurons *in vivo*. *Nature*, 421:844–848, 2003. doi: 10.1038/nature01374.

Thomas Klausberger, László F Márton, Agnes Baude, J David B Roberts, Peter J Magill, and Peter Somogyi. Spike timing of dendrite-targeting bistratified cells during hippocampal network oscillations *in vivo*. *Nat. Neurosci.*, 7:41–47, 2004. doi: 10.1038/nn1159.

Thomas Klausberger, Laszlo F. Marton, Joseph O'Neill, Jojanneke H. J. Huck, Yannis Dalezios, Pablo Fuentealba, Wai Yee Suen, Edit Papp, Takeshi Kaneko, Masahiko Watanabe, Jozsef Csicsvari, and Peter Somogyi. Complementary roles of cholecystokinin- and parvalbumin-expressing GABAergic neurons in hippocampal network oscillations. *J. Neurosci.*, 25:9782–9793, 2005. doi: 10.1523/JNEUROSCI.3269-05.2005.

R Klee, E Ficker, and U Heinemann. Comparison of voltage-dependent potassium currents in rat pyramidal neurons acutely isolated from hippocampal regions ca1 and ca3. *Journal of neurophysiology*, 74:1982–1982, 1995.

Michael M Kohl and Ole Paulsen. The roles of GABA B receptors in cortical network activity. *Advances in pharmacology*, 58:205–229, 2010. doi: 10.1016/S1054-3589(10)58009-8.

R_ Kramis, CH Vanderwolf, and B Hi Bland. Two types of hippocampal rhythmical slow activity in both the rabbit and the rat: relations to behavior and effects of atropine, diethyl ether, urethane, and pentobarbital. *Experimental neurology*, 49(1):58–85, 1975.

Esther Krook-Magnuson, Lillian Luu, Sang-Hun Lee, Csaba Varga, and Ivan Soltesz. Ivy and neurogliaform interneurons are a major target of μ-opioid receptor modulation. *The Journal of Neuroscience*, 31(42):14861–14870, 2011. doi: 10.1523/JNEUROSCI.2269-11.2011.

B Lancaster, RA Nicoll, and DJ Perkel. Calcium activates two types of potassium channels in rat hippocampal neurons in culture. *The Journal of neuroscience*, 11(1):23–30, 1991.

Damien Lapray, Balint Lasztoczi, Michael Lagler, Tim James Viney, Linda Katona, Ornella Valenti, Katja Hartwich, Zsolt Borhegyi, Peter Somogyi, and Thomas Klausberger. Behavior-dependent specialization of identified hippocampal interneurons. *Nature neuroscience*, 15(9):1265–1271, 2012. doi: 10.1038/nn.3176.

Ramon Latorre, Andres Oberhauser, Pedro Labarca, and Osvaldo Alvarez. Varieties of calcium-activated potassium channels. *Annual Review of Physiology*, 51(1):385–399, 1989. doi: 10.1146/annurev.ph.51.030189.002125.

M.G. Lee, J.J. Chrobak, A. Sik, R.G. Wiley, and G. Buzsaki. Hippocampal theta activity following selective lesion of the septal cholinergic system. *Neuroscience*, 62(4):1033 – 1047, 1994. doi: 10.1016/0306-4522(94)90341-7.

Sang-Hun Lee, Csaba Foldy, and Ivan Soltesz. Distinct endocannabinoid control of GABA release at perisomatic and dendritic synapses in the hippocampus. *J. Neurosci.*, 30:7993–8000, 2010. doi: 10.1523/JNEUROSCI.6238-09.2010.

Sang-Hun Lee, Ivan Marchionni, Marianne Bezaire, Csaba Varga, Nathan Danielson, Matthew Lovett-Barron, Attila Losonczy, and Ivan Soltesz. Parvalbumin-positive basket cells differentiate among hippocampal pyramidal cells. *Neuron*, 82(5):1129–1144, 2014. doi: 10.1016/j.neuron.2014.03.034.

Sang-Hun Lee, Esther Krook-Magnuson, and Ivan Soltesz. Intracellular, *in vitro* somatic membrane potential recordings from whole cell patch clamped rodent hippocampal CA1 neurons. *CRCNS.org*, 2016. doi: http://dx.doi.org/10.6080/K00P0WXQ.

Cheng-Chang Lien and Peter Jonas. Kv3 potassium conductance is necessary and kinetically optimized for high-frequency action potential generation in hippocampal interneurons. *The Journal of neuroscience*, 23(6):2058–2068, 2003.

John E Lisman and Marco A Idiart. Storage of 7+/-2 short-term memories in oscillatory subcycles. *Science*, 267(5203):1512–1515, 1995. doi: 10.1126/science.7878473.

John E Lisman and Ole Jensen. The theta-gamma neural code. *Neuron*, 77(6):1002–1016, 2013. doi: 10.1016/j.neuron.2013.03.007.

Gianmaria Maccaferri, J. David, B. Roberts, Peter Szucs, Carol A. Cottingham, and Peter Somogyi. Cell surface domain specific postsynaptic currents evoked by identified GABAergic neurones in rat hippocampus *in vitro*. *J. Physiol.*, 524:91–116, 2000. doi: 10.1111/j.1469-7793.2000.t01-3-00091.x.

Jeffrey C Magee. Dendritic hyperpolarization-activated currents modify the integrative properties of hippocampal ca1 pyramidal neurons. *The Journal of neuroscience*, 18(19):7613–7624, 1998.

Nikolaus Maier, Álvaro Tejero-Cantero, Anja L Dorrn, Jochen Winterer, Prateep S Beed, Genela Morris, Richard Kempter, James FA Poulet, Christian Leibold, and Dietmar Schmitz. Coherent phasic excitation during hippocampal ripples. *Neuron*, 72(1):137–152, 2011. doi: 10.1016/j.neuron.2011.08.016.

Joseph R Manns, Eric A Zilli, Kimberly C Ong, Michael E Hasselmo, and Howard Eichenbaum. Hippocampal CA1 spiking during encoding and retrieval: relation to theta phase. *Neurobiology of learning and memory*, 87(1):9–20, 2007. doi: 10.1016/j.nlm.2006.05.007.

Eric Maris, Pascal Fries, and Freek van Ede. Diverse phase relations among neuronal rhythms and their potential function. *Trends in neurosciences*, 2016. doi: 10.1016/j.tins.2015.12.004.

Henry Markram, Eilif Muller, Srikanth Ramaswamy, Michael W Reimann, Marwan Abdellah, Carlos Aguado Sanchez, Anastasia Ailamaki, Lidia Alonso-Nanclares, Nicolas Antille, Selim Arsever, et al. Reconstruction and simulation of neocortical microcircuitry. *Cell*, 163(2):456–492, 2015. doi: 10.1016/j.cell.2015.09.029.

Ferenc Matyas, Tamas F Freund, and Attila I Gulyas. Convergence of excitatory and inhibitory inputs onto CCK-containing basket cells in the CA1 area of the rat hippocampus. *European Journal of Neuroscience*, 19(5):1243–1256, 2004. doi: 10.1111/j.1460-9568.2004.03225.x.

M. Megías, Zs. Emri, T.F. Freund, and A.I. Gulyás. Total number and distribution of inhibitory and excitatory synapses on hippocampal CA1 pyramidal cells. *Neuroscience*, 102:527–540, 2001. doi: 10.1016/S0306-4522(00)00496-6.

Audrey Mercer, Karen Eastlake, Hayley L Trigg, and Alex M Thomson. Local circuitry involving parvalbumin-positive basket cells in the CA2 region of the hippocampus. *Hippocampus*, 22(1): 43–56, 2012.

Alexia E Metz, Tim Jarsky, Marco Martina, and Nelson Spruston. R-type calcium channels contribute to afterdepolarization and bursting in hippocampal CA1 pyramidal neurons. *The Journal of neuroscience : the official journal of the Society for Neuroscience*, 25 (24):5763–73, June 2005. ISSN 1529-2401. doi: 10.1523/JNEUROSCI.0624-05.2005. URL http://www.jneurosci.org/content/25/24/5763?ijkey=d8e5c52dea199141b6f797da6aef6b485505cdad&key

M Migliore, EP Cook, DB Jae, DA Turner, and D Johnston. Computer simulations of morphologically reconstructed ca3 hippocampal neurons. *Journal of neurophysiology*, 73(3), 1995.

Michele Migliore, DA Hoffman, JC Magee, and D Johnston. Role of an A-type K+ conductance in the back-propagation of action potentials in the dendrites of hippocampal pyramidal neurons. *Journal of computational neuroscience*, 7(1):5–15, 1999. doi: 10.1023/A:1008906225285.

Michele Migliore, C Cannia, William W Lytton, Henry Markram, and Michael L Hines. Parallel network simulations with neuron. *Journal of computational neuroscience*, 21(2):119–129, 2006. doi: 10.1007/s10827-006-7949-5.

Kenji Mizuseki, Anton Sirota, Eva Pastalkova, and György Buzsáki. Theta oscillations provide temporal windows for local circuit computation in the entorhinal-hippocampal loop. *Neuron*, 64:267–280, 2009.

E Moczydlowski and R Latorre. Gating kinetics of Ca2+-activated K+ channels from rat muscle incorporated into planar lipid bilayers. Evidence for two voltage-dependent Ca2+ binding reactions. *The Journal of general physiology*, 82(4):511–542, 1983. doi: 10.1085/jgp.82.4.511.

Robert J Morgan and Ivan Soltesz. Nonrandom connectivity of the epileptic dentate gyrus predicts a major role for neuronal hubs in seizures. *Proceedings of the National Academy of Sciences*, 105 (16):6179–6184, 2008a.

Robert J Morgan and Ivan Soltesz. Nonrandom connectivity of the epileptic dentate gyrus predicts a major role for neuronal hubs in seizures. *Proceedings of the National Academy of Sciences*, 105 (16):6179–6184, 2008b. doi: 10.1073/pnas.0801372105.

Edvard I Moser, Emilio Kropff, and May-Britt Moser. Place cells, grid cells, and the brain's spatial representation system. *Annu. Rev. Neurosci.*, 31:69–89, 2008. doi: 10.1146/annurev.neuro.31.061307.090723.

Samuel A Neymotin, Maciej T Lazarewicz, Mohamed Sherif, Diego Contreras, Leif H Finkel, and William W Lytton. Ketamine disrupts theta modulation of gamma in a computer model of hippocampus. *The Journal of Neuroscience*, 31(32):11733–11743, 2011a. doi: 10.1523/JNEUROSCI.0501-11.2011.

Samuel A Neymotin, Heekyung Lee, Eunhye Park, André A Fenton, and William W Lytton. Emergence of physiological oscillation frequencies in a computer model of neocortex. *Frontiers in computational neuroscience*, 5, 2011b. doi: 10.3389/fncom.2011.00019.

RE Numann, WJ Wadman, and RK Wong. Outward currents of single hippocampal cells obtained from the adult guinea-pig. *The Journal of physiology*, 393(1):331–353, 1987. doi: 10.1113/jphysiol.1987.sp016826.

Orsolya I Papp, Mária R Karlócai, Irén E Tóth, Tamás F Freund, and Norbert Hájos. Different input and output properties characterize parvalbumin-positive basket and axo-axonic cells in the hippocampal CA3 subfield. *Hippocampus*, 23(10):903–918, 2013. doi: 10.1002/hipo.22147.

N Poolos, M Migliore, and D Johnston. Pharmacological upregulation of h-channels reduces the excitability of pyramidal neuron dendrites. *Nat. Neurosci.*, 5:767–774, 2002. doi: 10.1038/nn891.

Christopher J Price, Bruno Cauli, Endre R Kovacs, Akos Kulik, Bertrand Lambolez, Ryuichi Shigemoto, and Marco Capogna. Neurogliaform neurons form a novel inhibitory network in the hippocampal CA1 area. *The Journal of neuroscience*, 25(29):6775–6786, 2005. doi: 10.1523/JNEUROSCI.1135-05.2005.

Giulia Quattrocolo and Gianmaria Maccaferri. Novel GABAergic circuits mediating excitation/inhibition of Cajal-Retzius cells in the developing hippocampus. *The Journal of Neuroscience*, 33(13):5486–5498, 2013. doi: 10.1523/JNEUROSCI.5680-12.2013.

Giulia Quattrocolo and Gianmaria Maccaferri. Firing pattern of O-LM cells in mouse hippocampal ca1. *CRCNS.org*, 2016. doi: http://dx.doi.org/10.6080/K0HQ3WTH.

Srikanth Ramaswamy, Jean-Denis Courcol, Marwan Abdellah, Stanislaw R Adaszewski, Nicolas Antille, Selim Arsever, Guy Atenekeng, Ahmet Bilgili, Yury Brukau, Athanassia Chalimourda, et al. The neocortical microcircuit collaboration portal: a resource for rat somatosensory cortex. *Frontiers in neural circuits*, 9, 2015. doi: 10.3389/fncir.2015.00044.

Miguel Remondes and Erin M Schuman. Role for a cortical input to hippocampal area CA1 in the consolidation of a long-term memory. *Nature*, 431(7009):699–703, 2004. doi: 10.1038/nature02965.

David Robbe, Sean M Montgomery, Alexander Thome, Pavel E Rueda-Orozco, Bruce L McNaughton, and György Buzsaki. Cannabinoids reveal importance of spike timing coordination in hippocampal function. *Nature neuroscience*, 9(12):1526–1533, 2006. doi: 10.1038/nn1801.

Horacio G Rotstein, Dmitri D Pervouchine, Corey D Acker, Martin J Gillies, John A White, Eberhardt H Buhl, Miles A Whittington, and Nancy Kopell. Slow and fast inhibition and an h-current interact to create a theta rhythm in a model of CA1 interneuron network. *Journal of Neurophysiology*, 94(2):1509–1518, 2005. doi: 10.1152/jn.00957.2004.

Pankaj Sah. Ca2+-activated K+ currents in neurones: types, physiological roles and modulation. *Trends in neurosciences*, 19(4):150–154, 1996. doi: 10.1016/S0166-2236(96)80026-9.

Vijayalakshmi Santhakumar, Ildiko Aradi, and Ivan Soltesz. Role of mossy fiber sprouting and mossy cell loss in hyperexcitability: a network model of the dentate gyrus incorporating cell types and axonal topography. *Journal of neurophysiology*, 93(1):437–453, 2005a.

Vijayalakshmi Santhakumar, Ildiko Aradi, and Ivan Soltesz. Role of mossy fiber sprouting and mossy cell loss in hyperexcitability: a network model of the dentate gyrus incorporating cell types and axonal topography. *Journal of neurophysiology*, 93(1):437–453, 2005b. doi: 10.1152/jn.00777.2004.

F Saraga, CP Wu, L Zhang, and FK Skinner. Active dendrites and spike propagation in multicompartment models of oriens-lacunosum/moleculare hippocampal interneurons. *The Journal of physiology*, 552(3):673–689, 2003. doi: 10.1113/jphysiol.2003.046177.

Ausra Saudargiene, Stuart Cobb, and Bruce P Graham. A computational study on plasticity during theta cycles at schaffer collateral synapses on CA1 pyramidal cells in the hippocampus. *Hippocampus*, 25(2):208–218, 2015. doi: 10.1002/hipo.22365.

Calvin J Schneider, Hermann Cuntz, and Ivan Soltesz. Linking macroscopic with microscopic neuroanatomy using synthetic neuronal populations. *PLOS Comput Biol*, 10(10):e1003921, 2014. doi: 10.1371/journal.pcbi.1003921.

Erik W Schomburg, Costas A Anastassiou, György Buzsáki, and Christof Koch. The spiking component of oscillatory extracellular potentials in the rat hippocampus. *The Journal of Neuroscience*, 32(34):11798–11811, 2012. doi: 10.1523/JNEUROSCI.0656-12.2012.

Erik W Schomburg, Antonio Fernández-Ruiz, Kenji Mizuseki, Antal Berényi, Costas A Anastassiou, Christof Koch, and György Buzsáki. Theta phase segregation of input-specific gamma patterns in entorhinal-hippocampal networks. *Neuron*, 84(2):470–485, 2014. doi: 10.1016/j.neuron.2014.08.051.

Terrence Joseph Sejnowski, Christof Koch, and Patricia Smith Churchland. Computational neuroscience. *Science*, 241(4871):1299–1306, 1988. doi: 10.1126/science.3045969.

Joshua H Siegle and Matthew A Wilson. Enhancement of encoding and retrieval functions through theta phase-specific manipulation of hippocampus. *eLife*, 3:e03061, 2014. doi: 10.7554/eLife.03061.

Peter J Siekmeier. Evidence of multistability in a realistic computer simulation of hippocampus subfield CA1. *Behavioural brain research*, 200(1):220–231, 2009.

I Soltesz and M Deschenes. Low-and high-frequency membrane potential oscillations during theta activity in CA1 and CA3 pyramidal neurons of the rat hippocampus under ketamine-xylazine anesthesia. *Journal of neurophysiology*, 70:97–97, 1993.

Ivan Soltesz. *Diversity in the Neuronal Machine: Order and Variability in Interneuronal Microcircuits*. Oxford University Press, New York, 2006. doi: 10.1093/acprof:oso/9780195177015.001.1.

Larry R Squire. Memory and the hippocampus: a synthesis from findings with rats, monkeys, and humans. *Psychological review*, 99(2):195, 1992. doi: 10.1037/0033-295X.99.2.195.

Eran Stark, Ronny Eichler, Lisa Roux, Shigeyoshi Fujisawa, Horacio G Rotstein, and György Buzsáki. Inhibition-induced theta resonance in cortical circuits. *Neuron*, 80(5):1263–1276, 2013. doi: 10.1016/j.neuron.2013.09.033.

David Sterratt, Bruce Graham, Andrew Gillies, and David Willshaw. *Principles of computational modelling in neuroscience*. Cambridge University Press, 2011. doi: 10.1017/CBO9780511975899.

Johan F Storm. Potassium currents in hippocampal pyramidal cells. *Progress in brain research*, 83: 161–187, 1990. doi: 10.1016/S0079-6123(08)61248-0.

Attila Szűcs. Applications of the spike density function in analysis of neuronal firing patterns. *Journal of neuroscience methods*, 81(1):159–167, 1998. doi: 10.1016/S0165-0270(98)00033-8.

Jiannis Taxidis, Kenji Mizuseki, Robert Mason, and Markus R Owen. Influence of slow oscillation on hippocampal activity and ripples through cortico-hippocampal synaptic interactions, analyzed by a cortical-CA3-CA1 network model. *Front Comput Neurosci*, 7, 2013. doi: 10.3389/fncom.2013.00003.

Julian Tejada and Antonio C Roque. Computational models of dentate gyrus with epilepsy-induced morphological alterations in granule cells. *Epilepsy & Behavior*, 38:63–70, 2014. doi: 10.1016/j.yebeh.2014.02.007.

Evan A Thomas, Christopher A Reid, Samuel F Berkovic, and Steven Petrou. Prediction by modeling that epilepsy may be caused by very small functional changes in ion channels. *Archives of neurology*, 66(10):1225–1232, 2009. doi: 10.1001/archneurol.2009.219.

Evan A Thomas, Christopher A Reid, and Steven Petrou. Mossy fiber sprouting interacts with sodium channel mutations to increase dentate gyrus excitability. *Epilepsia*, 51(1):136–145, 2010. doi: 10.1111/j.1528-1167.2009.02202.x.

Adriano BL Tort, Robert W Komorowski, Joseph R Manns, Nancy J Kopell, and Howard Eichenbaum. Theta–gamma coupling increases during the learning of item–context associations. *Proceedings of the National Academy of Sciences*, 106(49):20942–20947, 2009. doi: 10.1073/pnas.0911331106.

Ludovic Tricoire, Kenneth A Pelkey, Brian E Erkkila, Brian W Jeffries, Xiaoqing Yuan, and Chris J McBain. A blueprint for the spatiotemporal origins of mouse hippocampal interneuron diversity. *The Journal of Neuroscience*, 31(30):10948–10970, 2011.

Shreejoy J Tripathy, Judith Savitskaya, Shawn D Burton, Nathaniel N Urban, and Richard C Gerkin. NeuroElectro: a window to the world's neuron electrophysiology data. *Frontiers in neuroinformatics*, 8, 2014. doi: 10.3389/fninf.2014.00040.

Csaba Varga, Peyman Golshani, and Ivan Soltesz. Frequency-invariant temporal ordering of interneuronal discharges during hippocampal oscillations in awake mice. *Proceedings of the National Academy of Sciences*, 109(40):E2726–E2734, 2012. doi: 10.1073/pnas.1210929109.

Csaba Varga, Mikko Oijala, Jonathan Lish, Gergely G Szabo, Marianne Bezaire, Ivan Marchionni, Peyman Golshani, and Ivan Soltesz. Functional fission of parvalbumin interneuron classes during fast network events. *eLife*, 3:e04006, 2014. doi: 10.7554/eLife.04006.

Diek W Wheeler, Charise M White, Christopher L Rees, Alexander O Komendantov, David J Hamilton, and Giorgio A Ascoli. Hippocampome.org: a knowledge base of neuron types in the rodent hippocampus. *eLife*, 4:e09960, 2015. doi: 10.7554/eLife.09960.

Raphael Winkels, Peter Jedlicka, Felix K Weise, Christian Schultz, Thomas Deller, and Stephan W Schwarzacher. Reduced excitability in the dentate gyrus network of βiv-spectrin mutant mice in vivo. *Hippocampus*, 19(7):677–686, 2009. doi: 10.1002/hipo.20549.

Thilo Womelsdorf, Jan-Mathijs Schoffelen, Robert Oostenveld, Wolf Singer, Robert Desimone, Andreas K Engel, and Pascal Fries. Modulation of neuronal interactions through neuronal synchronization. *science*, 316(5831):1609–1612, 2007. doi: 10.1126/science.1139597.

Aarne Ylinen, Iván Soltész, Anatol Bragin, Markku Penttonen, Attila Sik, and György Buzsáki. Intracellular correlates of hippocampal theta rhythm in identified pyramidal cells, granule cells, and basket cells. *Hippocampus*, 5(1):78–90, 1995. doi: 10.1002/hipo.450050110.

GLF Yuen and D Durand. Reconstruction of hippocampal granule cell electrophysiology by computer simulation. *Neuroscience*, 41(2):411–423, 1991. doi: 10.1016/0306-4522(91)90337-N.

Appendices

A Experimental Cell Characterization

These experimental cells were whole cell patch clamped to record the intracellular somatic membrane potential during a range of current injections ("current sweep"). The firing rates of each cell type are plotted in separate graphs, shown in Appendix Figure 1. The electrophysiological properties of each cell type are given in Appendix Table 1. In Appendix - Section 2, the model cells are compared with this experimental data using the same calculations and properties.

The cell references and animals they came from (both rat and mouse (RRID:IMSR_JAX:008069, RRID:IMSR_JAX:007905, RRID:IMSR_JAX:000664), species identified for each experimental cell) are provided here, as well as in two CRCNS entries online (Quattrocolo Maccaferri: http://dx.doi.org/10.6080/K0HQ3WTH and Lee et al: http://dx.doi.org/10.6080/K00P0WXQ) where the raw AxoClamp files of these experiments are also provided (Lee et al., 2016; Quattrocolo and Maccaferri, 2016). The tables of experimental conditions associated with the data entries in CRCNS.org are reproduced here for convenience, in Appendix Table 2.

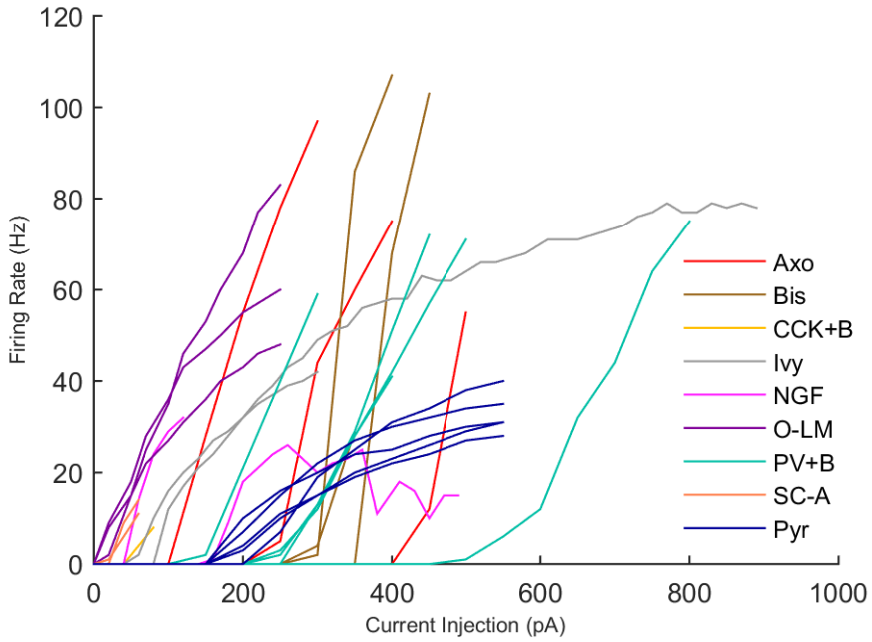

Appendix Figure 1: Firing Rates of Experimental Cells. Rebound spiking, which occurs in some O-LM cells at hyperpolarized current injection levels, is not shown in this graph.

The properties were calculated as follows:

RMP Resting membrane potential, in units of mV, is calculated as the average membrane potential

Cell Type	n	RMP (mV)	Input Resistance (MΩ)	Sag Amplitude (mV)	Sag Tau (ms)	Membrane Tau (ms)	Rheobase (pA)	ISI (ms)	Threshold (mV)	Spike Amplitude (mV)	AHP (mV)
From mouse											
Pyr	17	-70.7 ± 1.2	139.5 ± 38.8	7.0 ± 2.2	34.4 ± 11.0	21.5 ± 8.6	182.4 ± 55.7	134.0 ± 44.0	-36.7 ± 2.6	78.2 ± 7.2	8.6 ± 2.1
Axo	3	-64.4 ± 4.5	122.0 ± 57.5	1.7 ± 0.6	45.4 ± 6.9	11.9 ± 2.2	283.3 ± 152.8	47.8 ± 28.5	-31.8 ± 3.4	44.5 ± 6.7	16.6 ± 3.5
Bis	3	-63.6 ± 4.7	109.1 ± 30.5	1.7 ± 0.6	62.3 ± 13.7	12.2 ± 0.6	333.3 ± 57.7	24.5 ± 21.8	-31.9 ± 4.2	47.3 ± 6.8	22.6 ± 0.7
O-LM	3	-64.8 ± 1.3	592.3 ± 97.0	10.4 ± 3.8	78.5 ± 22.0	41.4 ± 11.7	20.0 ± 0.0	101.9 ± 30.1	-44.2 ± 2.3	76.3 ± 6.1	22.1 ± 4.7
PV+B	7	-61.4 ± 2.0	65.2 ± 16.2	1.8 ± 0.5	62.9 ± 16.3	13.3 ± 5.4	307.1 ± 109.7	74.2 ± 36.4	-35.3 ± 3.7	51.1 ± 9.0	18.0 ± 2.7
From rat											
CCK+B	1	-61.2	298.1	2.7	72.1	56.0	60.0	261.0	-37.7	63.7	15.5
Ivy	2	-62.3 ± 0.3	267.2 ± 107.9	2.4 ± 2.5	91.1 ± 120.9	171.9 ± 45.6	80.0 ± 28.3	74.9 ± 20.6	-32.8 ± 0.7	48.2 ± 5.1	20.1 ± 2.6
NGF	2	-66.7 ± 13.4	260.0 ± 73.6	1.8 ± 1.6	61.7 ± 77.0	77.2 ± 66.2	110.0 ± 70.7	80.0 ± 28.4	-34.0 ± 2.2	34.7 ± 4.9	16.2 ± 6.3
SC-A	2	-57.0 ± 4.3	529.9 ± 2.9	7.9 ± 6.2	91.1 ± 21.7	74.2 ± 37.3	30.0 ± 14.1	132.4 ± 29.4	-34.3 ± 2.2	58.7 ± 4.5	12.6 ± 2.0

Appendix Table 1: Intrinsic electrophysiological properties of experimental cells.

during a current injection of 0 pA. If 0 was not part of the injection sweep, then the average membrane potential prior to the onset of a different current injection value is used.

Input Resistance Units of MegaOhms ($M\Omega$), is the input resistance calculated from the least hyperpolarized current injection level.

Sag Amplitude Units of mV, computed from the most hyperpolarized current injection level as the difference between the stead state membrane potential towards the end of the current injection and the most hyperpolarized potential achieved towards the beginning of the current injection.

Sag Tau Units of ms, also computed from the most hyperpolarized current injection level, as the time constant required for an equation of the form $A * (1 - exp(-t/\tau))^4$ to best fit the potential trajectory from the most hyperpolarized point during the current injection until the trace reaches steady state.

Membrane Tau Units of ms, computed from the least hyperpolarized current injection level, as the time constant required for an equation of the form $A * (exp(-t/\tau_m))$ to best fit the potential trajectory from the onset of the current injection until the trace reaches steady state.

Rheobase Units of pA, the least depolarized current injection level that resulted in the cell spiking during the current injection (i.e., not as a rebound spike after the injection ends, which can happen for certain cell types after a sufficiently hyperpolarized injection).

ISI Units of ms, average time interval between spike threshold time points for the least depolarized current injection level where the cell spiked regularly.

Threshold Units of mV, the average threshold of the first three spikes for the least depolarized current injection level where the cell spiked regularly. For all experimental and model cells except for the experimental pyramidal cells, the threshold was calculated using CellData's method #2, where the threshold is the first point where dV/dt exceeds some cutoff value (Cooper et al., 2003; Metz et al., 2005); in our case the cutoff was 28 mV/ms. Because calculating the threshold of the experimental pyramidal cells by this method resulted in a threshold point that was visually too depolarized given the shape of the action potential, CellData's method #1 was used

instead, in which the threshold is the first point where $dV/dt > mean(dV/dt) + 2 * std(dV/dt)$, meaning the derivative of potential with time exceeds two standard deviations of the average (Atherton and Bevan, 2005).

Spike Amplitude Units of mV, the difference between the membrane potential at the peak of the action potential and the membrane potential at the threshold of the action potential, averaged for the first three spikes of the least depolarized current injection where the cell spiked regularly.

Slow AHP Amplitude Units of mV, also referred to simply as "AHP" in this Appendix, the difference between the membrane potential at the most hyperpolarized potential following the action potential and the membrane potential at the threshold of the action potential, averaged for the first three spikes of the least depolarized current injection where the cell spiked regularly.

Further properties characterized from experimental cells (recorded and published by other labs) are available at NeuroElectro's website (http://neuroelectro.org), although the data included there are from a wide variety of conditions, animal types, and experimental protocols (and the calculations of properties may have been carried out differently).

Cell Type	Lab	Cell Name	Species	Current Inj. Levels (pA)	Original Use & Methods Reference
Axo-axonic	Soltesz	CA203LF57	mouse	-200:50:+500	unpublished
Axo-axonic	Soltesz	CA204LF59	mouse	-200:50:+300	unpublished
Axo-axonic	Soltesz	CA204RF59	mouse	-200:50:+400	unpublished
Bistratified	Soltesz	PV16IM	mouse	-300:50:+400	unpublished
Bistratified	Soltesz	PV74	mouse	-300:50:+350	unpublished
Bistratified	Soltesz	PV27IM	mouse	-300:50:+450	unpublished
PV+ Basket	Soltesz	PV34	mouse	-300:50:+500	Lee et al. (2014)
PV+ Basket	Soltesz	PV36	mouse	-300:50:+800	Lee et al. (2014)
PV+ Basket	Soltesz	PV37	mouse	-300:50:+500	Lee et al. (2014)
PV+ Basket	Soltesz	PV38	mouse	-300:50:+300	Lee et al. (2014)
PV+ Basket	Soltesz	PV72	mouse	-300:50:+400	Lee et al. (2014)
PV+ Basket	Soltesz	PV80	mouse	-300:50:+450	Lee et al. (2014)
Deep Pyramidal	Soltesz	D1_25abf	mouse	-400:50:+550	Lee et al. (2014)
Deep Pyramidal	Soltesz	D1_45abf	mouse	-400:50:+550	Lee et al. (2014)
Deep Pyramidal	Soltesz	D2_06abf	mouse	-400:50:+550	Lee et al. (2014)
Deep Pyramidal	Soltesz	D2_49abf	mouse	-400:50:+550	Lee et al. (2014)
Deep Pyramidal	Soltesz	D3_55abf	mouse	-400:50:+550	Lee et al. (2014)
Deep Pyramidal	Soltesz	D4_11abf	mouse	-400:50:+550	Lee et al. (2014)
Deep Pyramidal	Soltesz	D5_15abf	mouse	-400:50:+550	Lee et al. (2014)
Deep Pyramidal	Soltesz	D6_19abf	mouse	-400:50:+550	Lee et al. (2014)
Deep Pyramidal	Soltesz	D7	mouse	-400:50:+550	Lee et al. (2014)
Super. Pyramidal	Soltesz	S1_04abf	mouse	-400:50:+550	Lee et al. (2014)
Super. Pyramidal	Soltesz	S1_47abf	mouse	-400:50:+550	Lee et al. (2014)
Super. Pyramidal	Soltesz	S2_08abf	mouse	-400:50:+550	Lee et al. (2014)
Super. Pyramidal	Soltesz	S2_31abf	mouse	-400:50:+550	Lee et al. (2014)
Super. Pyramidal	Soltesz	S2_51abf	mouse	-400:50:+550	Lee et al. (2014)
Super. Pyramidal	Soltesz	S3_13abf	mouse	-400:50:+550	Lee et al. (2014)
Super. Pyramidal	Soltesz	S4	mouse	-400:50:+550	Lee et al. (2014)
Super. Pyramidal	Soltesz	S5_21abf	mouse	-400:50:+550	Lee et al. (2014)
Ivy	Soltesz	0422-1 (File 5)	rat	-100:20:+890	Krook-Magnuson et al. (2011)
Ivy	Soltesz	0428-1 (File 4)	rat	-100:20:+300	Krook-Magnuson et al. (2011)
Neurogliaform	Soltesz	09o21 (File 4)	rat	-100:20:+120	Krook-Magnuson et al. (2011)
Neurogliaform	Soltesz	09o27 (File 7)	rat	-100:20:+490	Krook-Magnuson et al. (2011)
CCK+ Basket	Soltesz	sh108_BC	rat	-100:20:+80	Lee et al. (2010)
Sch. Coll.-Assoc.	Soltesz	sh114_SCA	rat	-100:20:+60	Lee et al. (2010)
Sch. Coll.-Assoc.	Soltesz	sh153_SCA	rat	-100:20:+60	Lee et al. (2010)
O-LM	Maccaferri	1May2012_P3	mouse	-100:30:+250	Quattrocolo and Maccaferri (2013)
O-LM	Maccaferri	20Sept2011_P2	mouse	-100:30:+250	Quattrocolo and Maccaferri (2013)
O-LM	Maccaferri	24October2012_C2	mouse	-100:30:+250	Quattrocolo and Maccaferri (2013)

Appendix Table 2: AxoClamp raw data files. Sch. Coll.-Assoc.: Schaffer Collateral-Associated; Super: superficial.

B Model Cell Characterization

Model cell numbers and structural connectivity are based on Bezaire and Soltesz (2013).

In terms of electrophysiology, each model cell is characterized in experimental terms and compared to the experimental data presented above. A graphical summary of electrophysiological comparison is shown below in Appendix Figures 2 - 4, and further details of intrinsic physiology and synaptic characterization follows. The detailed information is presented as a single figure spanning two pages per cell, where the subfigure panels may contain figures or tables, to better group and arrange the data. For each cell type, the same information is provided:

A: Model Current Sweep The somatic intracellular membrane potential recording for the model cell is shown, in response to all hyperpolarized and the most depolarized current injection

B: Experimental Current Sweep The somatic intracellular membrane potential recording for an experimental cell (one of the ones featured in the previous section) is shown, in response to all hyperpolarized and the depolarized current injection level closest to the one shown for the model cell.

C: Model Electrophysiological Property Table The values of each electrophysiological property are shown for the model cell, measured or calculated in the same way as for the experimental cells in the previous section. The last column shows, in sparklines, a comparison of the model behavior with the behavior of the experimental cells. The gray rectangle shows a variable area from (in most cases) 0 to 2x the average experimental value. In cases of membrane potential, the rectange ranges 20 mV on either side of the experimental average. The experimental mean is displayed as a vertical line in the center of the rectange, while a horizontal line in the middle of the rectange ranges from the minimum to the maximum experimental value. The model value is shown as a blue circle on the same plot, or to the left or right of the rectange if it is out of range. All experimental data are taken from the cells used in Appendix - Section 1. More experimental data, obtained under a wider variety of conditions, are available at http://neuroelectro.org.

D: Firing Rates The firing rate of the model cell as a function of current injection is shown for a

range of currents. The firing rates of the experimental cells are shown as well (to identify specific experimental cells, see the firing rate graphs in Appendix - Section 1).

E: Ion Channel Table Each ion channel type present in the model cell type is listed here, along with the maximum conductance density of that channel (which may occur in the soma or in another part of the cell). Further details about the ion channels are available in Appendix - Sections 4 and 5.

F: Structural Connectivity Table The structural basis of the model connections is provided here in terms of both connections (comprising multiple synapses) and synapses, shown for convergence onto the cell (left side) and divergence emanating from the cell (right side). Connectivity involving pyramidal cells (either pre- or postsynaptically) is based on Bezaire and Soltesz (2013) while connectivity between interneurons is detailed in Appendix - Section 3. Blank or missing rows for specific cell types indicate that there were no connections with that cell type.

G,H: Model Paired Recordings - Experimental Conditions Table For incoming (G) and outgoing (H) connections involving a given cell type, any experimental constraints used to fit the model connections are cited here, including the conditions of the experiment that the model reproduced (the holding potential of the cell and the reversal potential of the synapse as set by the bath and pipette solutions used in the experiment), along with the model connection characterization (amplitude, 10-90% rise time, and decay time constant) and the percentage difference from the mean experimental properties. The model results were reported as the average from 10 random connections between the two cell types, and wherever possible were compared to an actual experimental mean (leaving out failed responses) rather than an effective experimental mean that factored in the synapse failure rate. For connections that were characterized in current clamp rather than voltage clamp, the data were colored in purple rather than black to indicate their different properties (half-width instead of decay time constant, for example). Because the experimental data did not routinely report or, in a standard way, calculate the junction potential of the experiment, we did not factor in the difference in holding potential (and hence driving force

of the synapse) due to junction potential; this resulted in a slight over or underestimation of the driving force and hence the actual synaptic conductance, depending on the junction potential value.

I: Model Synapse Parameters Table The model parameters used in the synapses (resulting from the experimental tuning above, or firing rate tuning if no experimental connection data were available) are listed here, with the parameters for connections onto that cell type from the other types listed on the left side, and the parameters for connections onto other cell types, from that cell type, listed on the right side.

J: Model Physiological Connections Table All connections in the model were recharacterized under the same condition, as experimental data were gathered under diverse conditions where different connections could not be directly compared. In this table, all connections were recorded using the physiological reversal potential while holding the postsynaptic cell at -50 mV voltage clamp (and not accounting for any junction potential as would occur if an experiment were to replicate these model simulation conditions). The connections from other cell types to the given cell type are shown on the left side; connections from the given cell type to other cell types are shown on the right side. Blank lines or missing rows indicate there is not a connection between those cell types in the model.

K, L: Model Physiological Connections The postsynaptic current (PSC) responses for all the physiological connections as detailed in Table J above are graphed here, with connections from other cell types to the given cell type shown in panel K, and connections from the given cell type to other cells shown in panel L.

The model cell types can be further characterized as desired by using the artificially generated AxoClamp files included as Appendix - Source Data. These AxoClamp files were generated from our CellClamp tool within SimTracker, providing the same data format (but with generic header lines for the first ten lines), as the tab-delimited ATF file format.

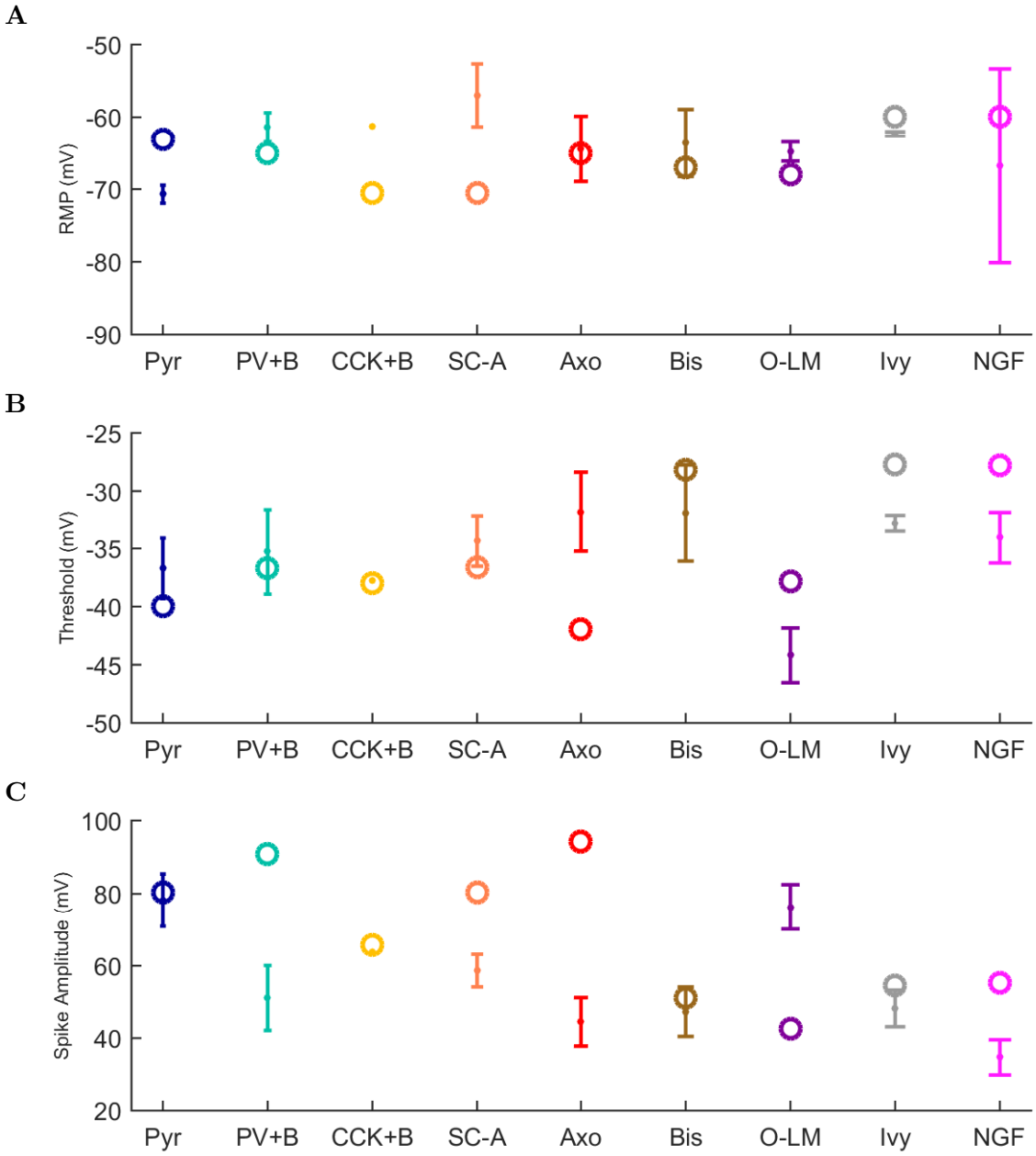

Appendix Figure 2: Physiological properties of experimental and model cells. Experimental data are shown with closed markers for the mean and error bars for cell types where n>1. The model cell properties are plotted as open circles. Calculation of properties is explained in the text. (A) resting membrane potential, (B) threshold, and (C) spike amplitude.

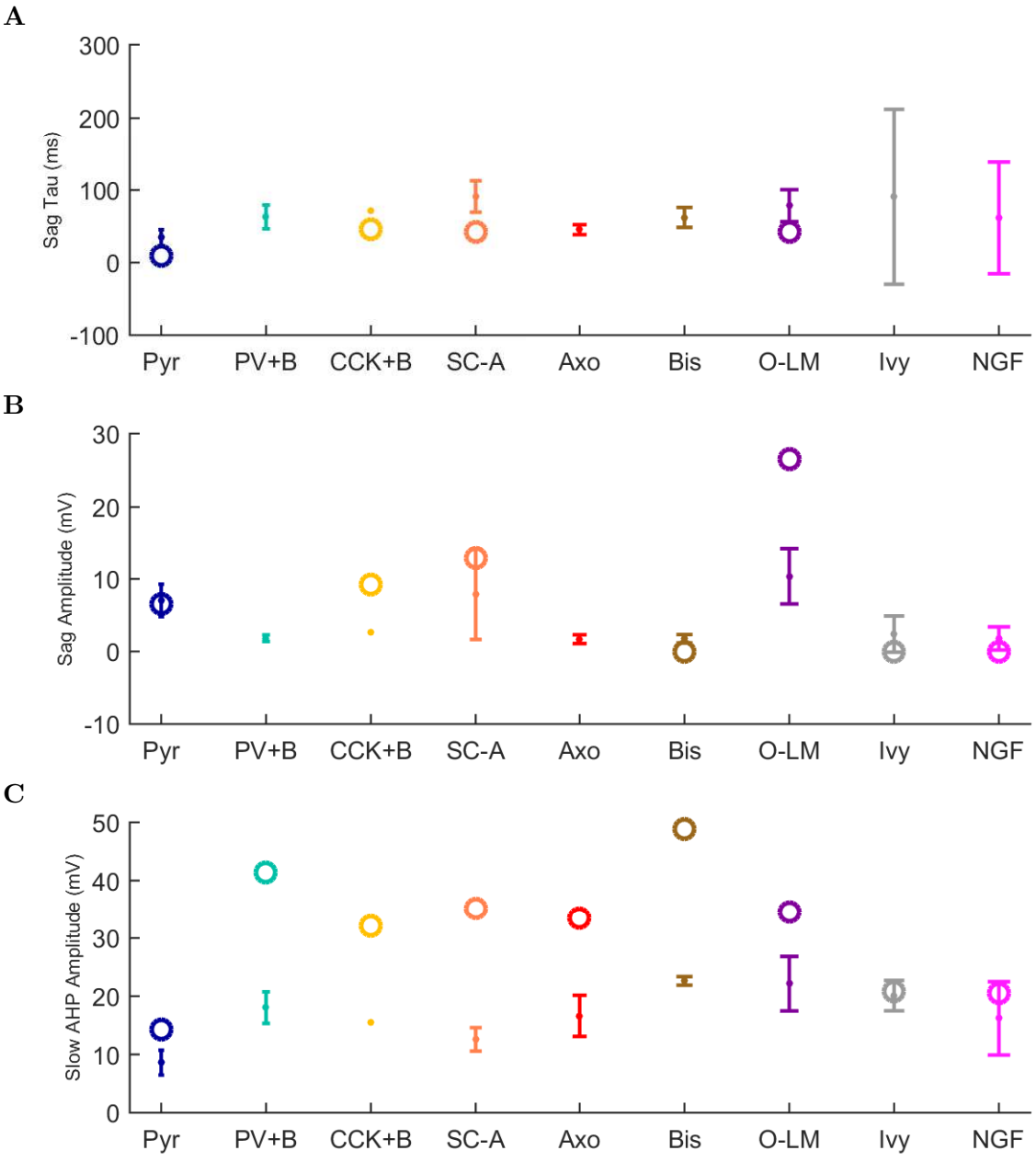

Appendix Figure 3: Physiological properties, continued. (A) sag time constant, (B) sag amplitude, and (C) amplitude of afterhyperpolarization (AHP).

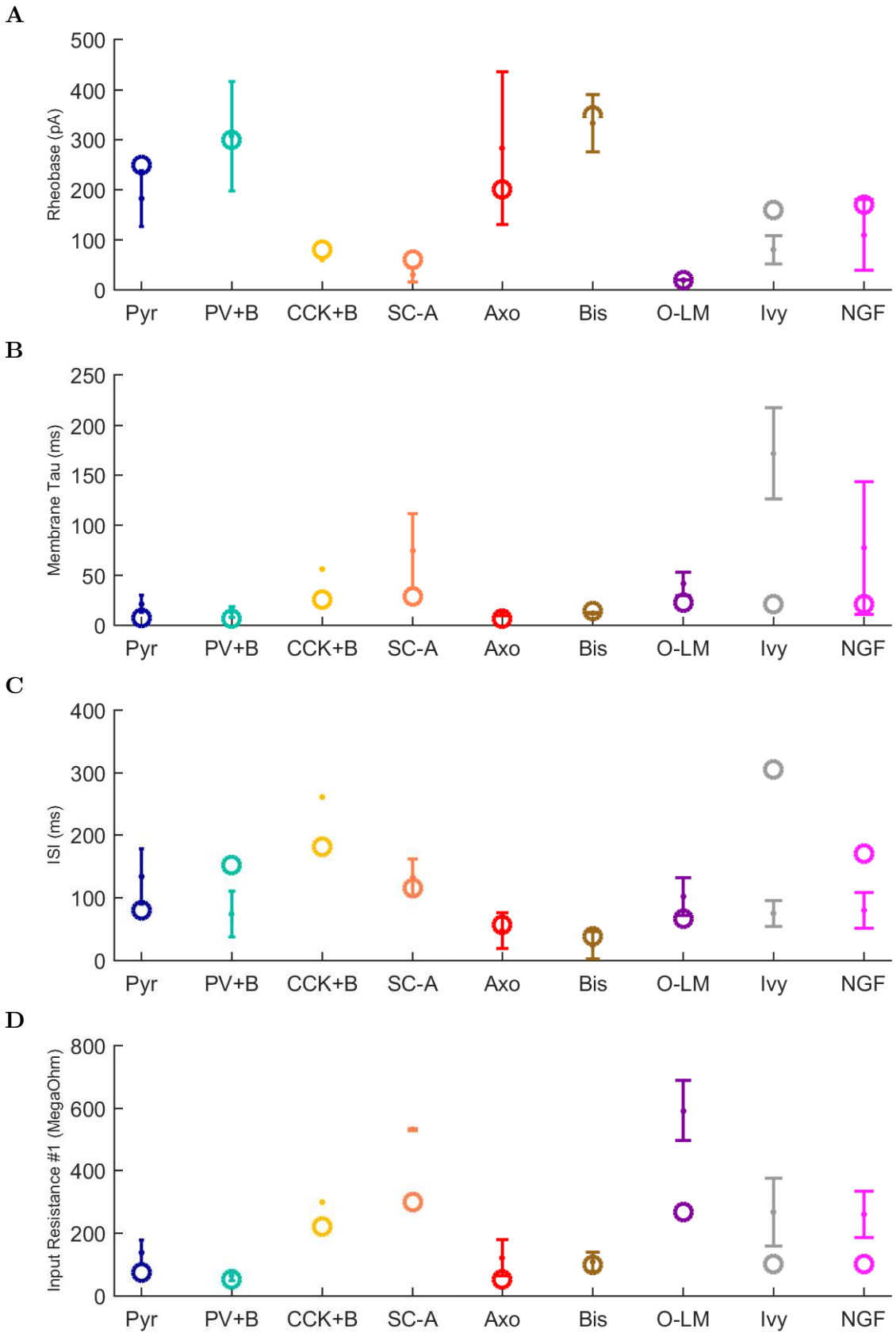

Appendix Figure 4: Physiological properties, continued. (A) rheobase, (B) membrane time constant, (C) interspike interval (ISI), and (D) input resistance.

Cell type	Page

Pyramidal Cell: Principal Cell (311500 Cells)

Model and Experimental Electrophysiology

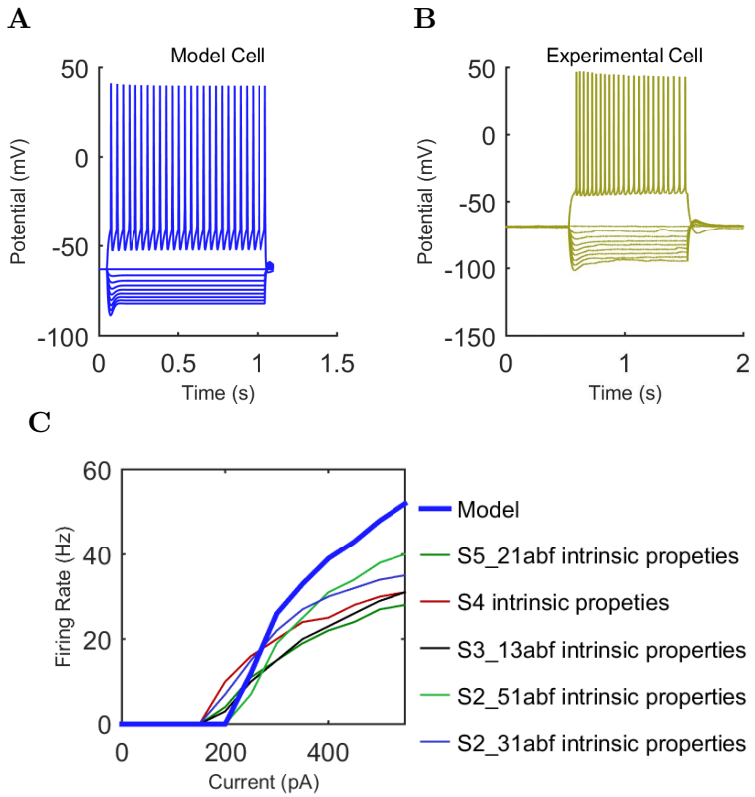

Appendix Figure 5: Pyramidal (A) model and (B) experimental current sweep. (C) Firing rates of model and experimental cells.

Property	**Value**	
RMP	-63.0	mV
Input Resistance	76.1	MΩ
Sag Amplitude	6.5	mV
Sag Tau	9.6	ms
Membrane Tau	7.1	ms
Rheobase	250.0	pA
ISI	80.7	ms
Threshold	-39.9	mV
Spike Amplitude	80.3	mV
Slow AHP Amplitude	14.3	mV

Appendix Table 3: Model Pyramidal cell electrophysiological properties.

	Highest Conductance
Channel	**G_{max} (S/cm^2)**
HCNp	4.968e-03
Kdrp	3.000e-03
KvAdistp	4.682e-02
KvAproxp	1.599e-02
Navaxonp	6.400e-02
Navp	3.200e-02

Appendix Table 4: Model Pyramidal cell ion channels and conductance at highest density location in cell.

Model and Experimental Connectivity

Other Type	Other Cell to Pyr # Conn.s	Syn.s /Conn.	# #	Post Loc.	Pyr to Other Cell # Conn.s	Syn.s /Conn.	# #	Post Loc.
Axo	6	6	36	axon	1	3	2	apical dendrite
Bis	10	10	100	any dendrite	3	3	7	apical dendrite
CCK+B	13	8	104	any dendrite				
Ivy	42	10	420	any dendrite	0	3	0	apical dendrite
NGF	14	10	140	apical dendrite				
O-LM	8	10	80	apical dendrite	13	3	37	basal dendrite
Pyr	197	1	197	apical dendrite	197	1	197	apical dendrite
PV+B	17	11	187	soma	8	3	22	apical dendrite
SC-A					0	3	0	apical dendrite
CA3	5985	2	11970	any dendrite				
ECIII	1299	2	2598	any dendrite				

Appendix Table 5: Structural connection parameters for Pyramidal cells, based on Bezaire and Soltesz (2013).

Experimental Connection Constraints

Pre Type	Exp. Ref.	Hold (mV)	E_{rev} (mV)	Amp. (pA,mV)	Diff. %	t_{10-90} (ms)	Diff. %	τ_{decay} (ms)	Diff. %
Axo	Maccaferri et al. 2000	-70.0	7.0	323.78	+5.1	0.83	+3.1	11.20	+0.0
Bis	Maccaferri et al. 2000	-70.0	7.0	143.21	-4.5	2.22	+11.2	15.40	-4.3
CCK+B	Lee et al. 2010	-70.0	-26.0	118.97	+3.1	0.53	-16.7	6.15	-4.9
Ivy	Fuentealba et al. 2008	-50.0	-88.0	8.17	+2.1	3.50	+25.0	15.43	-3.9
NGF	Price et al. 2008	-50.0	-89.0	5.25	+7.1	15.48	-3.9	32.73	-34.5
O-LM	Maccaferri et al. 2000	-70.0	7.0	24.35	-6.3	4.68	-24.6	18.88	-9.3
Pyr	Deuchars & Thomson 1996	-67.0	0.0	0.60	-14.5	6.00	+122.2	20.55	+22.3
PV+B	Szabadics et al. 2007	-70.0	-26.0	91.94	-13.9	0.50	-5.7	6.70	+4.7
SC-A	Lee et al. 2010	-70.0	-26.0	52.42	-12.9	1.63	+13.6	8.55	+3.0

Appendix Table 6: Experimental constraints for incoming connections onto Pyramidal cells (clamp: black=voltage; purple=current).

Post Type	Exp. Ref.	Hold (mV)	E_{rev} (mV)	Amp. (pA,mV)	Diff. %	t_{10-90} (ms)	Diff. %	τ_{decay} (ms)	Diff. %
Bis	Pawelzik et al. 2002	-66.0	0.0	0.77	-19.6	1.58	+31.3	16.75	+41.1
Ivy	Fuentealba et al. 2008	-65.8	-70.0	0.06	-97.9	1.38	-8.3	21.35	+41.1
Pyr	Deuchars & Thomson 1996	-67.0	0.0	0.60	-14.5	6.00	+122.2	19.05	+22.3
PV+B	Lee et al. 2014	-60.0	0.0	15.09	-67.7	0.28	-72.5	2.00	+22.3

Appendix Table 7: Experimental constraints for outgoing connections from Pyramidal cells (clamp: black=voltage; purple=current).

Model Synapse Parameters

Type	Other Cell to Pyr				Pyr to Other Cell			
	E_{rev} (mV)	G_{max} (nS)	τ_{rise} (ms)	τ_{decay} (ms)	E_{rev} (mV)	G_{max} (nS)	τ_{rise} (ms)	τ_{decay} (ms)
Axo	-60.0	1.150e-03	0.28	8.40	0.0	4.000e-05	0.30	0.60
Bis	-60.0	5.100e-04	0.11	9.70	0.0	1.900e-03	0.11	0.25
CCK+B	-60.0	5.200e-04	0.20	4.20				
Ivy	-60.0	4.100e-05	1.10	11.00	0.0	4.050e-04	0.30	0.60
NGF	-60.0	6.500e-05	9.00	39.00				
O-LM	-60.0	3.000e-04	0.13	11.00	0.0	2.000e-04	0.30	0.60
Pyr	0.0	7.000e-02	0.10	1.50	0.0	7.000e-02	0.10	1.50
PV+B	-60.0	2.000e-04	0.30	6.20	0.0	7.000e-04	0.07	0.20
SC-A					0.0	4.050e-04	0.30	0.60
CA3	0.0	2.000e-04	0.50	3.00				
ECIII	0.0	2.000e-04	0.50	3.00				

Appendix Table 8: Model synaptic parameters for Pyramidal cells in the control network.

Physiological Characterization of Model Connections

Type	Other Cell to Pyr					Pyr to Other Cell				
	Hold (mV)	E_{rev} (mV)	Amp. (pA)	t_{10-90} (ms)	τ_{decay} (ms)	Hold (mV)	E_{rev} (mV)	Amp. (pA)	t_{10-90} (ms)	τ_{decay} (ms)
Axo	-50.0	-60.0	36.45	0.85	11.57	-50.0	0.0	1.85	0.78	2.53
Bis	-50.0	-60.0	13.47	2.17	15.20	-50.0	0.0	64.48	0.28	1.42
CCK+B	-50.0	-60.0	24.86	0.52	6.03					
Ivy	-50.0	-60.0	1.63	3.63	15.35	-50.0	0.0	40.70	0.58	1.28
NGF	-50.0	-60.0	1.10	65.58	0.00					
O-LM	-50.0	-60.0	0.54	3.70	14.10	-50.0	0.0	17.47	0.60	1.53
Pyr	-50.0	0.0	22.13	2.22	9.65	-50.0	0.0	22.13	2.22	9.65
PV+B	-50.0	-60.0	20.56	0.50	6.70	-50.0	0.0	14.75	0.25	1.77
SC-A						-50.0	0.0	17.42	0.68	3.05
CA3	-50.0	0.0	7.15	1.83	7.08					
ECIII	-50.0	0.0	1.41	3.25	13.63					

Appendix Table 9: Model synaptic properties under voltage clamp at -50 mV with physiological reversal potentials

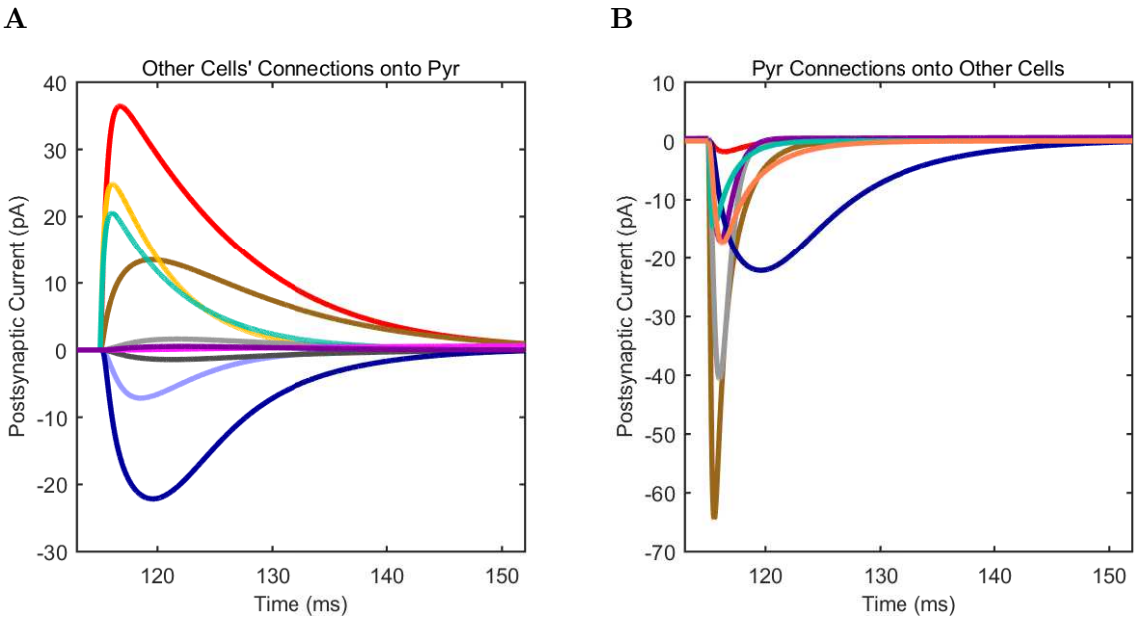

Appendix Figure 6: Connections onto (A) and (B) from model Pyramidal cells, under voltage clamp at -50 mV with physiological reversal potentials.

Axo-axonic Cell: Fast-Spiking Axonic Inhibitor (1470 Cells)

Model and Experimental Electrophysiology

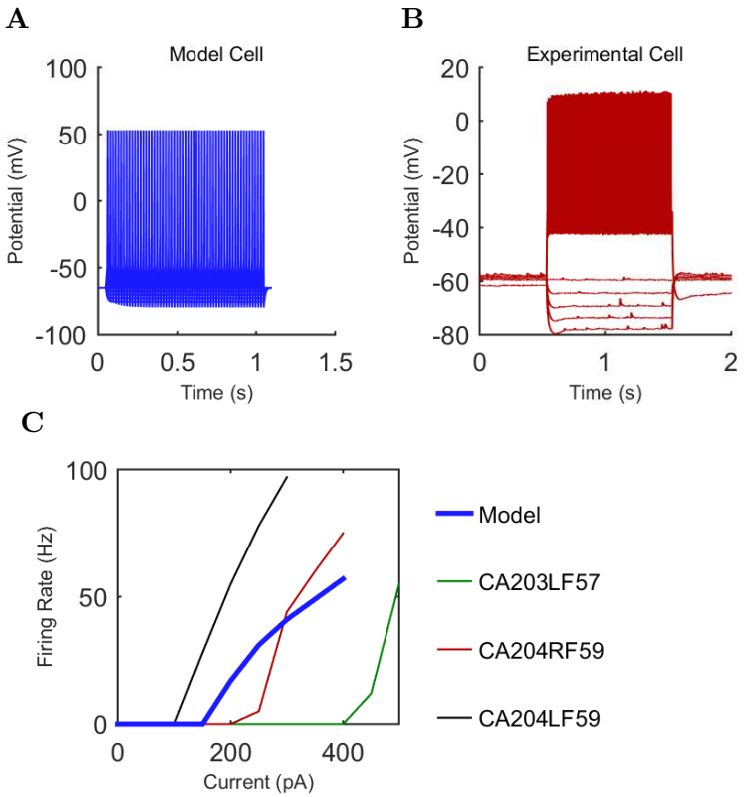

Appendix Figure 7: Axo-axonic (A) model and (B) experimental current sweep. (C) Firing rates of model and experimental cells.

Property	Value	
RMP	-65.0	mV
Input Resistance	52.3	MΩ
Sag Amplitude	NaN	mV
Sag Tau	NaN	ms
Membrane Tau	7.0	ms
Rheobase	200.0	pA
ISI	57.3	ms
Threshold	-42.0	mV
Spike Amplitude	94.3	mV
Slow AHP Amplitude	33.4	mV

Appendix Table 10: Model Axo-axonic cell electrophysiological properties.

Channel	G_{max} (S/cm^2)
CavL	5.000e-03
CavN	8.000e-04
KCaS	2.000e-06
Kdrfast	1.300e-02
KvA	1.500e-04
KvCaB	2.000e-07
Nav	1.500e-01
leak	1.800e-04

Appendix Table 11: Model Axo-axonic cell ion channels and conductance at highest density location in cell.

Model and Experimental Connectivity

Other Type	Other Cell to Axo # Conn.s	Syn.s /Conn.	#	Post Loc.	Axo to Other Cell # Conn.s	Syn.s /Conn.	#	Post Loc.
Bis	16	10	160	any dendrite				
CCK+B	12	8	96	any dendrite				
Ivy	24	10	240	any dendrite				
O-LM	8	10	80	apical dendrite				
Pyr	162	3	486	apical dendrite	1271	6	7628	axon
PV+B	39	1	39	soma				
SC-A	1	6	6	any dendrite				
CA3	4170	2	8340	any dendrite				
ECIII	485	2	970	any dendrite				

Appendix Table 12: Structural connection parameters for Axo-axonic cells, based on Bezaire and Soltesz (2013).

Experimental Connection Constraints

Note:No experimental constraints available for incoming synapses to Axo-axonic cells.

Post Type	Exp. Ref.	Hold (mV)	E_{rev} (mV)	Amp. (pA,mV)	Diff. %	t_{10-90} (ms)	Diff. %	τ_{decay} (ms)	Diff. %
Pyr	Maccaferri et al. 2000	-70.0	7.0	323.78	+5.1	0.83	+3.1	11.20	+0.0

Appendix Table 13: Experimental constraints for outgoing connections from Axo-axonic cells (clamp: black=voltage; purple=current).

Model Synapse Parameters

Type	Other Cell to Axo E_{rev} (mV)	G_{max} (nS)	τ_{rise} (ms)	τ_{decay} (ms)	Axo to Other Cell E_{rev} (mV)	G_{max} (nS)	τ_{rise} (ms)	τ_{decay} (ms)
Bis	-60.0	6.000e-04	0.29	2.67				
CCK+B	-60.0	7.000e-04	0.43	4.49				
Ivy	-60.0	5.700e-05	2.90	3.10				
O-LM	-60.0	1.200e-04	0.73	10.00				
Pyr	0.0	4.000e-05	0.30	0.60	-60.0	1.150e-03	0.28	8.40
PV+B	-60.0	1.200e-04	0.29	2.67				
SC-A	-60.0	6.000e-04	0.42	4.99				
CA3	0.0	1.200e-04	2.00	6.30				
ECIII	0.0	1.200e-04	2.00	6.30				

Appendix Table 14: Model synaptic parameters for Axo-axonic cells in the control network.

Physiological Characterization of Model Connections

	Other Cell to Axo					Axo to Other Cell				
Type	**Hold (mV)**	**E_{rev} (mV)**	**Amp. (pA)**	**t_{10-90} (ms)**	**τ_{decay} (ms)**	**Hold (mV)**	**E_{rev} (mV)**	**Amp. (pA)**	**t_{10-90} (ms)**	**τ_{decay} (ms)**
Bis	-50.0	-60.0	36.77	0.70	3.70					
CCK+B	-50.0	-60.0	47.29	0.75	5.27					
Ivy	-50.0	-60.0	4.34	2.13	6.57					
O-LM	-50.0	-60.0	4.76	2.55	12.03					
Pyr	-50.0	0.0	1.85	0.78	2.53	-50.0	-60.0	36.45	0.85	11.57
PV+B	-50.0	-60.0	1.08	0.45	3.13					
SC-A	-50.0	-60.0	24.00	1.00	6.13					
CA3	-50.0	0.0	10.85	2.30	8.80					
ECIII	-50.0	0.0	8.74	3.08	9.20					

Appendix Table 15: Model synaptic properties under voltage clamp at -50 mV with physiological reversal potentials

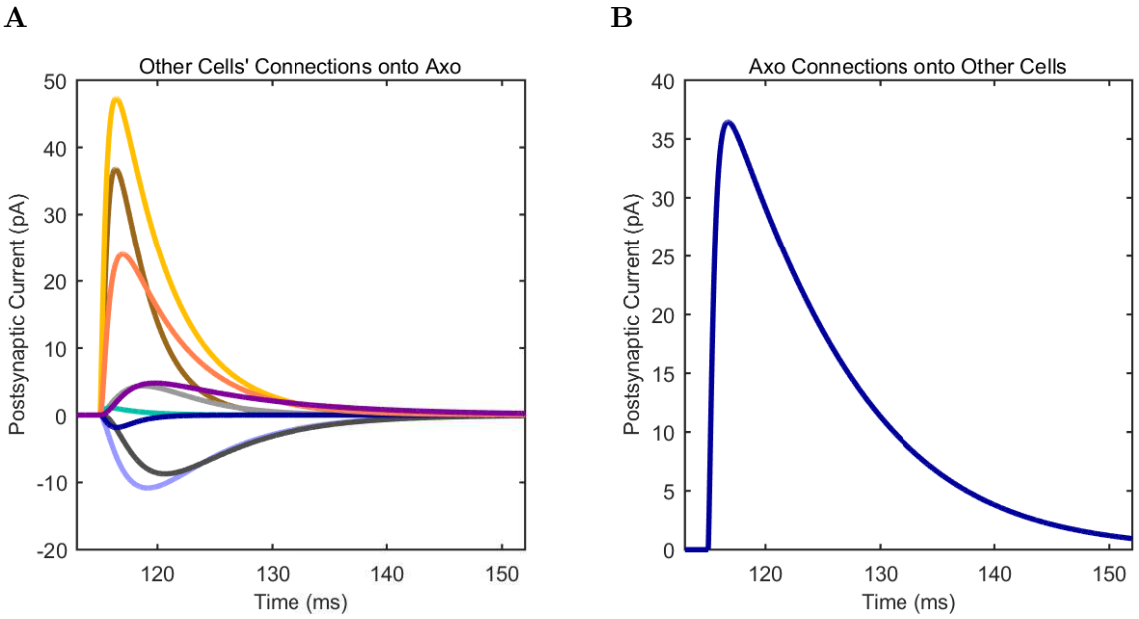

Appendix Figure 8: Connections onto (A) and (B) from model Axo-axonic cells, under voltage clamp at -50 mV with physiological reversal potentials.

Bistratified Cell: Fast-Spiking Dendritic Inhibitor (2210 Cells)

Model and Experimental Electrophysiology

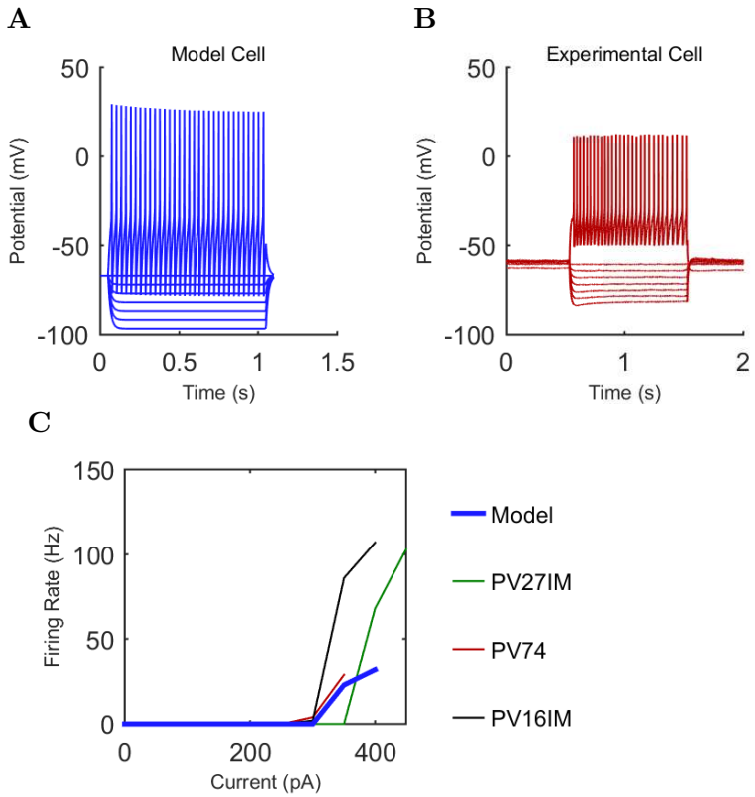

Appendix Figure 9: Bistratified (A) model and (B) experimental current sweep. (C) Firing rates of model and experimental cells.

Property	Value	
RMP	-67.0	mV
Input Resistance	98.8	MΩ
Sag Amplitude	0.0	mV
Sag Tau	NaN	ms
Membrane Tau	14.7	ms
Rheobase	350.0	pA
ISI	39.0	ms
Threshold	-28.1	mV
Spike Amplitude	51.2	mV
Slow AHP Amplitude	48.8	mV

Appendix Table 16: Model Bistratified cell electrophysiological properties.

Channel	G_{max} (S/cm^2)
CavL	4.000e-03
CavN	4.000e-04
KCaS	7.000e-07
Kdrfast	1.600e-02
KvA	5.000e-05
KvCaB	7.000e-08
Navbis	7.000e-02
leak	9.001e-05

Appendix Table 17: Model Bistratified cell ion channels and conductance at highest density location in cell.

Model and Experimental Connectivity

Other Type	Other Cell to Bis # Conn.s	Syn.s /Conn.	#	Post Loc.	Bis to Other Cell # Conn.s	Syn.s /Conn.	#	Post Loc.
Axo					11	10	106	any dendrite
Bis	16	10	160	any dendrite	16	10	160	any dendrite
CCK+B	12	8	96	any dendrite	26	10	260	any dendrite
Ivy	24	10	240	any dendrite	12	10	119	any dendrite
O-LM	8	10	80	apical dendrite	29	10	289	any dendrite
Pyr	366	3	1098	apical dendrite	1410	10	14095	any dendrite
PV+B	39	1	39	soma	40	10	400	any dendrite
SC-A	1	6	6	any dendrite	3	10	30	any dendrite
CA3	5782	2	11564	any dendrite				
ECIII	432	2	864	any dendrite				

Appendix Table 18: Structural connection parameters for Bistratified cells, based on Bezaire and Soltesz (2013).

Experimental Connection Constraints

Pre Type	Exp. Ref.	Hold (mV)	E_{rev} (mV)	Amp. (pA,mV)	Diff. %	t_{10-90} (ms)	Diff. %	τ_{decay} (ms)	Diff. %
Pyr	Pawelzik et al. 2002	-66.0	0.0	0.77	-19.6	1.58	+31.3	14.68	+41.1
PV+B	Cobb et al. 1997	-55.0	-70.0	0.27	-27.5	0.47	-52.5	7.30	+30.4

Appendix Table 19: Experimental constraints for incoming connections onto Bistratified cells (clamp: black=voltage; purple=current).

Post Type	Exp. Ref.	Hold (mV)	E_{rev} (mV)	Amp. (pA,mV)	Diff. %	t_{10-90} (ms)	Diff. %	τ_{decay} (ms)	Diff. %
Pyr	Maccaferri et al. 2000	-70.0	7.0	143.21	-4.5	2.22	+11.2	15.40	-4.3

Appendix Table 20: Experimental constraints for outgoing connections from Bistratified cells (clamp: black=voltage; purple=current).

Model Synapse Parameters

Type	Other Cell to Bis				Bis to Other Cell			
	E_{rev} (mV)	G_{max} (nS)	τ_{rise} (ms)	τ_{decay} (ms)	E_{rev} (mV)	G_{max} (nS)	τ_{rise} (ms)	τ_{decay} (ms)
Axo					-60.0	6.000e-04	0.29	2.67
Bis	-60.0	5.100e-04	0.29	2.67	-60.0	5.100e-04	0.29	2.67
CCK+B	-60.0	7.000e-04	0.43	4.49	-60.0	8.000e-04	0.29	2.67
Ivy	-60.0	7.700e-05	2.90	3.10	-60.0	5.000e-04	0.29	2.67
O-LM	-60.0	1.100e-04	0.60	15.00	-60.0	2.000e-05	1.00	8.00
Pyr	0.0	1.900e-03	0.11	0.25	-60.0	5.100e-04	0.11	9.70
PV+B	-60.0	2.900e-03	0.18	0.45	-60.0	9.000e-03	0.29	2.67
SC-A	-60.0	6.000e-04	0.42	4.99	-60.0	8.000e-04	0.29	2.67
CA3	0.0	1.500e-04	2.00	6.30				
ECIII	0.0	1.500e-04	2.00	6.30				

Appendix Table 21: Model synaptic parameters for Bistratified cells in the control network.

Physiological Characterization of Model Connections

Type	Other Cell to Bis					Bis to Other Cell				
	Hold (mV)	E_{rev} (mV)	Amp. (pA)	t_{10-90} (ms)	τ_{decay} (ms)	Hold (mV)	E_{rev} (mV)	Amp. (pA)	t_{10-90} (ms)	τ_{decay} (ms)
Axo						-50.0	-60.0	36.77	0.70	3.70
Bis	-50.0	-60.0	34.34	0.70	3.72	-50.0	-60.0	34.34	0.70	3.72
CCK+B	-50.0	-60.0	48.13	0.78	5.35	-50.0	-60.0	48.55	0.73	4.15
Ivy	-50.0	-60.0	6.39	2.15	6.63	-50.0	-60.0	43.40	0.60	3.17
O-LM	-50.0	-60.0	6.31	2.70	17.05	-50.0	-60.0	1.86	1.78	8.13
Pyr	-50.0	0.0	64.48	0.28	1.42	-50.0	-60.0	13.47	2.17	15.20
PV+B	-50.0	-60.0	24.45	0.17	0.73	-50.0	-60.0	429.34	0.57	4.13
SC-A	-50.0	-60.0	26.43	1.02	6.20	-50.0	-60.0	50.35	0.70	4.10
CA3	-50.0	0.0	13.81	2.38	8.82					
ECIII	-50.0	0.0	12.04	3.05	9.30					

Appendix Table 22: Model synaptic properties under voltage clamp at -50 mV with physiological reversal potentials

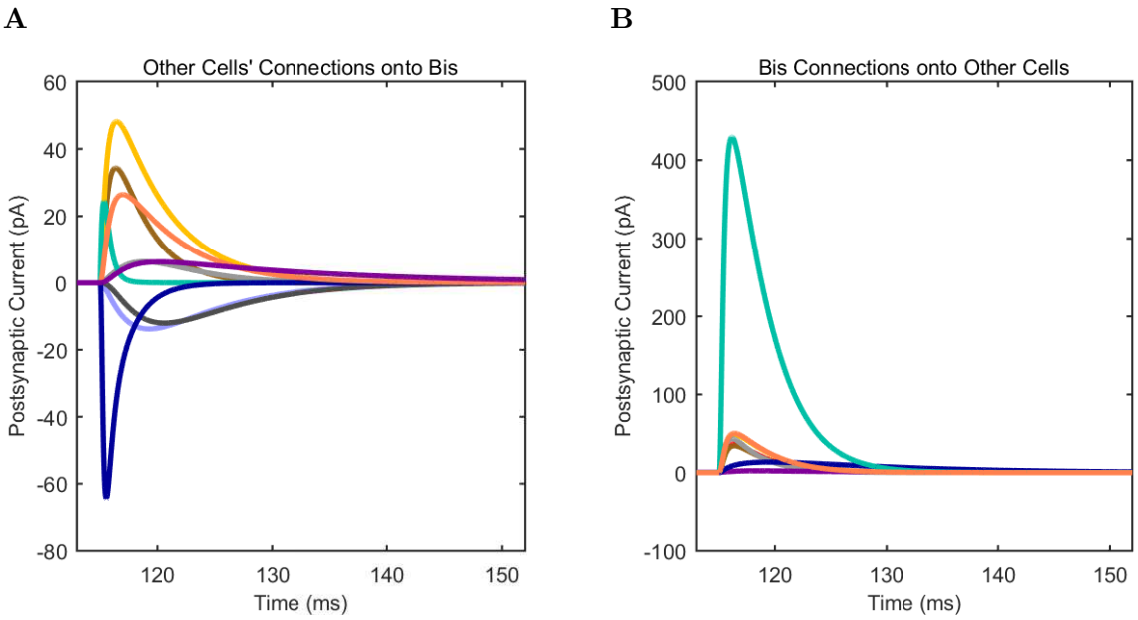

Appendix Figure 10: Connections onto (A) and (B) from model Bistratified cells, under voltage clamp at -50 mV with physiological reversal potentials.

CCK+ Basket Cell: Regular-Spiking Somatic Inhibitor (3600 Cells)

Model and Experimental Electrophysiology

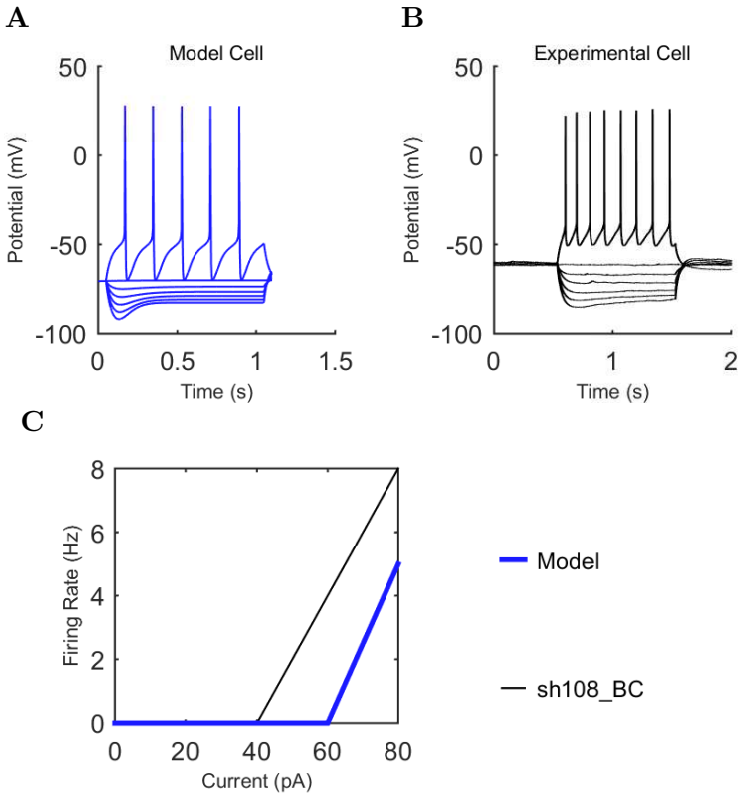

Appendix Figure 11: CCK+ Basket (A) model and (B) experimental current sweep. (C) Firing rates of model and experimental cells.

Property	Value	
RMP	-70.6	mV
Input Resistance	222.4	MΩ
Sag Amplitude	9.2	mV
Sag Tau	45.6	ms
Membrane Tau	25.5	ms
Rheobase	80.0	pA
ISI	180.8	ms
Threshold	-38.0	mV
Spike Amplitude	65.9	mV
Slow AHP Amplitude	32.1	mV

Appendix Table 23: Model CCK+ Basket cell electrophysiological properties.

Channel	G_{max} (S/cm^2)
CavL	2.700e-03
CavN	2.000e-05
HCN	1.000e-04
KCaS	4.000e-06
Kdrfast	8.000e-05
KvA	4.000e-04
KvCaB	4.000e-05
KvGroup	2.600e-03
Navcck	1.800e-02
leak	3.704e-05

Appendix Table 24: Model CCK+ Basket cell ion channels and conductance at highest density location in cell.

Model and Experimental Connectivity

	Other Cell to CCK+B				CCK+B to Other Cell			
Other Type	**# Conn.s**	**Syn.s /Conn.**	**# #**	**Post Loc.**	**# Conn.s**	**Syn.s /Conn.**	**# #**	**Post Loc.**
Axo					5	8	39	any dendrite
Bis	16	10	160	any dendrite	7	8	58	any dendrite
CCK+B	35	8	280	any dendrite	35	8	280	any dendrite
Ivy	96	10	960	any dendrite	20	8	156	any dendrite
O-LM	40	10	400	apical dendrite	9	8	72	any dendrite
Pyr					1125	8	8998	any dendrite
PV+B	38	1	38	soma	18	8	147	any dendrite
SC-A	6	6	36	any dendrite	3	8	24	any dendrite
CA3	2000	2	4000	any dendrite				
ECIII	559	2	1118	any dendrite				

Appendix Table 25: Structural connection parameters for CCK+ Basket cells, based on Bezaire and Soltesz (2013).

Experimental Connection Constraints

Note:No experimental constraints available for incoming synapses to CCK+ Basket cells.

Post Type	Exp. Ref.	Hold (mV)	E_{rev} (mV)	Amp. (pA,mV)	Diff. %	t_{10-90} (ms)	Diff. %	τ_{decay} (ms)	Diff. %
Pyr	Lee et al. 2010	-70.0	-26.0	118.97	+3.1	0.53	-16.7	6.15	-4.9

Appendix Table 26: Experimental constraints for outgoing connections from CCK+ Basket cells (clamp: black=voltage; purple=current).

Model Synapse Parameters

	Other Cell to CCK+B				CCK+B to Other Cell			
Type	E_{rev} (mV)	G_{max} (nS)	τ_{rise} (ms)	τ_{decay} (ms)	E_{rev} (mV)	G_{max} (nS)	τ_{rise} (ms)	τ_{decay} (ms)
Axo					-60.0	7.000e-04	0.43	4.49
Bis	-60.0	8.000e-04	0.29	2.67	-60.0	7.000e-04	0.43	4.49
CCK+B	-60.0	4.500e-04	0.43	4.49	-60.0	4.500e-04	0.43	4.49
Ivy	-60.0	3.700e-05	2.90	3.10	-60.0	3.000e-04	0.43	4.49
O-LM	-60.0	1.200e-03	0.73	20.20	-60.0	7.000e-04	1.00	8.00
Pyr					-60.0	5.200e-04	0.20	4.20
PV+B	-60.0	1.200e-03	0.29	2.67	-60.0	9.000e-03	0.43	4.49
SC-A	-60.0	8.500e-04	0.42	4.99	-60.0	7.000e-04	0.43	4.49
CA3	0.0	6.500e-04	2.00	6.30				
ECIII	0.0	6.500e-04	2.00	6.30				

Appendix Table 27: Model synaptic parameters for CCK+ Basket cells in the control network.

Physiological Characterization of Model Connections

	Other Cell to CCK+B					CCK+B to Other Cell				
Type	Hold (mV)	E_{rev} (mV)	Amp. (pA)	t_{10-90} (ms)	τ_{decay} (ms)	Hold (mV)	E_{rev} (mV)	Amp. (pA)	t_{10-90} (ms)	τ_{decay} (ms)
Axo						-50.0	-60.0	47.29	0.75	5.27
Bis	-50.0	-60.0	48.55	0.73	4.15	-50.0	-60.0	48.13	0.78	5.35
CCK+B	-50.0	-60.0	32.19	0.73	5.30	-50.0	-60.0	32.19	0.73	5.30
Ivy	-50.0	-60.0	3.00	2.25	6.95	-50.0	-60.0	22.34	0.80	5.05
O-LM	-50.0	-60.0	40.32	3.10	28.42	-50.0	-60.0	54.98	1.35	9.05
Pyr						-50.0	-60.0	24.86	0.52	6.03
PV+B	-50.0	-60.0	11.31	0.42	3.08	-50.0	-60.0	523.11	0.68	5.70
SC-A	-50.0	-60.0	33.81	1.05	6.90	-50.0	-60.0	49.55	0.70	5.38
CA3	-50.0	0.0	55.24	2.53	9.35					
ECIII	-50.0	0.0	43.27	3.40	10.87					

Appendix Table 28: Model synaptic properties under voltage clamp at -50 mV with physiological reversal potentials

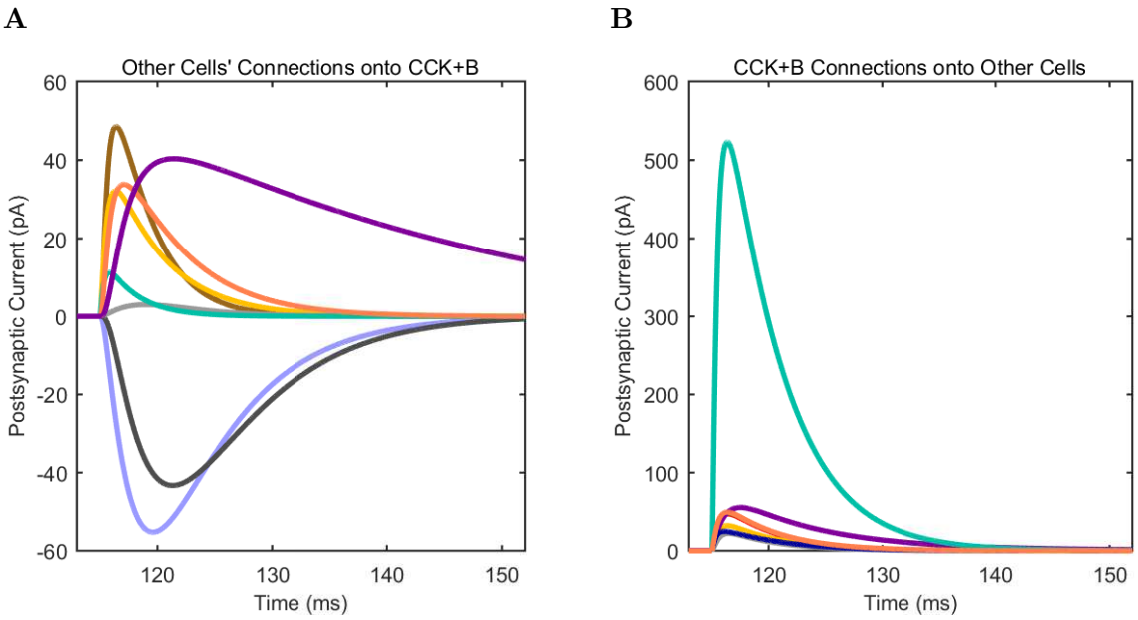

Appendix Figure 12: Connections onto (A) and (B) from model CCK+ Basket cells, under voltage clamp at -50 mV with physiological reversal potentials.

Ivy Cell: Late-spiking Cell (8810 Cells)

Model and Experimental Electrophysiology

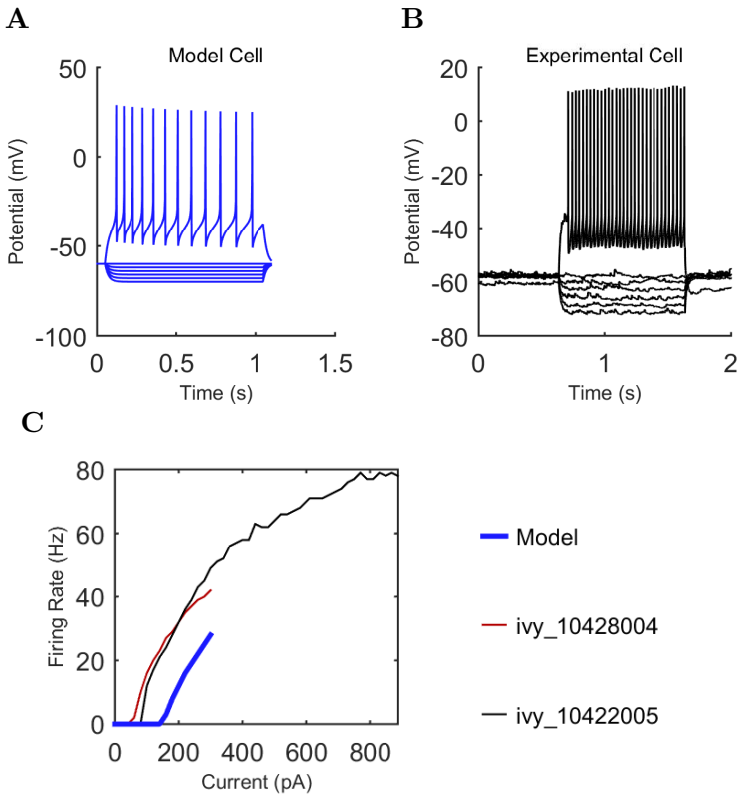

Appendix Figure 13: Ivy (A) model and (B) experimental current sweep. (C) Firing rates of model and experimental cells.

Property	Value	
RMP	-60.0	mV
Input Resistance	100.7	MΩ
Sag Amplitude	0.0	mV
Sag Tau	NaN	ms
Membrane Tau	21.3	ms
Rheobase	160.0	pA
ISI	305.5	ms
Threshold	-27.7	mV
Spike Amplitude	54.6	mV
Slow AHP Amplitude	20.9	mV

Appendix Table 29: Model Ivy cell electrophysiological properties.

Channel	G_{max} (S/cm^2)
CavL	5.611e-02
CavN	5.817e-04
KCaS	4.515e-07
Kdrfastngf	1.551e-01
KvAngf	5.220e-06
KvCaB	1.024e-06
Navngf	3.786e+00
leak	8.471e-05

Appendix Table 30: Model Ivy cell ion channels and conductance at highest density location in cell.

Model and Experimental Connectivity

Other Type	Other Cell to Ivy # Conn.s	Syn.s /Conn.	Post #	Post Loc.	Ivy to Other Cell # Conn.s	Syn.s /Conn.	Post #	Post Loc.
Axo					4	10	40	any dendrite
Bis	3	10	30	any dendrite	6	10	60	any dendrite
CCK+B	8	8	64	any dendrite	39	10	392	any dendrite
Ivy	24	10	240	any dendrite	24	10	240	any dendrite
NGF					11	10	113	any dendrite
O-LM					25	10	253	any dendrite
Pyr	9	3	27	apical dendrite	1485	10	14850	any dendrite
PV+B	8	1	8	soma	15	10	150	any dendrite
SC-A	2	6	12	any dendrite	5	10	46	any dendrite
CA3	1923	2	3846	any dendrite				

Appendix Table 31: Structural connection parameters for Ivy cells, based on Bezaire and Soltesz (2013).

Experimental Connection Constraints

Pre Type	Exp. Ref.	Hold (mV)	E_{rev} (mV)	Amp. (pA,mV)	Diff. %	t_{10-90} (ms)	Diff. %	τ_{decay} (ms)	Diff. %
Pyr	Fuentealba et al. 2008	-65.8	-70.0	0.06	-97.9	1.38	-8.3	NaN	-4.9

Appendix Table 32: Experimental constraints for incoming connections onto Ivy cells (clamp: black=voltage; purple=current).

Post Type	Exp. Ref.	Hold (mV)	E_{rev} (mV)	Amp. (pA,mV)	Diff. %	t_{10-90} (ms)	Diff. %	τ_{decay} (ms)	Diff. %
Pyr	Fuentealba et al. 2008	-50.0	-88.0	8.17	+2.1	3.50	+25.0	15.43	-3.9

Appendix Table 33: Experimental constraints for outgoing connections from Ivy cells (clamp: black=voltage; purple=current).

Model Synapse Parameters

Type	Other Cell to Ivy				Ivy to Other Cell			
	E_{rev} (mV)	G_{max} (nS)	τ_{rise} (ms)	τ_{decay} (ms)	E_{rev} (mV)	G_{max} (nS)	τ_{rise} (ms)	τ_{decay} (ms)
Axo					-60.0	5.700e-05	2.90	3.10
Bis	-60.0	5.000e-04	0.29	2.67	-60.0	7.700e-05	2.90	3.10
CCK+B	-60.0	3.000e-04	0.43	4.49	-60.0	3.700e-05	2.90	3.10
Ivy	-60.0	5.700e-05	2.90	3.10	-60.0	5.700e-05	2.90	3.10
NGF					-60.0	5.700e-05	2.90	3.10
O-LM					-60.0	5.700e-05	2.90	3.10
Pyr	0.0	4.050e-04	0.30	0.60	-60.0	4.100e-05	1.10	11.00
PV+B	-60.0	1.600e-04	0.29	2.67	-60.0	7.000e-04	2.90	3.10
SC-A	-60.0	8.500e-04	0.42	4.99	-60.0	3.700e-05	2.90	3.10
CA3	0.0	3.000e-04	2.00	6.30				

Appendix Table 34: Model synaptic parameters for Ivy cells in the control network.

8 **Physiological Characterization of Model Connections**

Type	Other Cell to Ivy					Ivy to Other Cell				
	Hold (mV)	E_{rev} (mV)	Amp. (pA)	t_{10-90} (ms)	τ_{decay} (ms)	Hold (mV)	E_{rev} (mV)	Amp. (pA)	t_{10-90} (ms)	τ_{decay} (ms)
Axo						-50.0	-60.0	4.34	2.13	6.57
Bis	-50.0	-60.0	43.40	0.60	3.17	-50.0	-60.0	6.39	2.15	6.63
CCK+B	-50.0	-60.0	22.34	0.80	5.05	-50.0	-60.0	3.00	2.25	6.95
Ivy	-50.0	-60.0	5.48	1.88	6.42	-50.0	-60.0	5.48	1.88	6.42
NGF						-50.0	-60.0	5.48	1.88	6.42
O-LM						-50.0	-60.0	5.32	2.10	6.33
Pyr	-50.0	0.0	40.70	0.58	1.28	-50.0	-60.0	1.63	3.63	15.35
PV+B	-50.0	-60.0	1.44	0.55	3.13	-50.0	-60.0	51.35	2.05	6.75
SC-A	-50.0	-60.0	46.62	0.85	5.58	-50.0	-60.0	3.09	2.22	6.88
CA3	-50.0	0.0	29.42	2.05	8.60					

Appendix Table 35: Model synaptic properties under voltage clamp at -50 mV with physiological reversal potentials

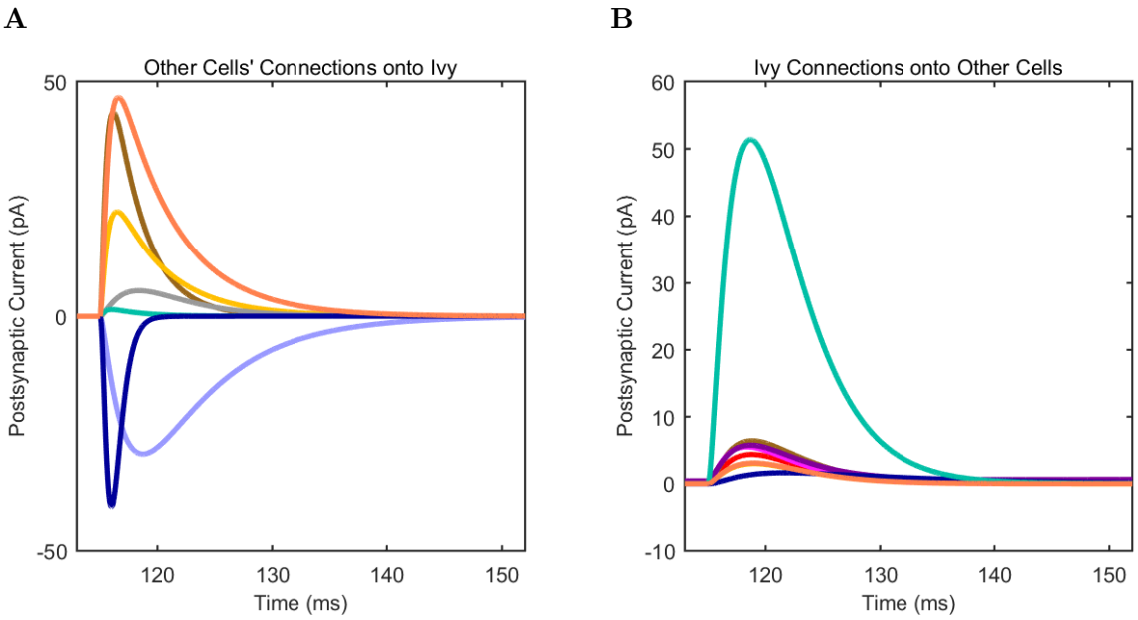

Appendix Figure 14: Connections onto (A) and (B) from model Ivy cells, under voltage clamp at -50 mV with physiological reversal potentials.

Neurogliaform Cell: Late-spiking Feed Forward Cell (3580 Cells)

Model and Experimental Electrophysiology

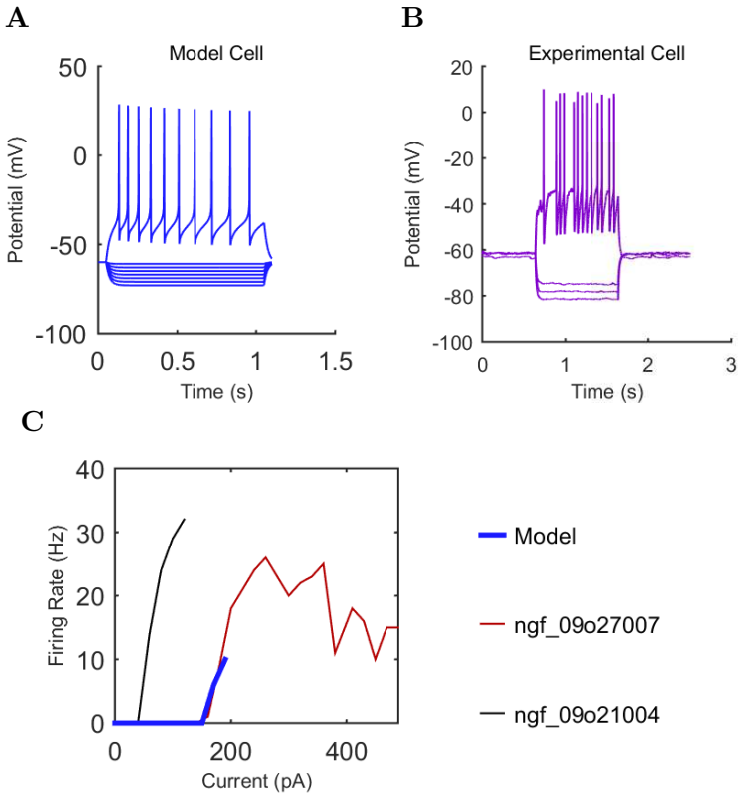

Appendix Figure 15: Neurogliaform (A) model and (B) experimental current sweep. (C) Firing rates of model and experimental cells.

Property	Value	
RMP	-60.0	mV
Input Resistance	100.8	MΩ
Sag Amplitude	0.0	mV
Sag Tau	NaN	ms
Membrane Tau	21.3	ms
Rheobase	170.0	pA
ISI	170.3	ms
Threshold	-27.8	mV
Spike Amplitude	55.2	mV
Slow AHP Amplitude	20.6	mV

Appendix Table 36: Model Neurogliaform cell electrophysiological properties.

Channel	G_{max} (S/cm^2)
CavL	5.611e-02
CavN	5.817e-04
KCaS	4.515e-07
Kdrfastngf	1.551e-01
KvAngf	5.220e-06
KvCaB	1.024e-06
Navngf	3.786e+00
leak	8.471e-05

Appendix Table 37: Model Neurogliaform cell ion channels and conductance at highest density location in cell.

Model and Experimental Connectivity

	Other Cell to NGF				NGF to Other Cell			
Other Type	**# Conn.s**	**Syn.s /Conn.**	**# #**	**Post Loc.**	**# Conn.s**	**Syn.s /Conn.**	**# #**	**Post Loc.**
Ivy	28	10	280	any dendrite				
NGF	17	10	170	apical dendrite	17	10	170	apical dendrite
O-LM	13	10	130	apical dendrite				
Pyr					1218	10	12181	apical dendrite
ECIII	523	2	1046	any dendrite				

Appendix Table 38: Structural connection parameters for Neurogliaform cells, based on Bezaire and Soltesz (2013).

Experimental Connection Constraints

Pre Type	Exp. Ref.	Hold (mV)	E_{rev} (mV)	Amp. (pA,mV)	Diff. %	t_{10-90} (ms)	Diff. %	τ_{decay} (ms)	Diff. %
NGF	Karayannis et al. 2010	-65.0	-11.0	85.50	+0.2	4.83	-1.7	32.03	-46.9
O-LM	Elfant et al. 2008	-50.0	-70.0	18.43	-4.0	1.98	-10.2	11.63	+7.6

Appendix Table 39: Experimental constraints for incoming connections onto Neurogliaform cells (clamp: black=voltage; purple=current).

Post Type	Exp. Ref.	Hold (mV)	E_{rev} (mV)	Amp. (pA,mV)	Diff. %	t_{10-90} (ms)	Diff. %	τ_{decay} (ms)	Diff. %
NGF	Karayannis et al. 2010	-65.0	-11.0	85.50	+0.2	4.83	-1.7	32.03	-46.9
Pyr	Price et al. 2008	-50.0	-89.0	5.25	+7.1	15.48	-3.9	32.73	-34.5

Appendix Table 40: Experimental constraints for outgoing connections from Neurogliaform cells (clamp: black=voltage; purple=current).

Model Synapse Parameters

	Other Cell to NGF				NGF to Other Cell			
Type	E_{rev} (mV)	G_{max} (nS)	τ_{rise} (ms)	τ_{decay} (ms)	E_{rev} (mV)	G_{max} (nS)	τ_{rise} (ms)	τ_{decay} (ms)
Ivy	-60.0	5.700e-05	2.90	3.10				
NGF	-60.0	1.600e-04	3.10	42.00	-60.0	1.600e-04	3.10	42.00
O-LM	-60.0	9.800e-05	1.30	10.20				
Pyr					-60.0	6.500e-05	9.00	39.00
ECIII	0.0	3.500e-03	2.00	6.30				

Appendix Table 41: Model synaptic parameters for Neurogliaform cells in the control network.

Physiological Characterization of Model Connections

	Other Cell to NGF					NGF to Other Cell				
Type	Hold (mV)	E_{rev} (mV)	Amp. (pA)	t_{10-90} (ms)	τ_{decay} (ms)	Hold (mV)	E_{rev} (mV)	Amp. (pA)	t_{10-90} (ms)	τ_{decay} (ms)
Ivy	-50.0	-60.0	5.48	1.88	6.42					
NGF	-50.0	-60.0	17.52	5.67	14.32	-50.0	-60.0	17.52	5.67	14.32
O-LM	-50.0	-60.0	9.14	1.98	11.63					
Pyr						-50.0	-60.0	1.10	65.58	0.00
ECIII	-50.0	0.0	324.35	2.13	8.80					

Appendix Table 42: Model synaptic properties under voltage clamp at -50 mV with physiological reversal potentials

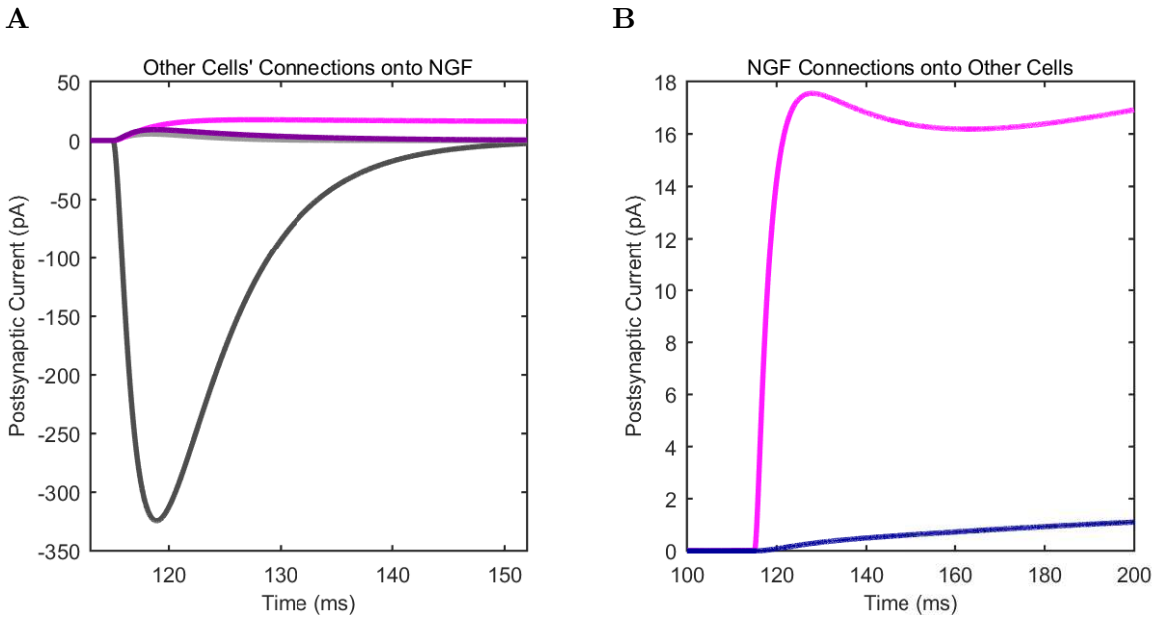

Appendix Figure 16: Connections onto (A) and (B) from model Neurogliaform cells, under voltage clamp at -50 mV with physiological reversal potentials.

O-LM Cell: Feed Back Cell (1640 Cells)

Model and Experimental Electrophysiology

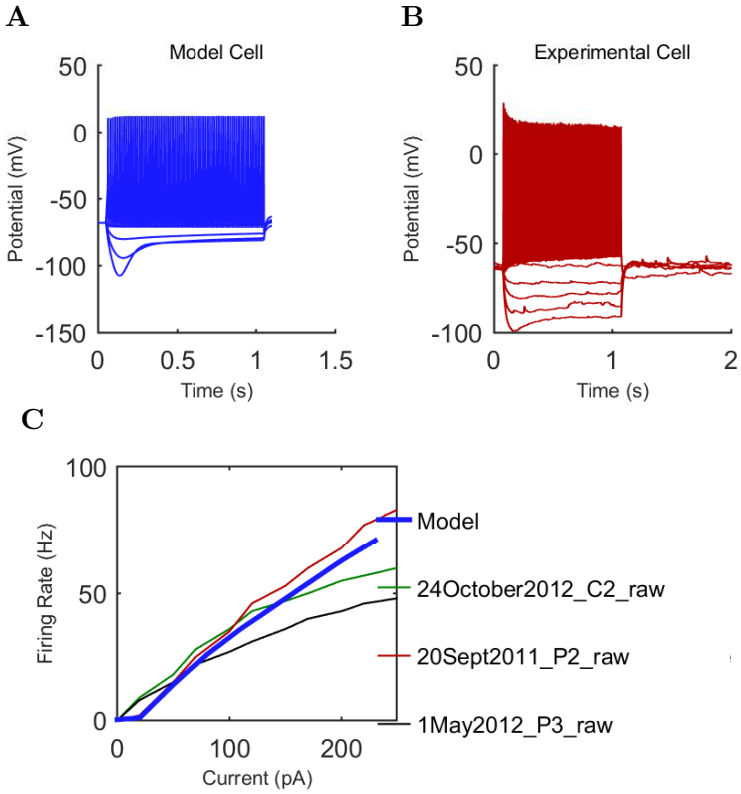

Appendix Figure 17: O-LM (A) model and (B) experimental current sweep. (C) Firing rates of model and experimental cells.

Property	Value	
RMP	-68.0	mV
Input Resistance	267.7	MΩ
Sag Amplitude	26.5	mV
Sag Tau	42.5	ms
Membrane Tau	22.7	ms
Rheobase	20.0	pA
ISI	66.9	ms
Threshold	-37.8	mV
Spike Amplitude	42.6	mV
Slow AHP Amplitude	34.6	mV

Appendix Table 43: Model O-LM cell electrophysiological properties.

Channel	G_{max} (S/cm^2)
HCNolm	5.000e-04
Kdrfast	1.174e-01
KvAolm	4.950e-03
Nav	2.340e-02
leak	1.000e-05

Appendix Table 44: Model O-LM cell ion channels and conductance at highest density location in cell.

Model and Experimental Connectivity

	Other Cell to O-LM				O-LM to Other Cell			
Other Type	**# Conn.s**	**Syn.s /Conn.**	**# #**	**Post Loc.**	**# Conn.s**	**Syn.s /Conn.**	**# #**	**Post Loc.**
Axo					7	10	71	apical dendrite
Bis	39	10	390	any dendrite	11	10	107	apical dendrite
CCK+B	20	8	160	any dendrite	88	10	878	apical dendrite
Ivy	136	10	1360	any dendrite				
NGF					28	10	283	apical dendrite
O-LM	6	10	60	basal dendrite	6	10	60	basal dendrite
Pyr	2379	3	7137	basal dendrite	1520	10	15195	apical dendrite
PV+B					27	10	269	apical dendrite
SC-A					10	10	97	apical dendrite

Appendix Table 45: Structural connection parameters for O-LM cells, based on Bezaire and Soltesz (2013).

Experimental Connection Constraints

Note:No experimental constraints available for incoming synapses to O-LM cells.

Post Type	Exp. Ref.	Hold (mV)	E_{rev} (mV)	Amp. (pA,mV)	Diff. %	t_{10-90} (ms)	Diff. %	τ_{decay} (ms)	Diff. %
NGF	Elfant et al. 2008	-50.0	-70.0	18.43	-4.0	1.98	-10.2	11.63	+7.6
Pyr	Maccaferri et al. 2000	-70.0	7.0	24.35	-6.3	4.68	-24.6	18.88	-9.3
SC-A	Elfant et al. 2008	-50.0	-70.0	17.06	-12.5	4.07	+114.5	30.08	-3.6

Appendix Table 46: Experimental constraints for outgoing connections from O-LM cells (clamp: black=voltage; purple=current).

15 ## Model Synapse Parameters

	Other Cell to O-LM				O-LM to Other Cell			
Type	E_{rev} (mV)	G_{max} (nS)	τ_{rise} (ms)	τ_{decay} (ms)	E_{rev} (mV)	G_{max} (nS)	τ_{rise} (ms)	τ_{decay} (ms)
Axo					-60.0	1.200e-04	0.73	10.00
Bis	-60.0	2.000e-05	1.00	8.00	-60.0	1.100e-04	0.60	15.00
CCK+B	-60.0	7.000e-04	1.00	8.00	-60.0	1.200e-03	0.73	20.20
Ivy	-60.0	5.700e-05	2.90	3.10				
NGF					-60.0	9.800e-05	1.30	10.20
O-LM	-60.0	1.200e-03	0.25	7.50	-60.0	1.200e-03	0.25	7.50
Pyr	0.0	2.000e-04	0.30	0.60	-60.0	3.000e-04	0.13	11.00
PV+B					-60.0	1.100e-03	0.25	7.50
SC-A					-60.0	1.500e-04	0.07	29.00

Appendix Table 47: Model synaptic parameters for O-LM cells in the control network.

16 ## Physiological Characterization of Model Connections

	Other Cell to O-LM					O-LM to Other Cell				
Type	Hold (mV)	E_{rev} (mV)	Amp. (pA)	t_{10-90} (ms)	τ_{decay} (ms)	Hold (mV)	E_{rev} (mV)	Amp. (pA)	t_{10-90} (ms)	τ_{decay} (ms)
Axo						-50.0	-60.0	4.76	2.55	12.03
Bis	-50.0	-60.0	1.86	1.78	8.13	-50.0	-60.0	6.31	2.70	17.05
CCK+B	-50.0	-60.0	54.98	1.35	9.05	-50.0	-60.0	40.32	3.10	28.42
Ivy	-50.0	-60.0	5.32	2.10	6.33					
NGF						-50.0	-60.0	9.14	1.98	11.63
O-LM	-50.0	-60.0	78.69	1.05	9.30	-50.0	-60.0	78.69	1.05	9.30
Pyr	-50.0	0.0	17.47	0.60	1.53	-50.0	-60.0	0.54	3.70	14.10
PV+B						-50.0	-60.0	35.53	1.65	10.18
SC-A						-50.0	-60.0	7.91	3.90	29.83

Appendix Table 48: Model synaptic properties under voltage clamp at -50 mV with physiological reversal potentials

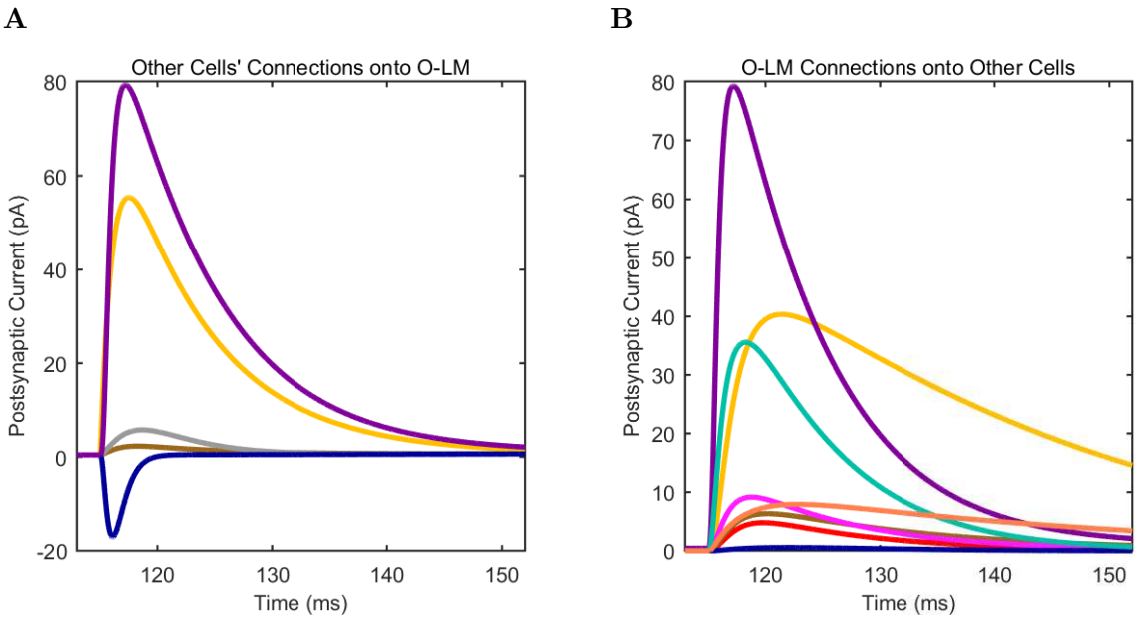

Appendix Figure 18: Connections onto (A) and (B) from model O-LM cells, under voltage clamp at -50 mV with physiological reversal potentials.

PV+ Basket Cell: Fast-Spiking Somatic Inhibitor (5530 Cells)

Model and Experimental Electrophysiology

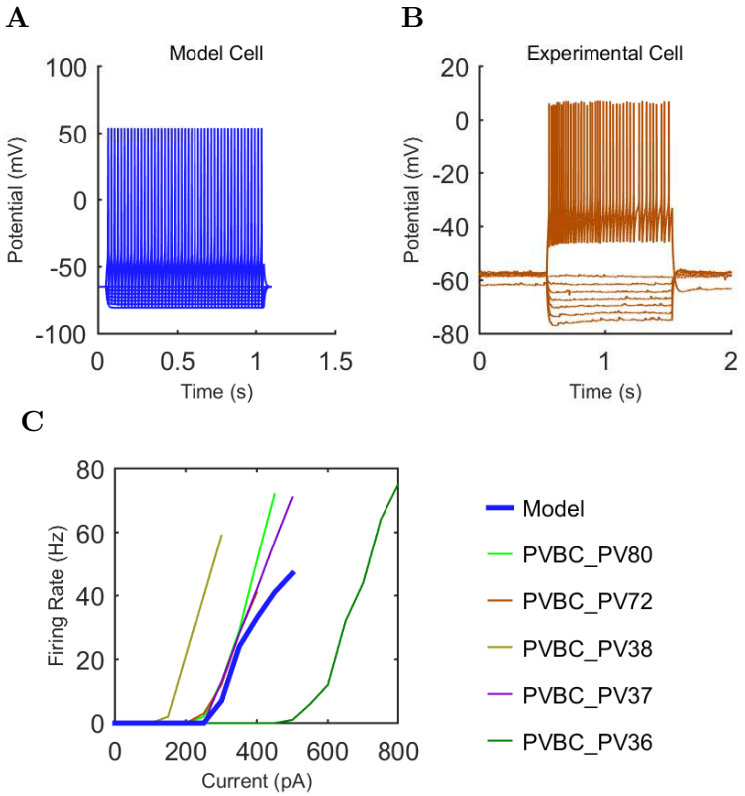

Appendix Figure 19: PV+ Basket (A) model and (B) experimental current sweep. (C) Firing rates of model and experimental cells.

Property	Value	
RMP	-65.0	mV
Input Resistance	52.1	MΩ
Sag Amplitude	NaN	mV
Sag Tau	NaN	ms
Membrane Tau	7.0	ms
Rheobase	300.0	pA
ISI	151.4	ms
Threshold	-36.7	mV
Spike Amplitude	90.7	mV
Slow AHP Amplitude	41.4	mV

Appendix Table 49: Model PV+ Basket cell electrophysiological properties.

Channel	G_{max} (S/cm^2)
CavL	5.000e-03
CavN	8.000e-04
KCaS	2.000e-06
Kdrfast	1.300e-02
KvA	1.500e-04
KvCaB	2.000e-07
Navaxonp	1.500e-01
leak	1.800e-04

Appendix Table 50: Model PV+ Basket cell ion channels and conductance at highest density location in cell.

Model and Experimental Connectivity

	Other Cell to PV+B				PV+B to Other Cell			
Other Type	**# Conn.s**	**Syn.s /Conn.**	**# #**	**Post Loc.**	**# Conn.s**	**Syn.s /Conn.**	**# #**	**Post Loc.**
Axo					10	1	10	soma
Bis	16	10	160	any dendrite	16	1	15	soma
CCK+B	12	8	96	any dendrite	25	1	24	soma
Ivy	24	10	240	any dendrite	13	1	12	soma
O-LM	8	10	80	apical dendrite				
Pyr	424	3	1272	apical dendrite	958	11	10533	soma
PV+B	39	1	39	soma	39	1	39	soma
SC-A					2	1	1	soma
CA3	6047	2	12094	any dendrite				

Appendix Table 51: Structural connection parameters for PV+ Basket cells, based on Bezaire and Soltesz (2013).

Experimental Connection Constraints

Pre Type	Exp. Ref.	Hold (mV)	E_{rev} (mV)	Amp. (pA,mV)	Diff. %	t_{10-90} (ms)	Diff. %	τ_{decay} (ms)	Diff. %
Pyr	Lee et al. 2014	-60.0	0.0	15.09	-67.7	0.28	-72.5	1.83	-55.7
PV+B	Cobb et al. 1997	-59.0	-70.0	0.29	+14.9	2.67	+105.8	14.72	-45.5

Appendix Table 52: Experimental constraints for incoming connections onto PV+ Basket cells (clamp: black=voltage; purple=current).

Post Type	Exp. Ref.	Hold (mV)	E_{rev} (mV)	Amp. (pA,mV)	Diff. %	t_{10-90} (ms)	Diff. %	τ_{decay} (ms)	Diff. %
Bis	Cobb et al. 1997	-55.0	-70.0	0.27	-27.5	0.47	-52.5	11.85	+30.4
Pyr	Szabadics et al. 2007	-70.0	-26.0	91.94	-13.9	0.50	-5.7	6.70	+4.7
PV+B	Cobb et al. 1997	-59.0	-70.0	0.29	+14.9	2.67	+105.8	13.45	-45.5

Appendix Table 53: Experimental constraints for outgoing connections from PV+ Basket cells (clamp: black=voltage; purple=current).

Model Synapse Parameters

	Other Cell to PV+B				PV+B to Other Cell			
Type	E_{rev} (mV)	G_{max} (nS)	τ_{rise} (ms)	τ_{decay} (ms)	E_{rev} (mV)	G_{max} (nS)	τ_{rise} (ms)	τ_{decay} (ms)
Axo					-60.0	1.200e-04	0.29	2.67
Bis	-60.0	9.000e-03	0.29	2.67	-60.0	2.900e-03	0.18	0.45
CCK+B	-60.0	9.000e-03	0.43	4.49	-60.0	1.200e-03	0.29	2.67
Ivy	-60.0	7.000e-04	2.90	3.10	-60.0	1.600e-04	0.29	2.67
O-LM	-60.0	1.100e-03	0.25	7.50				
Pyr	0.0	7.000e-04	0.07	0.20	-60.0	2.000e-04	0.30	6.20
PV+B	-60.0	1.600e-03	0.08	4.80	-60.0	1.600e-03	0.08	4.80
SC-A					-60.0	6.000e-04	0.29	2.67
CA3	0.0	2.200e-04	2.00	6.30				

Appendix Table 54: Model synaptic parameters for PV+ Basket cells in the control network.

Physiological Characterization of Model Connections

Type	Other Cell to PV+B					PV+B to Other Cell				
	Hold (mV)	**E_{rev} (mV)**	**Amp. (pA)**	**t_{10-90} (ms)**	**τ_{decay} (ms)**	**Hold (mV)**	**E_{rev} (mV)**	**Amp. (pA)**	**t_{10-90} (ms)**	**τ_{decay} (ms)**
Axo						-50.0	-60.0	1.08	0.45	3.13
Bis	-50.0	-60.0	429.34	0.57	4.13	-50.0	-60.0	24.45	0.17	0.73
CCK+B	-50.0	-60.0	523.11	0.68	5.70	-50.0	-60.0	11.31	0.42	3.08
Ivy	-50.0	-60.0	51.35	2.05	6.75	-50.0	-60.0	1.44	0.55	3.13
O-LM	-50.0	-60.0	35.53	1.65	10.18					
Pyr	-50.0	0.0	14.75	0.25	1.77	-50.0	-60.0	20.56	0.50	6.70
PV+B	-50.0	-60.0	13.94	0.23	5.25	-50.0	-60.0	13.94	0.23	5.25
SC-A						-50.0	-60.0	5.71	0.42	3.08
CA3	-50.0	0.0	19.71	2.38	8.78					

Appendix Table 55: Model synaptic properties under voltage clamp at -50 mV with physiological reversal potentials

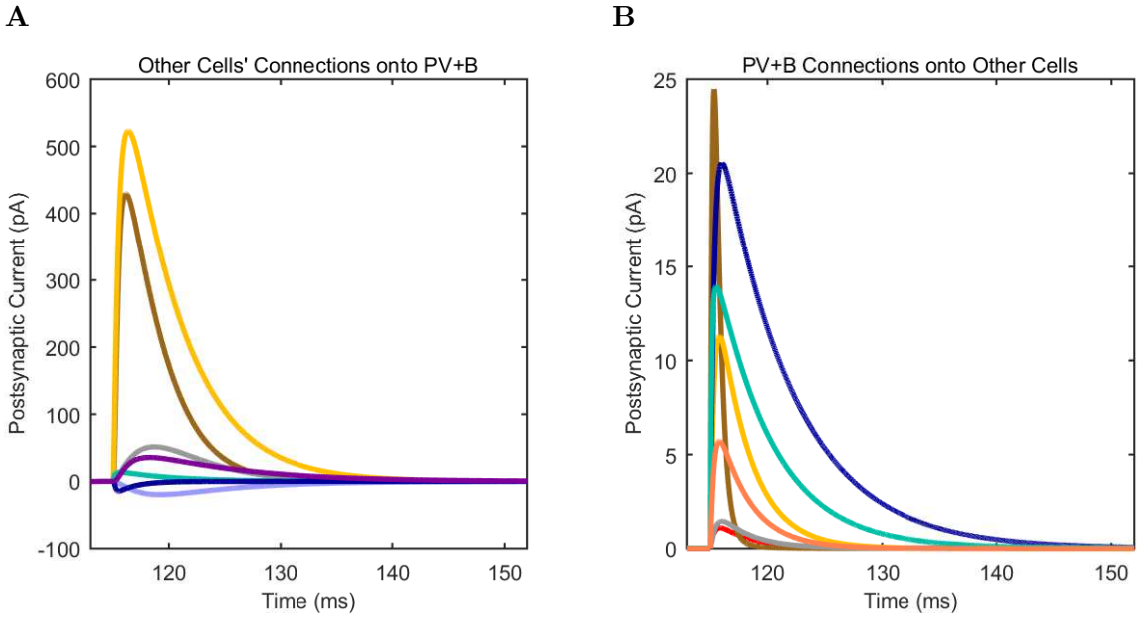

Appendix Figure 20: Connections onto (A) and (B) from model PV+ Basket cells, under voltage clamp at -50 mV with physiological reversal potentials.

Schaffer Collateral-Associated Cell: Regular-Spiking Dendritic Inhibitor (400 Cells)

Model and Experimental Electrophysiology

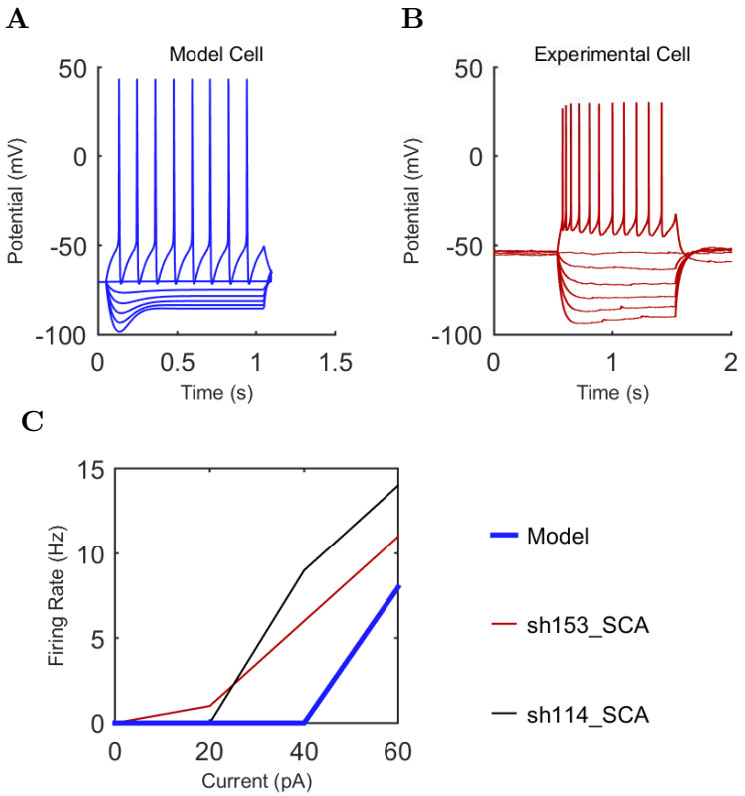

Appendix Figure 21: Schaffer Collateral-Associated (A) model and (B) experimental current sweep. (C) Firing rates of model and experimental cells.

Property	Value	
RMP	-70.5	mV
Input Resistance	300.0	MΩ
Sag Amplitude	12.9	mV
Sag Tau	41.7	ms
Membrane Tau	28.9	ms
Rheobase	60.0	pA
ISI	115.9	ms
Threshold	-36.6	mV
Spike Amplitude	80.3	mV
Slow AHP Amplitude	35.2	mV

Appendix Table 56: Model Schaffer Collateral-Associated cell electrophysiological properties.

Channel	G_{max} (S/cm^2)
CavL	1.000e-03
CavN	2.000e-05
HCN	7.000e-05
KCaS	1.000e-06
Kdrfast	6.000e-05
KvA	1.000e-04
KvCaB	7.000e-06
KvGroup	2.200e-03
Navcck	4.000e-02
leak	2.857e-05

Appendix Table 57: Model Schaffer Collateral-Associated cell ion channels and conductance at highest density location in cell.

Model and Experimental Connectivity

	Other Cell to SC-A				SC-A to Other Cell			
Other Type	**# Conn.s**	**Syn.s /Conn.**	**# #**	**Post Loc.**	**# Conn.s**	**Syn.s /Conn.**	**# #**	**Post Loc.**
Axo					4	6	22	any dendrite
Bis	17	10	170	any dendrite	6	6	33	any dendrite
CCK+B	27	8	216	any dendrite	54	6	324	any dendrite
Ivy	102	10	1020	any dendrite	44	6	264	any dendrite
O-LM	40	10	400	apical dendrite				
Pyr	105	3	315	apical dendrite				
PV+B	24	1	24	soma				
CA3	1940	2	3880	any dendrite				
ECIII	573	2	1146	any dendrite				

Appendix Table 58: Structural connection parameters for Schaffer Collateral-Associated cells, based on Bezaire and Soltesz (2013).

Experimental Connection Constraints

Pre Type	Exp. Ref.	Hold (mV)	E_{rev} (mV)	Amp. (pA,mV)	Diff. %	t_{10-90} (ms)	Diff. %	τ_{decay} (ms)	Diff. %
O-LM	Elfant et al. 2008	-50.0	-70.0	17.06	-12.5	4.07	+114.5	30.08	-3.6
SC-A	Pawelzik et al. 2002	-58.0	-70.0	1.53	-405.6	2.35	-41.3	22.90	-33.2

Appendix Table 59: Experimental constraints for incoming connections onto Schaffer Collateral-Associated cells (clamp: black=voltage; purple=current).

Post Type	Exp. Ref.	Hold (mV)	E_{rev} (mV)	Amp. (pA,mV)	Diff. %	t_{10-90} (ms)	Diff. %	τ_{decay} (ms)	Diff. %
Pyr	Lee et al. 2010	-70.0	-26.0	52.42	-12.9	1.63	+13.6	8.55	+3.0
SC-A	Pawelzik et al. 2002	-58.0	-70.0	1.53	-405.6	2.35	-41.3	27.98	-33.2

Appendix Table 60: Experimental constraints for outgoing connections from Schaffer Collateral-Associated cells (clamp: black=voltage; purple=current).

11

Model Synapse Parameters

	Other Cell to SC-A				SC-A to Other Cell			
Type	E_{rev} (mV)	G_{max} (nS)	τ_{rise} (ms)	τ_{decay} (ms)	E_{rev} (mV)	G_{max} (nS)	τ_{rise} (ms)	τ_{decay} (ms)
Axo					-60.0	6.000e-04	0.42	4.99
Bis	-60.0	8.000e-04	0.29	2.67	-60.0	6.000e-04	0.42	4.99
CCK+B	-60.0	7.000e-04	0.43	4.49	-60.0	8.500e-04	0.42	4.99
Ivy	-60.0	3.700e-05	2.90	3.10	-60.0	8.500e-04	0.42	4.99
O-LM	-60.0	1.500e-04	0.07	29.00				
Pyr	0.0	4.050e-04	0.30	0.60				
PV+B	-60.0	6.000e-04	0.29	2.67				
CA3	0.0	3.000e-04	2.00	6.30				
ECIII	0.0	4.500e-04	2.00	6.30				

Appendix Table 61: Model synaptic parameters for Schaffer Collateral-Associated cells in the control network.

12

Physiological Characterization of Model Connections

Type	Other Cell to SC-A Hold (mV)	E_{rev} (mV)	Amp. (pA)	t_{10-90} (ms)	τ_{decay} (ms)	SC-A to Other Cell Hold (mV)	E_{rev} (mV)	Amp. (pA)	t_{10-90} (ms)	τ_{decay} (ms)
Axo						-50.0	-60.0	24.00	1.00	6.13
Bis	-50.0	-60.0	50.35	0.70	4.10	-50.0	-60.0	26.43	1.02	6.20
CCK+B	-50.0	-60.0	49.55	0.70	5.38	-50.0	-60.0	33.81	1.05	6.90
Ivy	-50.0	-60.0	3.09	2.22	6.88	-50.0	-60.0	46.62	0.85	5.58
O-LM	-50.0	-60.0	7.91	3.90	29.83					
Pyr	-50.0	0.0	17.42	0.68	3.05					
PV+B	-50.0	-60.0	5.71	0.42	3.08					
CA3	-50.0	0.0	27.10	2.35	9.13					
ECIII	-50.0	0.0	31.82	3.38	10.47					

Appendix Table 62: Model synaptic properties under voltage clamp at -50 mV with physiological reversal potentials

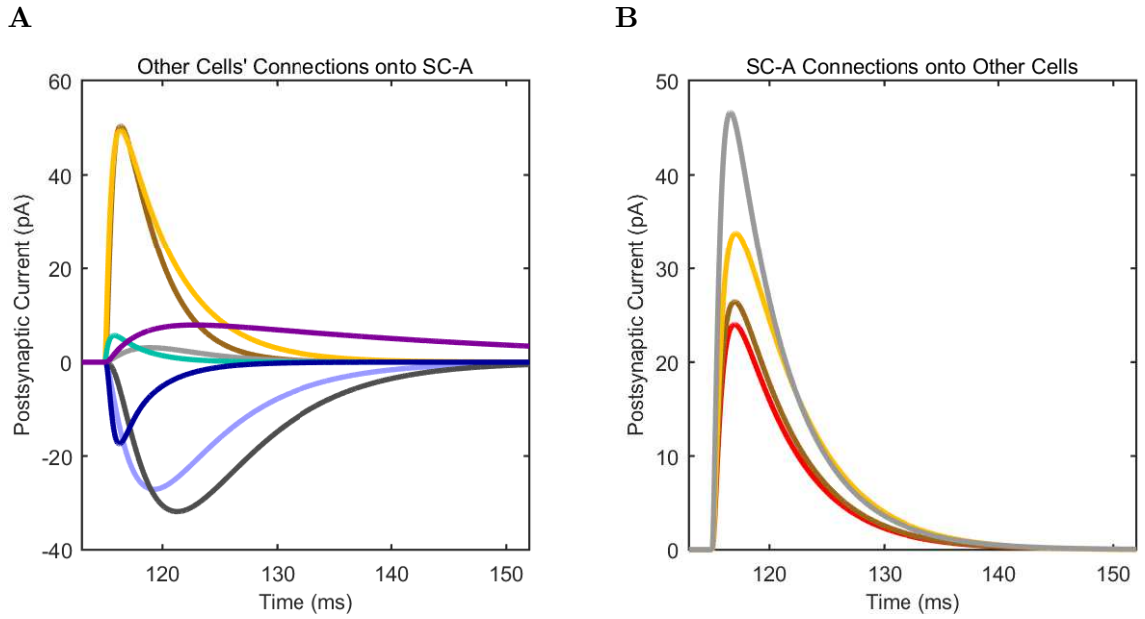

Appendix Figure 22: Connections onto (A) and (B) from model Schaffer Collateral-Associated cells, under voltage clamp at -50 mV with physiological reversal potentials.

C Inhibitory Connectivity

Although the connectivity of the hippocampal CA1 network was assessed in Bezaire and Soltesz (2013), detailed connectivity estimates were only made for pyramidal cells, while the convergence onto inhibitory cells and especially the inhibitory-inhibitory connections were only estimated at a high level due to lack of sufficiently specific experimental data. Here, we performed additional calculations and made use of additional data to arrive at specific estimates for each interneuron type.

First, we gathered previously published morphology data about each interneuron type. As there were not data available for ivy and neurogliaform cells, we performed the necessary experiments in

our lab by filling ivy and neurogliaform cells in hippocampal CA1 slices from Wistar rats and then measuring their somatic area and dendrites. While we performed this experiment in slices, these cell types have relatively compact morphology, allowing us to characterize a significant amount of their dendritic extent. The data for ivy and neurogliaform cells are available in Appendix Table 63. The somatic and dendritic lengths used for each interneuron type in this work are given in Appendix Table 64.

Next, we gathered data about the somatic and dendritic synaptic densities for each cell class (Appendix Table 65) and then multiplied the areas and lengths by their respective synaptic densities to arrive at the estimated excitatory and inhibitory synapses on the somata and dendrites of each cell types (Appendix Table 66). Finally, using our previous estimate of the excitatory and inhibitory boutons available for synapsing on interneurons in CA1 (Bezaire and Soltesz, 2013), we evenly distributed the boutons available for synapsing on each neurite type in each layer across the available postsynaptic densities of that neurite type and transmitter type, so that each interneuron received approximately the same level of coverage of its incoming synapses, while respecting specific observations about interneuron connectivity, such as that CCK+ basket cells have never been observed to receive direct monosynaptic excitement from local CA1 pyramidal cells (Lee et al., 2010) and O-LM cells receive almost all of their excitatory connections from local collaterals (Blasco-Ibáñez and Freund, 1995). The final connectivity between each cell type, including interneurons, is given in the manuscript, Table 1.

Cell Type	Cell Name	# Sections	Dendritic Length (μm))				Somatic Diameter (μm)	Calculated Synaptic Area (μm^2)
			SO	SP	SR	SLM		
Ivy	0217-1 DAB 3_2_10 left slice	1	129.2	64.5	1200.6	0	38.9	1188.5
Ivy	9n23-7 DAB 12_16_09 left+middle slice	2	0	0	2703.2	300.3	45.2	1604.6
Ivy	9n23-6 DAB 06_10 left slice	1	75.4	133.8	2115.4	0	36.6	1052.1
Ivy	9n16-3 DAB 12_29_09 left slice	1	0	0	1015.2	0	52.5	2164.8
Ivy	Average		51.15	49.575	1758.6	75.075		1502.5
Neurogliaform	9n 12-5 DAB 1_06_09	1	0	0	2097.7	525	34.4	929.4
Neurogliaform	91021 DAB 3_18_10 2nd,3rd,4th from left slice	3	0	0	1230.7	780.1	28	615.8
Neurogliaform	9d 8-3 DAB 1_15_10 left and right slice	2	0	0	2328.2	1382.4	32.2	814.3
Neurogliaform	Average		0	0	1885.5	895.8		786.5

Appendix Table 63: Measured dendritic lengths and somatic diameters for ivy and neurogliaform cells from the hippocampal CA1 area in Wistar rats, with calculation of somatic surface area included. Cells were characterized in our lab and their function has been reported in Krook-Magnuson et al. (2011). Source Data available in Appendix Table 1 - Source Data.

Interneuron	Soma area (100 μm^2)	Dendritic Length (μm^2) Total	SO	SP	SR	SLM	Reference
Ivy	1502	1934.4	51.15	49.575	1758.6	75.075	See below
Neurogliaform	786	2781.4	0	0	1885.5	895.8	See below
PV+ basket	3428	4359	1493	697	1877	292	Papp et al. (2013)
Bistratified	1006	4347.75	1074.57	248.28	2369.24	655.66	Gulyas et al. (1999)
Axo-axonic	2329	2825	570	659	1259	337	Papp et al. (2013)
CCK+ basket	966	6338.31	1213.92	310.61	3522.6	1291.18	Matyas et al. (2004)
SCA	966	6338.31	1213.92	310.61	3522.6	1291.18	Matyas et al. (2004)
O-LM	3007.78	4165.68	4165.68	0	0	0	Blasco-Ibáñez and Freund (1995)

Appendix Table 64: Estimated or observed somatic area and dendritic length. Experimental observations of the dendritic length of broad interneuron classes were used as the basis for these estimations. The relative lengths for PV+ basket cells and axo-axonic cells were further differentiated based on experimental observations in region CA3 (Papp et al., 2013). The observations published in Matyas et al. (2004) for CCK+ basket cells were also applied to the CCK+ Schaffer Collateral-Associated cells, based on the discussion in Matyas et al. (2004). The data for ivy and neurogliaform cells were based on measurements from filled cells from slices. Due to the compact nature of their morphology, especially the neurogliaform cells, the dendritic lengths within the slices were assumed to comprise most or all of the dendritic extents of those cells. See section below for raw data. The O-LM cell morphological measurements were taken from Blasco-Ibáñez and Freund (1995).

	Somatic		Dendritic								
			SO		SP		SR		SLM		
Reference	**Exc**	**Inh**	**Exc**	**Inh**	**Exc**	**Inh**	**Exc**	**Inh**	**Exc**	**Inh**	**Ref**
Ivy	21.8	16.1	172.2	23.7	163.3	38.5	193.8	25.3	97.4	31.7	Calc. from average
Neurogliaform	21.8	16.1	172.2	23.7	163.3	38.5	193.8	25.3	97.4	31.7	Calc. from average
PV+ basket	40.7	18.1	342.5	19.2	345	16.1	371.2	18.3	132.2	28.6	Gulyas et al. (1999)
Bistratified	40.7	18.1	342.5	19.2	345	16.1	371.2	18.3	132.2	28.6	Gulyas et al. (1999)
Axo-axonic	40.7	18.1	342.5	19.2	345	16.1	371.2	18.3	132.2	28.6	Gulyas et al. (1999)
CCK+ basket	3.4	16.1	84.3	32.5	52.7	87.4	82	37.8	86.5	58.8	Matyas et al. (2004)
SCA	3.4	16.1	84.3	32.5	52.7	87.4	82	37.8	86.5	58.8	Matyas et al. (2004)
O-LM	21.8	16.1	172.2	23.7	163.3	38.5	193.8	25.3	97.4	31.7	Calc. from average

Appendix Table 65: The synaptic densities (# boutons per 100 μm of dendritic length, or # boutons per 100 μm^2 of somatic area) on the soma and dendrites of PV cells, given in Gulyas et al. (1999), were applied to the axo-axonic, PV+ basket, and bistratified cells. The synaptic densities of CCK+ cells (Matyas et al., 2004) were applied to the CCK+ basket and the Schaffer Collateral-Associated cells. For the ivy, neurogliaform, and O-LM cells, there were not sufficient experimental data published to constrain the synaptic density, and so an average of all synaptic densities for all cell classes was computed and applied to these cell types.

Ref	Somatic		Dendritic										Ref
			SO		SP		SR		SLM		Total		
	Exc	Inh	Exc	Inh	Exc	Inh	Exc	Inh	Exc	Inh	Exc	Inh	
Ivy	326.9	242.3	88	12	82	19	3408	445	73	24	3651	500	Calculated
Neurogliaform	171.1	126.8	0	0	0	0	3654	477	873	284	4527	761	Calculated
PV+ basket	1395.2	620.1	4230	237	866	40	9449	466	840	182	15385	925	Calculated
Bistratified	409.4	182	3681	206	856	40	8796	434	867	188	14200	868	Calculated
Axo-axonic	947.9	421.3	1615	90	819	38	6338	313	969	210	9741	651	Calculated
CCK+ basket	32.8	155.7	1024	394	164	271	2887	1332	1117	759	5192	2756	Calculated
SCA	32.8	155.7	1024	394	164	271	2887	1332	1117	759	5192	2756	Calculated
O-LM	654.6	485.2	6527	1632	0	0	0	0	0	0	6527	1632	Calculated

Appendix Table 66: Estimated numbers of excitatory and inhibitory synapses on each cell type, calculated by multiplying the somatic area or dendritic length by the respective synaptic density. About 20% of synapses onto O-LM cells are GABAergic, while at least 60% are from local excitatory collaterals (Kispersky et al., 2012). Therefore, we conserved the total (inhibitory + excitatory) synaptic density of O-LM cells as calculated previously, but set 20% of that total to be inhibitory and the rest to be excitatory synapses.

D Ion Channel Descriptions

Ion Channel	Description	Model Type	Pyramidal	Axo-axonic	Bistratified	CCK+ Basket	Ivy	Neurogliaform	O-LM	PV+ Basket	S.C.-Assoc.
$Ca_{v,L}$	L-type Calcium	GHK		•	•	•	•	•		•	•
$Ca_{v,N}$	N-type Calcium	Q-O		•	•	•	•	•		•	•
HCN	Hyperpol.-act, Cyclic Nucleo.-gated	Q-O				•					•
HCN_{OLM}	Hyperpol.-act, Cyclic Nucleo.-gated for O-LM cells	Q-O							•		
HCN_p	Hyperpol.-act, Cyclic Nucleo.-gated for Pyr. cells	Q-O	•								
$K_{Ca,S}$	Small (SK) Calcium-activated potassium	Q-O		•	•	•	•	•		•	•
$K_{dr,fast}$	Fast delayed rectifier potassium	Q-O		•	•	•			•	•	•
$K_{dr,fast,ngf}$	Fast delayed rectifier potassium for NGF-family cells	Q-O					•	•			
$K_{dr,p}$	Delayed rectifier potassium for Pyr. cells	Q-O	•								
$K_{v,A}$	A-type voltage-act. potassium	Q-O		•	•	•				•	•
$K_{v,A,dist,p}$	A-type voltage-act. potassium for dist. Pyr. dendrites	Q-O	•								
$K_{v,A,ngf}$	A-type voltage-act. potassium for NGF-family cells	Q-O					•	•			
$K_{v,A,olm}$	A-type voltage-act. potassium for O-LM cells	Q-O							•		
$K_{v,A,prox,p}$	A-type voltage-act. potassium for prox. Pyr. dendrites	Q-O	•								
$K_{v,Ca,B}$	Big (BK) Calcium-act., voltage-dep. potassium	Q-O		•	•	•	•	•		•	•
$K_{v,Group}$	Multiple slower voltage-dep. potassium	Q-O				•					•
leak	Leak	Q-O		•	•	•	•	•	•	•	•
Na_v	Voltage-dep. sodium	Q-O		•				•		•	
$Na_{v,bis}$	Voltage-dep. sodium for bistratified cells	Q-O			•						
$Na_{v,cck}$	Voltage-dep. sodium for CCK+ cells	Q-O				•					•
$Na_{v,ngf}$	Voltage-dep. sodium for NGF-family cells	Q-O					•	•			
$Na_{v,p}$	Voltage-dep. sodium for Pyr. cells	Q-O	•								
pas	Leak	Q-O	•								

Appendix Table 67: Ion channels included in the model. GHK: based on Goldman-Hodgkin-Katz equation; Q-O: quasi-ohmic; Hyperpol.-act: Hyperpolarization-activated; Nucleo.-gated: Nucleotide-gated; voltage-act.: voltage activated; voltage-dep.: voltage dependent; Calcium-act.: Calcium-activated; Pyr.: pyramidal; NGF: neurogliaform; dist.: distal; prox.: proximal.

Appendix Table 67 lists which model ion channels are found in each model cell type. The channels are further described below, summarized from Bezaire (2015), and their equations are included as well. The activation/inactivation curves and current-voltage relations are reproduced here from Bezaire (2015).

Calcium channels

The calcium channels were adapted from previous Soltesz Lab models (Santhakumar et al., 2005a; Dyhrfjeld-Johnsen et al., 2007a; Morgan and Soltesz, 2008a) and include an L-type and N-type channel (Appendix Figure 23); the L-type channel does not inactivate and the N-type channel inactivates.

$Ca_{v,L}$ Channel Jaffe et al. (1994) developed this channel based on activation data from CA1 and CA3 hippocampal neurons in adult guinea pigs, at room temperature. It has been further used in many other models implemented by Migliore. The voltage of half-activation was shifted by -10 mV, accounting for ionic differences in the experimental preparation compared to the model condition. It uses the GHK equation to calculate the driving force through the channel, allowing a mild dependence on calcium concentration.

$Ca_{v,N}$ Channel Jaffe et al. (1994) also developed this channel, using the same preparation as for the $Ca_{v,L}$ channel. Aradi and Holmes (1999) then modified the channel code, replacing the GHK calculation with a quasi-ohmic calculation of the driving force. In addition, its behavior was altered somewhat compared to previous implementations such as Morgan and Soltesz (2008a) and Santhakumar et al. (2005a). Their implementations contained a typo in the channel definition that caused its equations to differ from those presented in Aradi and Holmes (1999), and had the effect of reducing the conductance of the channel below its intended magnitude.

At high levels of activation, the channel conductance decreases slightly (Appendix Figure 23), a behavior that resulted from replacing of the GHK calculation with a quasi-ohmic expression. However, it may not have too large of an effect since it only happens at very depolarized potentials, potentials

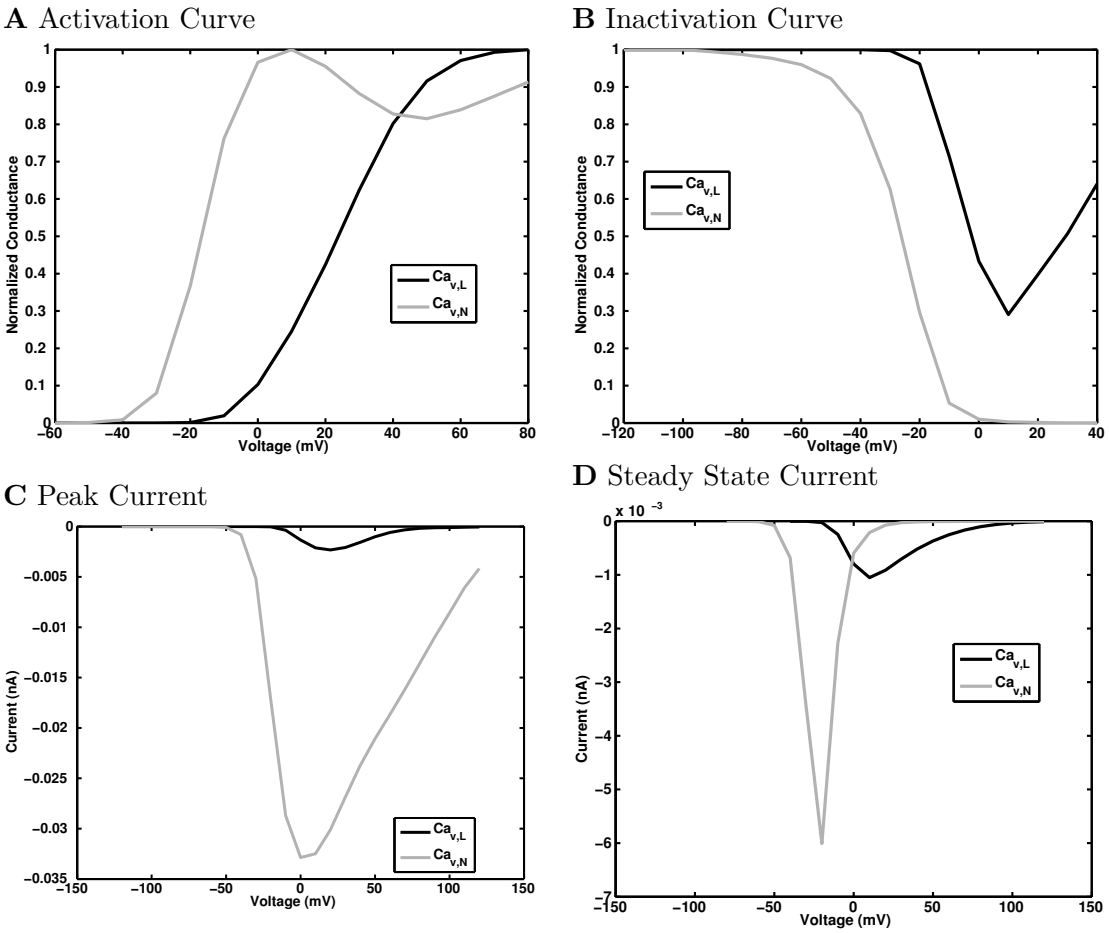

Appendix Figure 23: Calcium channel currents.

that are likely to be achieved only at the peak of a spike.

HCN channels

The characteristic behavior of HCN channels, their hyperpolarized voltage-dependent activation is captured in these models, but not their cyclic-nucleotide gating. Because they are hyperpolarization-activated, the protocol used to characterize the inactivating of other channels was used to characterize the activation of the HCN channels. In Appendix Figure 24, the differing behavior of the HCN channels can be seen.

HCN Channel The HCN channel model was based on experiments carried out in CA1 pyramidal cells of Sprague-Dawley rats at room temperature (Chen et al., 2001). The original channel model included fast and slow components and used separate, artificial ion definitions for each. We only

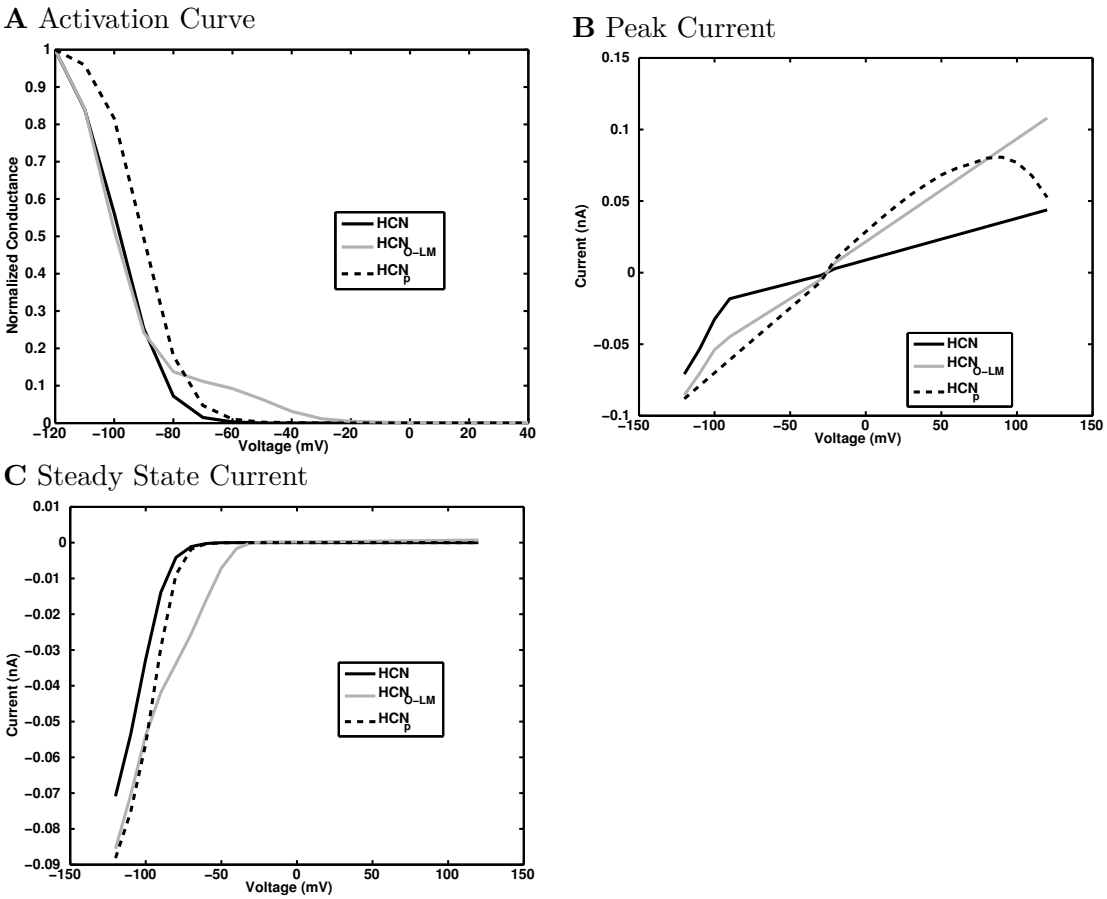

Appendix Figure 24: HCN channel currents.

retained the slow component as the inclusion of the fast component caused a non-physiological, oscillating sag when included in cells. We also reduced the voltage dependence of the slow component slightly to further decrease the oscillation of the sag.

HCN_{OLM} Channel Saraga et al. (2003) developed this channel model based on data from young Sprague-Dawley rats at a warm room temperature, and Cutsuridis et al. (2010) included it in a model O-LM cell, which we incorporated into our model.

HCN_p Channel Cutsuridis et al. (2010) developed this channel model based experimental data from adult Sprague-Dawley rats at 23^o or 33^o (Magee, 1998) and included it in a model pramidal cell.

Potassium channels

We included several potassium channels: delayed rectifier, A-type potassium channels, calcium-dependent potassium channels, and leak channels. We developed multiple variations, which enabled us to tune their thresholds and voltage dependence to the voltage-dependent behavior of the cells into which we placed them.

Delayed Rectifier Potassium Channels

The delayed rectifier models had a voltage-dependent activation component but not an inactivating component.

In Appendix Figure 25, the differing behavior of the delayed rectifiers can be seen.

$K_{dr,fast}$ Channel Yuen and Durand (1991) originally implemented this model, based on another model of a fast delayed rectifier in a squid axon. They adjusted its parameters so their model cell action potential wave form matched that produced by an experimental mouse cell. Aradi and Holmes (1999) later modified the model to shift the voltage dependence slightly.

$K_{dr,fast,ngf}$ Channel To better fit the behavior of experimental neurogliaform cells, we shifted by -10 mV the voltage dependence of the $K_{dr,fast}$ channels within the neurogliaform and ivy cells, which

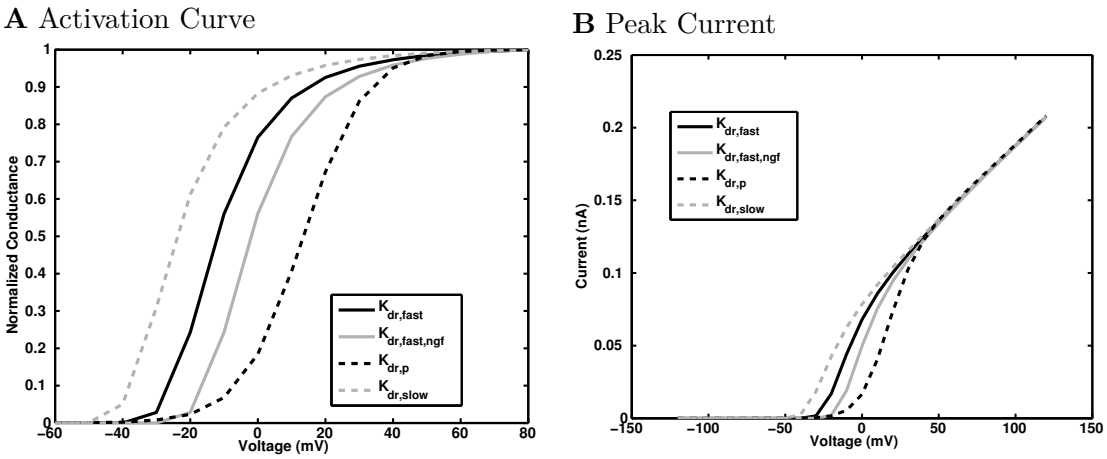

Appendix Figure 25: Delayed rectifier potassium channel currents.

usually have a higher threshold than other cells.

$K_{dr,p}$ Channel This channel, implemented by Migliore based on experimental data from hippocampal cells in rat pups at room temperature (Klee et al., 1995), was used in the pyramidal cell model we included in our model (Poolos et al., 2002).

A-type Potassium Channels

A-type potassium channels are transient and quickly-inactivating; they activate near the action potential threshold, delaying action potential onset, increasing action potential threshold, and even modulating early repolarization after an action potential (Storm, 1990).

$K_{v,A}$ Channel Migliore et al. (1995) developed this channel model, starting with the equations of Borg-Graham (1991) and modifying them to account for Ficker and Heinemann (1992) and Numann et al. (1987) to get the burst behavior they were investgating.

$K_{v,A,dist,p}$ Channel Migliore et al. (1995) also developed this channel for use in the CA1 pyramidal cell model of Poolos et al. (2002), based on rat hippocampal pyramidal cell data from Klee et al.

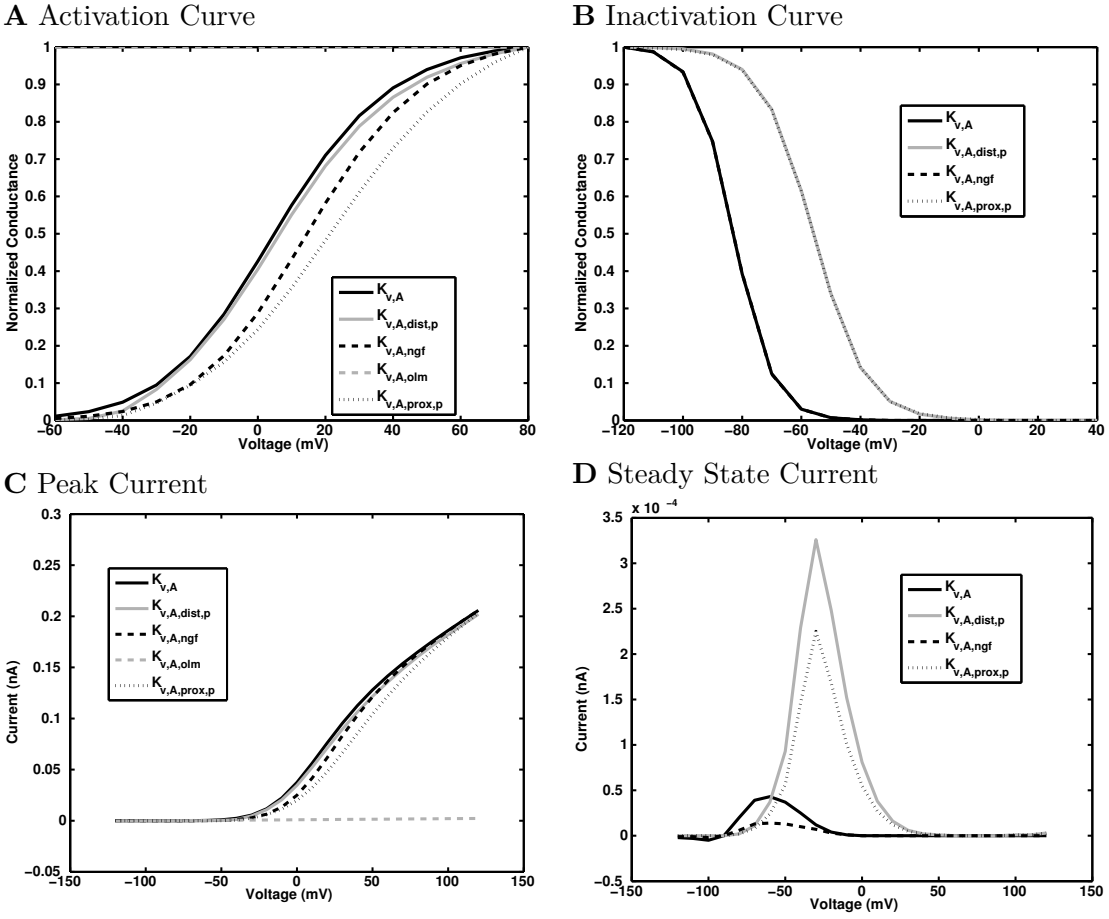

Appendix Figure 26: A-type potassium channel currents.

(1995).

$K_{v,A,prox,p}$ Channel Migliore et al. (1995) also developed this channel model, which differs slightly from the $K_{v,A,dist,p}$ channel model in timing and voltage.

$K_{v,A,ngf}$ Channel We modified the activation and inactivation equations of the KvA A-type channel developed by Migliore et al. (1995) for use in neurogliaform and ivy cells. We offset the voltage dependence by +10 mV to better fit the high-threshold neurogliaform cell family.

$K_{v,A,olm}$ Channel Saraga et al. (2003) developed this channel based on experimental data from the McBain lab and others, and Cutsuridis et al. (2010) used it in the O-LM cell model that we included in our model.

Other Potassium Channels

Some of the potassium channels included in the model were not voltage dependent in the same way as the above ones. The leak and KCaS channels are not voltage activated nor inactivating. The KvCaB channel was voltage-dependent, but was also Ca^{2+} gated. KvGroup was voltage-dependent activation but had no inactivating component.

$K_{Ca,S}$ Channel The model of this calcium-activated potassium channel (known as the small or "'SK"' channel), was developed by Yuen and Durand (1991) and modified by Aradi and Holmes (1999) based on data from Beck et al. (1997), Latorre et al. (1989), Sah (1996), and Lancaster et al. (1991).

$K_{v,Ca,B}$ Channel This big ("'BK"') potassium channel, both voltage dependent and calcium-gated, was implemented by Migliore et al. (1995) based on a model from Moczydlowski and Latorre (1983) and has been modified somewhat.

The behavior of these other channels is shown as a function of voltage (Appendix Figure 27) and as a function of internal Ca^{2+} concentration for the calcium-gated potassium channels (Appendix Figure 28).

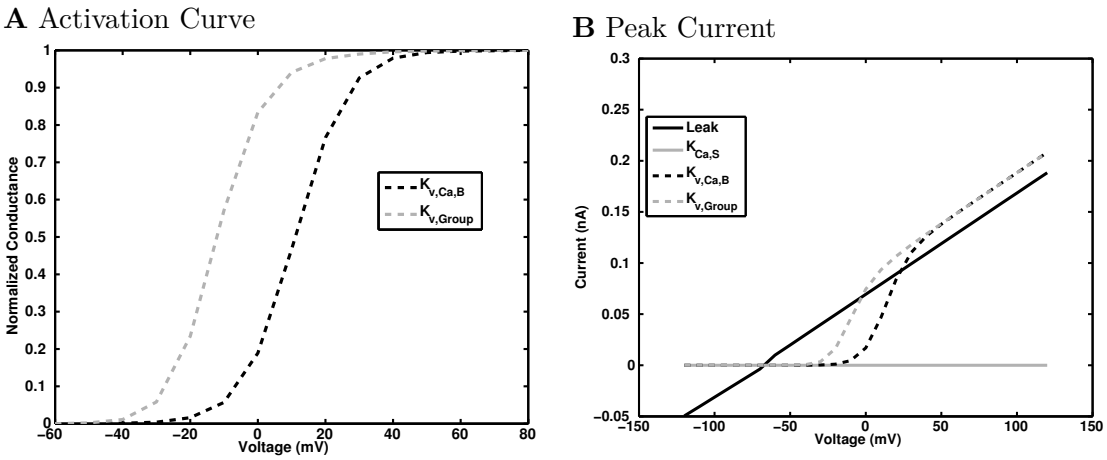

Appendix Figure 27: Other potassium channel currents. Because they didn't have a voltage-sensitive inactivation component, only the activation curve, which is equivalent to the IV Peak curve, need be shown here.

$K_{v,Group}$ Channel We implemented a new potassium channel model, starting with the fast delayed rectifier potassium channel, and adjusting the parameters to match the channel behavior of Lien and Jonas (2003) which was presented as a model of the Kv3.1b channel. However, the methods used in Lien and Jonas (2003) are likely to have included multiple potassium channel types in their channel characterization: they added 300 uM of 4-AP, billed as a low enough dose that it would block only Kv3.1b channels, and subtracted the intracellular potential recording of the cell in the presence of that blocker from the control recording and attributed that entire difference to Kv3.1b. However, it is possible to block other potassium channel types with doses of 4-AP as low as 5-10 μM (Campanac et al., 2013), so two or more potassium channel types were likely blocked in Lien and Jonas (2003), meaning that more than one potassium channel type contributes to the dynamics of the model channel fit by Lien and Jonas (2003), so we called it "KvGroup".

leak Channel The leak channel is a very simple, quasi-ohmic model component that employs a non-specific current with a reversal potential set near but depolarized from the potassium reversal

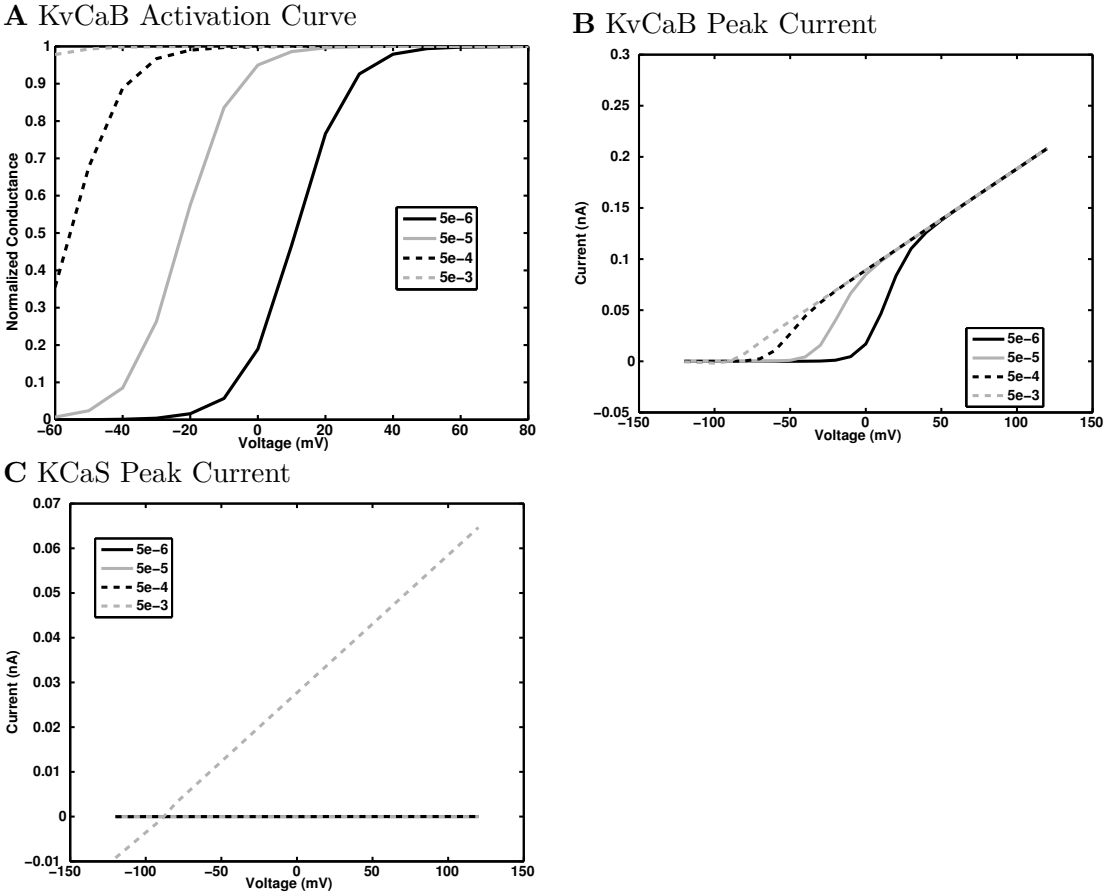

Appendix Figure 28: Calcium-dependent potassium channel dependence on calcium concentration. (a) The normalized conductance of the channels are plotted as a function of test voltage step and calcium concentration. (b) and (c) The current-voltage relation is shown at several calcium concentrations for (b) KvCaB channel and (c) KCaS channel. Note that the KCaS channel is only active at the highest calcium concentration and is not dependent on voltage (although the voltage continues to set the driving force) when it is active.

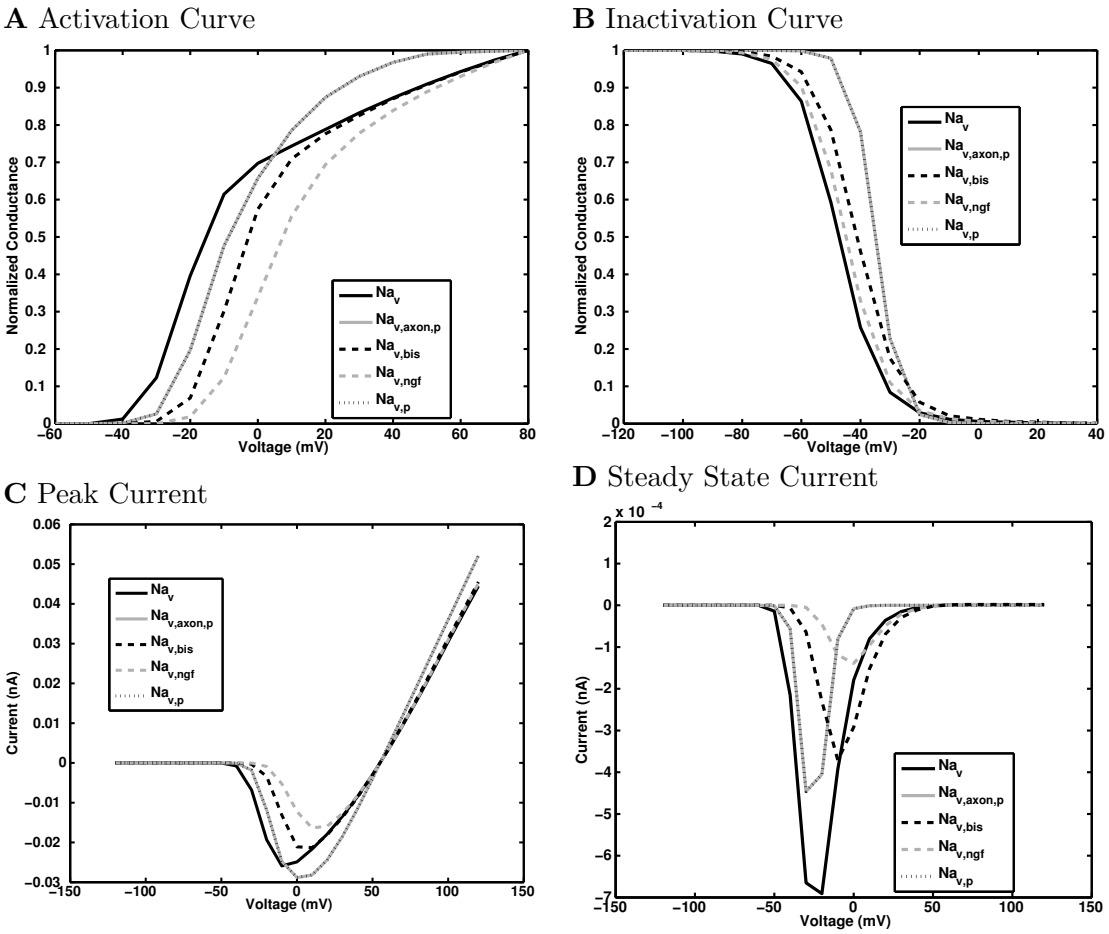

Appendix Figure 29: Sodium channel voltage dependence. The normalized conductance of the sodium channel is plotted as (a) a function of test voltage step to show activation and (b) as a function of holding voltage prior to the test step to show inactivation.

potential. Its conductance is inversely related to the membrane resistance.

Sodium channels

As with the potassium channels, we implemented variations of the fast activating, fast-inactivating sodium channel to enable each cell type to achieve a physiologically realistic threshold.

In Appendix Figure 29, the differing behavior of the sodium channels can be seen.

Na_v Channel Yuen and Durand (1991) originally developed this channel model, which was then modified by Aradi and Holmes (1999).

$Na_{v,bis}$ Channel We depolarized the threshold of the ch_Nav channel slightly, to better fit the bistratified cell behavior. Additionally, the voltage dependence of its activation has been shifted by -5 mV and inactivation by -3 mV. The coefficients have also been adjusted.

$Na_{v,cck}$ Channel This channel is modified from ch_Nav to have a higher threshold and a slow inactivation component to help realize the spike adaptation observed in experimental CCK+ cells. The voltage dependence of its activation has been shifted by -1 mV and its coefficients have been adjusted as well.

$Na_{v,ngf}$ Channel We modified this channel from ch_Nav, giving it a much higher threshold suitable for neurogliaform family cells. We offset its activation and inactivation voltage dependences have been offset by about -19 mV, and the coefficients have been slightly modified as well.

$Na_{v,cck}$ Channel We modified this channel from the ch_Nav model to have slightly different kinetics, mainly adjusting the coefficients (with only minor adjustments to the voltage dependence) to achieve more realistic CCK+ cell behavior.

$Na_{v,p}$ Channel Migliore et al. (1999) developed this channel, using it in their pyramidal cell model that we incorporated into our model Poolos et al. (2002). We only implemented the fast inactivating option of this channel, though a slow option was also available in the original implementation Poolos et al. (2002).

E Ion Channel Equations

For each ion channel, the equations used to compute the conductance are laid out below, with the following conventions:

- I_{ion} gives the specific current/area through the channels (of that type) within a small area of the membrane; it is multiplied by the area of the neuron section it covers to arrive at a total current estimate.
- E_{ion} gives the reversal potential of the channel
- The ions flowing through HCN and leak channels (usually a combination of sodium and potassium) are not explicitly specified in the code, so instead they are denoted with an H or *leak*.
- The units of variables and quantities are listed to their right in blue text
- T ^oC = temperature of model, 34^oC in this network
- T K = temperature of model converted to kelvins, $307.15K$ in this network (or $307.16K$ in some channels that convert the temperature differently).
- $g_{max}\frac{nS}{cm^2}$ = max. conductance, set when cell is defined
- dt ms = time step
- $t_{inc}\ ms = -dt\ ms * q_{10}$
- v mV = membrane potential local to the ion channel
- F kC = $96.487\frac{kC}{mol}$ (Faraday's constant)
- Temperature may be listed with units of Celsius (^oC) or units of kelvin (K) depending on what was used in the original code equation. For equations in this appendix section listing units of kelvin, the equation has been simplified so as not to show the conversion of temperature from units of Celsius to kelvin, even though this conversion takes place explicitly in the equation of the code file itself. Ex: equations in the code files including the term $273.15 + T$ (or $273.16 + T$ if converting relative to the freezing point of water rather than the more correct triple point

of water), representing the conversion from Celsius to kelvin ($1K - 1^oC = 273.15$ degrees), are instead displayed with TK in the equations of this section.

- The universal gas constant R, commonly listed in units of Joules per K*mol, is listed here in the alternative units of Coulomb * Volt per K*mol ($CVK^{-1}mol^{-1}$) to be consistent with the units used for the other terms in the equations.

Unless otherwise specified, for each channel, the temperature dependence can be given by:

$$q_{10} = 3^{\frac{T-34\ ^oC}{10\ ^oC}} \tag{4}$$

The equations specific to each channel are given below. For each channel, first any equations for constants, which only need to be solved once, are listed. Next, equations that need to be solved each time step are listed. Because of the way the NEURON simulator works, some equations may even be solved multiple times per time step. Also, at each instance of the ion channel (at each point within each section of the cell where the ion channel is inserted), the equations need to be solved again.

CavL

The following equations are solved each time step of simulation, as explained above, using the membrane potential v in the section of the membrane where the ion channel is located:

$$g\ \frac{S}{cm^2} = g_{max}\ \frac{S}{cm^2} * m^2 * h \tag{5}$$

$$I_L\ \frac{mA}{cm^2} = g\ \frac{S}{cm^2} * ghk(v\ mV, [Ca^{2+}]_i\ mM, [Ca^{2+}]_o\ mM) \tag{6}$$

The activation of channel conductance is represented by m (v mVoltage-dependent activation) and h (calcium-dependent activation). The driving force through the channel, ghk, is calculated using the Goldman-Hodgkin-Katz (GHK) equation. The values of ghk, m and h are also solved each time step, by calculating the following equations.

For ghk:

$$f\ mV = \frac{\frac{25\ mV}{293.15\ K} * T\ K}{2} \tag{7}$$

$$ghk\ mV = -f\ mV * \left(1 - \left(\frac{[Ca^{2+}]_i\ mM}{[Ca^{2+}]_o\ mM}\right) * exp\left(\frac{v\ mV}{f\ mV}\right)\right) * \frac{\frac{v\ mV}{f\ mV}}{exp(\frac{v\ mV}{f\ mV}) - 1} \tag{8}$$

For m:

$$\alpha\ ms^{-1} = \frac{15.69\ ms^{-1} * (-1.0 * v + 81.5\ mV)}{exp\left(\frac{-1.0 * v + 81.5\ mV}{10.0\ mV}\right) - 1.0} \tag{9}$$

$$\beta\ ms^{-1} = 0.29\ ms^{-1} * exp\left(\frac{-v}{10.86\ mV}\right) \tag{10}$$

$$\tau_m\ ms = \frac{1}{(\alpha\ ms^{-1} + \beta\ ms^{-1})} \tag{11}$$

$$m_\infty = \alpha\ ms^{-1} * \tau_m\ ms \tag{12}$$

$$\frac{dm}{dt\ ms} = \frac{m_\infty - m}{\tau_m\ ms} \tag{13}$$

For h:

$$h = \frac{0.001\ mM}{0.001\ mM + [Ca^{2+}]_i\ mM} \tag{14}$$

CavN

The following equations are solved each time step:

$$g\ \frac{S}{cm^2} = g_{max}\ \frac{S}{cm^2} * c^2 * d \tag{15}$$

$$I_{Ca}\ \frac{mA}{cm^2} = g\ \frac{S}{cm^2} * (v\ mV - E_{Ca}\ mV) \tag{16}$$

The values of c and d are also solved each time step, by calculating the following equations:

$$\alpha_c \; ms^{-1} = -0.19 \; ms^{-1} * \frac{v \; mV - 19.88 \; mV}{exp(\frac{v \; mV - 19.88 \; mV}{10 \; mV}) - 1} \tag{17}$$

$$\beta_c \; ms^{-1} = 0.046 \; ms^{-1} * exp\left(\frac{-v}{20.73 \; mV}\right) \tag{18}$$

$$\tau_c \; ms = \frac{1}{\alpha_c \; ms^{-1} + \beta_c \; ms^{-1}} \tag{19}$$

$$c_\infty = \frac{\alpha_c \; ms^{-1}}{\alpha_c \; ms^{-1} + \beta_c \; ms^{-1}} \tag{20}$$

$$\alpha_d \; ms^{-1} = 0.00016 \; ms^{-1} * exp\left(\frac{-v}{48.4 \; mV}\right) \tag{21}$$

$$\beta_d \; ms^{-1} = \frac{1}{exp\left(\frac{-v + 39 \; mV}{10 \; mV}\right) + 1} \tag{22}$$

$$\tau_d \; ms = \frac{1}{\alpha_d \; ms^{-1} + \beta_d \; ms^{-1}} \tag{23}$$

$$d_\infty = \frac{\alpha_d \; ms^{-1}}{\alpha_d \; ms^{-1} + \beta_d \; ms^{-1}} \tag{24}$$

$$c_{exp} = 1 - exp\left(\frac{t_{inc} \; ms}{\tau_c \; ms}\right), \qquad d_{exp} = 1 - exp\left(\frac{t_{inc} \; ms}{\tau_d \; ms}\right) \tag{25}$$

$$c = c + c_{exp} * (c_\infty - c), \qquad d = d + d_{exp} * (d_\infty - d) \tag{26}$$

HCN

Since the HCN channel conducts a mixture of sodium and potassium, the reversal potential E_H is set to lie between their reversal potentials, usually around -30 mV. The following equations are solved

each time step:

$$g\ \frac{S}{cm^2} = g_{max}\ \frac{S}{cm^2} * h^2 \tag{27}$$

$$I_H\ \frac{mA}{cm^2} = g\ \frac{S}{cm^2} * (v\ mV - E_H\ mV) \tag{28}$$

The value of h is also solved each time step, by calculating the following equations:

$$\tau_{slow}\ ms = \left(80 * 1.5\ ms + \frac{.75 * 172.7\ ms}{1 + exp(\frac{-(v\ mV + 59.3\ mV)}{-0.83\ mV})} \right) * \frac{1}{q_{10}} \tag{29}$$

$$h_\infty = \frac{1}{1 + exp\left(\frac{v\ mV + 91\ mV}{10\ mV}\right)} \tag{30}$$

$$\frac{dh}{dt\ ms} = \frac{h_\infty - h}{\tau_{slow}\ ms} \tag{31}$$

HCNolm

Since the HCN channel conducts a mixture of sodium and potassium, the reversal potential E_H is set to lie between their reversal potentials, usually around -30 mV. The following equations are solved each time step of simulation:

$$g\ \frac{S}{cm^2} = g_{max}\ \frac{S}{cm^2} * r \tag{32}$$

$$I_H\ \frac{mA}{cm^2} = g\ \frac{S}{cm^2} * (v\ mV - E_H\ mV) \tag{33}$$

The value of r is also solved each time, by calculating the following equations:

$$r_\infty = \frac{1}{1 + exp\left(\frac{v\ mV + 84.1\ mV}{10.2\ mV}\right)} \tag{34}$$

$$\tau_r = 100\ ms + \frac{1\ ms}{exp(-17.9\ mV - 0.116 * v\ mV) + exp(-1.84\ mV + 0.09 * v\ mV)} \tag{35}$$

$$r_{exp} = 1 - exp\left(\frac{-dt\ ms}{\tau_r\ ms}\right) \tag{36}$$

$$\frac{dr}{dt\ ms} = \frac{r_\infty - r}{\tau_r\ ms} \tag{37}$$

HCNp

A different temperature dependence was calculated for this channel than the default calculation specified at the beginning of the section:

$$q_t = 4.5^{\frac{T - 33\ ^oC}{10\ ^oC}} \tag{38}$$

As with the other HCN channels, the reversal potential E_H was set to lie between the sodium and potassium reversal potentials, around -30 mV. Then, the following equations are solved each time step:

$$g\ \frac{S}{cm^2} = g_{max}\ \frac{S}{cm^2} * l \tag{39}$$

$$I_H\ \frac{mA}{cm^2} = g\ \frac{S}{cm^2} * (v\ mV - E_H\ mV) \tag{40}$$

The value of l is also solved each time step, by calculating the following equations:

$$\alpha = exp(0.0378\ mV^{-1} * 2.2 * (v\ mV + 75\ mV)) \tag{41}$$

$$\beta = exp(0.0378\ mV^{-1} * 2.2 * 0.4 * (v\ mV + 75\ mV)) \tag{42}$$

$$l_\infty = \frac{1}{1 + exp(0.0378\ mV^{-1} * 4 * (v\ mV + 90\ mV))} \tag{43}$$

$$\tau_l\ ms = \frac{\beta}{q_t * 0.011\ ms^{-1} * (1 + \alpha)} \tag{44}$$

$$\frac{dl}{dt\ ms} = \frac{l_\infty - l}{\tau_l\ ms} \tag{45}$$

KCaS

The following equations are solved each time step of simulation:

$$g\ \frac{S}{cm^2} = g_{max}\ \frac{S}{cm^2} * q^2 \tag{46}$$

$$I_K\ \frac{mA}{cm^2} = g\ \frac{S}{cm^2} * (v\ mV - E_K\ mV) \tag{47}$$

The value of q is also solved each time, by calculating the following equations:

$$\alpha_q\ ms^{-1} = 15\ mM^{-2} ms^{-1} * \left([Ca^{2+}]_i\ mM\right)^2 \tag{48}$$

$$\beta_q\ ms^{-1} = 0.00025\ ms^{-1} \tag{49}$$

$$\tau_q\ ms = \frac{1}{q_{10} * (\alpha_q\ ms^{-1} + \beta_q\ ms^{-1})} \tag{50}$$

$$q_\infty = \alpha_q\ ms^{-1} * \tau_q\ ms \tag{51}$$

$$q_{exp} = 1 - exp\left(\frac{-dt\ ms}{\tau_q\ ms}\right) \tag{52}$$

$$q = q + q_{exp} * (q_\infty - q) \tag{53}$$

Kdrfast

The following equations are solved each time step of simulation:

$$g \ \frac{S}{cm^2} = g_{max} \ \frac{S}{cm^2} * n^4 \tag{54}$$

$$I_K \ \frac{mA}{cm^2} = g \ \frac{S}{cm^2} * (v \ mV - E_K \ mV) \tag{55}$$

The value of n is also solved each time step, by calculating the following equations:

$$\alpha_n \ ms^{-1} = -0.07 \ ms^{-1} * \frac{v \ mV + 18 \ mV}{exp\left(\frac{v \ mV + 18 \ mV}{-6 \ mV}\right) - 1} \tag{56}$$

$$\beta_n \ ms^{-1} = 0.264 \ ms^{-1} * exp\left(\frac{v \ mV + 43 \ mV}{40 \ mV}\right) \tag{57}$$

$$\tau_n \ ms = \frac{1}{\alpha_n \ ms^{-1} + \beta_n \ ms^{-1}} \tag{58}$$

$$n_\infty = \frac{\alpha_n \ ms^{-1}}{\alpha_n \ ms^{-1} + \beta_n \ ms^{-1}} \tag{59}$$

$$n_{exp} = 1 - exp\left(\frac{t_{inc} \ ms}{\tau_n \ ms}\right) \tag{60}$$

$$n = n + n_{exp} * (n_\infty - n) \tag{61}$$

Kdrfastngf

The following equations are solved each time step of simulation:

$$g \ \frac{S}{cm^2} = g_{max} \ \frac{S}{cm^2} * n^4 \tag{62}$$

$$I_K \ \frac{mA}{cm^2} = g \ \frac{S}{cm^2} * (v \ mV - E_K \ mV) \tag{63}$$

The value of n is also solved each time, by calculating the following equations:

$$\alpha_n \ ms^{-1} = -0.07 \ ms^{-1} * \frac{v \ mV + 8 \ mV}{exp\left(\frac{v \ mV + 8 \ mV}{-6 \ mV}\right) - 1} \tag{64}$$

$$\beta_n \ ms^{-1} = 0.264 \ ms^{-1} * exp\left(\frac{v \ mV + 33 \ mV}{40 \ mV}\right) \tag{65}$$

$$\tau_n \ ms = \frac{1}{\alpha_n \ ms^{-1} + \beta_n \ ms^{-1}} \tag{66}$$

$$n_\infty = \frac{\alpha_n \ ms^{-1}}{\alpha_n \ ms^{-1} + \beta_n \ ms^{-1}} \tag{67}$$

$$n_{exp} = 1 - exp\left(\frac{t_{inc} \ ms}{\tau_n \ ms}\right) \tag{68}$$

$$n = n + n_{exp} * (n_\infty - n) \tag{69}$$

Kdrp

A different temperature dependence was implemented for this channel:

$$q_t = 1^{\frac{T - 24 \ ^oC}{10 \ ^oC}} \tag{70}$$

Then, the following equations are solved each time step:

$$g\ \frac{S}{cm^2} = g_{max}\ \frac{S}{cm^2} * n \tag{71}$$

$$I_K\ \frac{mA}{cm^2} = g\ \frac{S}{cm^2} * (v\ mV - E_K\ mV) \tag{72}$$

The values of n and l are also solved each time step, by calculating the following equations, where the ideal gas constant R is 8.315 $CVK^{-1}mol^{-1}$ and the conversion of Volts to milliVolts is given as 1.0e−3 VmV^{-1}:

$$n_\infty = \frac{1}{1 + exp\left(\frac{\text{1.0e−3 } VmV^{-1} * (-3) * (v\ mV - 13\ mV) * 9.648e4\ Cmol^{-1}}{8.315\ CVK^{-1}mol^{-1} * T\ K}\right)} \tag{73}$$

$$\tau_n\ ms = \frac{exp\left(\frac{\text{1.0e−3 } VmV^{-1} * (-3) * 0.7 * (v\ mV - 13\ mV) * 9.648e4\ Cmol^{-1}}{8.315\ CVK^{-1}mol^{-1} * T\ K}\right)}{q_t * 0.02\ ms^{-1} * \left(1 + exp\left(\frac{\text{1.0e−3 } VmV^{-1} * (-3) * (v\ mV - 13\ mV) * 9.648e4\ Cmol^{-1}}{8.315\ CVK^{-1}mol^{-1} * T\ K}\right)\right)} \tag{74}$$

$$\frac{dn}{dt\ ms} = \frac{n_\infty - n}{\tau_n\ ms} \tag{75}$$

Kdrslow

The following equations are solved each time step of simulation:

$$g\ \frac{S}{cm^2} = g_{max}\ \frac{S}{cm^2} * n^4 \tag{76}$$

$$I_K\ \frac{mA}{cm^2} = g\ \frac{S}{cm^2} * (v\ mV - E_K\ mV) \tag{77}$$

The value of n is also solved each time, by calculating the following equations:

$$\alpha_n \ ms^{-1} = -0.028 \ ms^{-1} mV^{-1} * \frac{v \ mV + 30 \ mV}{exp\left(\frac{v \ mV + 30 \ mV}{-6 \ mV}\right) - 1} \tag{78}$$

$$\beta_n \ ms^{-1} = 0.1056 \ ms^{-1} * exp\left(\frac{v \ mV + 55 \ mV}{40 \ mV}\right) \tag{79}$$

$$\tau_n \ ms = \frac{1}{\alpha_n \ ms^{-1} + \beta_n \ ms^{-1}} \tag{80}$$

$$n_\infty = \frac{\alpha_n \ ms^{-1}}{\alpha_n \ ms^{-1} + \beta_n \ ms^{-1}} \tag{81}$$

$$n_{exp} = 1 - exp\left(\frac{t_{inc} \ ms}{\tau_n \ ms}\right) \tag{82}$$

$$n = n + n_{exp} * (n_\infty - n) \tag{83}$$

KvA

A different temperature dependence was implemented for this channel:

$$q_{10} = 3^{\frac{T - 30 \ ^oC}{10 \ ^oC}} \tag{84}$$

Then, the following equations are solved each time step of simulation, for every section within the cell, using the membrane potential v in the section of the membrane where the ion channel is located.

$$g \ \frac{S}{cm^2} = g_{max} \ \frac{S}{cm^2} * n * l \tag{85}$$

$$I_A \ \frac{mA}{cm^2} = g \ \frac{S}{cm^2} * (v \ mV - E_K \ mV) \tag{86}$$

The values of n and l are also solved each time step, by calculating the following equations, where the ideal gas constant R is 8.315 $CVK^{-1}mol^{-1}$ and the conversion of Volts to milliVolts is given as 1.0e−3 VmV^{-1}:

$$n_\infty = \frac{1}{1 + exp\left(\frac{\text{1.0e−3 } VmV^{-1} * (-3) * (v\ mV + 33.6\ mV) * 9.648e4\ Cmol^{-1}}{8.315\ CVK^{-1}mol^{-1} * T\ K}\right)} \tag{87}$$

$$\tau_n\ ms = \frac{exp\left(\frac{\text{1.0e−3 } VmV^{-1} * (-3) * 0.6 * (v\ mV + 33.6\ mV) * 9.648e4\ Cmol^{-1}}{8.315\ CVK^{-1}mol^{-1} * T\ K}\right)}{q_{10} * 0.02\ ms^{-1} * \left(1 + exp\left(\frac{\text{1.0e−3 } VmV^{-1} * (-3) * (v\ mV + 33.6\ mV) * 9.648e4\ Cmol^{-1}}{8.315\ CVK^{-1}mol^{-1} * T\ K}\right)\right)} \tag{88}$$

$$l_\infty = \frac{1}{1 + exp\left(\frac{\text{1.0e−3 } VmV^{-1} * 4 * (v\ mV + 83\ mV) * 9.648e4\ Cmol^{-1}}{8.315\ CVK^{-1}mol^{-1} * T\ K}\right)} \tag{89}$$

$$\tau_l = \frac{exp\left(\frac{\text{1.0e−3 } VmV^{-1} * 4 * (v\ mV + 83\ mV) * 9.648e4\ Cmol^{-1}}{8.315\ CVK^{-1}mol^{-1} * T\ K}\right)}{q_{10} * 0.08\ ms^{-1} * \left(1 + exp\left(\frac{\text{1.0e−3 } VmV^{-1} * 4 * (v\ mV + 83\ mV) * 9.648e4\ Cmol^{-1}}{8.315\ CVK^{-1}mol^{-1} * T\ K}\right)\right)} \tag{90}$$

$$\frac{dn}{dt\ ms} = \frac{n_\infty - n}{\tau_n\ ms} \tag{91}$$

$$\frac{dl}{dt\ ms} = \frac{l_\infty - l}{\tau_l\ ms} \tag{92}$$

KvAdistp

This channel implemented a different temperature dependence than usual:

$$q_t = 3^{\frac{T - 24\ ^oC}{10\ ^oC}} \tag{93}$$

Then, the following equations are solved each time step of simulation, for every section within the cell, using the membrane potential v in the section of the membrane where the ion channel is located.

$$g \ \frac{S}{cm^2} = g_{max} \ \frac{S}{cm^2} * n * l \tag{94}$$

$$I_A \ \frac{mA}{cm^2} = g \ \frac{S}{cm^2} * (v \ mV - E_K \ mV) \tag{95}$$

The values of n and l are also solved each time, by calculating the following equations, where the ideal gas constant R is 8.315 $CVK^{-1}mol^{-1}$ and the conversion of Volts to milliVolts is given as 1.0e−3 VmV^{-1}:

$$\frac{dn}{dt \ ms} = \frac{n_\infty - n}{\tau_n \ ms} \tag{96}$$

$$\frac{dl}{dt \ ms} = \frac{l_\infty - l}{\tau_l \ ms} \tag{97}$$

$$\alpha_n = exp\left(\frac{1.0\text{e}{-3} \ VmV^{-1} * \left(\frac{-1}{1 + exp\left(\frac{v \ mV + 40 \ mV}{5 \ mV}\right)} - 1.8\right) * (v \ mV + 1 \ mV) * 9.648e4 \ Cmol^{-1}}{8.315 \ CVK^{-1}mol^{-1} * T \ K}\right) \tag{98}$$

$$\beta_n = exp\left(\frac{1.0\text{e}{-3} \ VmV^{-1} * \left(\frac{-1}{1 + exp\left(\frac{v \ mV + 40 \ mV}{5 \ mV}\right)} - 1.8\right) * 0.39 * (v \ mV + 1 \ mV) * 9.648e4 \ Cmol^{-1}}{8.315 \ CVK^{-1}mol^{-1} * T \ K}\right) \tag{99}$$

$$n_\infty = \frac{1}{1+\alpha_n} \tag{100}$$

$$\tau_n\ ms = \frac{\beta_n}{q_t * 0.1\ ms^{-1} * (1+\alpha_n)} \tag{101}$$

$$\alpha_l = exp\left(\frac{1.0\text{e}{-3}\ VmV^{-1} * 3 * (v\ mV + 56\ mV) * 9.648e4\ Cmol^{-1}}{8.315\ CVK^{-1}mol^{-1} * T\ K}\right) \tag{102}$$

$$l_\infty = \frac{1}{1+\alpha_l} \tag{103}$$

$$\tau_l\ ms = 0.26\ ms * mV^{-1} * (v\ mV + 50\ mV) \tag{104}$$

KvAngf

This channel used a different form of temperature dependence:

$$q_{10} = 3^{\frac{T-30\ ^oC}{10\ ^oC}} \tag{105}$$

The following equations are solved each time step of simulation, for every section within the cell, using the membrane potential v in the section of the membrane where the ion channel is located.

$$g\ \frac{S}{cm^2} = g_{max}\ \frac{S}{cm^2} * n * l \tag{106}$$

$$I_A\ \frac{mA}{cm^2} = g\ \frac{S}{cm^2} * (v\ mV - E_K\ mV) \tag{107}$$

The values of n and l are also solved each time, by calculating the following equations:

$$n_\infty = \frac{1}{1 + exp\left(\frac{\text{1.0e}{-3}\ VmV^{-1} * (-3) * (v\ mV + 23.6\ mV) * 9.648e4\ Cmol^{-1}}{8.315\ CVK^{-1}mol^{-1} * T\ K}\right)} \tag{108}$$

$$\tau_n\ ms = \frac{exp\left(\frac{\text{1.0e}{-3}\ VmV^{-1} * (-3) * 0.6 * (v\ mV + 23.6\ mV) * 9.648e4\ Cmol^{-1}}{8.315\ CVK^{-1}mol^{-1} * T\ K}\right)}{q_{10} * 0.02\ ms^{-1} * \left(1 + exp\left(\frac{\text{1.0e}{-3}\ VmV^{-1} * (-3) * (v\ mV + 23.6\ mV) * 9.648e4\ Cmol^{-1}}{8.315\ CVK^{-1}mol^{-1} * T\ K}\right)\right)} \tag{109}$$

$$l_\infty = \frac{1}{1 + exp\left(\frac{\text{1.0e}{-3}\ VmV^{-1} * 4 * (v\ mV + 83\ mV) * 9.648e4\ Cmol^{-1}}{8.315\ CVK^{-1}mol^{-1} * T\ K}\right)} \tag{110}$$

$$\tau_l\ ms = \frac{exp\left(\frac{\text{1.0e}{-3}\ VmV^{-1} * 4 * (v\ mV + 83\ mV) * 9.648e4\ Cmol^{-1}}{8.315\ CVK^{-1}mol^{-1} * T\ K}\right)}{q_{10} * 0.08\ ms^{-1} * \left(1 + exp\left(\frac{\text{1.0e}{-3}\ VmV^{-1} * 4 * (v\ mV + 83\ mV) * 9.648e4\ Cmol^{-1}}{8.315\ CVK^{-1}mol^{-1} * T\ K}\right)\right)} \tag{111}$$

$$\frac{dn}{dt\ ms} = \frac{n_\infty - n}{\tau_n\ ms} \tag{112}$$

$$\frac{dl}{dt\ ms} = \frac{l_\infty - l}{\tau_l\ ms} \tag{113}$$

KvAolm

The following equations are solved each time step of simulation, for every section within the cell, using the membrane potential v in the section of the membrane where the ion channel is located:

$$g\ \frac{S}{cm^2} = g_{max}\ \frac{S}{cm^2} * a * b \tag{114}$$

$$I_A\ \frac{mA}{cm^2} = g\ \frac{S}{cm^2} * (v\ mV - E_K\ mV) \tag{115}$$

The values of a and b are also solved each time, by calculating the following equations:

$$\tau_a \ ms = 5 \ ms \tag{116}$$

$$a_\infty = \frac{1}{1 + exp\left(\frac{-(v \ mV + 14 \ mV)}{16.6 \ mV}\right)} \tag{117}$$

$$\alpha_b \ ms^{-1} = \frac{0.000009 \ ms^{-1}}{exp\left(\frac{v \ mV - 26 \ mV}{18.5 \ mV}\right)} \tag{118}$$

$$\beta_b \ ms^{-1} = \frac{0.014 \ ms^{-1}}{exp\left(\frac{v \ mV + 70 \ mV}{-11 \ mV}\right) + 0.2} \tag{119}$$

$$\tau_b \ ms = \frac{1}{\alpha_b \ ms^{-1} + \beta_b \ ms^{-1}} \tag{120}$$

$$b_\infty = \frac{1}{1 + exp\left(\frac{v \ mV + 71 \ mV}{7.3 \ mV}\right)} \tag{121}$$

$$a_{exp} = 1 - exp\left(\frac{-dt \ ms}{\tau_a \ ms}\right), \qquad b_{exp} = 1 - exp\left(\frac{-dt \ ms}{\tau_b \ ms}\right) \tag{122}$$

$$a = a + a_{exp} * (a_\infty - a), \qquad b = b + b_{exp} * (b_\infty - b) \tag{123}$$

KvAproxp

This channel implemented a different temperature dependence:

$$q_{10} = 3^{\frac{T - 24 \ ^oC}{10 \ ^oC}} \tag{124}$$

Then, the following equations are solved each time step:

$$g\ \frac{S}{cm^2} = g_{max}\ \frac{S}{cm^2} * n * l \tag{125}$$

$$I_A\ \frac{mA}{cm^2} = g\ \frac{S}{cm^2} * (v\ mV - E_K\ mV) \tag{126}$$

The values of n and l are also solved each time step, by calculating the following equations, where the ideal gas constant R is 8.315 $CVK^{-1}mol^{-1}$ and the conversion of Volts to milliVolts is given as 1.0e−3 VmV^{-1}:

$$\frac{dn}{dt\ ms} = \frac{n_\infty - n}{\tau_n\ ms} \tag{127}$$

$$\frac{dl}{dt\ ms} = \frac{l_\infty - l}{\tau_l\ ms} \tag{128}$$

$$\alpha_n = exp\left(\frac{1.0\text{e}{-3}\ VmV^{-1} * \left(\frac{-1}{1 + exp\left(\frac{v\ mV + 40\ mV}{5\ mV}\right)} - 1.5\right) * (v\ mV - 11\ mV) * 9.648e4\ Cmol^{-1}}{8.315\ CVK^{-1}mol^{-1} * T\ K}\right) \tag{129}$$

$$\beta_n = exp\left(\frac{1.0\text{e}{-3}\ VmV^{-1} * \left(\frac{-1}{1 + exp\left(\frac{v\ mV + 40\ mV}{5\ mV}\right)} - 1.5\right) * 0.55 * (v\ mV - 11\ mV) * 9.648e4\ Cmol^{-1}}{8.315\ CVK^{-1}mol^{-1} * T\ K}\right) \tag{130}$$

$$n_\infty = \frac{1}{1+\alpha_n} \tag{131}$$

$$\tau_n\ ms = \frac{\beta_n}{q_t * 0.05\ ms^{-1} * (1+\alpha_n)} \tag{132}$$

$$\alpha_l = exp\left(\frac{1.0\text{e}{-3}\ VmV^{-1} * 3 * (v\ mV + 56\ mV) * 9.648e4\ Cmol^{-1}}{8.315\ CVK^{-1}mol^{-1} * T\ K}\right) \tag{133}$$

$$l_\infty = \frac{1}{1+\alpha_l} \tag{134}$$

$$\tau_l\ ms = 0.26\ ms * mV^{-1} * (v\ mV + 50\ mV) \tag{135}$$

KvCaB

The following equations are solved each time step, where the ideal gas constant R is 8.313424 $CVK^{-1}mol^{-1}$ and F is Faraday's constant, $9.648e4\ Cmol^{-1}$. In the code for this channel, F is reported in units of kC rather than C, but it is always multiplied by the voltage in units of mV instead of V, so the conversion is implicit ($mV * kC = V * C$).

$$g\ \frac{S}{cm^2} = g_{max}\ \frac{S}{cm^2} * n \tag{136}$$

$$I_K\ \frac{mA}{cm^2} = g\ \frac{S}{cm^2} * (v\ mV - E_K\ mV) \tag{137}$$

The value of n is also solved each time, by calculating the following equations that depend on voltage and internal calcium concentration:

$$\alpha_n\ ms^{-1} = [Ca^{2+}]_i\ mM * \frac{0.28\ ms^{-1}}{[Ca^{2+}]_i\ mM + \left(0.48\text{e}{-3}\ mM * exp\left(\frac{-2 * 0.84 * F\ Cmol^{-1} * v\ mV}{R\ CVK^{-1}mol^{-1} * T\ K}\right)\right)} \tag{138}$$

$$\beta_n\ ms^{-1} = \frac{0.48\ ms^{-1}}{1 + \frac{[Ca^{2+}]_i\ mM}{0.13\text{e}{-6}\ mM * exp\left(\frac{-2 * F\ Cmol^{-1} * v\ mV}{R\ CVK^{-1}mol^{-1} * T\ K}\right)}} \tag{139}$$

$$\tau_n\ ms = \frac{1}{\alpha_n\ ms^{-1} + \beta_n\ ms^{-1}} \tag{140}$$

$$n_\infty = \alpha_n\ ms^{-1} * \tau_n\ ms \tag{141}$$

$$n_{exp} = 1 - exp\left(\frac{t_{inc}\ ms}{\tau_n\ ms}\right) \tag{142}$$

$$n = n + n_{exp} * (n_\infty - n) \tag{143}$$

KvGroup

The following equations are solved each time step of simulation:

$$g\ \frac{S}{cm^2} = g_{max}\ \frac{S}{cm^2} * n \tag{144}$$

$$I_{Group}\ \frac{mA}{cm^2} = g\ \frac{S}{cm^2} * (v\ mV - E_K\ mV) \tag{145}$$

The value of n is also solved each time, by calculating the following equations:

$$\alpha_n \ ms^{-1} = 0.0189324 \ ms^{-1} * \frac{-(v \ mV - 4.18371 \ mV)}{exp\left(\frac{-(v \ mV - 4.18371 \ mV)}{6.42606 \ mV}\right) - 1} \tag{146}$$

$$\beta_n \ ms^{-1} = 0.015857 \ ms^{-1} * exp\left(\frac{-v \ mV}{25.4834 \ mV}\right) \tag{147}$$

$$\tau_n \ ms = \frac{1}{\alpha_n \ ms^{-1} + \beta_n \ ms^{-1}} \tag{148}$$

$$n_\infty = \frac{\alpha_n \ ms^{-1}}{\alpha_n \ ms^{-1} + \beta_n \ ms^{-1}} \tag{149}$$

$$n_{exp} = 1 - exp\left(\frac{t_{inc} \ ms}{\tau_n \ ms}\right) \tag{150}$$

$$n = n + n_{exp} * (n_\infty - n) \tag{151}$$

KvM

This channel used a different temperature dependence than usual:

$$q_{10} = 5^{\frac{T - 35 \ ^oC}{10 \ ^oC}} \tag{152}$$

Then, the following equations are solved each time step of simulation, for every section within the cell, using the membrane potential v in the section of the membrane where the ion channel is located.

$$g \ \frac{S}{cm^2} = g_{max} \ \frac{S}{cm^2} * m \tag{153}$$

$$I_M \ \frac{mA}{cm^2} = g \ \frac{S}{cm^2} * (v \ mV - E_K \ mV) \tag{154}$$

The value of m is also solved each time, by calculating the following equations:

$$m_\infty = \frac{1}{1 + exp\left(\frac{v\ mV + 40\ mV}{-10\ mV}\right)} \tag{155}$$

$$\tau_m\ ms = 120\ ms + \frac{exp(0.0378 * 7 * .4 * (v\ mV + 42\ mV))}{0.009\ ms^{-1} * (1 + exp(0.0378 * 7 * (v\ mV + 42\ mV)))} \tag{156}$$

$$\frac{dm}{dt\ ms} = \frac{m_\infty - m}{\tau_m\ ms} \tag{157}$$

leak

The following equations are solved each time step of simulation, for every section within the cell, using the membrane potential v in the section of the membrane where the ion channel is located. Since the leak channel conducts mostly potassium, the reversal potential E_{leak} is set close to the potassium reversal potential E_K.

$$g\ \frac{S}{cm^2} = g_{max}\ \frac{S}{cm^2} \tag{158}$$

$$I_{leak}\ \frac{mA}{cm^2} = g\ \frac{S}{cm^2} * (v\ mV - E_{leak}\ mV) \tag{159}$$

Nav

The following equations are solved each time step:

$$g\ \frac{S}{cm^2} = g_{max}\ \frac{S}{cm^2} * m^3 * h \tag{160}$$

$$I_{Na}\ \frac{mA}{cm^2} = g\ \frac{S}{cm^2} * (v\ mV - E_{Na}\ mV) \tag{161}$$

The values of m and h are also solved each time, by calculating the following equations:

$$\alpha_m \ ms^{-1} = -0.3 \ ms^{-1} * \frac{v \ mV + 43 \ mV}{exp\left(\frac{v \ mV + 43 \ mV}{-5 \ mV}\right) - 1} \tag{162}$$

$$\beta_m \ ms^{-1} = 0.3 \ ms^{-1} * \frac{v \ mV + 15 \ mV}{exp\left(\frac{v \ mV + 15 \ mV}{5 \ mV}\right) - 1} \tag{163}$$

$$\tau_m \ ms = \frac{1}{\alpha_m \ ms^{-1} + \beta_m \ ms^{-1}} \tag{164}$$

$$m_\infty = \frac{\alpha_m \ ms^{-1}}{\alpha_m \ ms^{-1} + \beta_m \ ms^{-1}} \tag{165}$$

$$\alpha_h \ ms^{-1} = \frac{0.23 \ ms^{-1}}{exp\left(\frac{v \ mV + 65 \ mV}{20 \ mV}\right)} \tag{166}$$

$$\beta_h \ ms^{-1} = \frac{3.33 \ ms^{-1}}{1 + exp\left(\frac{v \ mV + 12.5 \ mV}{-10 \ mV}\right)} \tag{167}$$

$$\tau_h \ ms = \frac{1}{\alpha_h \ ms^{-1} + \beta_h \ ms^{-1}} \tag{168}$$

$$h_\infty = \frac{\alpha_h \ ms^{-1}}{\alpha_h \ ms^{-1} + \beta_h \ ms^{-1}} \tag{169}$$

$$m_{exp} = 1 - exp\left(\frac{t_{inc} \ ms}{\tau_m \ ms}\right), \qquad h_{exp} = 1 - exp\left(\frac{t_{inc} \ ms}{\tau_h \ ms}\right) \tag{170}$$

$$m = m + m_{exp} * (m_\infty - m), \qquad h = h + h_{exp} * (h_\infty - h) \tag{171}$$

Navaxonp

Within the ion channel, these equations solve to constants:

$$q_t = 1^{\frac{T-24\ ^oC}{10\ ^oC}} \tag{172}$$

Then, the following equations are solved each time step:

$$g\ \frac{S}{cm^2} = g_{max}\ \frac{S}{cm^2} * m^3 * h \tag{173}$$

$$I_{Na}\ \frac{mA}{cm^2} = g\ \frac{S}{cm^2} * (v\ mV - E_{Na}\ mV) \tag{174}$$

The values of m and h are also solved each time step, by calculating the following equations:

$$InAct = 1 \tag{175}$$

$$\frac{dm}{dt\ ms} = \frac{m_\infty - m}{\tau_m\ ms} \tag{176}$$

$$\frac{dh}{dt\ ms} = \frac{h_\infty - h}{\tau_h\ ms} \tag{177}$$

$$\alpha_m\ ms^{-1} = \frac{Ra\ ms^{-1} * (v\ mV + 15\ mV)}{1 - exp\left(\frac{-(v\ mV + 15\ mV)}{7.2\ mV}\right)} \tag{178}$$

$$\beta_m\ ms^{-1} = \frac{Rb\ ms^{-1} * (-v - 15\ mV)}{1 - exp\left(\frac{-(-v - 15\ mV)}{7.2\ mV}\right)} \tag{179}$$

$$\tau_m\ ms = \frac{1}{(\alpha_m\ ms^{-1} + \beta_m\ ms^{-1}) * q_t} \tag{180}$$

$$m_\infty = \frac{\alpha_m\ ms^{-1}}{\alpha_m\ ms^{-1} + \beta_m\ ms^{-1}} \tag{181}$$

$$\alpha_h = \frac{Rd\ ms^{-1} * (v\ mV + 30\ mV)}{1 - exp\left(\frac{-(v\ mV + 30\ mV)}{1.5\ mV}\right)} \tag{182}$$

$$\beta_h = \frac{Rg\ ms^{-1} * (-v - 30\ mV)}{1 - exp\left(\frac{-(-v - 30\ mV)}{1.5\ mV}\right)} \tag{183}$$

$$\tau_h\ ms = \frac{1}{(\alpha_h\ ms^{-1} + \beta_h\ ms^{-1}) * q_t} \tag{184}$$

$$h_\infty = \frac{1}{1 + exp\left(\frac{v\ mV + 35\ mV}{4\ mV}\right)} \tag{185}$$

$$\tag{186}$$

Navbis

The following equations are solved each time step:

$$g\ \frac{S}{cm^2} = g_{max}\ \frac{S}{cm^2} * m^3 * h \tag{187}$$

$$I_{Na}\ \frac{mA}{cm^2} = g\ \frac{S}{cm^2} * (v\ mV - E_{Na}\ mV) \tag{188}$$

The values of m and h are also solved each time, by calculating the following equations:

$$\alpha_m\ ms^{-1} = -0.2\ ms^{-1} * \frac{v\ mV + 38\ mV}{exp\left(\frac{v\ mV + 38\ mV}{-5\ mV}\right) - 1} \tag{189}$$

$$\beta_m\ ms^{-1} = 0.5\ ms^{-1} * \frac{v\ mV + 10\ mV}{exp\left(\frac{v\ mV + 10\ mV}{5\ mV}\right) - 1} \tag{190}$$

$$\tau_m\ ms = \frac{1}{\alpha_m\ ms^{-1} + \beta_m\ ms^{-1}} \tag{191}$$

$$m_\infty = \frac{\alpha_m\ ms^{-1}}{\alpha_m\ ms^{-1} + \beta_m\ ms^{-1}} \tag{192}$$

$$\alpha_h \ ms^{-1} = \frac{0.23 \ ms^{-1}}{exp\left(\frac{v \ mV + 62 \ mV}{20 \ mV}\right)} \tag{193}$$

$$\beta_h \ ms^{-1} = \frac{2 \ ms^{-1}}{1 + exp\left(\frac{v \ mV + 9.5 \ mV}{-10 \ mV}\right)} \tag{194}$$

$$\tau_h \ ms = \frac{1}{\alpha_h \ ms^{-1} + \beta_h \ ms^{-1}} \tag{195}$$

$$h_\infty = \frac{\alpha_h \ ms^{-1}}{\alpha_h \ ms^{-1} + \beta_h \ ms^{-1}} \tag{196}$$

$$m_{exp} = 1 - exp\left(\frac{t_{inc} \ ms}{\tau_m \ ms}\right), \qquad h_{exp} = 1 - exp\left(\frac{t_{inc} \ ms}{\tau_h \ ms}\right) \tag{197}$$

$$m = m + m_{exp} * (m_\infty - m), \qquad h = h + h_{exp} * (h_\infty - h) \tag{198}$$

Navcck

The following equations are solved each time step:

$$g \ \frac{S}{cm^2} = g_{max} \ \frac{S}{cm^2} * m^3 * h * s \tag{199}$$

$$I_{Na} \ \frac{mA}{cm^2} = g \ \frac{S}{cm^2} * (v \ mV - E_{Na} \ mV) \tag{200}$$

The values of m, h (fast inactivation) and s (slow inactivation) are also solved each time, by calculating the following equations:

$$\alpha_m \ ms^{-1} = -0.5 \ ms^{-1} * \frac{v \ mV + 42 \ mV}{exp\left(\frac{v \ mV + 42 \ mV}{-5 \ mV}\right) - 1} \tag{201}$$

$$\beta_m \ ms^{-1} = 0.3 \ ms^{-1} * \frac{v \ mV + 13 \ mV}{exp\left(\frac{v \ mV + 13 \ mV}{5 \ mV}\right) - 1} \tag{202}$$

$$\tau_m \ ms = \frac{1}{\alpha_m \ ms^{-1} + \beta_m \ ms^{-1}} \tag{203}$$

$$m_\infty = \frac{\alpha_m \ ms^{-1}}{\alpha_m \ ms^{-1} + \beta_m \ ms^{-1}} \tag{204}$$

$$\alpha_h \ ms^{-1} = \frac{0.6 \ ms^{-1}}{exp\left(\frac{v \ mV + 65 \ mV}{20 \ mV}\right)} \tag{205}$$

$$\beta_h \ ms^{-1} = \frac{1.31 \ ms^{-1}}{1 + exp\left(\frac{v \ mV + 12.5 \ mV}{-10 \ mV}\right)} \tag{206}$$

$$\tau_h \ ms = \frac{1}{\alpha_h \ ms^{-1} + \beta_h \ ms^{-1}} \tag{207}$$

$$h_\infty = \frac{\alpha_h \ ms^{-1}}{\alpha_h \ ms^{-1} + \beta_h \ ms^{-1}} \tag{208}$$

$$\alpha_s \ ms^{-1} = \frac{0.003 \ ms^{-1}}{exp\left(\frac{v \ mV + 45 \ mV}{6 \ mV}\right)} \tag{209}$$

$$\beta_s \ ms^{-1} = \frac{0.005 \ ms^{-1}}{1 + exp\left(\frac{v \ mV + 35 \ mV}{-20 \ mV}\right)} \tag{210}$$

$$\tau_s \ ms = \frac{1}{\alpha_s \ ms^{-1} + \beta_s \ ms^{-1}} \tag{211}$$

$$s_\infty = \frac{\alpha_s \ ms^{-1}}{\alpha_s \ ms^{-1} + \beta_s \ ms^{-1}} \tag{212}$$

$$m_{exp} = 1 - exp\left(\frac{t_{inc}\ ms}{\tau_m\ ms}\right), \qquad h_{exp} = 1 - exp\left(\frac{t_{inc}\ ms}{\tau_h\ ms}\right), \qquad s_{exp} = 1 - exp\left(\frac{t_{inc}\ ms}{\tau_s\ ms}\right) \tag{213}$$

$$m = m + m_{exp} * (m_\infty - m), \qquad h = h + h_{exp} * (h_\infty - h), \qquad s = s + s_{exp} * (s_\infty - s) \tag{214}$$

Navngf

The following equations are solved each time step:

$$g\ \frac{S}{cm^2} = g_{max}\ \frac{S}{cm^2} * m^3 * h \tag{215}$$

$$I_{Na}\ \frac{mA}{cm^2} = g\ \frac{S}{cm^2} * (v\ mV - E_{Na}\ mV) \tag{216}$$

The values of m and h are also solved each time, by calculating the following equations:

$$\alpha_m\ ms^{-1} = -0.34133\ ms^{-1} * \frac{v\ mV + 24\ mV}{exp\left(\frac{v\ mV + 24\ mV}{-5\ mV}\right) - 1} \tag{217}$$

$$\beta_m\ ms^{-1} = 0.28483\ ms^{-1} * \frac{v\ mV - 4\ mV}{exp\left(\frac{v\ mV - 4\ mV}{5\ mV}\right) - 1} \tag{218}$$

$$\tau_m\ ms = \frac{1}{\alpha_m\ ms^{-1} + \beta_m\ ms^{-1}} \tag{219}$$

$$m_\infty = \frac{\alpha_m\ ms^{-1}}{\alpha_m\ ms^{-1} + \beta_m\ ms^{-1}} \tag{220}$$

$$\alpha_h \ ms^{-1} = \frac{0.29648 \ ms^{-1}}{exp\left(\frac{v \ mV + 64.4184 \ mV}{20 \ mV}\right)} \tag{221}$$

$$\beta_h \ ms^{-1} = \frac{3.0931 \ ms^{-1}}{1 + exp\left(\frac{v \ mV + 12.1463 \ mV}{-10 \ mV}\right)} \tag{222}$$

$$\tau_h \ ms = \frac{1}{\alpha_h \ ms^{-1} + \beta_h \ ms^{-1}} \tag{223}$$

$$h_\infty = \frac{\alpha_h \ ms^{-1}}{\alpha_h \ ms^{-1} + \beta_h \ ms^{-1}} \tag{224}$$

$$m_{exp} = 1 - exp\left(\frac{t_{inc} \ ms}{\tau_m \ ms}\right), \qquad h_{exp} = 1 - exp\left(\frac{t_{inc} \ ms}{\tau_h \ ms}\right) \tag{225}$$

$$m = m + m_{exp} * (m_\infty - m), \qquad h = h + h_{exp} * (h_\infty - h) \tag{226}$$

Navp

This channel model has a different dependence on temperature:

$$q_t = 1^{\frac{T - 24 \ ^oC}{10 \ ^oC}} \tag{227}$$

Then, the following equations are solved each time step:

$$g \ \frac{S}{cm^2} = g_{max} \ \frac{S}{cm^2} * m^3 * h * s \tag{228}$$

$$I_{Na} \ \frac{mA}{cm^2} = g \ \frac{S}{cm^2} * (v \ mV - E_{Na} \ mV) \tag{229}$$

The values of m, h, and s are also solved each time step, by calculating the following equations, where the ideal gas constant R is 8.315 $CVK^{-1}mol^{-1}$ and the conversion of Volts to milliVolts is given as 1.0e−3 VmV^{-1}:

$$InAct = 1 \tag{230}$$

$$\frac{dm}{dt\ ms} = \frac{m_\infty - m}{\tau_m\ ms} \tag{231}$$

$$\frac{dh}{dt\ ms} = \frac{h_\infty - h}{\tau_h\ ms} \tag{232}$$

$$\frac{ds}{dt\ ms} = \frac{s_\infty - s}{\tau_s\ ms} \tag{233}$$

$$\alpha_m\ ms^{-1} = \frac{Ra\ ms^{-1} * (v\ mV - (-15)\ mV)}{1 - exp\left(\frac{-(v\ mV - (-15)\ mV)}{7.2\ mV}\right)} \tag{234}$$

$$\beta_m\ ms^{-1} = \frac{Rb\ ms^{-1} * (-v - (15)\ mV)}{1 - exp\left(\frac{-(-v - (15)\ mV)}{7.2\ mV}\right)} \tag{235}$$

$$\tau_m\ ms = \frac{1}{(\alpha_m\ ms^{-1} + \beta_m\ ms^{-1}) * q_t} \tag{236}$$

$$m_\infty = \frac{\alpha_m}{\alpha_m + \beta_m} \tag{237}$$

$$\alpha_h\ ms^{-1} = \frac{Rd\ ms^{-1} * (v\ mV - (-30)\ mV)}{1 - exp\left(\frac{-(v\ mV - (-30)\ mV)}{1.5\ mV}\right)} \tag{238}$$

$$\beta_h\ ms^{-1} = \frac{Rg\ ms^{-1} * (-v - (30)\ mV)}{1 - exp\left(\frac{-(-v - (30)\ mV)}{1.5\ mV}\right)} \tag{239}$$

$$\tau_h = \frac{1}{(\alpha_h\ ms^{-1} + \beta_h\ ms^{-1}) * q_t} \tag{240}$$

$$h_\infty = \frac{1}{1 + exp\left(\frac{v\ mV + 35\ mV}{4\ mV}\right)} \tag{241}$$

$$s_\infty = \frac{1}{\left(1 + exp\left(\frac{v\ mV + 43\ mV}{2\ mV}\right)\right)} + InAct * (1 - \frac{1}{\left(1 + exp\left(\frac{v\ mV + 43\ mV}{2\ mV}\right)\right)}) \tag{242}$$

$$\tau_s\ ms = \frac{exp\left(\frac{1.0\text{e}{-3}\ VmV^{-1} * 12 * 0.2 * (v\ mV + 45\ mV) * 9.648e4\ Cmol^{-1}}{8.315\ CVK^{-1}mol^{-1} * T\ K}\right)}{0.0003\ ms^{-1} * \left(1 + exp\left(\frac{1.0\text{e}{-3}\ VmV^{-1} * 12 * (v\ mV + 45\ mV) * 9.648e4\ Cmol^{-1}}{8.315\ CVK^{-1}mol^{-1} * T\ K}\right)\right)} \tag{243}$$

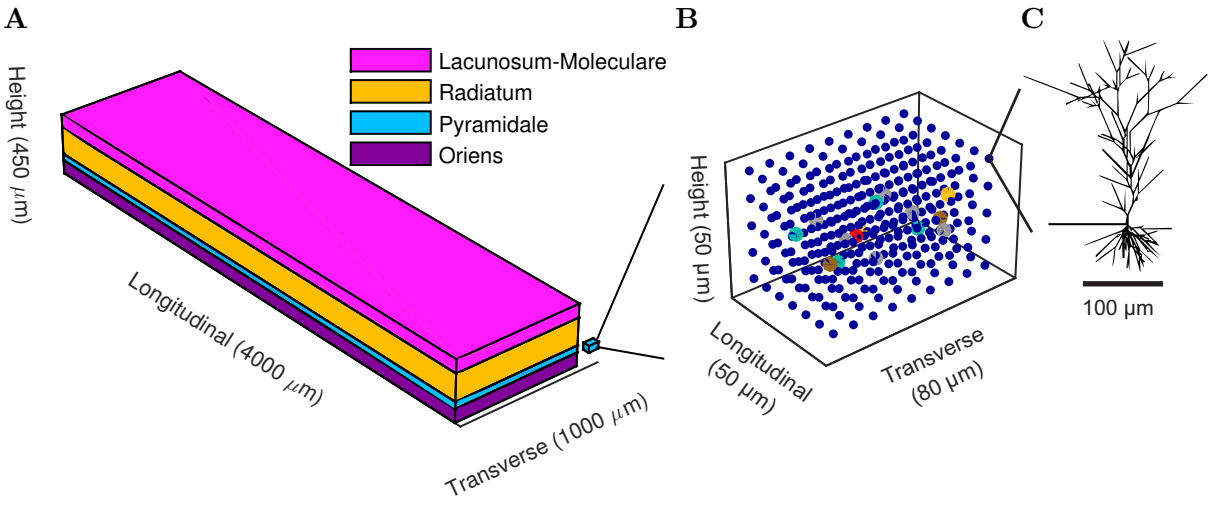
A
B
C
Lacunosum-Moleculare
Radiatum
Pyramidale
Oriens
Height (450 μm)
Longitudinal (4000 μm)
Transverse (1000 μm)
Height (50 μm)
Longitudinal (50 μm)
Transverse (80 μm)
100 μm

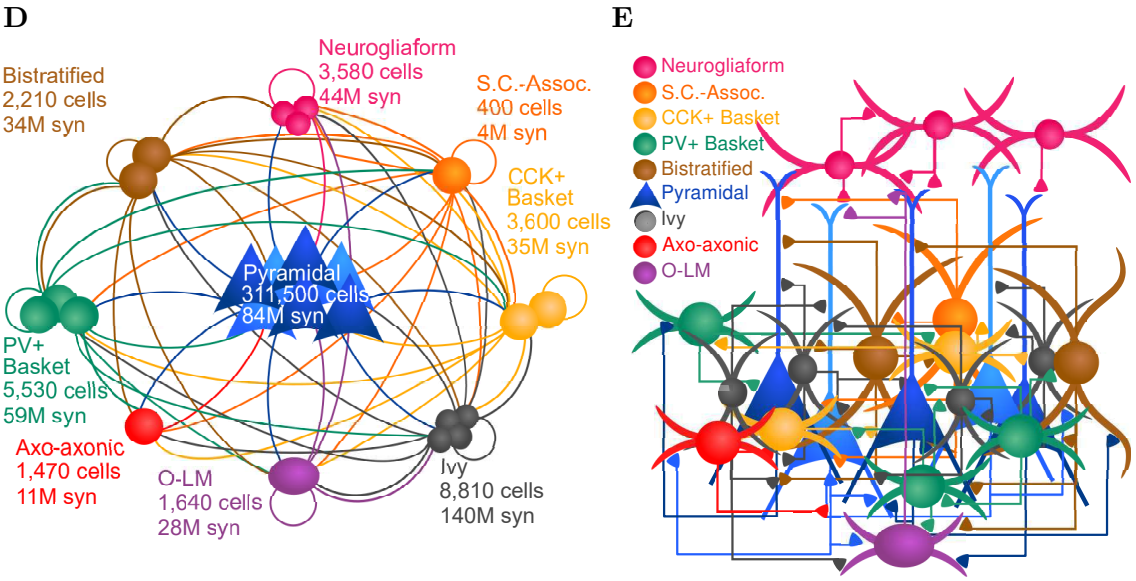
D
E
Neurogliaform
3,580 cells
44M syn
Bistratified
2,210 cells
34M syn
S.C.-Assoc.
400 cells
4M syn
CCK+
Basket
3,600 cells
35M syn
Pyramidal
311,500 cells
84M syn
PV+
Basket
5,530 cells
59M syn
Axo-axonic
1,470 cells
11M syn
O-LM
1,640 cells
28M syn
Ivy
8,810 cells
140M syn
Neurogliaform
S.C.-Assoc.
CCK+ Basket
PV+ Basket
Bistratified
Pyramidal
Ivy
Axo-axonic
O-LM

A

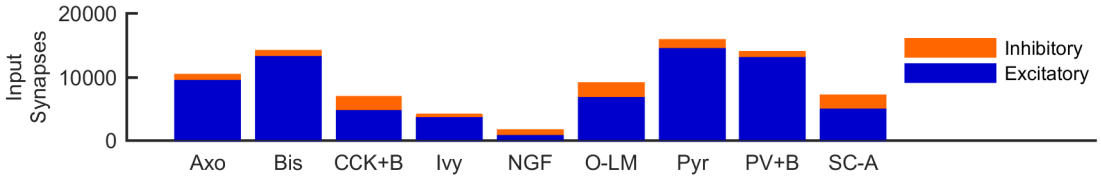
20000
10000
0
Input Synapses
Axo
Bis
CCK+B
Ivy
NGF
O-LM
Pyr
PV+B
SC-A
Inhibitory
Excitatory

B

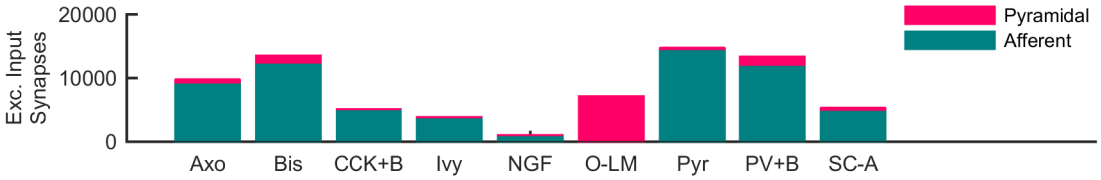
20000
10000
0
Exc. Input Synapses
Axo
Bis
CCK+B
Ivy
NGF
O-LM
Pyr
PV+B
SC-A
Pyramidal
Afferent

C

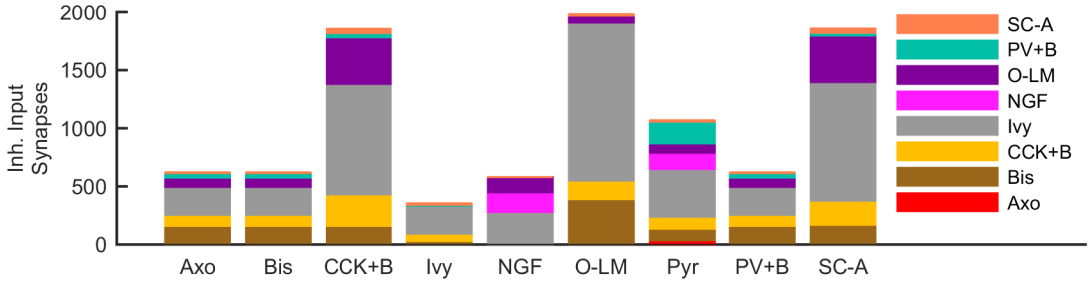
2000
1500
1000
500
0
Inh. Input Synapses
Axo
Bis
CCK+B
Ivy
NGF
O-LM
Pyr
PV+B
SC-A
SC-A
PV+B
O-LM
NGF
Ivy
CCK+B
Bis
Axo

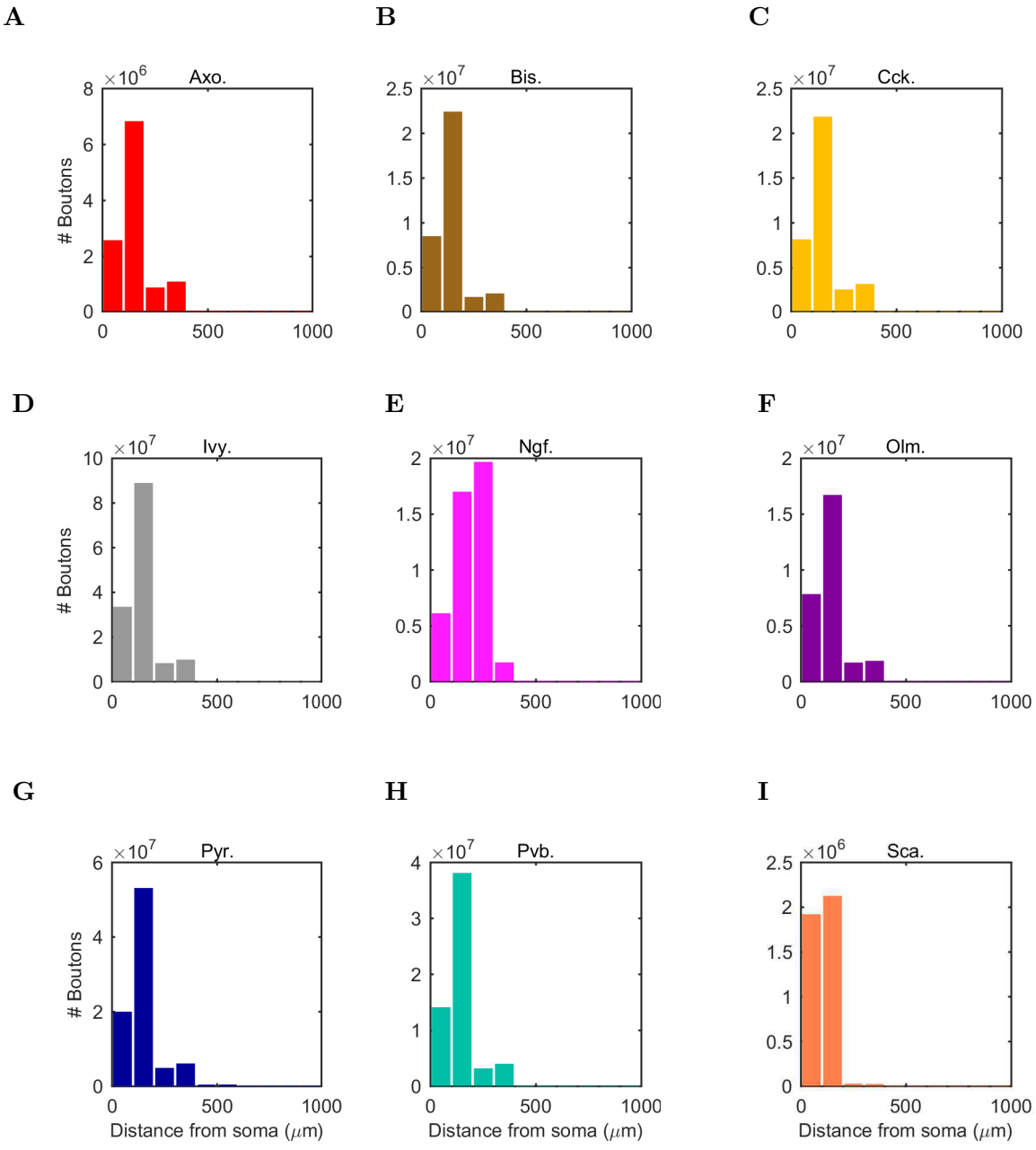
A
B
C
D
E
F
G
H
I
Axo.
Bis.
Cck.
Ivy.
Ngf.
Olm.
Pyr.
Pvb.
Sca.
Boutons
Distance from soma (μm)
×10^6
×10^7
0
500
1000

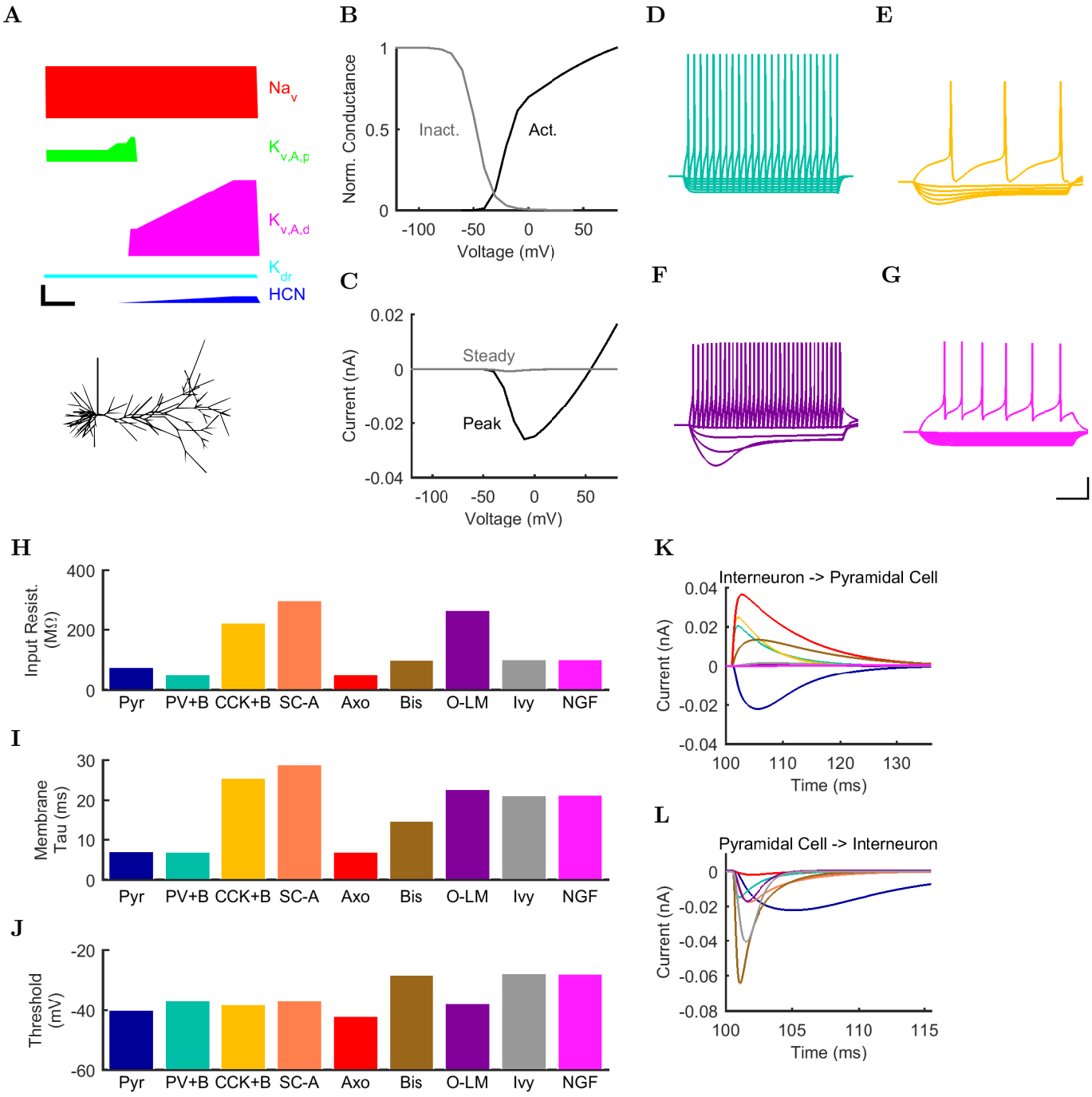
A
Na v
K v,A,p
K v,A,d
K dr
HCN
B
Norm. Conductance
1
0.5
0
Inact.
Act.
-100
-50
0
50
Voltage (mV)
C
Current (nA)
0.02
0
-0.02
-0.04
Steady
Peak
-100
-50
0
50
Voltage (mV)
D
E
F
G
H
Input Resist. (MΩ)
400
200
0
Pyr
PV+B
CCK+B
SC-A
Axo
Bis
O-LM
Ivy
NGF
I
Membrane Tau (ms)
30
20
10
0
Pyr
PV+B
CCK+B
SC-A
Axo
Bis
O-LM
Ivy
NGF
J
Threshold (mV)
-20
-40
-60
Pyr
PV+B
CCK+B
SC-A
Axo
Bis
O-LM
Ivy
NGF
K
Interneuron -> Pyramidal Cell
Current (nA)
0.04
0.02
0
-0.02
-0.04
100
110
120
130
Time (ms)
L
Pyramidal Cell -> Interneuron
Current (nA)
0
-0.02
-0.04
-0.06
-0.08
100
105
110
115
Time (ms)

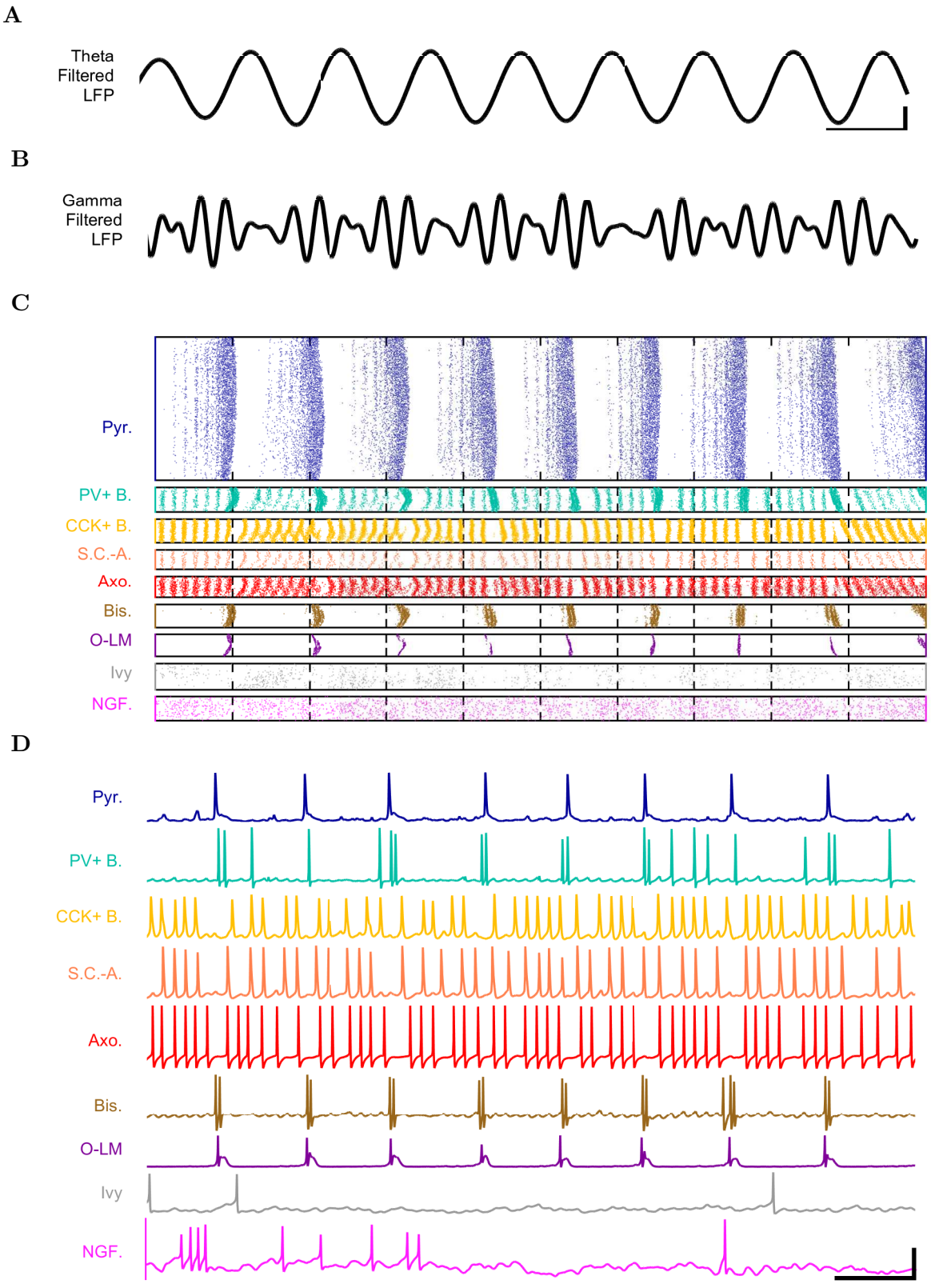
A
Theta
Filtered
LFP
B
Gamma
Filtered
LFP
C
Pyr.
PV+ B.
CCK+ B.
S.C.-A.
Axo.
Bis.
O-LM
Ivy
NGF.
D
Pyr.
PV+ B.
CCK+ B.
S.C.-A.
Axo.
Bis.
O-LM
Ivy
NGF.

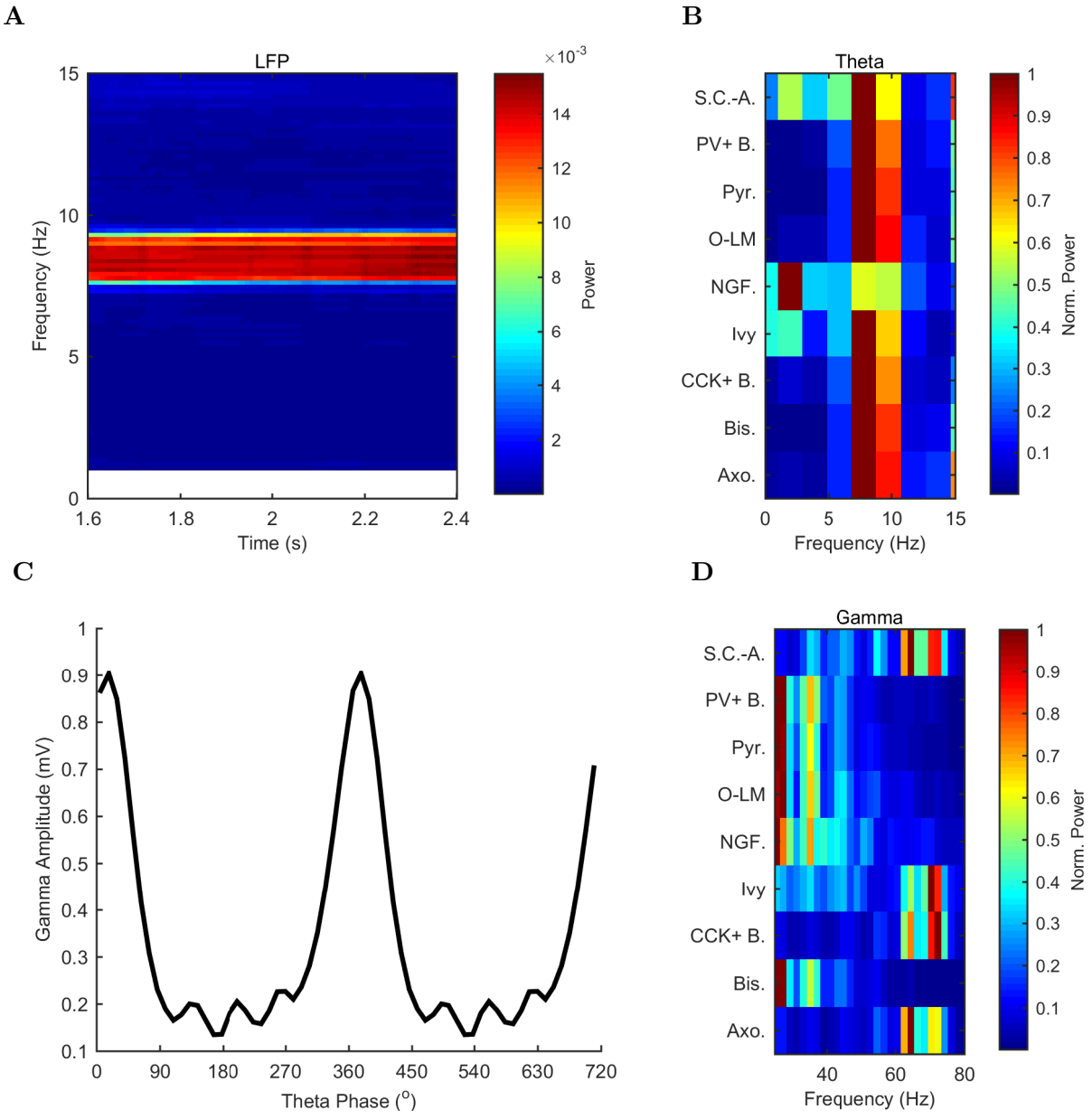
A
LFP
×10-3
Frequency (Hz)
Time (s)
Power
B
Theta
S.C.-A.
PV+ B.
Pyr.
O-LM
NGF.
Ivy
CCK+ B.
Bis.
Axo.
Frequency (Hz)
Norm. Power
C
Gamma Amplitude (mV)
Theta Phase (°)
D
Gamma
Frequency (Hz)
Norm. Power

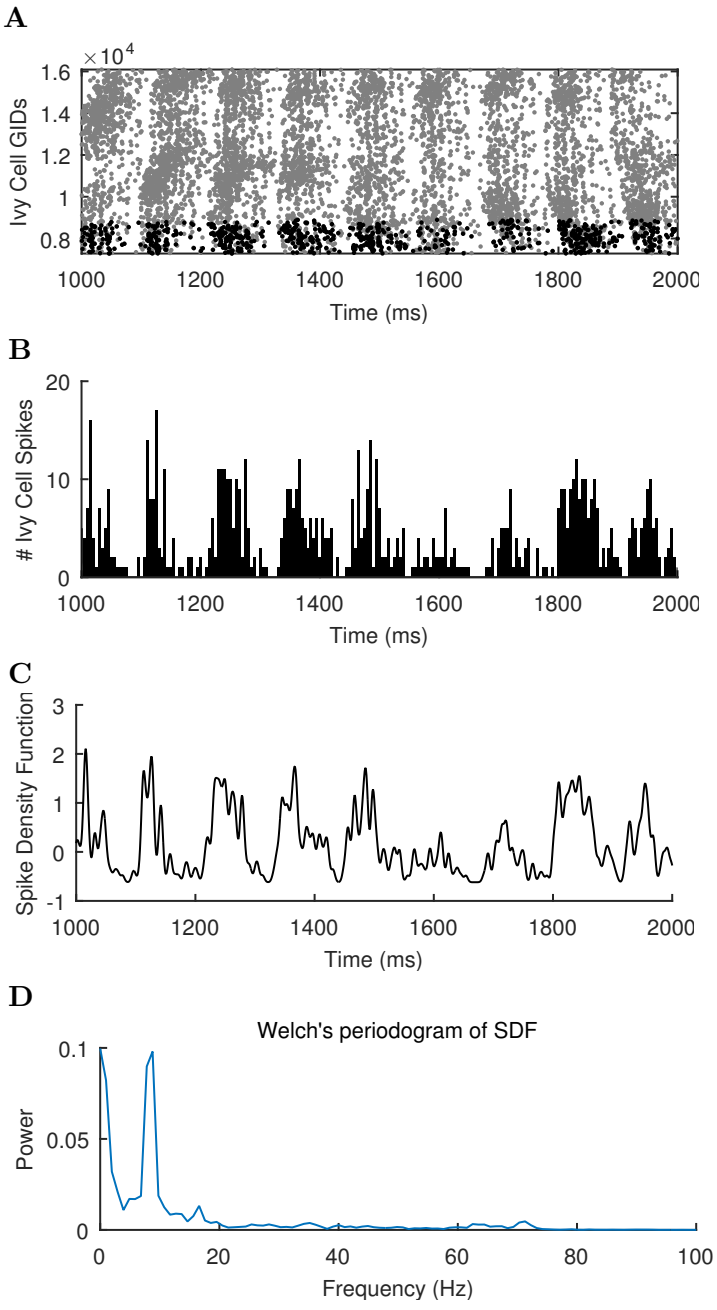
A
×10^4
1.6
1.4
1.2
1
0.8
Ivy Cell GIDs
1000
1200
1400
1600
1800
2000
Time (ms)
B
20
10
0
Ivy Cell Spikes
1000
1200
1400
1600
1800
2000
Time (ms)
C
3
2
1
0
-1
Spike Density Function
1000
1200
1400
1600
1800
2000
Time (ms)
D
Welch's periodogram of SDF
0.1
0.05
0
Power
0
20
40
60
80
100
Frequency (Hz)

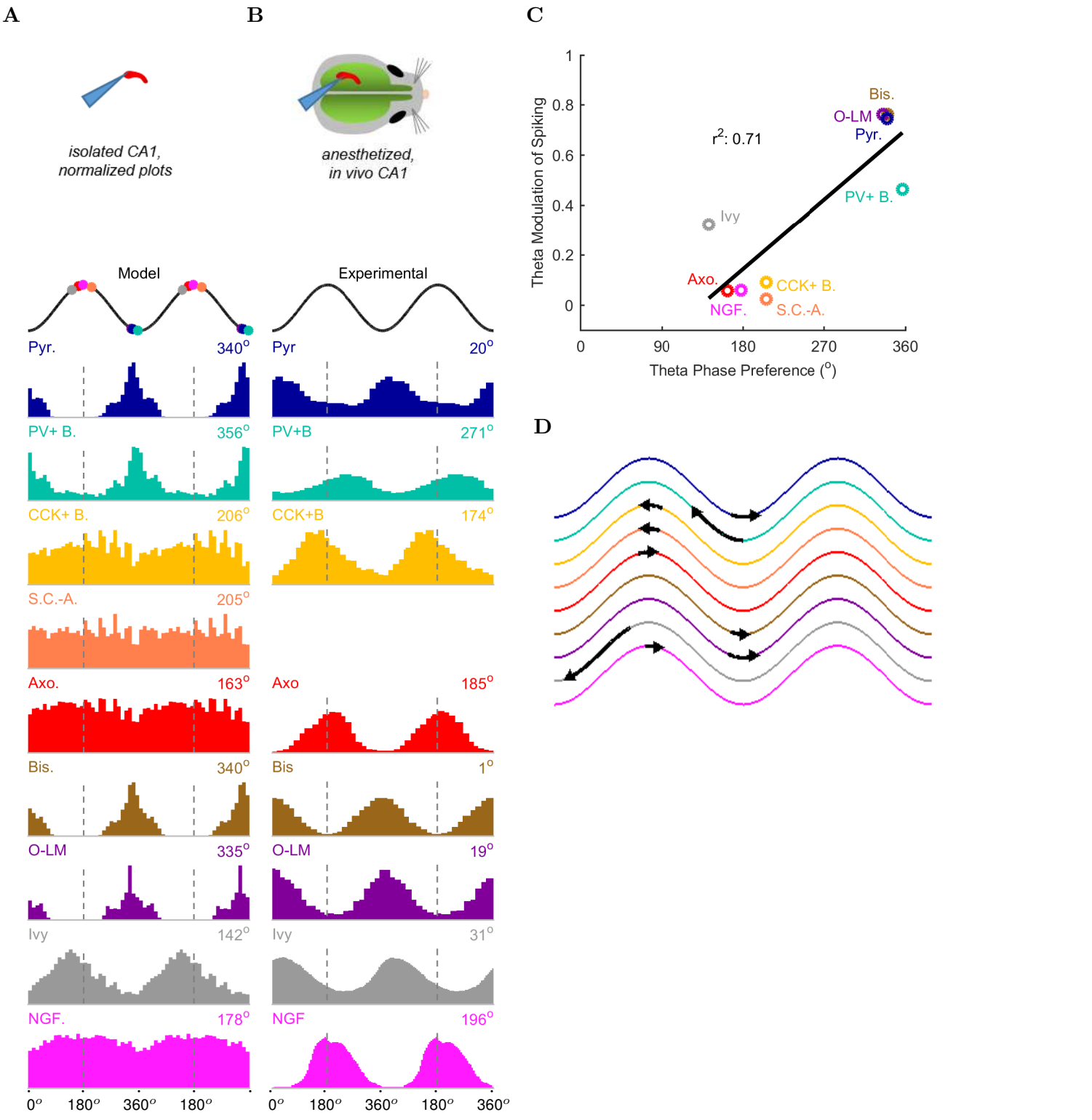
A
B
C
D
isolated CA1,
normalized plots
anesthetized,
in vivo CA1
Model
Experimental
Pyr. 340°
Pyr 20°
PV+ B. 356°
PV+B 271°
CCK+ B. 206°
CCK+B 174°
S.C.-A. 205°
Axo. 163°
Axo 185°
Bis. 340°
Bis 1°
O-LM 335°
O-LM 19°
Ivy 142°
Ivy 31°
NGF. 178°
NGF 196°
0° 180° 360° 180°
0° 180° 360° 180° 360°
Theta Modulation of Spiking
Theta Phase Preference (°)
r2: 0.71
Bis.
O-LM
Pyr.
PV+ B.
Ivy
Axo.
CCK+ B.
NGF.
S.C.-A.
0
0.2
0.4
0.6
0.8
1
0
90
180
270
360

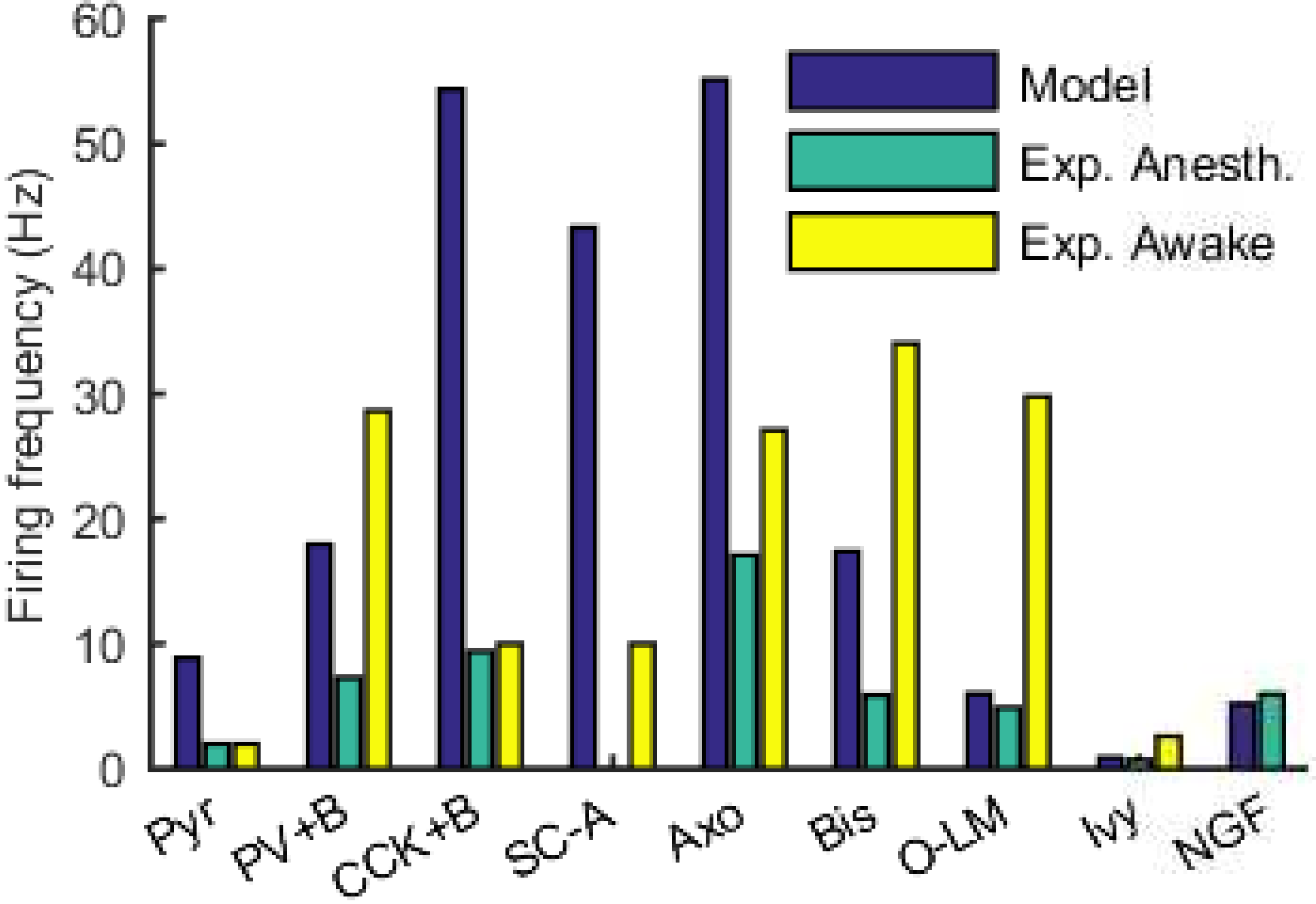
Firing frequency (Hz)
0
10
20
30
40
50
60
Model
Exp. Anesth.
Exp. Awake
Pyr
PV+B
CCK+B
SC-A
Axo
Bis
O-LM
Ivy
NGF

A

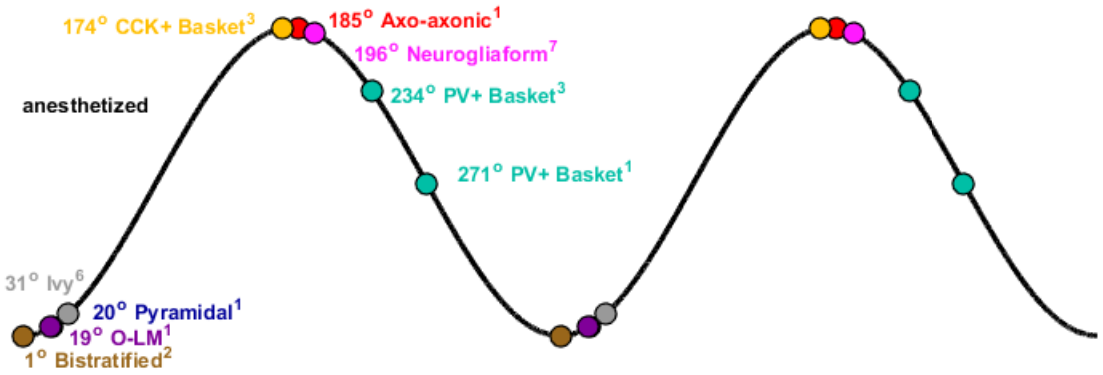
174° CCK+ Basket3
185° Axo-axonic1
196° Neurogliaform7
234° PV+ Basket3
anesthetized
271° PV+ Basket1
31° Ivy6
20° Pyramidal1
19° O-LM1
1° Bistratified2

B

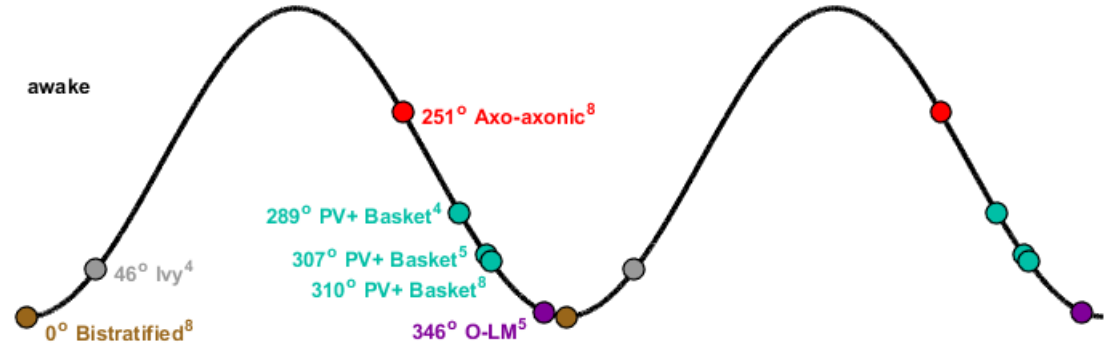
awake
251° Axo-axonic8
289° PV+ Basket4
307° PV+ Basket5
310° PV+ Basket8
46° Ivy4
0° Bistratified8
346° O-LM5

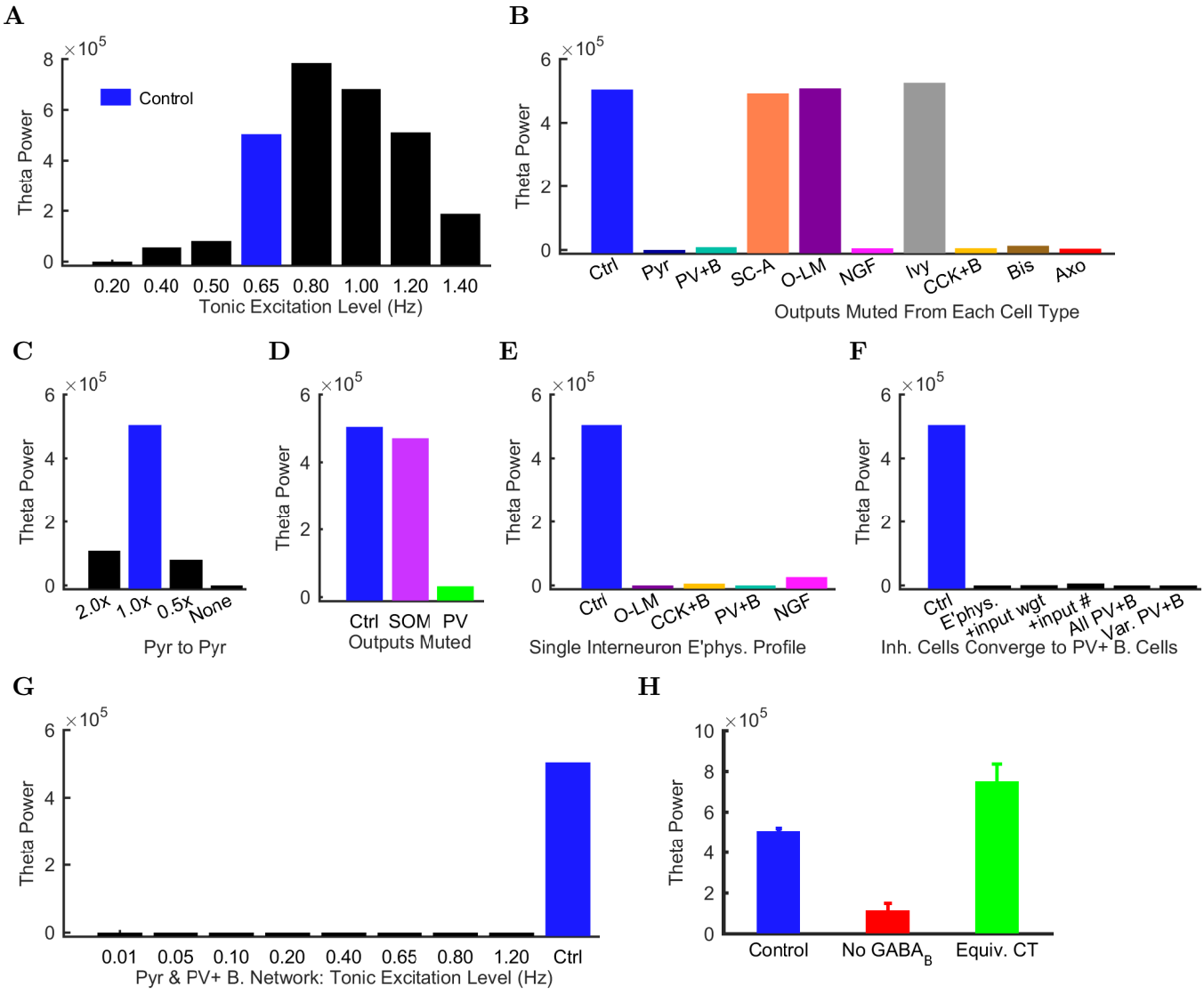
A
×10^5
Theta Power
Control
0.20 0.40 0.50 0.65 0.80 1.00 1.20 1.40
Tonic Excitation Level (Hz)
B
Theta Power
Ctrl Pyr PV+B SC-A O-LM NGF Ivy CCK+B Bis Axo
Outputs Muted From Each Cell Type
C
Theta Power
2.0x 1.0x 0.5x None
Pyr to Pyr
D
Theta Power
Ctrl SOM PV
Outputs Muted
E
Theta Power
Ctrl O-LM CCK+B PV+B NGF
Single Interneuron E'phys. Profile
F
Theta Power
Ctrl E'phys. +input wgt +input # All PV+B Var. PV+B
Inh. Cells Converge to PV+ B. Cells
G
Theta Power
0.01 0.05 0.10 0.20 0.40 0.65 0.80 1.20 Ctrl
Pyr & PV+ B. Network: Tonic Excitation Level (Hz)
H
Theta Power
Control
No GABA_B
Equiv. CT

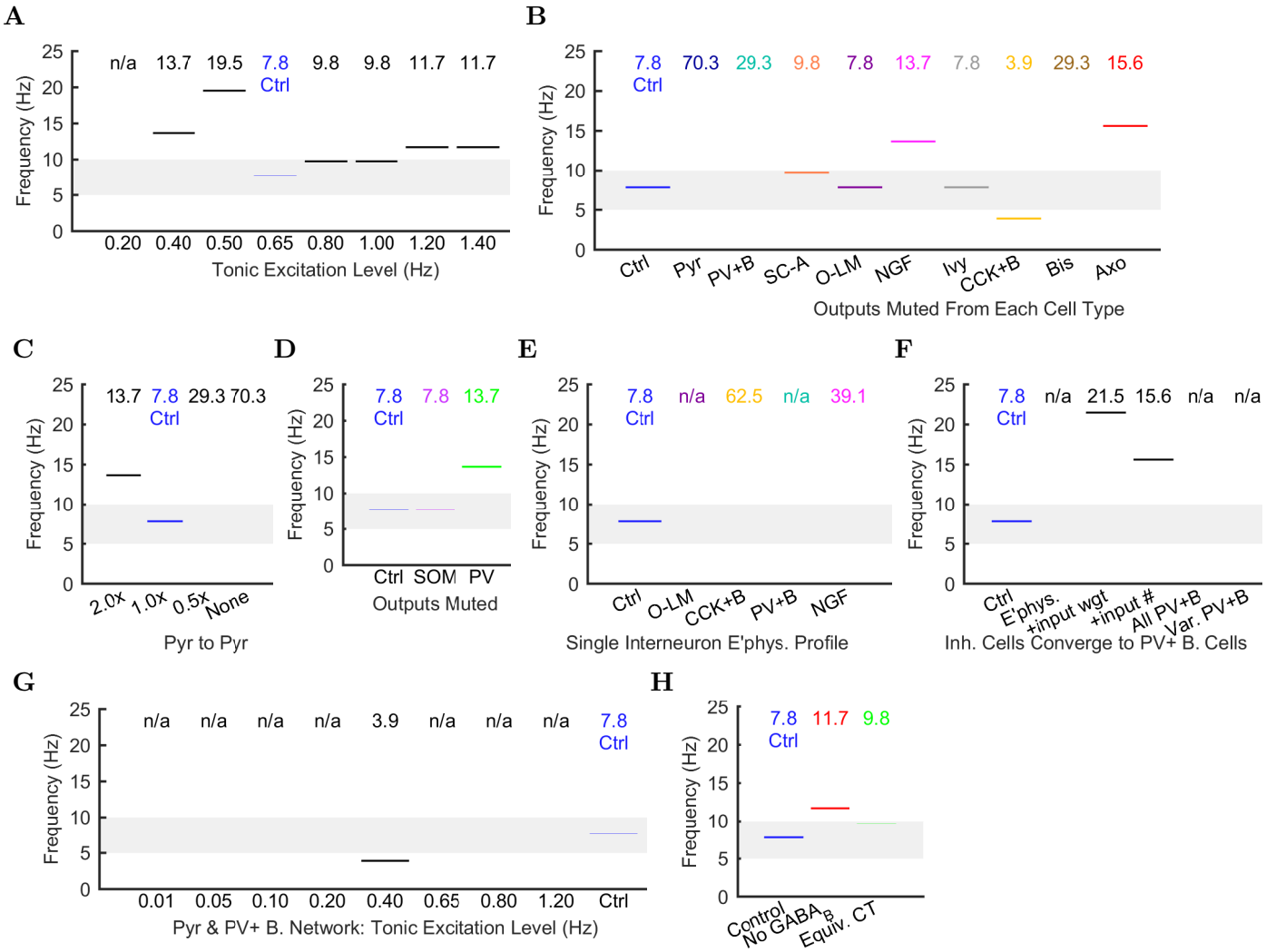
A
n/a 13.7 19.5 7.8 9.8 9.8 11.7 11.7
Ctrl
Frequency (Hz)
0.20 0.40 0.50 0.65 0.80 1.00 1.20 1.40
Tonic Excitation Level (Hz)
B
7.8 70.3 29.3 9.8 7.8 13.7 7.8 3.9 29.3 15.6
Ctrl
Frequency (Hz)
Ctrl Pyr PV+B SC-A O-LM NGF Ivy CCK+B Bis Axo
Outputs Muted From Each Cell Type
C
13.7 7.8 29.3 70.3
Ctrl
Frequency (Hz)
2.0x 1.0x 0.5x None
Pyr to Pyr
D
7.8 7.8 13.7
Ctrl
Frequency (Hz)
Ctrl SOM PV
Outputs Muted
E
7.8 n/a 62.5 n/a 39.1
Ctrl
Frequency (Hz)
Ctrl O-LM CCK+B PV+B NGF
Single Interneuron E'phys. Profile
F
7.8 n/a 21.5 15.6 n/a n/a
Ctrl
Frequency (Hz)
Ctrl E'phys. +input wgt +input # All PV+B Var. PV+B
Inh. Cells Converge to PV+ B. Cells
G
n/a n/a n/a n/a 3.9 n/a n/a n/a 7.8
Ctrl
Frequency (Hz)
0.01 0.05 0.10 0.20 0.40 0.65 0.80 1.20 Ctrl
Pyr & PV+ B. Network: Tonic Excitation Level (Hz)
H
7.8 11.7 9.8
Ctrl
Frequency (Hz)
Control
No GABA_B
Equiv. CT

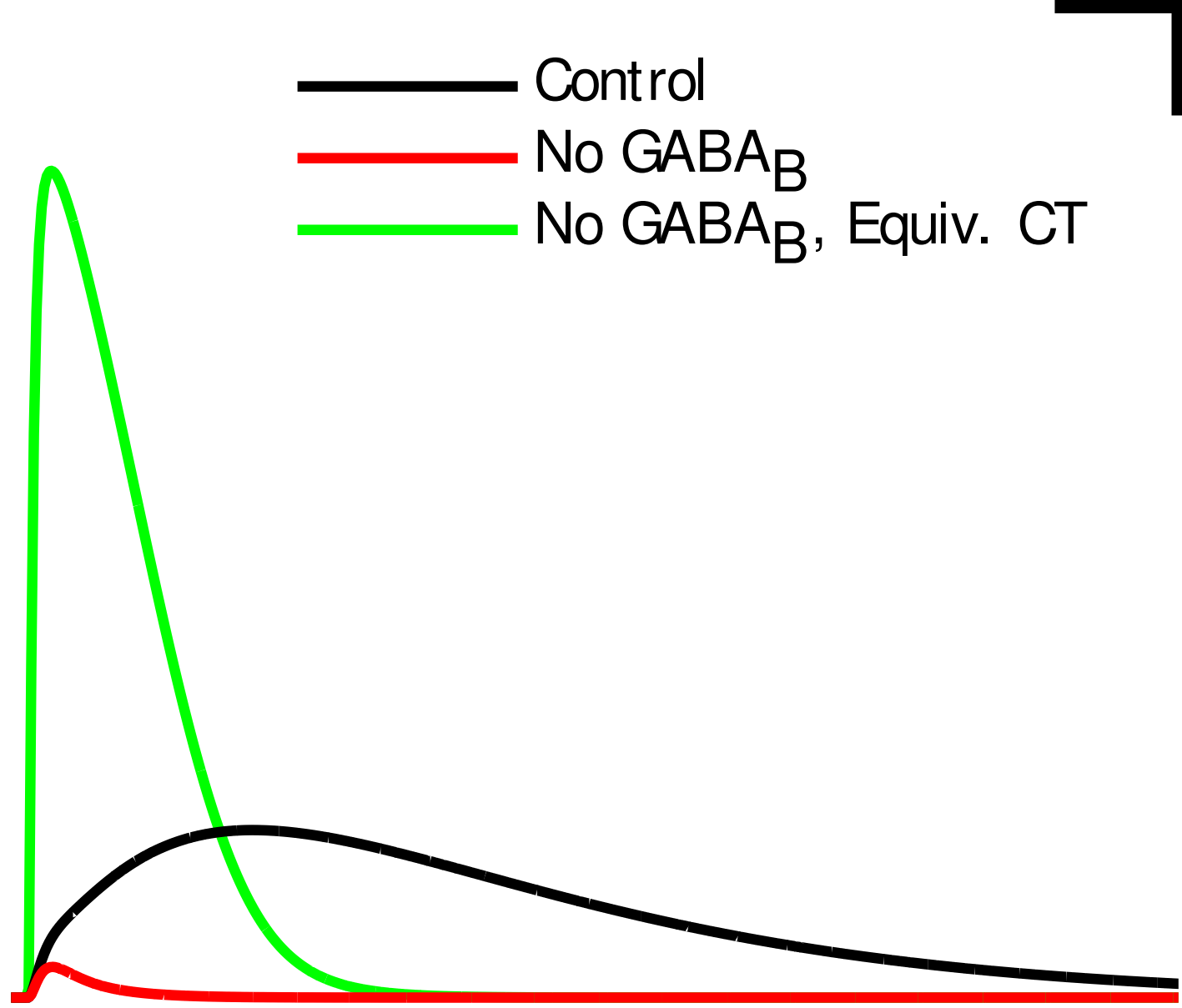
Control
No GABA$_B$
No GABA$_B$, Equiv. CT

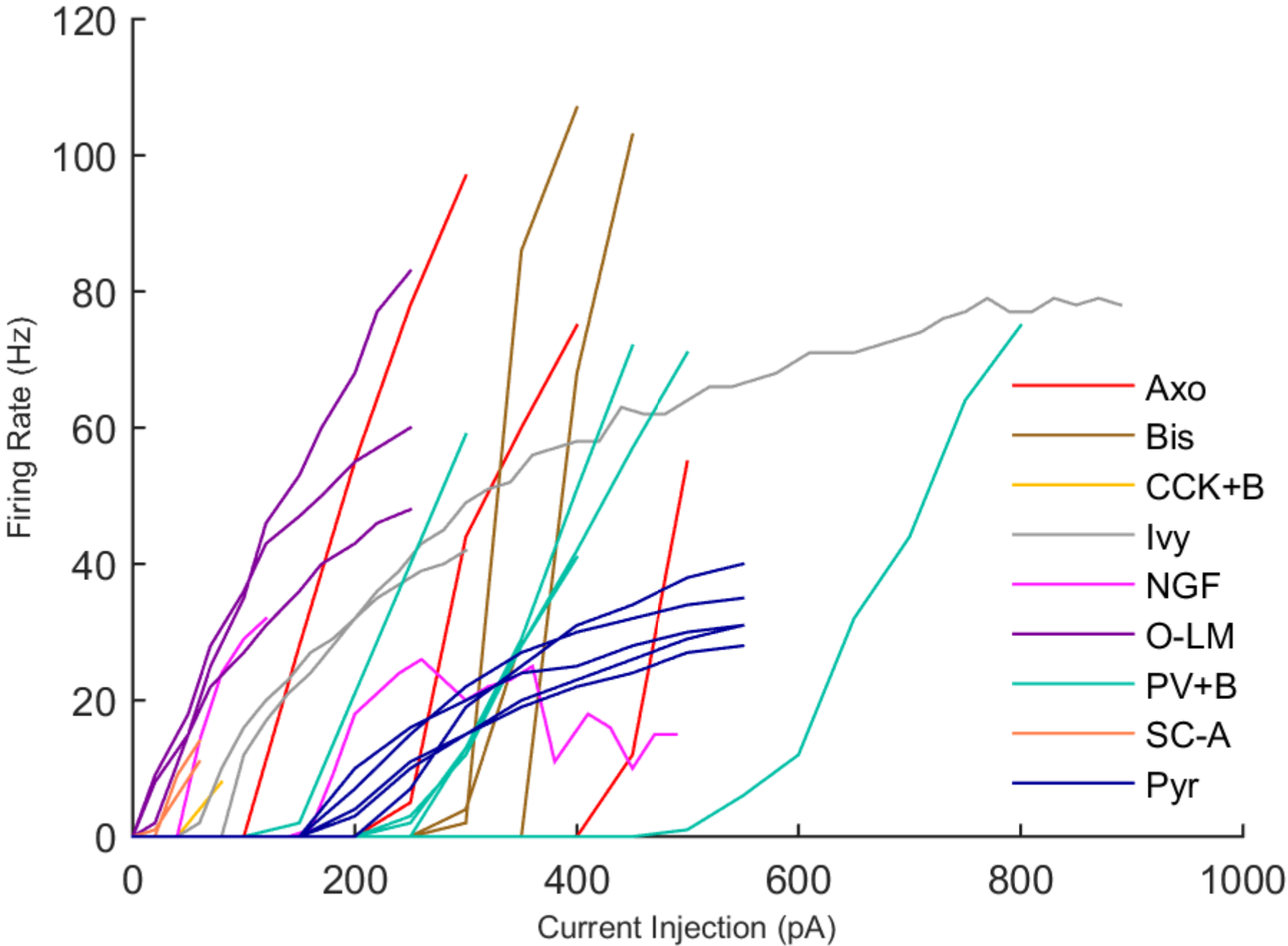
120
100
80
60
40
20
0
Firing Rate (Hz)
0
200
400
600
800
1000
Current Injection (pA)
Axo
Bis
CCK+B
Ivy
NGF
O-LM
PV+B
SC-A
Pyr

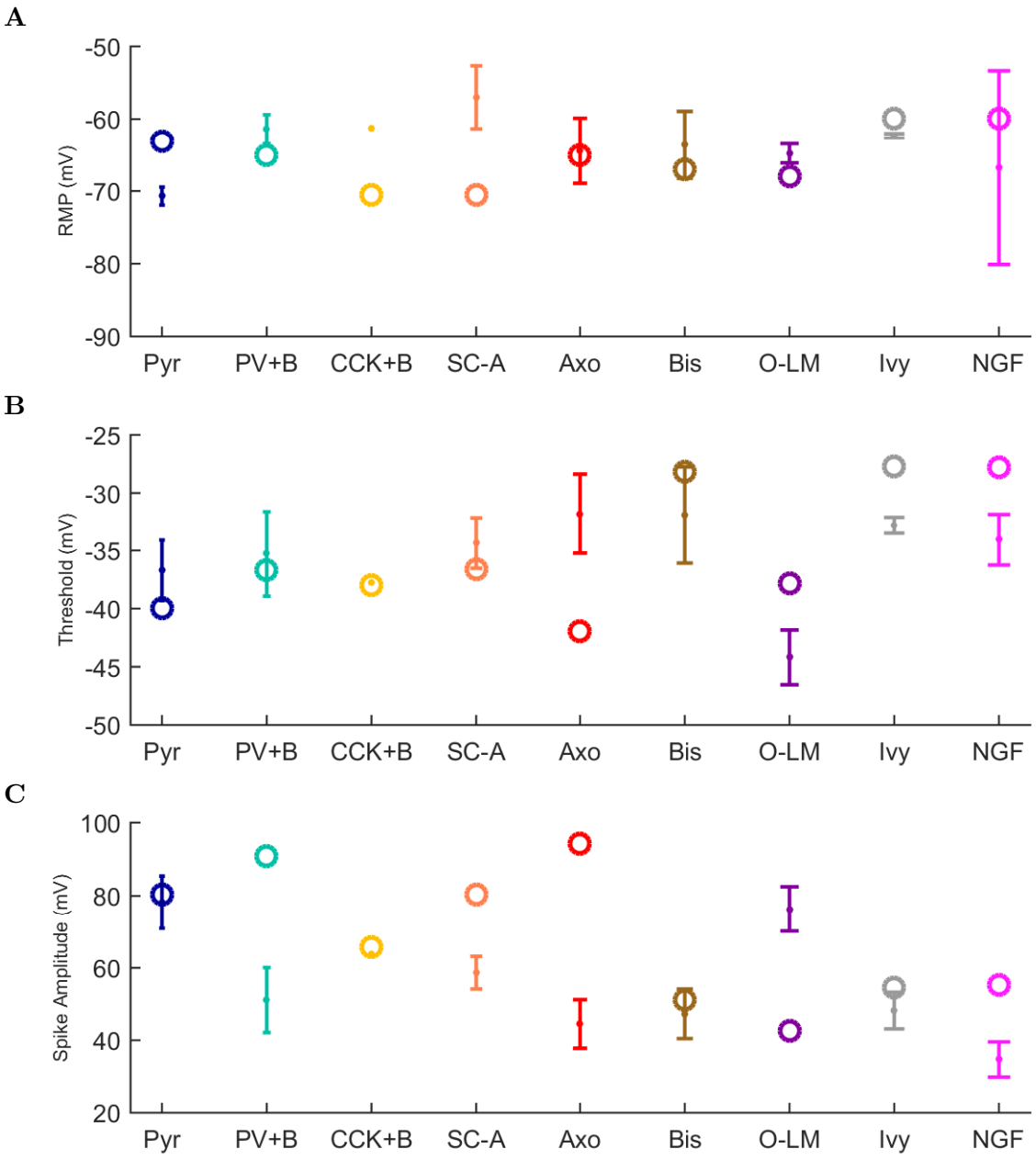
A
RMP (mV)
-50
-60
-70
-80
-90
Pyr
PV+B
CCK+B
SC-A
Axo
Bis
O-LM
Ivy
NGF
B
Threshold (mV)
-25
-30
-35
-40
-45
-50
Pyr
PV+B
CCK+B
SC-A
Axo
Bis
O-LM
Ivy
NGF
C
Spike Amplitude (mV)
100
80
60
40
20
Pyr
PV+B
CCK+B
SC-A
Axo
Bis
O-LM
Ivy
NGF

A

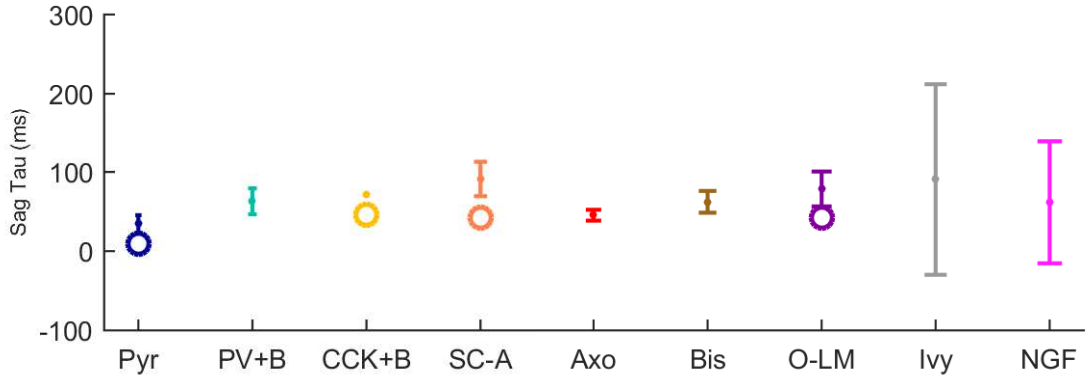
Sag Tau (ms)
300
200
100
0
-100
Pyr
PV+B
CCK+B
SC-A
Axo
Bis
O-LM
Ivy
NGF

B

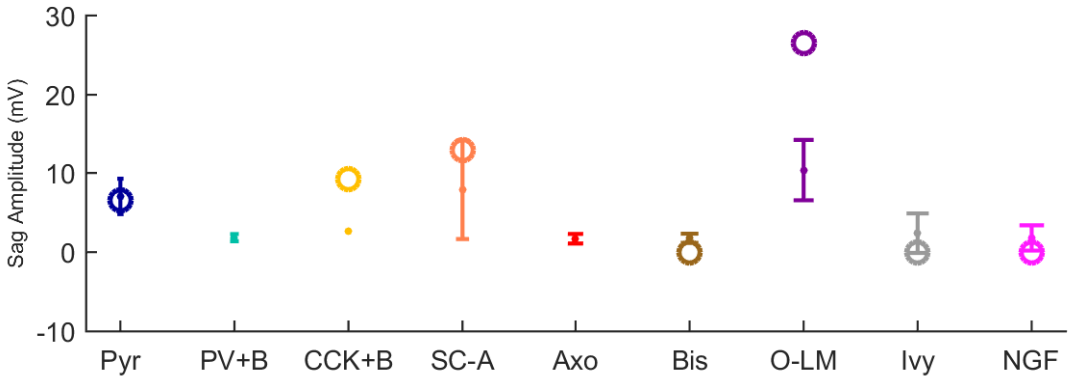
Sag Amplitude (mV)
30
20
10
0
-10
Pyr
PV+B
CCK+B
SC-A
Axo
Bis
O-LM
Ivy
NGF

C

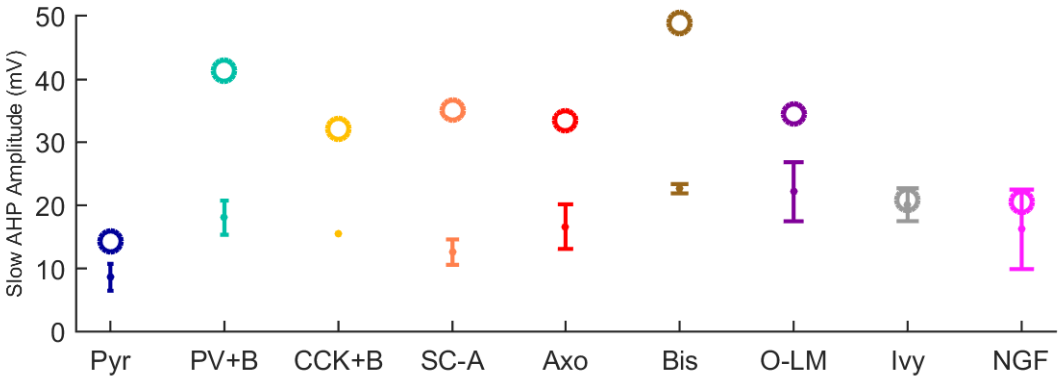
Slow AHP Amplitude (mV)
50
40
30
20
10
0
Pyr
PV+B
CCK+B
SC-A
Axo
Bis
O-LM
Ivy
NGF

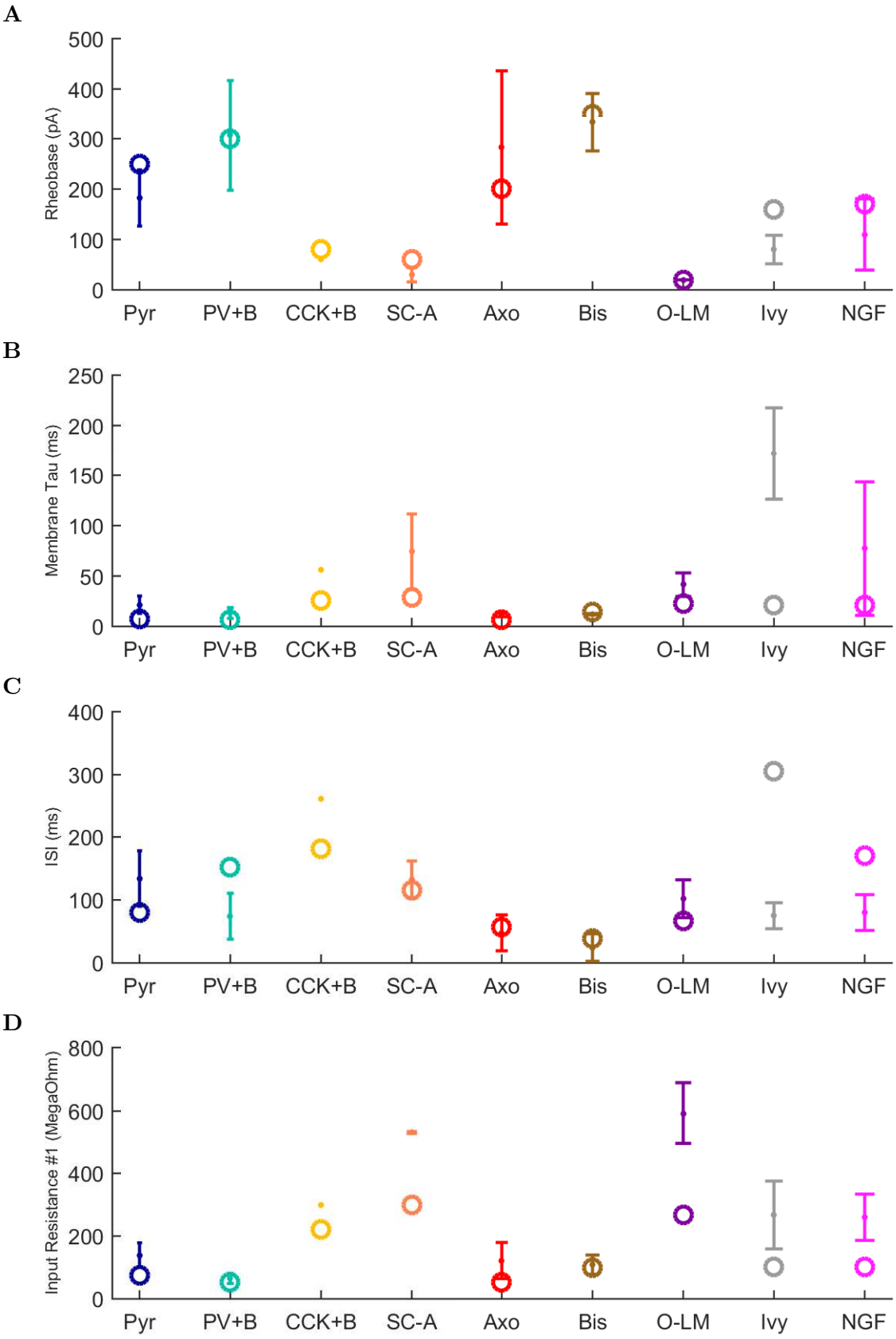
A
Rheobase (pA)
500
400
300
200
100
0
Pyr
PV+B
CCK+B
SC-A
Axo
Bis
O-LM
Ivy
NGF
B
Membrane Tau (ms)
250
200
150
100
50
0
Pyr
PV+B
CCK+B
SC-A
Axo
Bis
O-LM
Ivy
NGF
C
ISI (ms)
400
300
200
100
0
Pyr
PV+B
CCK+B
SC-A
Axo
Bis
O-LM
Ivy
NGF
D
Input Resistance #1 (MegaOhm)
800
600
400
200
0
Pyr
PV+B
CCK+B
SC-A
Axo
Bis
O-LM
Ivy
NGF

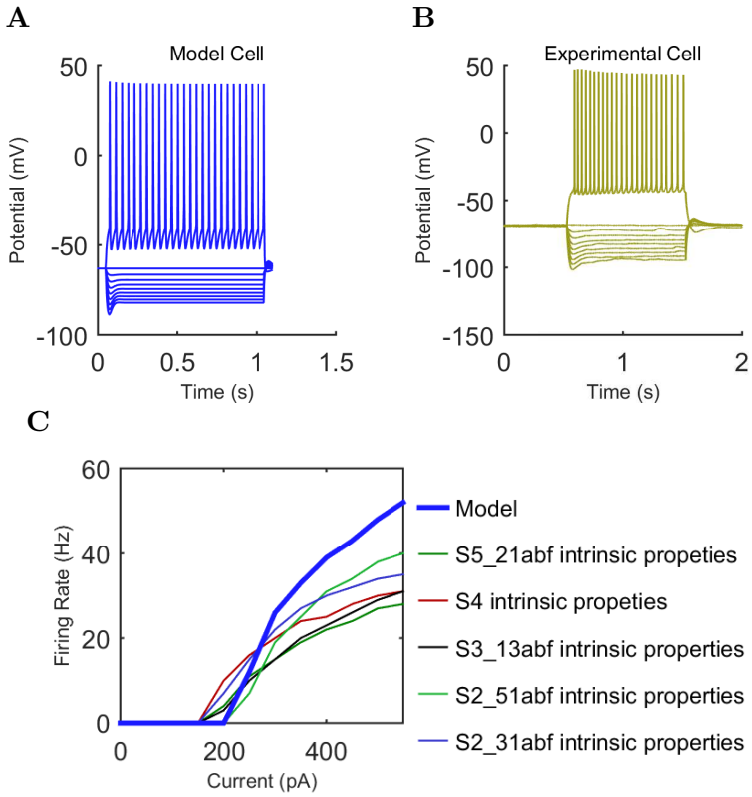
A
Model Cell
Potential (mV)
50
0
-50
-100
0
0.5
1
1.5
Time (s)
B
Experimental Cell
Potential (mV)
50
0
-50
-100
-150
0
1
2
Time (s)
C
Firing Rate (Hz)
60
40
20
0
0
200
400
Current (pA)
Model
S5_21abf intrinsic propeties
S4 intrinsic propeties
S3_13abf intrinsic properties
S2_51abf intrinsic properties
S2_31abf intrinsic properties

A

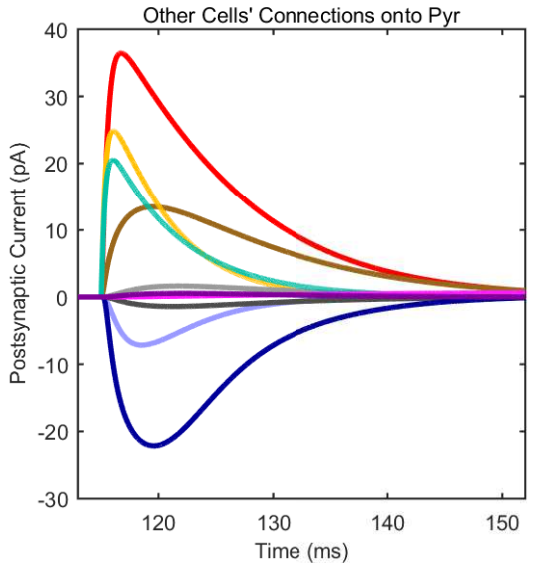
Other Cells' Connections onto Pyr
Postsynaptic Current (pA)
40
30
20
10
0
-10
-20
-30
120
130
140
150
Time (ms)

B

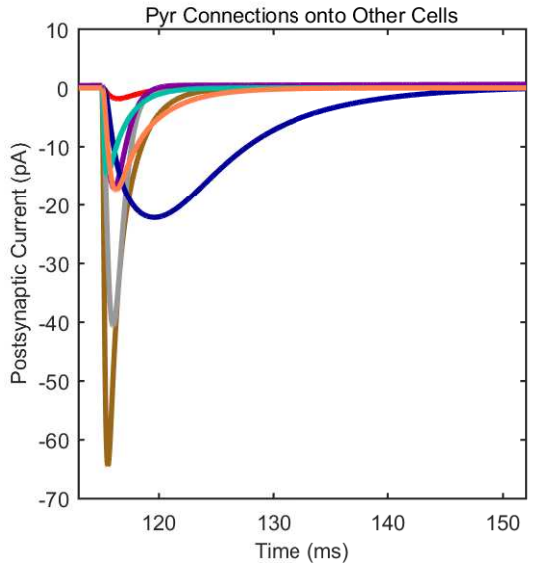
Pyr Connections onto Other Cells
Postsynaptic Current (pA)
10
0
-10
-20
-30
-40
-50
-60
-70
120
130
140
150
Time (ms)

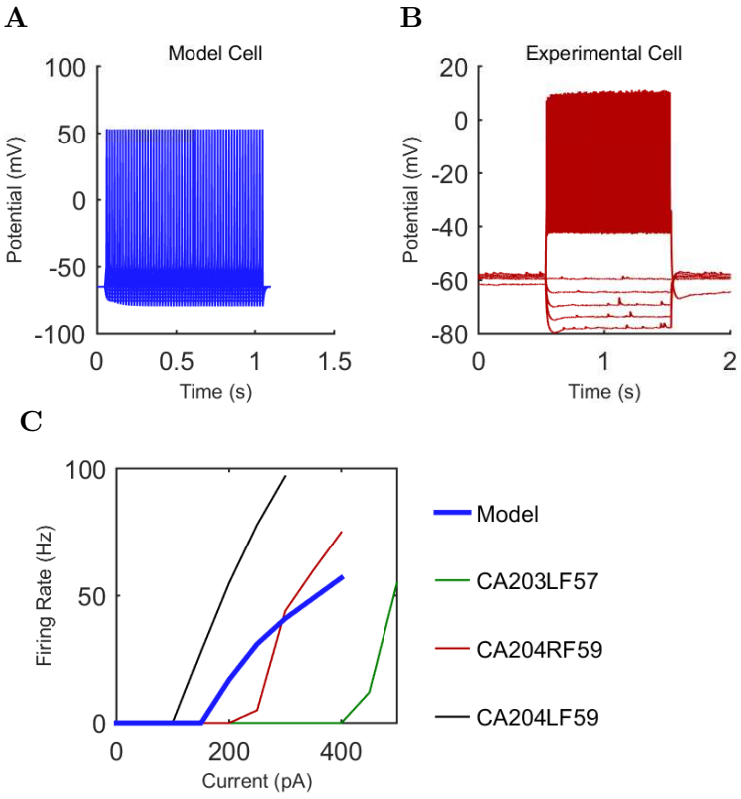
A
Model Cell
Potential (mV)
100
50
0
-50
-100
0
0.5
1
1.5
Time (s)
B
Experimental Cell
Potential (mV)
20
0
-20
-40
-60
-80
0
1
2
Time (s)
C
Firing Rate (Hz)
100
50
0
0
200
400
Current (pA)
Model
CA203LF57
CA204RF59
CA204LF59

A

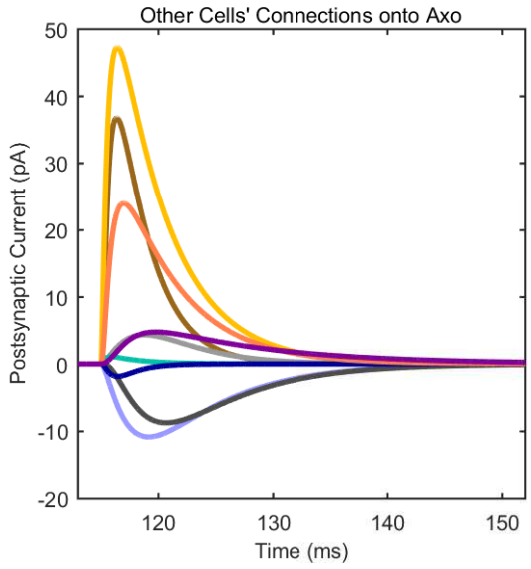
Other Cells' Connections onto Axo
Postsynaptic Current (pA)
50
40
30
20
10
0
-10
-20
120
130
140
150
Time (ms)

B

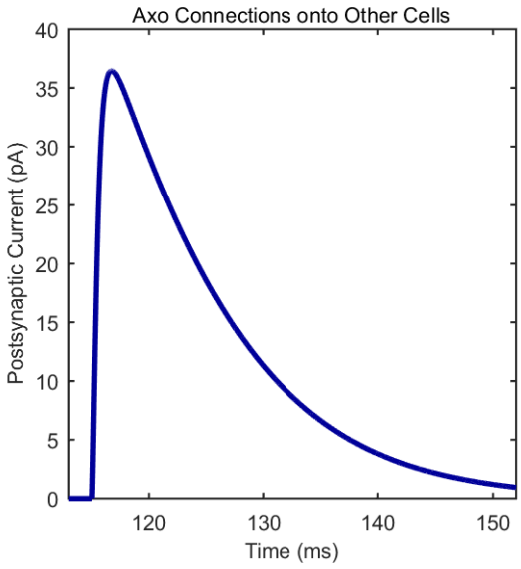
Axo Connections onto Other Cells
Postsynaptic Current (pA)
40
35
30
25
20
15
10
5
0
120
130
140
150
Time (ms)

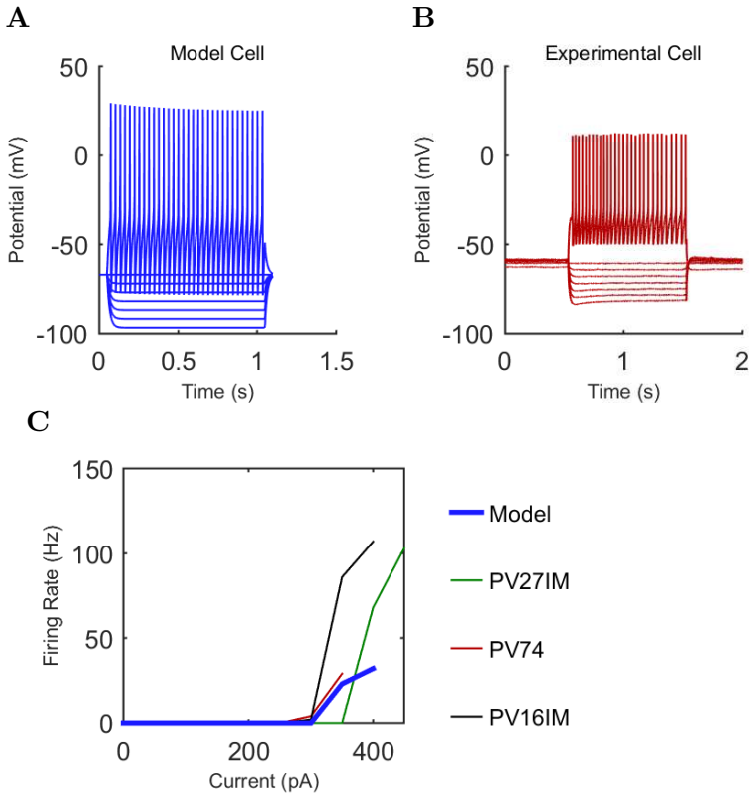
A
Model Cell
Potential (mV)
50
0
-50
-100
0
0.5
1
1.5
Time (s)
B
Experimental Cell
Potential (mV)
50
0
-50
-100
0
1
2
Time (s)
C
Firing Rate (Hz)
150
100
50
0
0
200
400
Current (pA)
Model
PV27IM
PV74
PV16IM

A

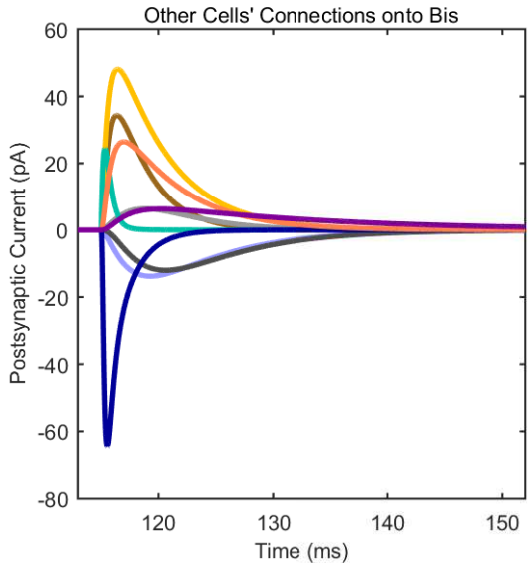
Other Cells' Connections onto Bis
Postsynaptic Current (pA)
60
40
20
0
-20
-40
-60
-80
120
130
140
150
Time (ms)

B

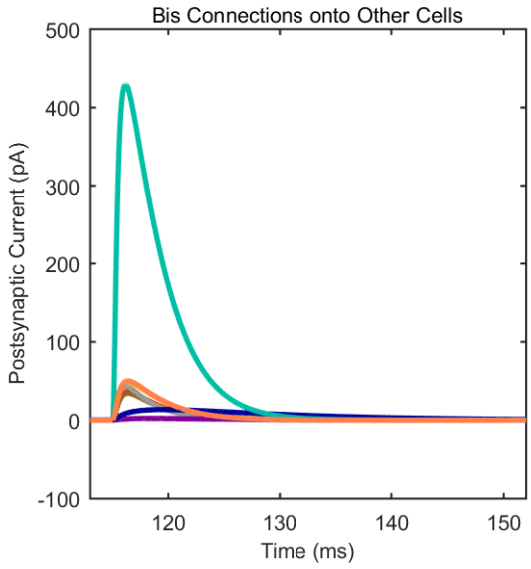
Bis Connections onto Other Cells
Postsynaptic Current (pA)
500
400
300
200
100
0
-100
120
130
140
150
Time (ms)

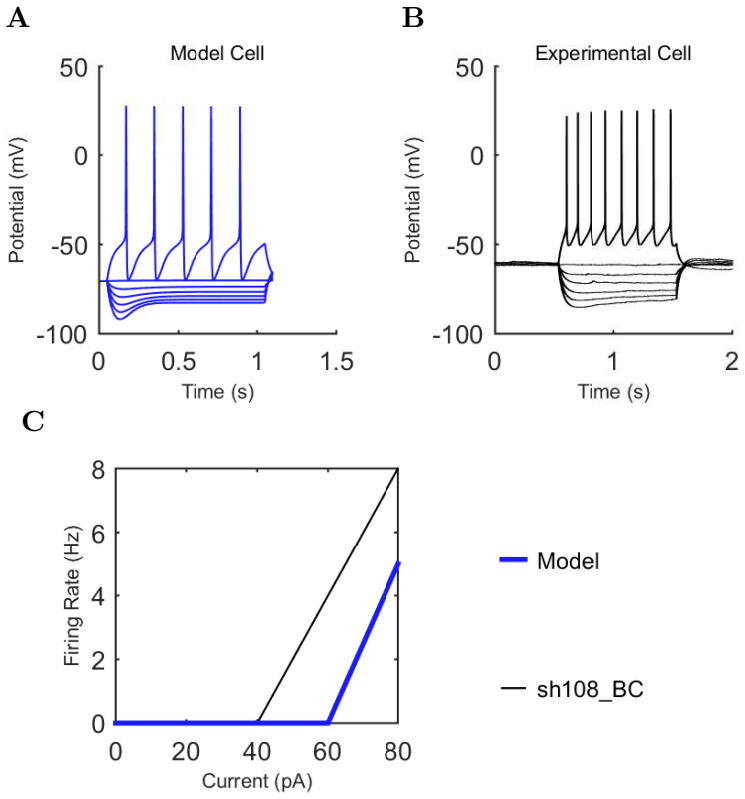
A
Model Cell
Potential (mV)
50
0
-50
-100
0
0.5
1
1.5
Time (s)
B
Experimental Cell
Potential (mV)
50
0
-50
-100
0
1
2
Time (s)
C
Firing Rate (Hz)
8
6
4
2
0
0
20
40
60
80
Current (pA)
Model
sh108_BC

A

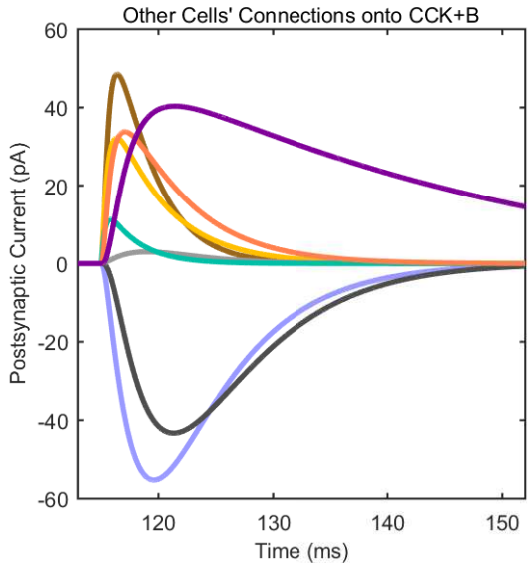
Other Cells' Connections onto CCK+B
Postsynaptic Current (pA)
60
40
20
0
-20
-40
-60
120
130
140
150
Time (ms)

B

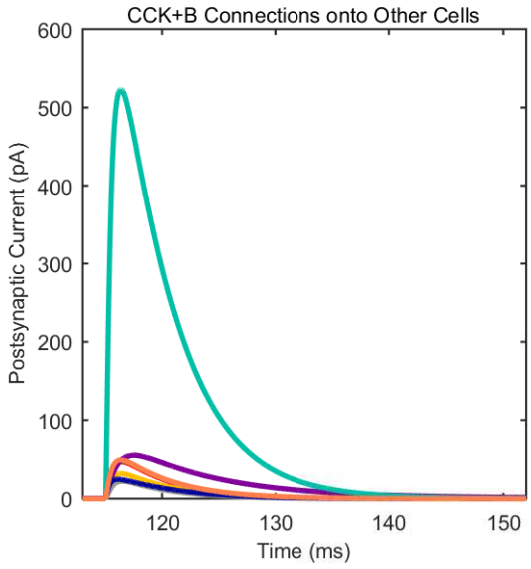
CCK+B Connections onto Other Cells
Postsynaptic Current (pA)
600
500
400
300
200
100
0
120
130
140
150
Time (ms)

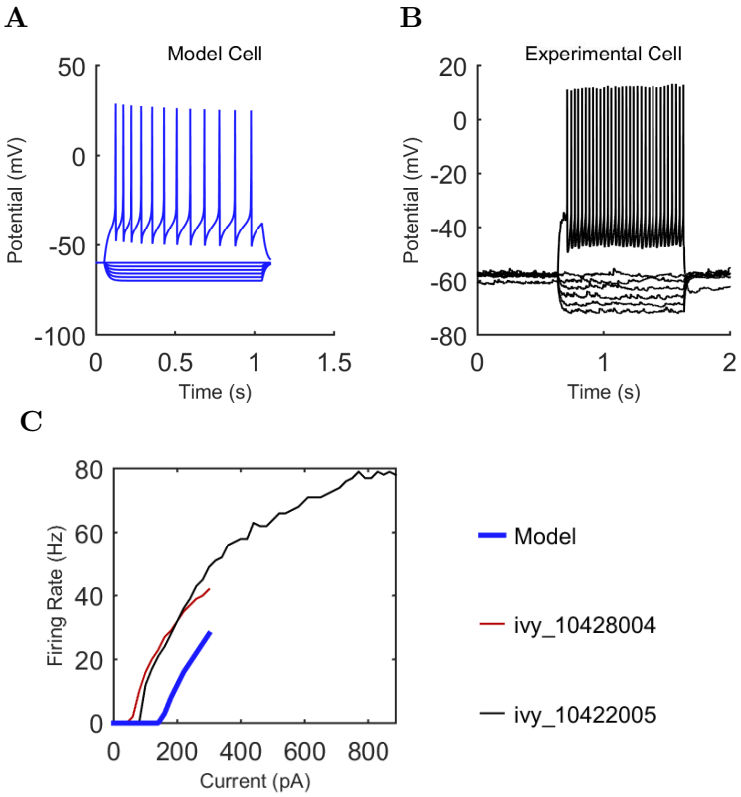
A
Model Cell
Potential (mV)
50
0
-50
-100
0
0.5
1
1.5
Time (s)
B
Experimental Cell
Potential (mV)
20
0
-20
-40
-60
-80
0
1
2
Time (s)
C
Firing Rate (Hz)
80
60
40
20
0
0
200
400
600
800
Current (pA)
Model
ivy_10428004
ivy_10422005

A

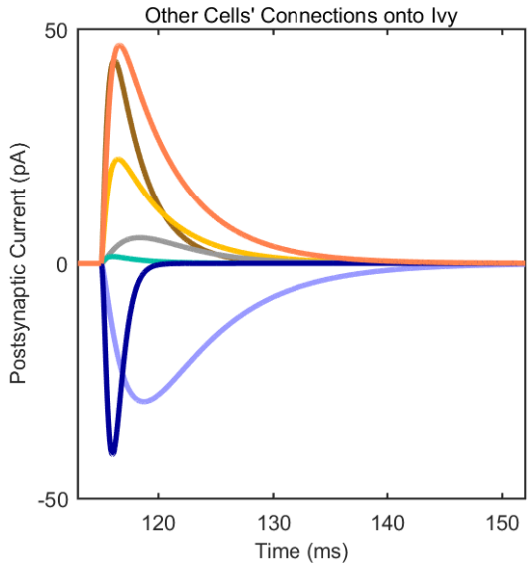
Other Cells' Connections onto Ivy
Postsynaptic Current (pA)
50
0
-50
120
130
140
150
Time (ms)

B

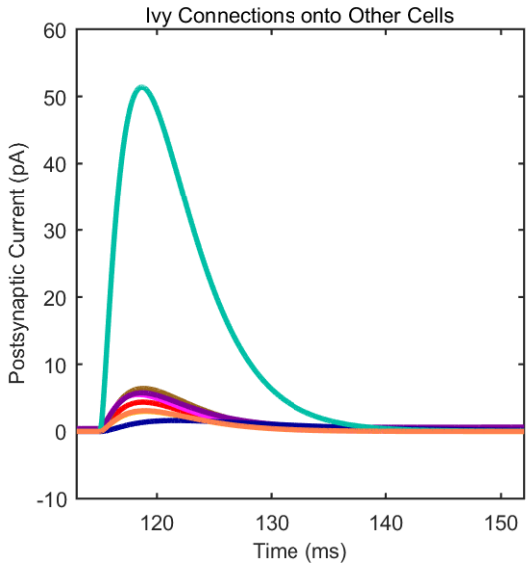
Ivy Connections onto Other Cells
Postsynaptic Current (pA)
60
50
40
30
20
10
0
-10
120
130
140
150
Time (ms)

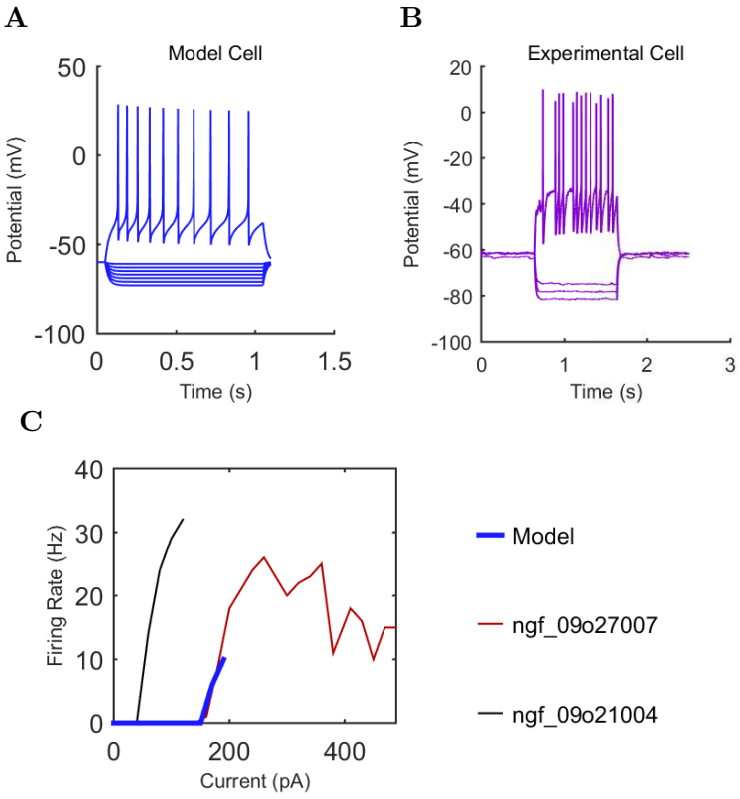
A
Model Cell
Potential (mV)
50
0
-50
-100
0
0.5
1
1.5
Time (s)
B
Experimental Cell
Potential (mV)
20
0
-20
-40
-60
-80
-100
0
1
2
3
Time (s)
C
Firing Rate (Hz)
40
30
20
10
0
0
200
400
Current (pA)
Model
ngf_09o27007
ngf_09o21004

A

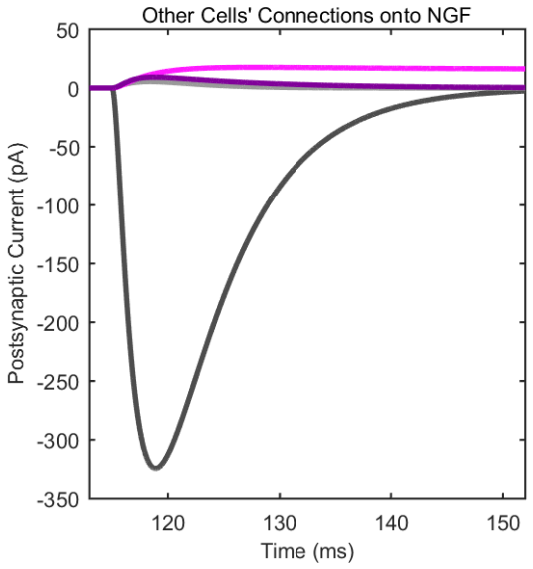
Other Cells' Connections onto NGF
Postsynaptic Current (pA)
50
0
-50
-100
-150
-200
-250
-300
-350
120
130
140
150
Time (ms)

B

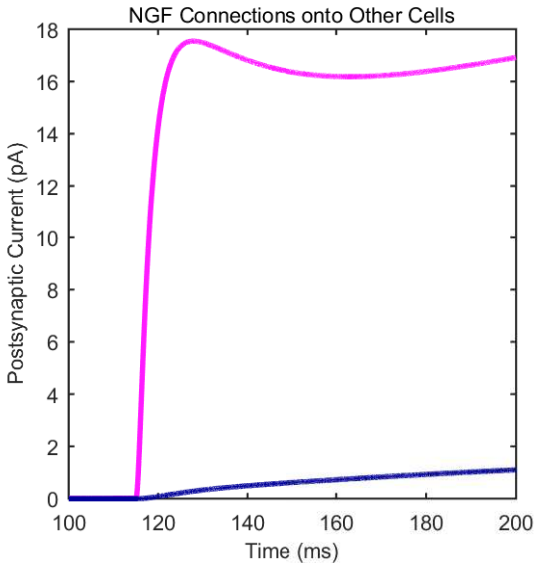
NGF Connections onto Other Cells
Postsynaptic Current (pA)
18
16
14
12
10
8
6
4
2
0
100
120
140
160
180
200
Time (ms)

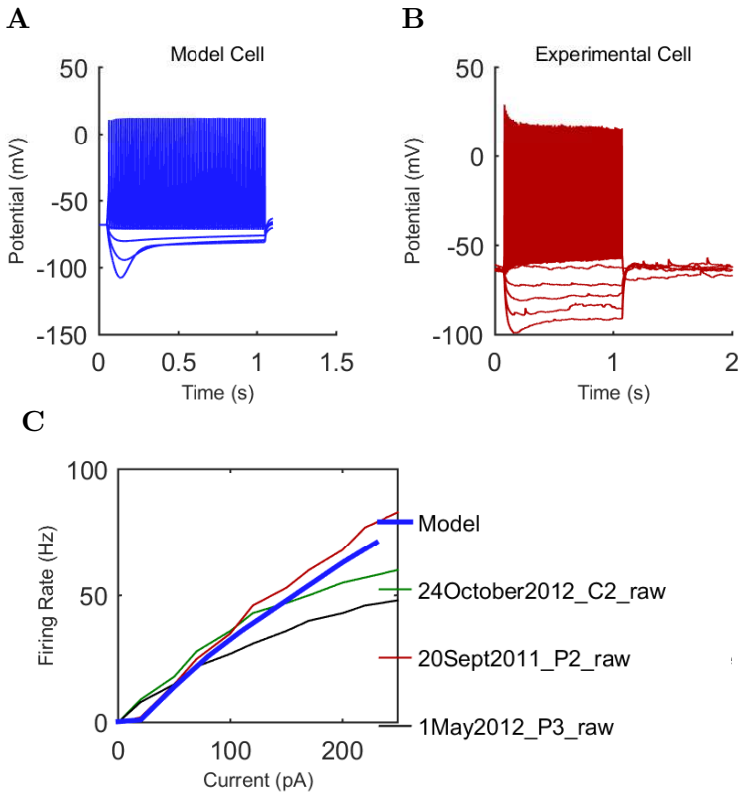
A
Model Cell
Potential (mV)
50
0
-50
-100
-150
0
0.5
1
1.5
Time (s)
B
Experimental Cell
Potential (mV)
50
0
-50
-100
0
1
2
Time (s)
C
Firing Rate (Hz)
100
50
0
0
100
200
Current (pA)
Model
24October2012_C2_raw
20Sept2011_P2_raw
1May2012_P3_raw

A

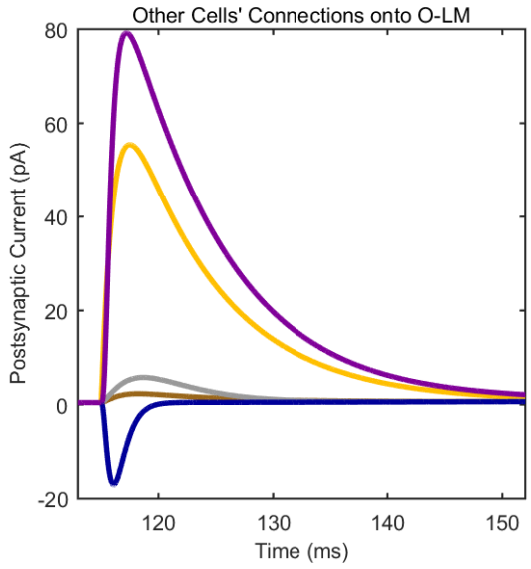
Other Cells' Connections onto O-LM
Postsynaptic Current (pA)
80
60
40
20
0
-20
120
130
140
150
Time (ms)

B

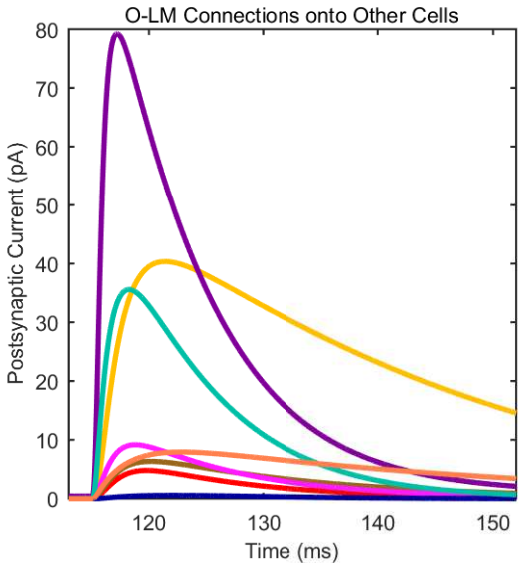
O-LM Connections onto Other Cells
Postsynaptic Current (pA)
80
70
60
50
40
30
20
10
0
120
130
140
150
Time (ms)

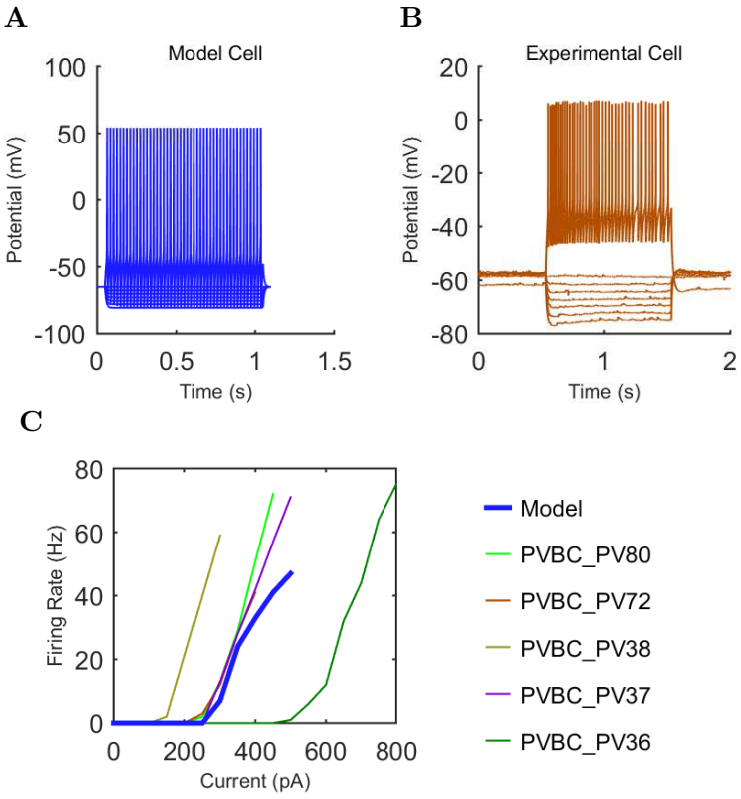
A
Model Cell
Potential (mV)
100
50
0
-50
-100
0
0.5
1
1.5
Time (s)
B
Experimental Cell
Potential (mV)
20
0
-20
-40
-60
-80
0
1
2
Time (s)
C
Firing Rate (Hz)
80
60
40
20
0
0
200
400
600
800
Current (pA)
Model
PVBC_PV80
PVBC_PV72
PVBC_PV38
PVBC_PV37
PVBC_PV36

A

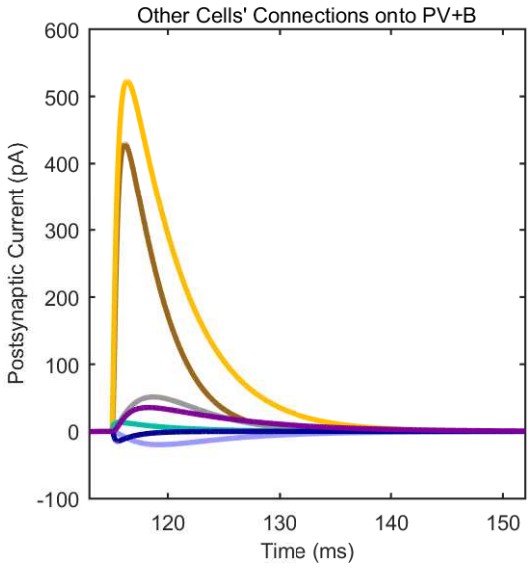
Other Cells' Connections onto PV+B
Postsynaptic Current (pA)
600
500
400
300
200
100
0
-100
120
130
140
150
Time (ms)

B

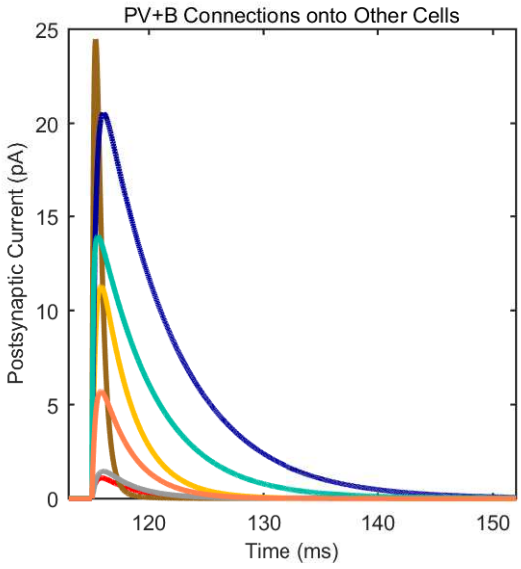
PV+B Connections onto Other Cells
Postsynaptic Current (pA)
25
20
15
10
5
0
120
130
140
150
Time (ms)

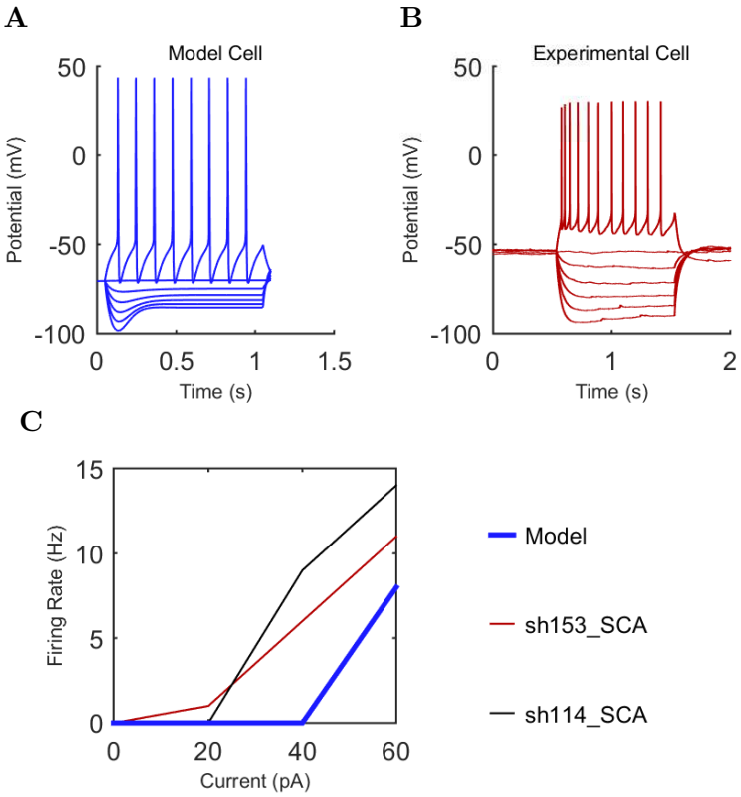
A
Model Cell
Potential (mV)
50
0
-50
-100
0
0.5
1
1.5
Time (s)
B
Experimental Cell
Potential (mV)
50
0
-50
-100
0
1
2
Time (s)
C
Firing Rate (Hz)
15
10
5
0
0
20
40
60
Current (pA)
Model
sh153_SCA
sh114_SCA

A

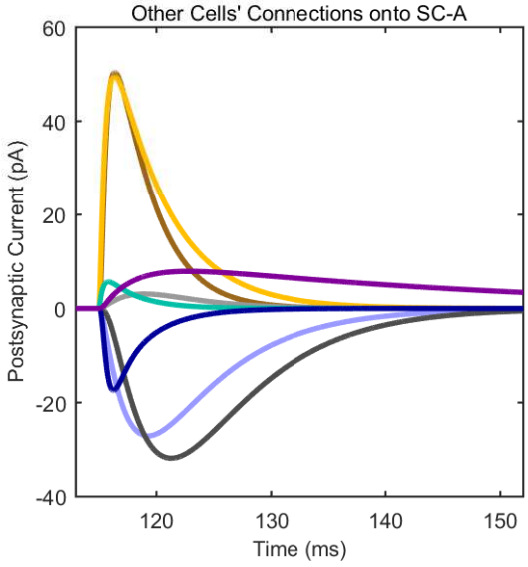
Other Cells' Connections onto SC-A
Postsynaptic Current (pA)
60
40
20
0
-20
-40
120
130
140
150
Time (ms)

B

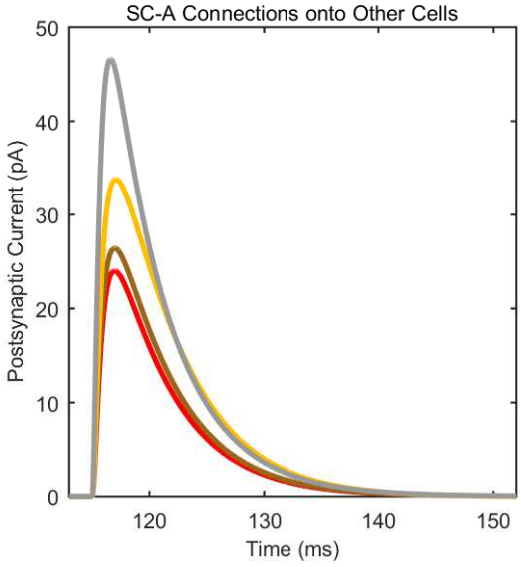
SC-A Connections onto Other Cells
Postsynaptic Current (pA)
50
40
30
20
10
0
120
130
140
150
Time (ms)

A Activation Curve

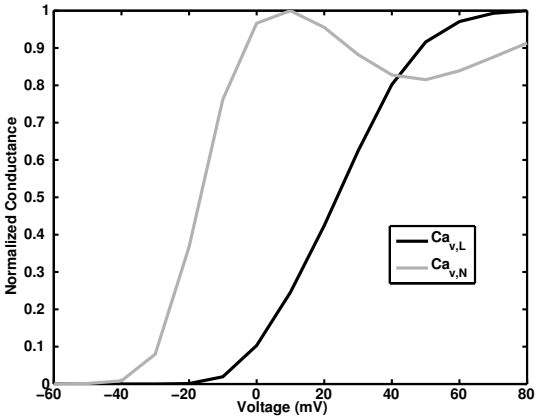

B Inactivation Curve

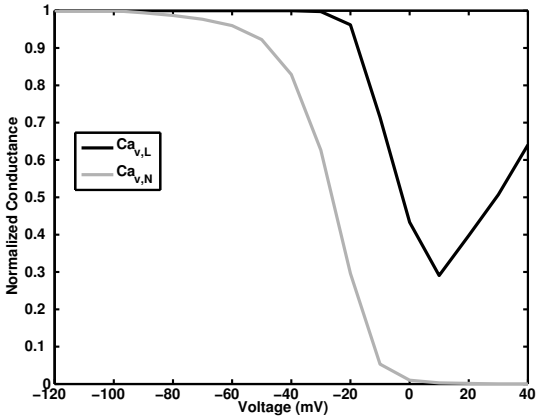

C Peak Current

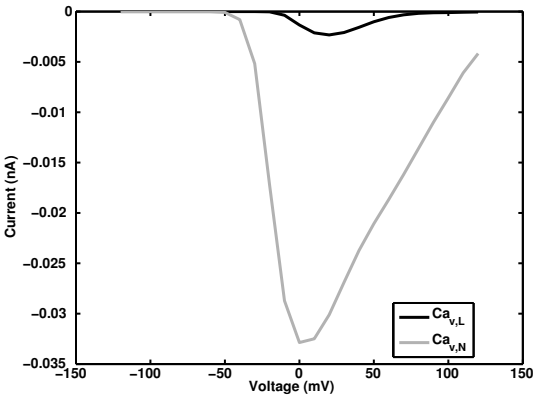

D Steady State Current

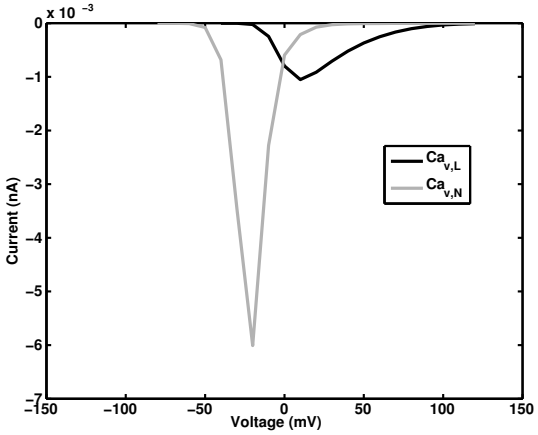

A Activation Curve

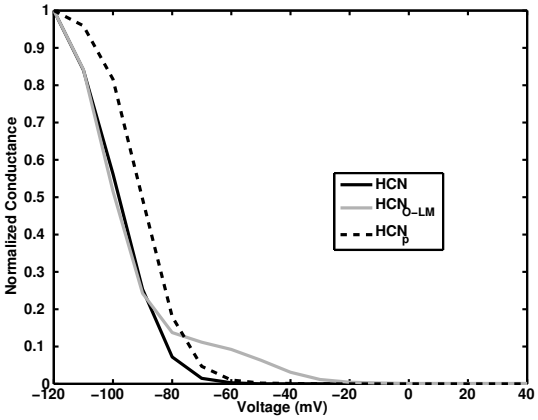

B Peak Current

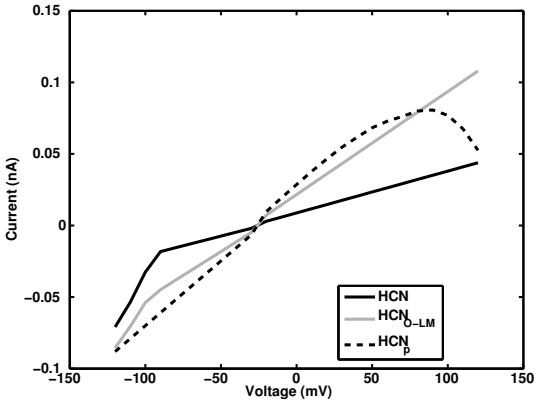

C Steady State Current

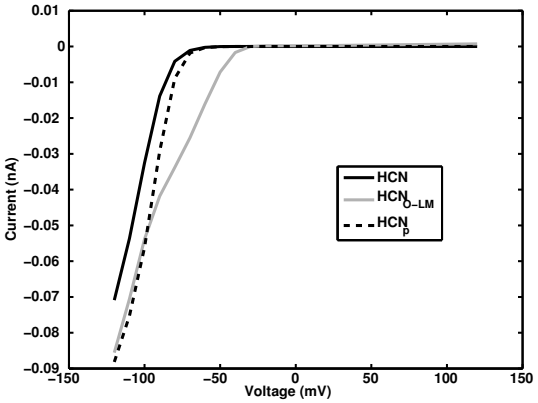

A Activation Curve

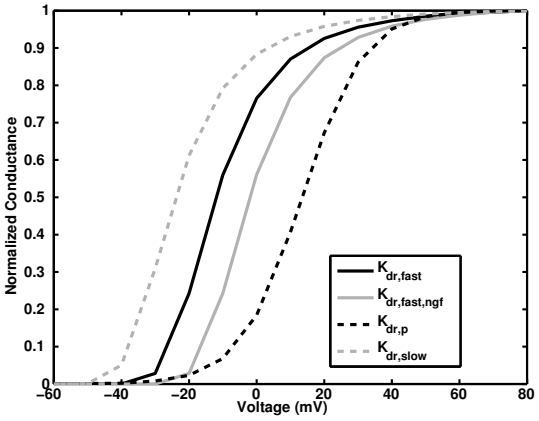

B Peak Current

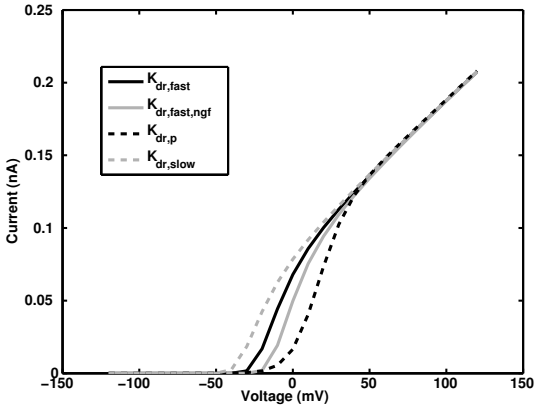

A Activation Curve

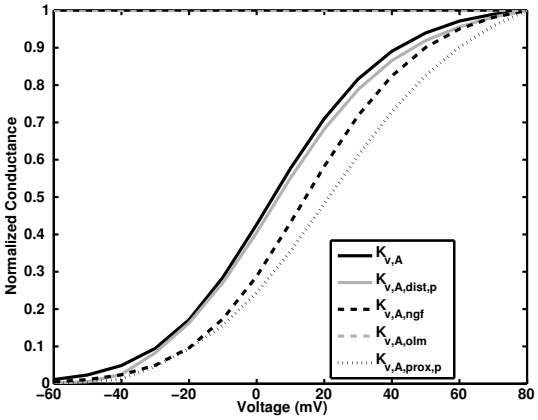

B Inactivation Curve

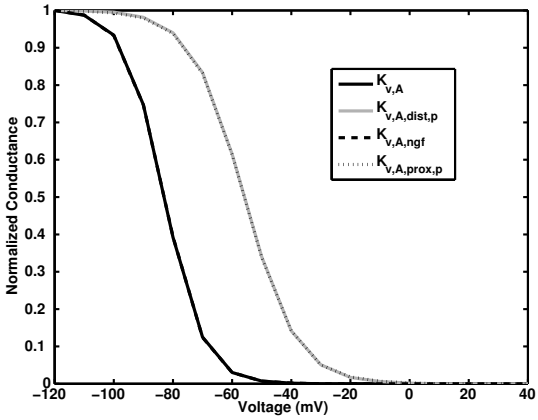

C Peak Current

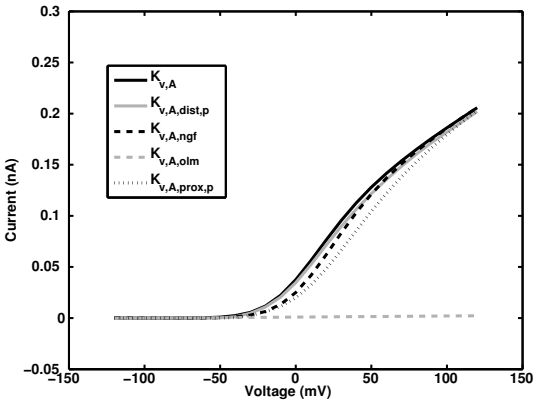

D Steady State Current

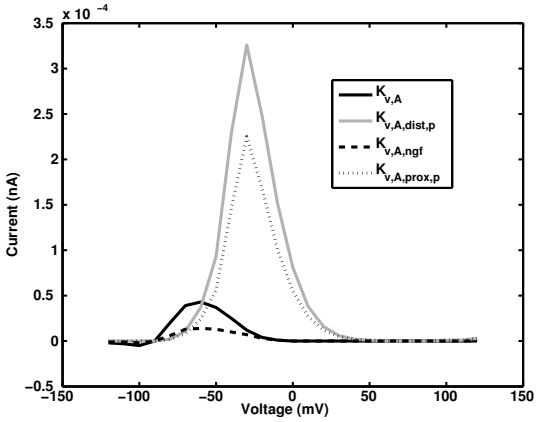

A Activation Curve

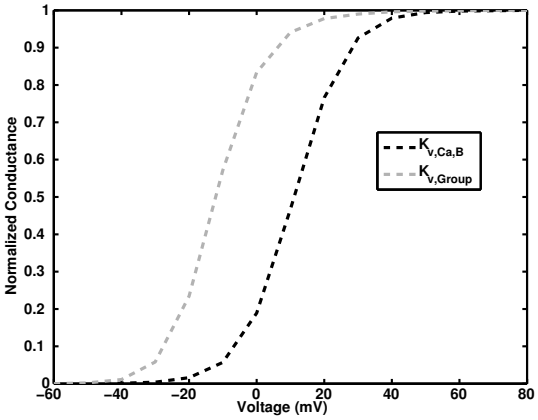

B Peak Current

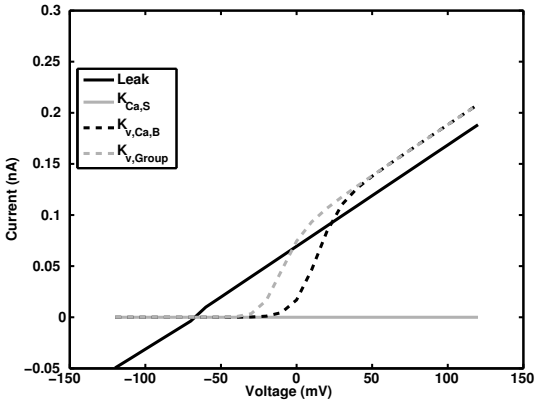

A KvCaB Activation Curve

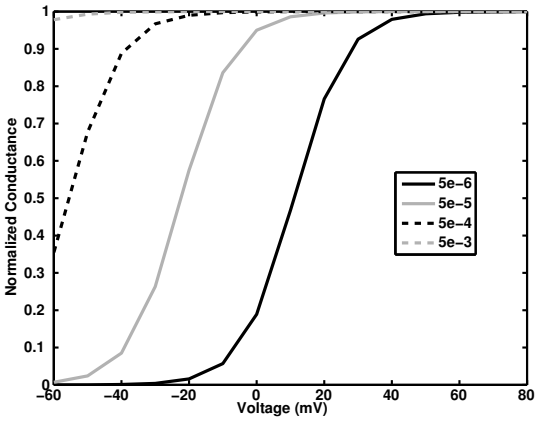

B KvCaB Peak Current

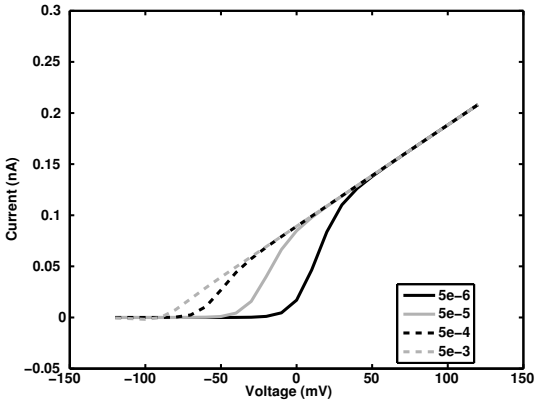

C KCaS Peak Current

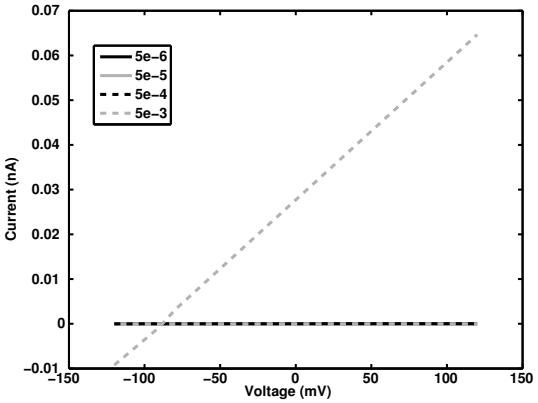

A Activation Curve

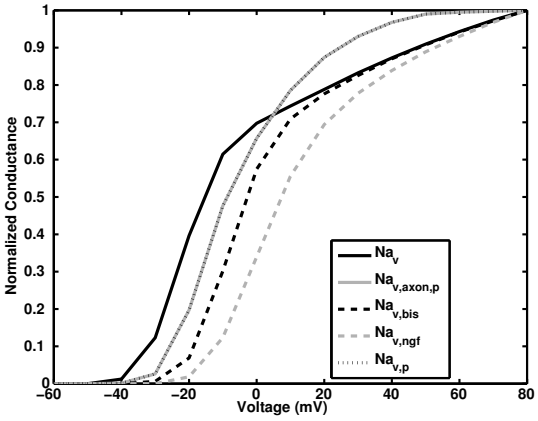

B Inactivation Curve

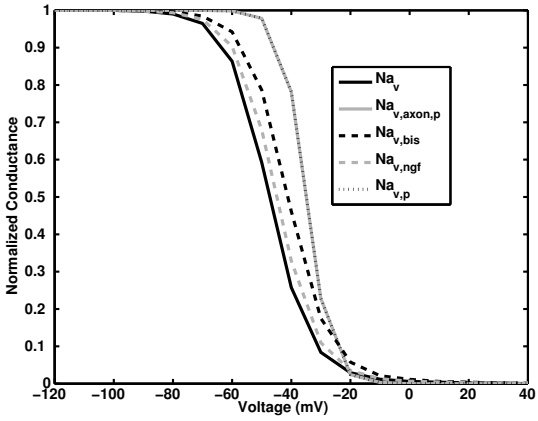

C Peak Current

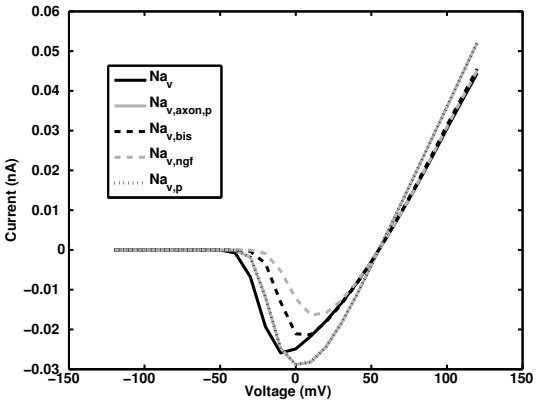

D Steady State Current